Inaugural-Dissertation

zur
Erlangung der Doktorwürde
der
Naturwissenschaftlich-Mathematischen Gesamtfakultät
der
Ruprecht-Karls-Universität Heidelberg

Vorgelegt von
Marko Hermsen
aus
Bonn

Tag der mündlichen Prüfung: 25. Oktober 2018

Quantum Chemical Investigations in Homogeneous Catalysis: Dehydroperoxidation and Asymmetric Reductive Amination

Quantenchemische Untersuchungen in der homogenen Katalyse: Dehydroperoxidierung und asymmetrische reduktive Aminierung

Erster Gutachter: Prof. Dr. Peter Comba
Zweiter Gutachter: Prof. Dr. Andreas Dreuw

"I would desire [...] to establish the conviction, that Chemistry, as an independent science, offers one of the most powerful means towards the attainment of a higher mental cultivation; that the study of Chemistry is profitable, not only inasmuch as it promotes the material interests of mankind, but also because it furnishes us with insight into those wonders of creation which immediately surround us, and with which our existence, life and development, are most closely connected.
It is so congenial to the ever-active human intellect to inquire into the causes of natural phenomena, and into the changes which we daily observe in all that surrounds us, that those sciences which give satisfactory answers to our inquiries exercise more influence on the progress of mental cultivation than any others."

— Justus von Liebig,
Familiar Letters on Chemistry, **1851**,
Letter I, Importance of Chemistry, 3rd Edition, *IV*, 1.

Acknowledgments

It is important to mention, that during my studies of different projects in homogeneous catalysis, I had the pleasure to be part of three institutions: the Comba research group at Heidelberg University, the Catalysis Research Laboratory (CaRLa) and the Quantum Chemistry and Hybrid Modelling group ROM/CQ at BASF. I have been lucky to work and interact with many engaged, dedicated and knowledgeable people at all of these institutions. I would like to extend my first thanks therefore to the heads of these groups – their help, guidance and mentoring has been essential during my time as a PhD student.

Peter, thanks for being my principal investigator and advisor during the three years! Thanks for the opportunity to pursue my PhD in your group, the effort you put in for supporting me as an "external" PhD student at CaRLa and your ideas and suggestions for my projects. Although I have never worked on iron chemistry, you were nevertheless committed and enthusiastic regarding my research. Also thanks for the opportunity to attend the computational chemistry summer school in Notre Dame in 2016 and lastly the three ski seminars from which I learned how to ski (and hopefully will never forget)!

Ansgar, thanks for being my mentor in computational chemistry! I have certainly learned a lot in computational chemistry in the past three years. Despite your full schedule, you managed to discuss my projects every two weeks with me which was incredibly helpful. Be it general questions on quantum chemistry, problems with TURBOMOLE or any other issues I had during my PhD, I could always discuss them with you. I am also thankful for being given the opportunity to attend conferences around the world on both computational chemistry and homogeneous catalysis. I had a lot of fun presenting my research in the US, Portugal, Germany and Japan. Thanks also for my time at ROM/CQ – you have an amazing group working on exciting projects in many different areas of chemistry. Being able to learn how computational chemistry is applied in industry was a unique and very valuable experience!

Thomas, thanks for being my mentor in homogeneous catalysis! I guess there are not many

other computational chemistry PhDs who have had the opportunity to learn organometallic chemistry and homogeneous catalysis (and especially their role in industrial chemistry!) from someone as knowledgeable as you! A special thanks also for the opportunity to work on many different and interesting projects at CaRLa and the opportunity to interact with different projects and people at RCS, which gave me an in-depth look into the synthetic/experimental part of industrial research. Despite being the only PhD student and the only computational chemist at CaRLa, I have always felt as a full member of the group. Thanks also to you for letting me present my research at various conferences!

I would also like to thank Prof. Andreas Dreuw for taking up the second review of this thesis.

Thanks to all the people at CaRLa during my three years as a PhD. I am grateful for being accepted at CaRLa from the start, the friends I have made and the fruitful discussions I had with many of you. Special thanks to the postdocs who have worked with me on various projects:

Anna-Corina Schmidt who worked on the vanadium-based dehydroperoxidation. Thanks for borrowing me your folding cot when I moved to Heidelberg so that I did not have to sleep on the floor in my first week; also for the many other occasions where you helped me out!

Juan Gallardo-Donaire who worked on the direct asymmetric reductive amination. I learned a lot of organic chemistry from you! Thanks also for the trip to Barcelona and Tarragona!

Jessica Hamann, who worked on the chromium-catalyzed dehydroperoxidation. Thanks for the fun we had at the ISySyCat and in Lisbon!

I would also like to thank Tamal Gosh and Jedrzej Wysocki who continued the experimental work on the asymmetric reductive amination and Bilguun Bayarmagnai, Saumya Dabral and Aviel Anaby with whom I've worked on projects that did not make it into this thesis.

Thanks also go to Alexandre Dunlop-Brière for introducing me to squash, hiking trips and dinner nights, and also Naohisa Nakagawa from whom I inherited CaRLa's theoretician bike and who hosted me in Japan.

I also want to thank all members of the Comba research group for the good time I have had there! Although I worked only on CaRLa/BASF projects, I always felt that I was a full member of the Comba research group. I would like to thank two people in particular:

Annika, thank you! If it were not for your posting of the position at CaRLa, I probably would have never had the opportunity to do my PhD here.

Dieter, thanks for the great time! There are too many things I would have to list here; let's say Heidelberg's old town (or for that matter Chicago or London) was much more fun having you around!

I would like to thank my colleagues at ROM/CQ in BASF. Thanks for your help and support and the good time that I had at BASF! It is amazing to have a group of people specialized in so many aspects of computational chemistry that there is always someone to go to, no matter what the issue is. Special thanks go to my office colleagues Imke Müller and Nedko Drebov, without whom I would probably still try to figure out on how to run certain calculations with TURBOMOLE or COSMOtherm. Thanks also to Peter Deglmann, Jan-Marco Wilhelm and Oliver Sala of ROM/AM for the help with CP2K and advice on the molecular dynamics simulations.

I would like to thank Martin Rohbeck for his help with statistics in Python.

Thanks also to Klaus Kreuels and Arno Förster for proofreading of this thesis.

I am also grateful to CaRLa and BASF for funding this PhD thesis and providing computational resources that most PhD students in computational fields can probably only dream of.

Thanks to Frank Rominger from the OCI for the measurement of crystal structures and providing the CCDC database search results.

Anyone that I might have forgotten here: thank you!

Finally, I would like to thank my family for their support throughout all the years. Neither this dissertation nor my studies in chemistry would have been possible without you.

Quantum Chemical Investigations in Homogeneous Catalysis: Dehydroperoxidation and Asymmetric Reductive Amination

Abstract

This thesis describes the investigation of homogeneously catalyzed reactions with quantum chemical methods. Two different reactions were studied in this work: the dehydroperoxidation of alkyl hydroperoxides with both vanadium and chromium catalysts and the direct asymmetric reductive amination of ketones with ruthenium.

In the first part, the dehydroperoxidation of cyclohexyl and 4-heptyl hydroperoxide to the corresponding ketones with a vanadium dipicolinato complex is investigated. It is found that a radical-free mechanism is feasible and that it proceeds through hydrogen abstraction by the vanadium oxo group. The barrier difference for this process for both substrates is in line with higher experimental selectivities for the non-cyclic hydroperoxide. A mechanistic study on the chromium-catalyzed dehydroperoxidation follows, which shows that a similar mechanism is active for Cr. The better selectivity and activity of this catalyst in comparison with the vanadium system is reproduced as the activation energy for dehydroperoxidation is lower with chromium. Finally, we rule out that the reaction proceeds via an intramolecular hydrogen transfer in an alkoxy/alkylperoxo chromium species, which has been suggested in previous research on the topic.

The second part of the thesis explores the mechanism of the direct asymmetric reductive amination of ketones with a ruthenium (*S*,*S*)-*f*-binaphane complex. Acetophenone is used as the model ketone for this reaction. The investigations show that the rate-determining step of the reaction is the proton transfer from a σ-dihydrogen complex to liberate the amine. A thorough analysis of possible isomer/conformer combinations turns out to be crucial for a quantitative understanding of the reaction; following such an analysis, the experimental enantioselectivity is accurately reproduced for a series of catalysts with different halide ligands. These results are supplemented by studies on the chemoselectivity of the reaction. The mechanism is then applied to build a simple model for estimating the bite angle dependency of the reaction's enantioselectivity. It is predicted that larger bite angles should favor higher enantioselectivity. A search in the CCDC database reveals several promising ligand backbone candidates for an optimized binaphane ligand of which a biaryl motif is finally considered as the most promising candidate.

Quantenchemische Untersuchungen in der homogenen Katalyse: Dehydroperoxidierung und asymmetrische reduktive Aminierung

Kurzzusammenfassung

Diese Arbeit befasst sich mit der Untersuchung homogen katalysierter Reaktionen mit quantenchemischen Methoden. Zwei verschiedene Reaktionen wurden in dieser Arbeit untersucht: die Dehydroperoxidierung von Alkylhydroperoxiden mit Vanadium- und Chromkatalysatoren und die direkte asymmetrische reduktive Aminierung von Ketonen mit Ruthenium.

Im ersten Teil wird die Dehydroperoxidierung von Cyclohexyl- und 4-Heptylhydroperoxid zu den entsprechenden Ketonen mittels eines Vanadiumdipicolinatokomplexes untersucht. Es wird gezeigt, dass ein radikalfreier Mechanismus möglich ist und über eine Wasserstoffabstraktion durch die Vanadium-Oxo-Gruppe erfolgt. Die Barrierenunterschiede zwischen den beiden Substraten stimmen überein mit der besseren Selektivität für das nicht-zyklische Hydroperoxid. Es folgt eine mechanistische Studie der chromkatalysierten Dehydroperoxidierung, in der gezeigt wird, dass ein sehr ähnlicher Mechanismus für Cr aktiv ist. Die bessere Selektivität und Aktivität dieses Katalysators im Vergleich zu Vanadium wird bestätigt, da die Aktivierungsenergie für die Dehydroperoxidierung mit Chrom geringer ist. Abschließend wird ausgeschlossen, dass die Reaktion mittels eines intramolekularen Wasserstofftransfers einer Alkoxy/Alkylperoxo-Chromspezies abläuft, wie es in früheren Untersuchungen vorgeschlagen wurde.

Der zweite Teil der Arbeit untersucht den Mechanismus der direkten asymmetrischen reduktiven Aminierung von Ketonen mit einem Ruthenium-(*S*,*S*)-*f*-binaphan-Komplex. Acetophenon dient als Modellsubstrat für diese Reaktion. Die Untersuchungen zeigen, dass der geschwindigkeitsbestimmende Schritt der Protonentransfer von einem σ-Diwasserstoffkomplex zur Bildung des Amins ist. Es wird festgestellt, dass eine gründliche Analyse der möglichen Kombinationen von Isomeren und Konformeren nötig ist für das quantitative Verständnis der Reaktion. Dieser Analyse folgend, ist es möglich die experimentellen Enantioselektivitäten für mehrere Katalysatoren mit verschiedenen Halogenidliganden zu reproduzieren. Diese Ergebnisse werden dann um Studien zur Chemoselektivität der Reaktion erweitert. Der Mechanismus wird verwendet um ein einfaches Modell für die Abhängigkeit der Enantioselektivität vom Bisswinkel des Chelatliganden zu konstruieren. Es wird vorhergesagt, dass größere Bisswinkel in höherer Enantioselektivität resultieren sollten. Eine Suche in der CCDC-Datenbank bringt verschiedene Kandidaten für ein neues Binaphanrückgrat hervor, von denen ein Biarylmotiv letzten Endes am vielversprechendsten erscheint.

Previous Publications

Parts of this thesis have already been published in different academic journals over the last three years:

Dehydroperoxidation with Vanadium Catalysts

Schmidt, A. C.; Hermsen, M.; Rominger, F.; Dehn, R.; Teles, J. H.; Schäfer, A.; Trapp, O.; Schaub, T. Synthesis of Mono- and Dinuclear Vanadium Complexes and Their Reactivity toward Dehydroperoxidation of Alkyl Hydroperoxides. *Inorganic Chemistry* **2017**, *56*(3), 1319–1332.
https://doi.org/10.1021/acs.inorgchem.6b02322

Dehydroperoxidation with Chromium Catalysts

Hamann, J. N.; Hermsen, M.; Schmidt, A.-C.; Krieg, S.; Schießl, J.; Riedel, D.; Teles, J. H.; Schäfer, A.; Comba. P.; Hashmi, A. S. K.; Schaub, T. Selective Decomposition of Cyclohexyl Hydroperoxide using Homogeneous and Heterogeneous Cr(VI) Catalysts: Optimizing the Reaction by Evaluating the Reaction Mechanism. *ChemCatChem* **2018**, *10*, 2755-2767.
https://doi.org/10.1002/cctc.201701909

Direct Reductive Asymmetric Amination

Gallardo-Donaire, J.; Hermsen, M.; Wysocki, J.; Ernst, M.; Rominger, F.; Trapp, O.; Hashmi, A. S. K.; Schäfer, A.; Comba, P.; Schaub, T. Direct Asymmetric Ruthenium-Catalyzed Reductive Amination of Alkyl-Aryl Ketones with Ammonia and Hydrogen. *Journal of the American Chemical Society* **2018**, *140*(1), 355–361.
https://doi.org/10.1021/jacs.7b10496

Contents

List of Abbreviations

acac	Acetylacetonate
BDE	Bond Dissociation Energy
BO	Born-Oppenheimer
BJ	Becke-Johnson
COSMO-RS	Conductor-like Screening Model for Real Solvents
CCDC	Cambridge Crystallographic Data Centre
CSD	Cambridge Structural Database
CCSD	Coupled cluster theory with full single and double excitations
CCSD(T)	Coupled cluster theory with full single and double excitations and perturbatively treated triples
COD	Cyclooctadiene
CyOH	Cyclohexanol
CyOOH	Cyclohexyl Hydroperoxide
DCM	Dichloromethane
DFT	Density Functional Theory
dipic	Pyridine-2,6-dicarboxylic Acid
dppe	Diphenylphosphinoethane
ECP	Effective Core Potential
ee	Enantiomeric Excess
EHT	Extended Hückel Theory
Et	Ethyl (Group)
FD-MS	Field Desorption Mass Spectrometry
FT-IR	Fourier-transform Infrared Spectroscopy
GGA	Generalized Gradient Approximation
GTO	Gaussian-type Orbital
HeptOOH	4-Heptyl Hydroperoxide
HF	Hartree-Fock
ICP-MS	Inductively Coupled Plasma Mass Spectrometry

KA	Ketone-Alcohol
KS	Kohn-Sham
LCAO	Linear Combination of Atomic Orbitals
LDA	Local Density Approximation
MAD	Mean Absolute Deviation
MD	Molecular Dynamics
Me	Methyl (Group)
MP	Møller-Plesset
NMR	Nuclear Magnetic Resonance
NPT ensemble	Isothermal-isobaric ensemble
NVT ensemble	Canonical ensemble
PES	Potential Energy Surface
Ph	Phenyl (Group)
PNP (ligand)	Ligand with bridged phosphorous-nitrogen-phosphorous donor atoms
PPh_3	Triphenyl Phosphine
PVP	Poly(4-vinylpyridine)
py	Pyridine
QMC	Quantum Monte Carlo
RA	Reductive Amination
RI	Resolution of the Identity
RPA	Random Phase Approximation
SCF	Self-consistent field
STO	Slater-type Orbital
TBAI	Tetrabutyl Ammonium Iodide
*t*Bu	*tert*-Butyl (Group)
TDDFT	Time-dependent Density Functional Theory
TS	Transition State
UV/Vis	Ultraviolet-Visible
vdW	van der Waals
ZPVE	Zero-point Vibrational Energy

List of Mathematical and Natural Constants

i	Imaginary Unit	$\sqrt{-1}$
e	Euler's Number	2.7182818284
π	Archimedes' Constant	3.1415926535
k_B	Boltzmann Constant	$1.380\,648\,52 \times 10^{23}$ kg·m^2·s^{-2}·K^{-1}
h	Planck Constant	$6.626\,070\,040 \times 10^{-34}$ J·s
$\hbar$	Reduced Planck Constant	$1.054\,571\,800 \times 10^{-34}$ J·s
N_A	Avogadro Constant	$6.022\,140\,857 \times 10^{23}$ mol^{-1}
R	Gas Constant	8.314 459 8 J·mol^{-1}·K^{-1}
c	Speed of Light	299 792 458 m·s^{-1}
m_e	Electron Mass	$9.109\,383\,56 \times 10^{-31}$ kg
m_p	Proton Mass	$1.672\,621\,898 \times 10^{-27}$ kg
α	Fine Structure Constant	$7.297\,352\,566\,4 \times 10^{-3}$
e	Elementary Charge	$1.602\,176\,620\,8 \times 10^{-19}$ C
ϵ_0	Vacuum Permittivity	$8.854\,187\,817 \times 10^{-12}$ A·s^4·kg^{-1}·m^{-1}

1

Introduction

Chemistry is the study of compounds, their properties, structure and – perhaps most importantly – their transformations: chemical reactions, in which compounds interact to form a new set of compounds. It is therefore not surprising that understanding not only *which* reactions can occur and *what* compounds can be formed has been of particular interest, but more importantly, *how* these transformations, on a molecular, atomistic basis, exactly take place. The investigation of reaction mechanisms is essential for chemistry in that it provides insight into known reactions and explains the observed behavior of chemicals and reaction properties such as activity and selectivities. Extending further, the knowledge of reaction mechanisms of already established reactions has been a key driver for the discovery of new reactions and prediction of reaction outcomes for unknown chemical systems.

The actual investigation of a reaction mechanism, however, is not trivial. Any experimental attempt to elucidate the chemical events taking place during a reaction must almost exclusively rely on indirect observation of secondary properties. The actual molecular changes cannot be directly observed due to their size (usually less than a nanometer) and the speed with which they proceed (usually less than a picosecond). A very common approach is the study of reaction kinetics, where the rate of product formation and/or reactant depletion is observed

at different temperatures, pressures or solvents, but also isotopes, differently substituted substrates or varying acid/base strengths to see whether they influence the reaction and might therefore play a role in a potential mechanism. Besides kinetics, studying the products and intermediates and their distribution can give hints on the underlying reaction mechanism. The effect of substitution patterns on product selectivities may tell which of several reaction pathways might be most likely, reaction intermediates can be observed *in situ* or trapped to find stationary points that a transformation proceeds through. In a reaction yielding chiral products, the observed enantioselectivity may be a sign of how the reaction takes place spatially, retention/inversion of a chiral center can hint at intermediates in the reaction mechanism and cross-over experiments can potentially distinguish between inter- and intramolecular reaction mechanisms. Many more experiments and tests have been conceived, and almost always a combination of several is needed to give a satisfactory mechanistic interpretation. Accordingly, a plethora of analytical tools and methods have been developed that are still becoming more and more sophisticated, without which these experimental investigations would not be possible.

Nonetheless, there are many cases, especially in the complex chemistry of today, where experimental insight into reaction mechanisms can be severely limited. For a start, there are properties, effects or intermediates that are very hard to access through experiment for various reasons, and there are other entities that cannot be determined by experiment. It is therefore of high interest to be able to calculate or simulate the systems at hand using appropriate theory to complement the experiments. This is where computational chemistry comes into play.

Among the different branches of chemistry, it should be considered that computational chemistry is still a very young one. While the foundations were laid in the early 20th century with the emergence of quantum mechanics in physics and Schrödinger's famous 1926 paper[1] postulating the differential eigenvalue equation that is now central to quantum chemistry, it took some time until application of theory to synthetic problems became widely used. Shortly after Schrödinger's seminal paper, Hartree and Fock proposed what is now known as Hartree-Fock theory,[2,3] but it took until 1951 when Roothaan and Hall proposed the LCAO method[4,5] rendering calculations based on Hartree-Fock theory feasible, albeit being still computationally expensive considering computational resources at the time. Hence, semi-empirical methods were preferred, where neglection or approximation of integrals enabled calculation for chemically interesting systems and still provided reasonably good (qualitative) results. Hückel had already proposed a simple semi-empirical theory in the early thirties[6–9] to describe π-electron systems. Hoffmann developed the extended Hückel theory (EHT) in 1963, which could

also be used for σ bonds and thus be applied to whole organic molecules and reactions; very shortly afterwards, Woodward and Hoffmann proposed their rules for pericyclic reactions[10] supported by EHT calculations, perhaps one of the first and very elegant examples of how quantum chemistry could explain the mechanism of a whole group of reactions and guide experimental work through prediction. At the same time, in 1964, Hohenberg and Kohn published two theorems,[11] now named after them, which would lay the foundation of density functional theory – today the most widely applied method in computational chemistry. The Kohn-Sham formalism was published only a year later,[12] and the first local density approximation functionals appeared in the following years. In the 1970s and 1980s, algorithms were developed to facilitate the first accurate total energy calculations, analytical gradients enabled automated geometry optimizations and analytical second derivatives were implemented. The local density approximation was superseded by more accurate functionals based on the generalized gradient approximation, and relatively accurate quantitative predictions for a wide range of chemistry were possible for the first time. Beginning in 1990, a surge in publications on density functional theory started that continues until today; more and more researchers joined the field and applied density functional theory to their particular chemical problem of interest.

The success of computational chemistry may more generally be attributed to two factors: the exponential increase in available computational power (often referred to as Moore's law) and the development of more efficient quantum chemistry methods and their algorithmic implementations. For example, Intel's first commercial processor "Intel 4004" was released in 1971 and had a clock rate of 500 kHz with 2300 transistors; the first Pentium series processor released in 1993 already featured 3.1 million transistors and a clock rate of 60 MHz; as of writing this thesis, a recent generation processor has a clock rate of 3.0 GHz on multiple cores with 2.6 billion transistors (Intel i7-5960, 2014). Additional gains in computational power are anticipated from future use of quantum computers in computational chemistry. Likewise, DFT has turned into a fast and accurate method for electronic structure calculations. Coming from the local density and generalized gradient approximation, more accurate hybrid, meta-hybrid and dispersion-corrected functionals have been and are continously further developed, together with countless other functionals and methods which can already exceed experimental accuracy in some areas of research and approach chemical accuracy in others.

This rapid development has opened up possibilities to computationally investigate reaction mechanisms in the field of homogeneous transition metal catalysis, which the research at the Catalysis Research Laboratory (CaRLa) revolves around. At CaRLa, current problems in

industrial homogeneous catalysis are tackled, with experiment and theory working hand in hand. Computational chemistry is used in various ways: to evaluate whether new projects are feasible from a thermodynamic perspective, to visualize geometries of hypothetical ligands and complexes, for calculation of spectra or other properties such as pK_as or boiling points. The main focus, however, is the investigation of mechanisms for homogeneously catalyzed reactions. Insights from these investigations are not only helpful in understanding how a reaction works; they are used to guide the experimental work, generate new ideas, suggest useful experiments and make predictions.

In this thesis, two independent problems of industrial importance and their solutions developed at CaRLa have been studied computationally and will be described. The first is the oxidation of cyclohexane to cyclohexanone, an old and established industrial process, where we looked into the radical free decomposition of hydroperoxides, key intermediates during the reaction, to see whether an alternative process is feasible that could potentially increase selectivity in the current industrial cyclohexanone process. The chemistry of promising vanadium and later chromium-based complexes was evaluated with respect to a feasible mechanism of dehydroperoxidation. In the second topic of this thesis, the direct asymmetric reductive amination of ketones with ammonia and hydrogen was studied. This reaction is very challenging due to a number of factors, and has only very recently been achieved in our lab. The chiral ruthenium catalyst facilitating this reaction has been intensively studied in this work, since experimental insight was limited for this reaction, and mechanistic explanations are desired to understand and further improve this new system and predict potentially better catalyst candidates.

This thesis is purely computational, but in the concept of CaRLa, all work is based on and in cooperation with experimental work. The experiments mentioned have therefore not been performed by me, but by several of the postdoctoral researchers who worked on the different projects: Anna-Corina Schmidt and Jessica Nadine Hamann for the vanadium- and chromium-catalyzed dehydroperoxidation reactions, and Juan Gallardo-Donaire and Jedrzej Wysocki for the ruthenium-catalyzed direct reductive asymmetric amination of ketones.

2

Theory

This chapter shall explain some of the basic concepts and methods, as well as their theoretical background and foundation, that were necessary for the preparation of this thesis. By no means can this chapter be considered an extensive review of the following topics, rather, it is intended to explain the basics of the applied methods to get a sense of what is behind the quantum chemical programs that were used in this work.

2.1 Reaction Paths

The general idea behind reaction paths is, that any chemical reaction can be described as proceeding from its reactants to its products through intermediates which are connected through transition states. Intermediates are structural arrangements of atoms corresponding to minima on the potential energy surface, while transition states, the connections between intermediates, are saddle points where in direction of negative curvature two intermediates or minima can be found.

In the computational study of chemical reactions, including that of homogeneously catalyzed reactions, reaction paths have occupied an important place, the reason being that they provide

useful insights into the studied reactions with even predictive power at reasonable computational cost. It should be noted, that the exploration of reaction paths also comes with a central disadvantage – the intrinsic bias that the scope of possible intermediates and transition states is subject to the researcher's imagination. If one were to miss out on the actual path of a reaction, it is possible to make false conclusions about a reaction when other studied reaction paths seem reasonable. Ab initio molecular dynamics for the study of chemical reactions may therefore seem more suitable as it can potentially sample a much larger phase space, but since the timescales of many reactions lie on the order of milliseconds to hours or even days, it is usually not feasible. Similarly, the full exploration of a system's potential energy surface is computationally too expensive. To minimize the potential danger of accepting a proposed mechanism that is not occurring in reality, it is of importance that an extensive investigation into several plausible mechanisms is undertaken. Even more importantly, computational results should be validated by experiment and reproduce experimental findings. Different mechanistic proposals will yield different reaction paths, which are then weighted according to their energies. Generally, free enthalpies or Gibbs energies G are discussed. The path whose energetically highest transition state is the lowest relative to all other paths may usually be considered to be the dominating mechanism for a reaction.

Feasability of a reaction can be judged by the highest transition state that the reaction path proceeds through. Usually the Eyring equation[13] (eq. 2.1) is applied to estimate reaction rates, where for catalyzed reactions the reaction can usually be assumed to proceed in pseudo-first order kinetics.

$$k = \kappa \frac{k_B T}{h} e^{-\frac{\Delta G^{\ddagger}}{RT}} \tag{2.1}$$

The transmission coefficient κ, the fraction of successful transition state crossings, is usually taken as $\kappa = 1$. Under this assumption, the rate constant k of a reaction at given temperature T can then be calculated from the reaction's Gibbs free energy of activation $\Delta G^{\ddagger}$. For example, as a rule-of-thumb, reactions with an energetic gap (difference between the free enthalpies of the highest transition state and the lowest intermediate) of around 100 kJ·mol^{-1} are considered feasible at room temperature. Following this example, from equation 2.1, a rate constant of k = 1.88 $\times$ 10^{-5} s^{-1} can be deduced. For a pseudo-first order reaction, the half-life λ can be calculated as:

$$\lambda = \frac{\ln(2)}{k} \tag{2.2}$$

This translates into a reaction half-life of 10.2 h which is quite well on the temporal order of

magnitude of most reactions that are performed in organic chemistry. The observed reaction time will not only depend on $\Delta G^{\ddagger}$, but also on the temperature T and in principle on the pressure p. The latter is usually less of relevance as differences in concentration are accounted for through partial pressures or mole fractions, while direct influence of the pressure only has an effect for reactions where the volume of activation $\Delta V^{\ddagger}$ is significant or where the number of particles changes. For most homogeneously catalyzed reactions, the span of applied pressures is 1-100 bar, where pressure dependence of the free enthalpies can be neglected. The applied temperatures are of greater significance as they usually span a greater range. Furthermore, we can write the conversion x as a function of reaction time t of a reaction with half-life λ as:

$$x = 1 - \frac{1}{2^{\frac{t}{\lambda}}} \tag{2.3}$$

Similarly, the reaction time t can be written as:

$$t = \frac{\ln\left(\frac{1}{1-x}\right)}{\ln(2)}\lambda \tag{2.4}$$

Using the above equations, we can infer the maximum $\Delta G^{\ddagger}$ for a reaction with observed half-life λ at given temperature T:

$$\Delta G^{\ddagger} = RT \ln\left(\frac{\lambda k_B T}{h \ln(2)}\right) \tag{2.5}$$

Correspondingly, the reaction time t for a reaction with given activation energy $\Delta G^{\ddagger}$ at temperature t to achieve conversion x can be calculated:

$$t = \frac{h \ln\left(\frac{1}{1-x}\right)}{k_B T} e^{\frac{\Delta G^{\ddagger}}{RT}} \tag{2.6}$$

Graph 2.1 illustrates the upper limit on $\Delta G^{\ddagger}$ depending on the temperature T that can be considered under various criteria of reaction completion – here reaction times t to achieve certain conversions are given, which are more convenient than half-lifes. The strong temperature dependence of the reaction rate can be seen in Figure 2.2 – for example, a reaction with a barrier of 100 kJ·mol^{-1} takes around a day to complete at room temperature, but will proceed within a minute at 100 °C and around a second at 150 °C.

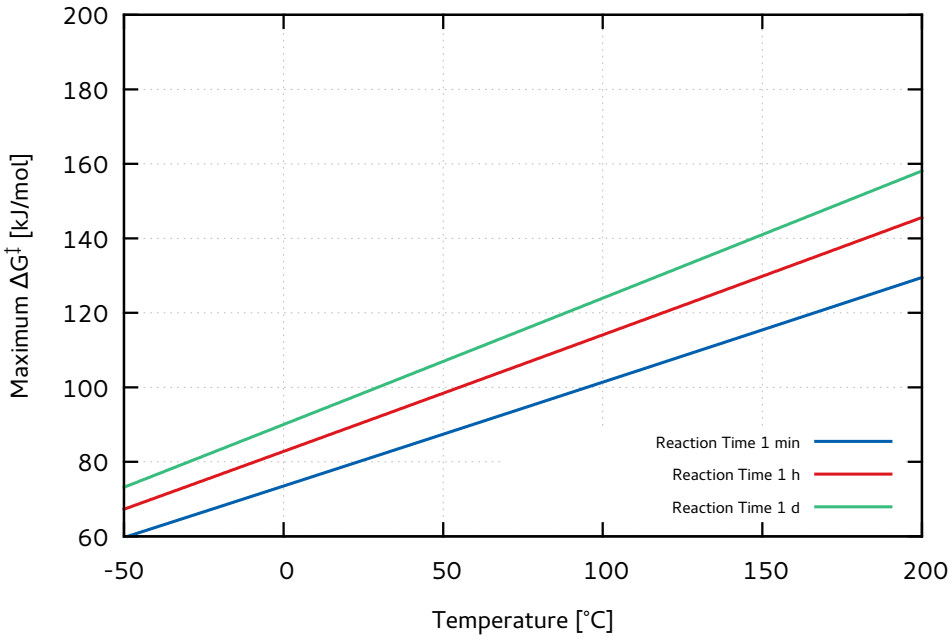

Figure 2.1: Maximum $\Delta G^{\ddagger}$ for reactions reaching 95% conversion after one hour, one minute and one day.

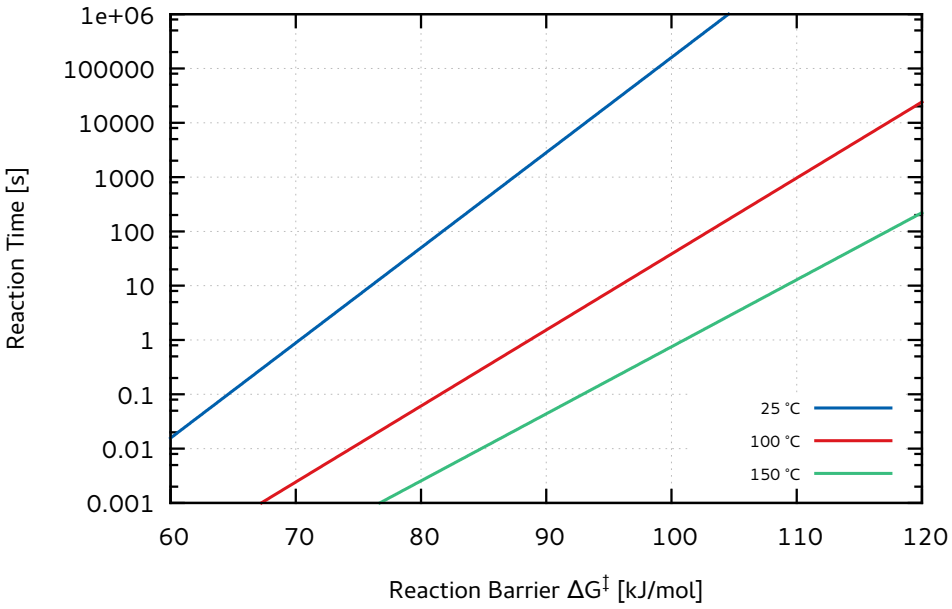

Figure 2.2: Expected reaction times for reactions with overall barrier $\Delta G^{\ddagger}$ to achieve 95% conversion at 25 °C, 100 °C and 150 °C.

Lastly, it should be noted that these are just guidelines for ranges of reasonable activation energies – the direct determination of absolute rate constants from computation still remains a challenge. The transmission coefficient κ can deviate substantially from 1 (sometimes by

several orders of magnitude), and in principle full knowledge of the potential energy surface is needed for an accurate estimation of κ.

2.2 Thermodynamic Corrections

The final computed free enthalpies G for all intermediates and transition states in reaction paths are composed of several contributions: the electronic energy of the system E_{el} in the gas phase, thermal corrections ΔG_{therm} to the specified thermodynamic state (temperature and pressure) in the gas phase and free enthalpies of solvation ΔG_{solv} as a correction from gas to condensed phase in a certain solvent.

$$G = E_{el} + \Delta G_{therm} + \Delta G_{solv} \tag{2.7}$$

Details on how the electronic energy E_{el} and solvation contributions ΔG_{solv} are obtained will be discussed in sections 2.3 and 2.4. The thermal corrections ΔG_{therm} are themselves the sum of several contributions: the zero-point vibrational energy (ZPVE) E_{ZPVE}, as well as translational, rotational and vibrational contributions to the kinetic energy (E_t, E_r, E_v).

$$\Delta G_{therm} = E_{ZPVE} + E_t + E_r + E_v \tag{2.8}$$

These contributions can all be derived from their respective partition functions q. The average rotational energy E_r is $\frac{RT}{2}$ per degree of freedom ($\frac{3}{2}RT$ for non-linear molecules, RT for linear molecules), while the average translational energy E_t is equal to $\frac{3}{2}RT$. Vibrational contributions E_v can be computed from the sum over all vibrational modes of the molecule ($3N-6$ modes for non-linear molecules, $3N-5$ modes for linear molecules):

$$E_v = R \sum_i \frac{1}{e^{\frac{h\nu_i}{k_B T}} - 1} \frac{h\nu_i}{k_B} \tag{2.9}$$

Similarly, the zero-point vibrational energy corresponds to the occupation of the lowest level of each vibrational mode and its contribution is:

$$E_{ZPVE} = R \sum_i \frac{1}{2} \frac{h\nu_i}{k_B} \tag{2.10}$$

2.3 Quantum Chemistry

Calculation of the electronic energy E_{el} of a molecule requires solving the Schrödinger equation[1] for that particular system. The time-dependent Schrödinger equation is as follows:

$$i\hbar\frac{\delta}{\delta t}\left|\Psi\right\rangle = \hat{H}\left|\Psi\right\rangle \tag{2.11}$$

For most stationary problems, including the questions of this thesis, it is sufficient to solve the time-independent Schrödinger equation:

$$\hat{H}\left|\Psi\right\rangle = E\left|\Psi\right\rangle \tag{2.12}$$

$\hat{H}$ is the Hamiltonian describing the physics of the system, $\left|\Psi\right\rangle$ the eigenfunction of $\hat{H}$ (also called wave function) and E is the (energy) eigenvalue. The meaning of the wave function $\left|\Psi\right\rangle$ has attracted some philosophical debate, but its squared modulus $\left|\Psi\right|^2$ can be interpreted as the probability density of the particles in Ψ. Here, $\hat{H}$ is the Hamiltonian in atomic units for a molecular system of i electrons and I nuclei

$$\hat{H} = -\sum_I \frac{1}{2M_I}\nabla_I^2 - \sum_i \frac{1}{2}\nabla_i^2 + \sum_{i>j}\frac{1}{r_{ij}} - \sum_{i,I}\frac{Z_I}{R_{Ii}} + \sum_{I,J}\frac{1}{2}\frac{Z_I Z_J}{R_{IJ}} \tag{2.13}$$

where r_{ij}, R_{Ii} and R_{IJ} denote the distances between the ith and jth electron, the Ith nucleus and the ith electron and the interatomic distances between the Ith and Jth nucleus. M_I is the mass of the Ith nucleus in units of electron mass m_e and Z_I is the nuclear charge. In almost all cases, a simplified Hamiltonian is applied within the so-called Born-Oppenheimer (BO) approximation, which is likely the most fundamental approximation in quantum chemistry. In brief, it simplifies the Hamiltonian $\hat{H}$ of a molecular system to give a Hamiltonian that only depends on the system's electrons and treats nuclei as fixed. At the core of the BO approximation lies the fact that electrons are far lighter than nuclei, even for the lightest isotope of hydrogen (ratio of proton mass to electron mass: $\frac{m_p}{m_e} \approx 1836$). Thus, the electrons' movement can be described by an effective Hamiltonian defined by the position of the nuclei, R_I. From the original, full Hamiltonian (eq. 2.13), the kinetic energy operators of nuclei movement are removed while the nuclei's positions R_I in the electron-nucleus interaction term are now fixed parameters and the term for nucleus-nucleus coulomb repulsion becomes a constant value. The latter is sometimes also excluded from $\hat{H}_{el}$, since a constant term only shifts

the eigenvalue without changing the eigenfunction Ψ of the operator.

$$\hat{H}_{el} = -\sum_i \frac{1}{2}\nabla_i^2 + \sum_{i>j}\frac{1}{r_{ij}} - \sum_{i,I}\frac{Z_I}{R_{Ii}} + \underbrace{\sum_{I,J}\frac{1}{2}\frac{Z_I Z_J}{R_{IJ}}}_{\text{constant}} \tag{2.14}$$

The electronic Hamiltonian in eq. 2.14 now allows for finding solutions to the electronic structure of the system without considering the quantum mechanics behind nuclear motion – however, the solutions are now dependent on the initially chosen nuclear configuration R_I. Unfortunately, analytic solutions to the Schrödinger equation only exist for very small (one-electron) systems – the many-body nature of the electron-electron Coulomb interaction prevents the finding of analytic or exact solutions. An exception is the helium atom, for which Hylleraas pioneered an exact solution which is non-analytic, but can in principle be numerically calculated to arbitrary precision.[14–16] Nevertheless, a number of methods have been developed to find approximate solutions for larger systems. These methods are called ab-initio when they are only based on fundamental physical constants.

2.3.1 Hartree-Fock Theory

Although pure Hartree-Fock (HF) theory is rarely applied on its own today, it still plays an important role – on the one hand being the first widely applied ab-initio method, on the other hand being the basis for many of today's more sophisiticated methods either indirectly where HF calculations are used to obtain first guesses for orbitals etc. or directly as in some density functionals which use exact exchange from Hartree-Fock theory, in multi-reference methods or in the more recent random-phase approximation.

As an approximation for a many-electron wave function Ψ with N electrons in k orbitals, one can use a product of one-electron wave functions χ, which is called Hartree product:

$$|\Psi\rangle = \left|\chi_i^1 \chi_j^2 \cdots \chi_k^N\right\rangle \tag{2.15}$$

These orbitals χ are spin orbitals, the product of a spatial wave function ψ and a spin function α or β for the two spin states of an electron (up or down). The spatial wave functions, spin functions and therefore also the spin orbitals χ are orthonormal, so that

$$\langle \psi_i | \psi_j \rangle = \delta_{ij} \tag{2.16}$$

$$\langle \alpha | \alpha \rangle = \langle \beta | \beta \rangle = 1 \tag{2.17}$$

$$\langle\alpha|\beta\rangle = \langle\beta|\alpha\rangle = 0 \tag{2.18}$$

$$\langle\chi_i|\chi_j\rangle = \delta_{ij} \tag{2.19}$$

Still, one requirement has not yet been met: the Pauli exclusion principle,[17,18] which states that the wave function of a quantum mechanical system is antisymmetric with respect to exchange of two fermions. It is a postulate independent from the Hamiltonian and adds the requirement of antisymmetry to the wave function, so that it changes sign upon exchange of two particles (electrons):

$$|\chi_i\chi_j\ldots\rangle = -\,|\chi_j\chi_i\ldots\rangle \tag{2.20}$$

The Hartree product itself does not satisfy the antisymmetry. An antisymmetric wave function can be obtained through a different form of wave function, the Slater determinant,[19] which utilizes the change of sign of a matrix' determinant upon exchange of two of its column vectors. The wave function is then written as

$$|\Psi\rangle = \frac{1}{\sqrt{N!}}\begin{vmatrix} \chi_1^1 & \chi_2^1 & \chi_3^1 & \cdots & \chi_n^1 \\ \chi_1^2 & \chi_2^2 & \chi_3^2 & \cdots & \chi_n^2 \\ \vdots & \vdots & \vdots & \ddots & \vdots \\ \chi_1^N & \chi_2^N & \chi_3^N & \cdots & \chi_n^N \end{vmatrix} \tag{2.21}$$

where $\frac{1}{\sqrt{N!}}$ is the normalization factor. This is the general form for a wave function in Hartree-Fock theory. Applying the Ritz variational principle[20] to the Hartree-Fock energy, which is a functional of the molecular orbitals, the orbitals are optimized under the constraint that they remain orthogonal and normalized. This can be done by using the method of Lagrange multipliers with the Lagrange function

$$\mathcal{L} = E\left\{\chi_i\right\} = \sum_{i,j}^{N} \epsilon_{ij}\left(\delta_{ij} - \langle\chi_i|\chi_j|\chi_i|\chi_j\rangle\right) \tag{2.22}$$

which ultimately yields the Hartree-Fock equations as

$$\hat{f}_i\chi_i = \epsilon_i\chi_i \tag{2.23}$$

where $\hat{f}$ is the one-electron Fock operator defined as

$$\hat{f}_i = -\frac{1}{2}\nabla_i^2 - \sum_I \frac{Z_I}{r_{iI}} + \sum_n \hat{J}_j - \hat{K}_j \tag{2.24}$$

$\hat{J}_j$ and $\hat{K}_j$ are the Coulomb and exchange operators

$$\hat{J}_j(1) = \int \frac{\chi_j^*(2)\chi_j(2)}{r_{12}} = \int \frac{|\chi_j(2)|^2}{r_{12}} dx_2 \tag{2.25}$$

$$\hat{K}_j(1) = \int \frac{\chi_j^*(2)\chi_i(2)}{r_{12}} dx_2 \tag{2.26}$$

which describe an average interaction of electron 1 and 2 in orbitals i and j – this approximation, referred to as mean-field approach eliminates the two-particle interaction from the original electronic Hamiltonian and transforms the problem into an independent particle model, which is the central idea in Hartree-Fock theory. While the Coulomb integrals arising from $\hat{J}$ can be interpreted as the interaction energy of an electron moving in an averaged potential formed by the probability density of another electron, no such interpretation is available for the exchange integrals of $\hat{K}$, which ultimately are a consequence of the antisymmetry of the wave function.

Even in this form, the Hartree-Fock equation is very difficult to solve as it constitutes a nonlinear, integrodifferential eigenvalue problem. The common solution in quantum mechanical applications is to transform this problem into a matrix eigenvalue problem. Roothaan introduced an idea in which the spatial orbitals are expanded as a linear combination of basis functions.[4] An electron in orbital Φ_i would then be described by a set of ν basis functions

$$\Phi_i(1) = \sum_\nu c_{\nu i}\phi_\nu(1) \tag{2.27}$$

Using this expression for the wave function in the Hartree-Fock equation, followed by multiplication from the left with ϕ_μ^* and integration gives

$$\sum_\nu c_{\nu i} \int \phi_\mu^*(1)\hat{f}(1)\phi_\nu(1)dx_1 = \epsilon_i \sum_\nu c_{\nu i} \int \phi_\mu^*\phi_\nu dx_1 \tag{2.28}$$

The integrals in 2.28 are the elements of two matrices: The Fock matrix F with elements

$$F_{\mu\nu} = \int \phi_\mu^*(1)\hat{f}(1)\phi_\nu(1)dx_1 \tag{2.29}$$

and the overlap matrix S with elements

$$S_{\mu\nu} = \int \phi_\mu^* \phi_\nu dx_1 \tag{2.30}$$

which can be used to write a final matrix equation, called the Roothaan-Hall equations

$$FC = SC\epsilon \tag{2.31}$$

where the wave function is represented by the matrix C, containing the linear expansion coefficients $c_{\nu i}$ as matrix elements where each column vector of C corresponds to one molecular orbital Φ_i. Solving the eigenvalue problem yields a diagonal matrix ϵ which has the orbital energies as diagonal elements. It is important to note that the Fock matrix F depends on the orbitals themselves. Therefore a solution can only be found iteratively: Starting from an initial set of orbitals, F is constructed, the Roothaan-Hall equations are solved, and a new set of orbitals is obtained. From these, a new Fock matrix F is obtained. The procedure is then repeated until the orbitals are not changing anymore – coining the term "self-consistent field" (SCF) method. HF theory is variational, which means that the obtained energy will be an upper bound to the true ground state energy. Within computational chemistry, the Hartree-Fock limit is the lowest energy that can be obtained when approaching an infinitely large or complete basis set. The difference between the Hartree-Fock limit and the true ground state energy is attributed to electron correlation and defines the correlation energy.[21]

2.3.2 Basis Sets

As shown in the Roothaan-Hall form of Hartree-Fock theory, it makes sense to describe the wave function of a system through a linear combination of atom-centered functions, called basis functions. A set of basis functions (with defined parameters) is consequently called basis set, and nearly all electronic structure methods rely on representing the wave function through appropriate basis functions. Theoretically speaking, a basis set would need an infinite number of basis functions to replicate the true wave function of a system. This is obviously not computationally possible, so that one has to resort to a finite number of basis functions which can be handled. Nevertheless, with increasing basis set size, convergence of the energy and most other properties is observed, and with a sufficiently large basis set, usually a good description of the wave function is obtained. In general, a variety of mathematical functions could be used for construction of a wave function. However, the computational cost which scales with approximately $\mathcal{O}(n^4)$ regarding the number of basis functions, makes it necessary to consider some features that a useful basis set should possess to keep the number of basis functions low and simplify computational procedures. Good basis functions should model the physical na-

ture of the problem correctly. For example, the wave function should decay with increasing distance to the nucleus; and that decay should be in some form exponential, similar to the wave function of hydrogen-like atoms. Another very important feature is that the basis functions (or more specifically, products of several basis functions) can be easily integrated as most of the computational cost is determined by calculation of the J and K integrals, which may include products of up to four different basis functions. We will focus on two types of basis functions that are very popular and nowadays widely used: the Slater-type orbitals (STOs) and Gaussian-type orbitals (GTOs). Note that in other cases, for example solid-state calculations with periodic systems, other basis functions may be more suitable (e.g. plane wave basis sets, which inherently reproduce the periodicity of the system).

Slater-type orbitals, as introduced by Slater in 1930,[22] are basis functions (written in polar coordinates) of the form

$$\chi_{nlm}(r,\theta,\phi) = NY_{lm}(\theta,\phi)r^{n-1}e^{-\zeta r} \tag{2.32}$$

where n, l and m are the quantum numbers, N is a normalization factor, Y_{lm} are the spherical harmonic functions (which introduce the correct angular dependence and nodal behavior for higher orbitals) and ζ is a shielding constant, representing the effective nuclear charge experienced by an electron. ζ can be ultimately calculated using Slater's rules,[22] which estimate an effective nuclear charge based on the n and l quantum numbers of an electron. The STOs have correct shape as e^{-ar} resembles the exponential decay as in the wave function of hydrogen-like atoms. More specifically, they also satisfy Kato's cusp condition,[23,24] which states that in an $\frac{1}{r}$ Coulomb potential, the electron density will have a cusp at $r = 0$. The applicability of STOs is however strongly limited by their difficulty when in comes to integration. For integrals of three- and four-center products of Slater-type orbitals no analytic solution exists, making their calculation difficult and computationally costly. STOs have therefore been mostly used for relatively small systems or semi-empirical methods like the Complete Neglect of Differential Overlap approximation (CNDO), where multi-center integrals are neglected entirely.

Gaussian-type orbitals as basis functions were first proposed by Boys,[25] and have the form

$$\chi_{nlm}(r,\theta,\phi) = NY_{lm}(\theta,\phi)r^{2n-2-l}e^{-\zeta r^2} \tag{2.33}$$

Despite being less physical than the Slater-type orbitals in that they have a too strong exponential decay (from $\sim e^{-r^2}$ as compared to e^{-r}) and do not satisfy the cusp condition since the derivative of a Gaussian is zero at $r = 0$, they are today the most widely used type of basis

function in use. The advantage of Gaussians is that they allow for much easier calculation of multi-center integrals, which was also Boys' initial proposal,[25] since due to the Gaussian product theorem, the product of two Gaussian functions can be written as a new single Gaussian function centered between the two:

$$e^{-\alpha_1 x_1^2} \cdot e^{-\alpha_2 x_2^2} = n e^{-(\alpha_1+\alpha_2)(x-x_0)} \quad \text{with} \quad x_0 = \frac{\alpha_1 x_1 + \alpha_2 x_2}{\alpha_1 + \alpha_2} \tag{2.34}$$

Thus, the three- and four-center integrals can be effectively written as integrals over a single Gaussian function. While the indefinite integral over a Gaussian function has no analytical expression (the well-known error function), the definite integral over the whole function is known and can be expressed:

$$\int_{-\infty}^{\infty} e^{-\alpha x^2} = \sqrt{\frac{\pi}{\alpha}} \tag{2.35}$$

This leads to a dramatic speed up in comparison with the more physical Slater-type orbitals. The disadvantages of GTOs can be compensated by using more functions to approximate what would otherwise be a single Slater-type orbital; even then calculations with Gaussian basis functions are faster by several orders of magnitude. The quality of a basis set is denoted by how many functions are used to describe the atomic orbitals. In a minimum or single zeta (SZ) basis set (ζ as in the Slater-type orbitals), only one function is used for each type of orbital ($1s$, $2s$, $2p_x$, $2p_y$, $2p_z$, ...) whereas double zeta (DZ), triple zeta (TZ) and quadruple zeta (QZ) basis sets use two, three and four functions for each orbital, allowing for a more accurate description. In most cases so called split-valence basis sets are used, where the inner electrons may for example only be described by a basis set of SZ quality while the valence shells are represented by a basis set of DZ quality. This is indicated by a "V", e.g. DZV, for a double zeta split-valence basis set. The rationale for split-valence basis sets is, that they reduce computational cost while keeping good accuracy for chemical bonding, since the inner electrons do usually only play a subordinate role for the chemistry at hand. Additionally, most basis sets include polarization functions, which are higher angular momentum functions than the elements would have as occupied orbitals in their ground state. As an example, hydrogen would gain additional p-functions to allow for distortion ("polarization") when bonding with another atom although it usually only possesses a single $1s$-function. Similarly, the p-block elements will get d-functions, d-block elements receive f-functions and so forth. Another basis set extension that is sometimes applied are diffuse functions. These are usually long-range exponentials with a slower decay, allowing for extension of electron density further away from the nucleus. While not always necessary, there are cases in which a good description may only be achieved with diffuse functions, especially with smaller basis sets, e.g. negatively charged

species or certain types of intermolecular interactions.

Many different basis sets of Gaussian-type orbitals have been constructed of which the most popular are: the different Pople basis sets,[26–31] the correlation-consistent basis sets by Dunning,[32] and the Karlsruhe basis sets developed in the group of Ahlrichs.[33–36] In this thesis, the Karlsruhe basis sets were used in their revisited "def2-" form, which are available for all atoms up to radon ($Z = 86$) in QZV quality.[35]

2.3.3 Coupled Cluster Theory

Of the different post-HF methods that have been developed to account for electron correlation, coupled cluster theory is of special importance. In its CCSD(T) variant, it is often referred to as the "gold standard of quantum chemistry", providing very accurate results and often used as a reference for electronic structure methods. To overcome the limitations of the single Slater determinant as in HF, the wave function in coupled cluster theory is written in an exponential ansatz:

$$|\Psi\rangle = e^{\hat{T}} |\Phi_0\rangle \tag{2.36}$$

Here, Φ_0 is the ground state Slater determinant as in Hartree-Fock theory and $\hat{T}$ is the cluster operator, which is a sum of n-electron excitation operators $\hat{T}_n$

$$\hat{T} = \sum_n \hat{T}_n = \hat{T}_1 + \hat{T}_2 + \hat{T}_3 + \ldots \tag{2.37}$$

The excitation operators to create all single ($\hat{T}_1$) and double excitations ($\hat{T}_2$), as in CCSD, can be written as

$$\hat{T}_1 = \sum_i \sum_a c_a^i \hat{a}_a^\dagger \hat{a}_i \tag{2.38}$$

$$\hat{T}_2 = \frac{1}{4} \sum_{i,j} \sum_{a,b} c_{ab}^{ij} \hat{a}_a^\dagger \hat{a}_b^\dagger \hat{a}_i \hat{a}_j \tag{2.39}$$

where $\hat{a}_a^\dagger$ and $\hat{a}_i$ are the creation and annihilation operators which generate the excited Slater determinants from Φ_0 in which electrons from orbitals i, j are excited to unoccupied orbitals a, b. The coefficients c_{ab}^{ij} determine the contribution of each excitation to the final wave function $|\Psi\rangle$ and are optimized in the coupled cluster calculation. With the Taylor or McLaurin

series expansion of e^x and the CCSD cluster operator, we obtain

$$e^{\hat{T}} = 1 + \hat{T} + \frac{1}{2}\hat{T}^2 + ... = 1 + \hat{T}_1 + \hat{T}_2 + \frac{1}{2}\hat{T}_1^2 + \hat{T}_1\hat{T}_2 + \frac{1}{2}\hat{T}_2^2 + ... \tag{2.40}$$

Therefore, even CCSD features higher than just double excitations which arise from the terms in the Taylor series expansion ($\frac{1}{2}\hat{T}_1^2$, $\hat{T}_1\hat{T}_2$, etc.). The "gold standard" CCSD(T) contains full single "S" and double excitations "D", and treats additional triple excitations "(T)" through perturbation theory (rather than within the coupled cluster framework). Despite its accuracy, coupled cluster theory may fail when the system under study exhibits strong multi-reference character, in which case the ground state HF wave function, from which the coupled cluster wave function is constructed, only poorly describes the ground state. Coupled cluster theory comes with considerable computational cost ($\sim \mathcal{O}(n^7)$), which makes it only feasible for relatively small molecules as large triple or quadruple zeta basis sets are required to obtain reliable energies.

2.3.4 Density Functional Theory

Density functional theory (DFT) is based on the Hohenberg-Kohn theorem[11] which states that the energy of any non-degenerate ground-state electronic system is a unique functional of the electron density $\rho(\vec{r})$, which uniquely defines the external potential $V(\vec{r})$, and therefore the corresponding Hamiltonian $\hat{H}$ and the ground state wave function Ψ as well as all other properties of the system.

The common proof of the theorem is by contradiction.[11] If there were two different potentials $V_1(\vec{r}) \neq V_2(\vec{r})$ and associated Hamiltonians $\hat{H}_1 \neq \hat{H}_2$ (which only differ in their potential) with eigenfunctions $\Psi_1 \neq \Psi_2$ having the same density, the variational principle states that the respective wave functions would both give an upper bound on the energy of each other. It therefore follows, that such two potentials cannot exist, which means that a unique relationship must exist between the density and potential. Similarly, all other properties, including the energy are defined – so that the energy is a functional of the electron density.

In contrast to the 3N-dimensional wave function, the electron density of any system is always a three-dimensional entity regardless of the number of electrons, which reduces computational complexity. While the Hohenberg-Kohn theorem shows the unique relationship between electron density and ground-state energy, it does not make any statement on the form of the functional and the true form of the functional is unknown. Such a functional would be com-

posed of different contributions:

$$E[\rho] = T[\rho] + J[\rho] + E_{nc}[\rho] \tag{2.41}$$

The kinetic energy T, the classical Coulomb interaction J and a non-classical interaction energy E_{nc}. An analytic expression is only known for the Coulomb energy J. To facilitate simpler calculation of the kinetic energy term, Kohn and Sham introduced an approach in which the electrons are non-interacting, but moving in an effective potential to recoup interaction effects.[12] For non-interacting electrons, the kinetic energy can be exactly determined. It is worth to note that almost all currently employed DFT methods follow the Kohn-Sham (KS) formalism.[37] In Kohn-Sham DFT, $\rho(r)$ is then described by a sum of N one-electron orbitals from a single Slater determinant

$$\rho(r) = \sum_i |\phi_i(r)|^2 \tag{2.42}$$

the corresponding energy functional can then be expressed as

$$E[\rho] = T_S[\rho] + J[\rho] + V_{ne}[\rho] + E_{XC}[\rho] \tag{2.43}$$

The kinetic energy of independent electrons $T_S[\rho]$, the classical Coulomb interaction $J[\rho]$ and the nucleus-electron interaction $V_{ne}[\rho]$ are known. The exchange-correlation functional E_{XC} consists of different terms

$$E_{XC}[\rho] = (T[\rho] - T_S[\rho]) + (J_{ee}[\rho] - J[\rho]) \tag{2.44}$$

and captures the difference in kinetic energy of interacting ($T[\rho]$) and non-interacting electrons ($T_S[\rho]$) as well as the remainder of the electron-electron interaction that is not contained in the classical Coulomb energy $J[\rho]$ where electrons move in an averaged field. E_{XC} is unknown and the main challenge in the current development of density functionals. While one may say that this merely shifts uncertainty about the functional form from the original kinetic energy to $T[\rho]$ to the exchange-correlation functional, the exchange-correlation energy $E_{XC}[\rho]$ is far smaller than all other contributions in the functional, justifying this approach. $E_{XC}[\rho]$ can be split into its exchange part which describes the interaction of same-spin electrons, while the correlation term accounts for the correlated movement of electrons rather than independently from each other as in the kinetic energy term. Note, that this is dynamic correlation – static correlation, which is the interaction of different electronic states instead of moving electrons of one electronic state is not accounted for. In fact, most DFT methods fail in cases where static correlation is significant and one has to resort to multireference ab initio

methods for an accurate description.

Local Density Approximation

The first approach to exchange-correlation functionals was the local density approximation (LDA) in which the electron density is treated at each point as a homogeneous electron gas of the same density. The exchange part ϵ_X of the functional is known[38] for a uniform electron gas and has the analytic form

$$\epsilon_X[\rho] = -\frac{3}{4}\left(\frac{3}{\pi}\right)^{\frac{1}{3}} \int \rho(r)^{\frac{4}{3}} dr \tag{2.45}$$

The correlation part is not known, but different approaches have been developed in the past for an approximative description, such as the VWN correlation functional by Vosko, Wilk and Nusair[39] or the PW92 functional by Perdew and Wang.[40] As the correlation energy can be obtained from quantum Monte Carlo (QMC) simulations, most LDA correlation functionals are fits to QMC data. For very high and low electron densities, the behavior of the correlation energy is known, and LDA functionals try to emulate this behavior together with interpolation of the QMC values. LDA functionals give relatively reasonable structures for molecules, while computed energies usually suffer from a larger error, preventing usage for most applications.

Generalized Gradient Approximation

A natural extension of the LDA was the development of the generalized gradient approximation (GGA).[41–43] In addition to the local electron density, GGA functionals incorporate information about the gradient of the electron density $\vec{\nabla}\rho$ into the functionals. Rather than replacing the LDA functional, the gradient is used to apply a correction to the LDA terms. An early and now widely applied GGA-type exchange functional was proposed by Becke[44] as a correction to the LDA exchange energy as in eq. 2.45:

$$\Delta\epsilon_X[\rho] = -\beta\rho^{\frac{4}{3}} \frac{x^2}{1 + 6\beta x \sinh^{-1}(x)} \quad \text{with} \quad x = \frac{|\vec{\nabla}\rho|}{\rho^{\frac{4}{3}}} \tag{2.46}$$

The β parameter was fitted to reproduce the exact Hartree-Fock exchange energies of the noble gas atoms (He - Rn). In a similar manner, Lee, Yang and Parr constructed a four-parameter GGA correlation functional known as LYP whose parameters were fitted to the Hartree-Fock helium atom,[45] and which has been applied widely. Another series of GGA functionals were introduced by Perdew and Wang,[40,46,47] as well as Perdew, Burke and Ernznerhof.[48,49] Rather than using an additive correction as in the approach by Becke (eq. 2.46), Perdew and Wang

used a scaling function for the LDA exchange energy in their 1986 functional:

$$\epsilon_X[\rho] = \epsilon_X^{LDA}[\rho]\, F^{GGA}(s) \tag{2.47}$$

$$F^{GGA}(s) = \left(1 + a\frac{s^2}{m} + bs^4 + cs^6\right)^m \quad \text{with} \quad s = \frac{|\vec{\nabla}\rho|}{\rho^{\frac{4}{3}}\sqrt[3]{24\pi^2}} \tag{2.48}$$

In general, GGA functionals present a large improvement over LDA functionals in that they greatly reduced errors with respect to energies reducing LDA's tendency to strongly overestimate the correlation energy ϵ_C. Calculations with GGA functionals have become precise enough to correctly model structures and energies of many systems, although not all of LDA's problems are addressed. For example, structures computed with LDA functionals usually underestimate bond lengths; GGAs tend to overcorrect this and produce bond lengths with a tendency of being too long. Also, atomization energies are often overestimated by GGA functionals.[50]

Hybrid Functionals

Besides GGA functionals, Becke proposed that a fraction of exact exchange from Hartree-Fock theory should be mixed into the GGA exchange-correlation functional.[51,52] In these so-called hybrid functionals, the exchange energy is partly replaced by exact exchange:

$$E_{xc} = \alpha E_x^{HF} + (1-\alpha)E_x^{GGA} + E_c^{GGA} \tag{2.49}$$

with E_x^{HF} defined like the K_{ij} exchange integrals as in Hartree-Fock theory:

$$E_x^{HF} = \frac{1}{2}\sum_{ij} K_{ij} = -\frac{1}{2}\sum_{ij}\int\int \chi_i^{1*}\chi_j^{1*}\frac{1}{r_{12}}\chi_i^2\chi_j^2\, dx_1 dx_2 \tag{2.50}$$

The amount α of exact exchange can be fitted to experimental data[52] or estimated from theory.[53–55] This approach has turned out to give very good results that can beat the accuracy of pure GGA functionals. Today, hybrid functionals are widely applied, with the famous B3LYP functional, combining Becke's 88 exchange[44] with the correlation functional of Lee, Yang and Parr[45] and a fraction of exact exchange,[52] as the most popular functional overall.

meta-Generalized Gradient Approximation

A further extension of GGA functionals, meta-GGA functionals include the curvature or second derivative of electron density. This is achieved either directly through the Laplacian of the electron density $\Delta\rho(r)$ or through the kinetic energy density $\tau(r)$, which is more common.

The kinetic energy density effectively contains the Laplacian of the electron density in form of the orbitals:

$$\tau(r) = \frac{1}{2} \sum_i |\nabla \chi_i(r)|^2 \tag{2.51}$$

Besides functionals that make use of the kinetic energy density, all functionals that utilize orbital information are usually also referred to as meta-GGA functionals. The TPSS functional[56] by Tao, Perdew, Staroverov and Scuseria is an example of a non-empirical exchange-correlation meta-GGA, which itself is a further development of the earlier meta-GGA PZKB functional.[57,58] Inclusion of HF exchange energies into meta-GGAs yield meta-hybrid functionals, of which the family of Minnesota functionals, developed by Truhlar and coworkers is probably the most popular. Among the Minnesota functionals, the suite of M06 functionals which use varying amounts of HF exchange[59,60] are most used.

2.3.5 Resolution of the Identity Approximation

A major contribution to the computational cost in Hartree-Fock or DFT is the calculation of two-electron four-center integrals, as they appear in the Coulomb (J) and exchange (K) part of the Fock operator as integrals over pairs of functions:

$$\langle \chi_\alpha \chi_\beta | \chi_\mu \chi_\nu \rangle \tag{2.52}$$

One way to reduce the computational effort in their calculation is the Resolution of the Identity (RI) approximation.[61,62] Using the RI approximation, pairs of functions are expanded in an auxiliary basis set:

$$|\chi_\mu \chi_\nu\rangle \approx \sum_i c_i |\varphi_i\rangle \tag{2.53}$$

The auxiliary basis set is chosen so that it fulfills the relationship

$$\sum_i |\varphi_i\rangle \langle \varphi_i| \approx 1 \tag{2.54}$$

which is the identity operator in the limit of a complete basis (therefore the name "Resolution of the Identity").[36] Expansion of both parts of the integral in an auxiliary basis set i/j, the two-center four-electron integral can be written as

$$\langle \chi_\alpha \chi_\beta | \chi_\mu \chi_\nu \rangle \approx \sum_i \sum_j c_i c_j \langle \chi_\alpha \chi_\beta | \varphi_i \rangle \langle \varphi_i | \varphi_j \rangle^{-1} \langle \varphi_j | \chi_\mu \chi_\nu \rangle \tag{2.55}$$

This effectively reduces four-center integrals $\langle\chi_\alpha\chi_\beta|\chi_\mu\chi_\nu\rangle$ to several three-center integrals $\langle\chi_\alpha\chi_\beta|\varphi_i\rangle$ which can be calculated considerably faster. The coefficients of the auxiliary basis set c_i, c_j are optimized to minimize the resulting integral error. For a complete auxiliary basis, the resolution of the identity approximation would be exact. In practice, the obtained error through the RI approximation is on the order of 0.1 kJ·mol^{-1}, which is well below the accuracy of most electronic structure methods and therefore negligible. At the same time, a dramatic speed-up of an order of magnitude or more can be observed, which makes the RI approximation very valuable.[63] The RI approximation is sometimes referred to as "density fitting", coming from the "refitting" of the electron densities in the Coulomb operator $\hat{J}$.

2.3.6 Dispersion Correction

One of the main disadvantages of currently available density functionals is the poor description of dispersion interaction. Dispersion is the main part of the van der Waals (vdW) interaction. Sometimes called London forces,[64,65] dispersion forces arise from spontaneous fluctuations in the electron density, creating a temporary dipole moment in a molecule/atom that can induce another dipole in an interacting molecule/atom. While generally being a weak interaction when compared with covalent bonds, neglection of dispersion can introduce error into calculations. Even qualitative description can be wrong without dispersion when dispersion forces are the major interaction between molecules, for example in dimers of benzene[66] or noble gas atoms,[67] which DFT calculations fail to predict as being bonded or heavily underestimate the interaction energy. Dispersion interaction can be generally described as an attractive potential U following

$$U \sim -\frac{C}{r^6} \tag{2.56}$$

which has its origin in a series expansion derived by London.[64,68] For short interatomic distances, other forces dominate the interaction energy, but for longer ranges, the interaction energy follows the $\frac{1}{r^6}$ behavior until asymptotically approaching zero. While there have been different approaches of incorporating dispersion effects into DFT, this section will briefly explain the DFT-D approach by Grimme et al. which has also been employed in this thesis. Note, that in this approach, the dispersion interaction energy is added on to the final DFT energy

$$E = E_{DFT} + E_{disp} \tag{2.57}$$

whereas other approaches include the dispersion energy into the functional itself by addition of terms to the Hamiltonian containing the Kohn-Sham potential. It is therefore inherently

different in methodology.

The dispersion energy E_{disp} in DFT-D is a sum of atom-pairwise interaction energies of the form[69]

$$E_{disp} = -\sum_{AB} \sum_{n=6,8,10,\ldots} s_n \frac{C_n^{AB}}{R_{AB}^n} f(R_{AB}) \tag{2.58}$$

in which each atom pair AB's contribution is the product of a scaling factor s_n, an atom pair dependent dispersion coefficient C_n^{AB} and a damping function f depending on the interatomic distance. For the currently widely applied third generation dispersion correction DFT-D3,[69,70] E_{disp} is expressed as

$$E_{disp} = -\sum_{AB} s_6 \frac{C_6^{AB}}{R_{AB}^6 + f\left(R_{AB}^0\right)^6} + s_8 \frac{C_8^{AB}}{R_{AB}^8 + f\left(R_{AB}^0\right)^8} \tag{2.59}$$

with the Becke-Johnson damping[71] function having the form

$$f(R_{AB}^0) = a_1 R_{AB}^0 + a_2 \quad \text{and} \quad R_{AB}^0 \sqrt{\frac{C_8^{AB}}{C_6^{AB}}} \tag{2.60}$$

The dispersion coefficients C_n^{AB} are dependent on the density functional and are finally obtained (in DFT-D3) from frequency-dependent dipole polarizabilities α computed with time-dependent density functional theory (TDDFT):

$$C_6^{AB} = \frac{3}{\pi} \int_0^\infty \alpha^A(i\omega)\alpha^B(i\omega)d\omega \tag{2.61}$$

The higher order dispersion coefficients C_8^{AB} can be inferred through a known relationship from C_6^{AB}. In the DFT-D3 approach, the polarizabilities are calculated for hydrides of A and B rather than the free atoms – the effect of the hydrogen atoms is then removed by subtraction of the corresponding polarizability of dihydrogen. While the different DFT-D dispersion corrections by Grimme et al. are nowadays very widely used, it should be noted that a similar approach of using pairwise atomic interaction energies with damping functions for description of dispersion was already proposed earlier by Cohen and Pack.[72]

2.3.7 Relativistic Effects

Particles approaching the speed of light will be subject to additional relativistic effects, altering the electronic structure of the system under study. This is the case for the inner electrons of heavier atoms. As a very rough estimate, we can use the average kinetic energy E_T in a

hydrogen-like atom with quantum number n = 1

$$E_T = \frac{1}{2}\mu c^2 Z^2 \alpha^2 \approx \frac{1}{2} m_e c^2 Z^2 \alpha^2 \quad \text{with} \quad \alpha = \frac{e^2}{4\pi c \epsilon_0 \hbar} \tag{2.62}$$

where μ is the reduced mass of the electron m_e and nucleus M

$$\mu = \frac{m_e M}{m_e + M} \tag{2.63}$$

which can be approximated as $\mu \approx m_e$ since $M \gg m_e$. Z is the atomic number or charge of the nucleus. From the classical kinetic energy formula, an estimate for the velocity of the electron using eq. 2.62 then is

$$v_e = \sqrt{\frac{2E_T}{m_e}} = cZ\alpha \tag{2.64}$$

For the hydrogen atom (Z = 1), a velocity of 0.007c is obtained, which explains why non-relativistic solutions can describe smaller atoms so well, but for typical transition metals in catalysis like ruthenium (Z = 44, v = 0.32c) or iridium (Z = 77, v = 0.56c) or heavier elements like gold (Z = 79, v = 0.58c), which owes its distinct color to relativistic effects,[73] the 1s electron speed approaches a significant fraction of c. One relativistic effect is the increase in particle mass when in the regime of relativistic velocities:

$$m = \frac{m_0}{\sqrt{1 - \frac{v}{c}}} \tag{2.65}$$

With increasing mass m, the orbitals undergo a corresponding contraction, which is also experienced by the valence shell. For example, the 1s orbital in a heavy atom will strongly contract due to the velocity of the 1s electron, but also higher s-functions will contract since they have to be orthogonal with respect to the inner s-functions. There are approximations to explicitly account for relativistic effects, but for the purposes of the investigations in this thesis they were not needed – the reason being, that some molecular properties can still be accurately described with simpler methods. Rather than explicitly treating the inner electrons of heavy atoms with relativistic methods, it is possible to replace the inner electrons with a potential that models their behavior as if they were behaving relativistically. These so called pseudopotentials, also effective core potentials (ECPs), are usually based on true relativistic all electron calculations or from fitting to atomic spectra, and enable very fast calculations while still using the non-relativistic Hamiltonian for outer electrons. Unless spin-orbit effects are of importance, the accuracy of relativistic pseudopotentials is similar to those of relativistic all-electron calculations, which has led to their widespread adoption in general computational chemistry.[74]

2.4 Solution Chemistry

In homogeneous catalysis, most reactions take place in liquid phase. The effects of solvation, however, have to be added onto the electronic energies and thermal corrections, as these were calculated for isolated (gas-phase) molecules. Explicit solvation, the introduction of solvent molecules around the molecule of interest, while sometimes necessary to capture special effects originating from relatively strong directed interactions, is problematic as it dramatically increases computational time due to larger system size and also usually requires extensive molecular dynamics (MD) simulations to obtain good averages, as one would otherwise suffer from slow or erratic convergence behavior when adding more and more solvent molecules. Therefore, the use of implicit solvation has become very popular, where solvation contributions are estimated through different means. While several approaches exist, this section will focus on the conductor-like screening model for real solvents (COSMO-RS),[75,76] which was used to obtain the solvation contribution to ΔG in this thesis.

COSMO-RS theory is solely based on the σ-profiles of the molecules constituting the solution. σ-Profiles are histograms of the screening charge surface density, which can be obtained from DFT calculations by applying the COSMO boundary conditions.[77] The molecular surfaces are segmented and the segments with their associated charge densities are grouped into a histogram $p(\sigma)$ which represents the σ-profile. The interactions between different segments of solvent and solute molecules are computed to obtain the chemical potential μ of all components in the solution, from which almost all other thermodynamic solution properties can be derived. For a surface segment with screening charge σ, the chemical potential $\mu(\sigma)$ can be calculated from the solvents σ-profile $p(\sigma')$ and the interaction energy between surfaces' screening charges $E_{int}(\sigma, \sigma')$.

$$\mu(\sigma) = -kT \ln \int p(\sigma') e^{-\frac{E_{int}(\sigma,\sigma') - \mu(\sigma')}{kT}} d\sigma' \tag{2.66}$$

The expression can only be solved iteratively as equation 2.66 itself depends on $\mu(\sigma')$. The interaction energy $E_{int}(\sigma, \sigma')$ consists of several terms describing interactions in liquids such as the Coulomb interaction, hydrogen bonding, Van-der-Waals interactions and combinatorial terms. They shall not be explained in detail here, but the parameters describing these interactions have been fitted to large sets of available thermochemistry data in the implementation by Klamt et al. that has been used in this thesis.[75,76]

Several approximations are incorporated into COSMO-RS theory:

- Contacts of surface segments govern the interaction based on their screening charges.
- Surfaces are in close contact.
- Only pairwise surface interactions are taken into account.
- The three-dimensional arrangement of surface segments can be neglected.

Of particular interest for homogeneous catalysis is the free enthalpy of solvation of molecules, to obtain reaction paths that describe the free enthalpy of a reaction in solution. Calculation of the free enthalpy of solvation ΔG_{solv} of a compound in the COSMO-RS framework[75,76,78] is possible from its chemical potentials at infinite dilution (μ_s) and in the ideal gas state (μ_{ig}) with ρ_S as the solvent density, V_{ig} as the molar volume of an ideal gas, and the solvent's molecular weight M_S.

$$\Delta G_{solv} = (\mu_s - \mu_{iG}) - RT \ln\left(\frac{\rho_S V_{ig}}{M_S}\right) \tag{2.67}$$

Adding ΔG_{solv} to the gas phase electronic energies and thermodynamic corrections gives the final free enthalpy G in solution.

2.5 Methodology

For DFT studies concerning reactions in homogeneous catalysis, a two-fold approach is being widely applied, wherein the optimization of the molecular structure and computation of vibrational frequencies is carried out at a faster and lower level of theory, followed by a higher level, more accurate single point calculation at the previously optimized geometry. This geometry is not a minimum on the potential energy surface of the higher level method. While it would therefore be certainly preferred to also conduct geometry optimizations and frequency calculations at the final higher level methodology, the size of many systems in homogeneous catalysis would make this prohibitively time-consuming. Thus, many studies have resorted to the above mentioned approach, which generally works relatively well. The reason is good error cancellation since one is mainly interested in relative energy differences between structures. While absolute energies might differ a lot, the error in not using the minimum structure of a higher level method is mostly systematic and cancels out when calculating energy differences.

In the following, the main choice of method for geometry optimization and final single point energies will be explained. More details on the computational methodology, the use of software packages and choice of thermodynamic reference points are given in the "Computational Details" sections of chapters 3 and 4.

In the whole manuscript, unless indicated otherwise, energies and energy differences refer to free enthalpies/Gibbs energies.

2.5.1 Geometry Optimization

For geometry optimizations, the BP86 functional with the def2-SV(P) basis set[35] was largely used. BP86 is a GGA-type functional and combines Becke's 1988 exchange functional[44] with Perdew's 1986 correlation functional.[46] The correlation part of the functional also contains the LDA functional by Vosko, Wilk and Nusair.[39]

Structure optimizations with BP86/def2-SV(P) have been used successfully in the literature due to the very good accuracy-to-cost ratio. Especially for larger molecules (>100 atoms), which are often studied in homogeneous catalysis due to the size of many ligands, computational cost can easily become an issue. For example, the (*S*,*S*)-*f*-binaphane ligand used in our work for the direct asymmetric reductive amination already has 97 atoms, including Fe in the ferrocene backbone. It is therefore necessary to perform geometry optimizations at lower

level and supplement the structures with more accurate electronic structure calculations later. Optimized structures usually show deviations, but these are in most cases very systematic, thus being cancelled out in studies where relative energy differences between structures are important.

For transition metal chemistry, BP86 has performed fairly well and reproduces crystal structures mostly accurately, with a general tendency for overestimation of bond lenghts by a few picometers that is well known.[50] The group of Schaefer studied a series of transition metal carbonyl complexes and showed good prediction of structures and vibrational frequencies from BP86.[79] Philipp Plessow compared computed structures to crystal structure data for different transition metal complexes in his thesis and also found a small overestimation of bond lengths (mean absolute deviation of 4.0 pm).[80] For ruthenium-related chemistry, Jensen and coworkers benchmarked structures of different ruthenium olefin metathesis catalysts from DFT methods against X-ray crystallography data and also found good performance of BP86 (again with a small, general overestimation of bond lengths), even outperforming the popular B3LYP and the more sophisticated M06 and M06L functionals.

2.5.2 Single Point Energies

Final electronic energies in this thesis were mostly obtained with the PBE0 functional using the def2-QZVPP basis set.[35] PBE0 is a hybrid functional in which a fraction of the exchange from the original GGA exchange-correlation functional of Perdew, Burke and Ernzerhof[48,49] (PBE) is replaced by exact exchange from Hartree-Fock theory.[53,55] Contrary to B3LYP,[44,45,52] where the amount of exact exchange was fitted to experimentally measured atomization energies, the exchange part of PBE0 contains a predefined amount of $\frac{1}{4}$ HF exchange:

$$E_x^{PBE0} = \frac{3}{4}E_x^{PBE} + \frac{1}{4}E_x^{HF} \tag{2.68}$$

Perdew, Ernzerhof and Burke rationalized the choice of $\frac{1}{4}E_x^{HF}$ by corresponding $\frac{1}{n}$ amounts of exact exchange with nth-order corrections from Møller-Plesset (MP) perturbation theory, where for $n = 4$ good results were obtained by Pople, Head-Gordon and Fox for the atomization and ionization energies of a set of molecules.[81] PBE0 is therefore regarded as non-empirical and has become the second most popular hybrid GGA functional right after "semi-empirical" B3LYP.[82] As mentioned earlier, a weakness of current density functionals is the description of dispersion effects. Therefore, PBE0 was supplemented with the third generation dispersion correction D3 by Grimme et al.[70] with Becke-Johnson (BJ) damping.[71]

In a study by Grimme et al., PBE0-D3(BJ) showed the best performance in a benchmark set of organometallic reactions among a wide variety of functionals against CCSD(T)/CBS data.[83] To check the suitability for the early transition metal chemistry, a small benchmark study was conducted. It should be kept in mind that due to the inaccessibility of absolute electronic energies from experiment for relevant models, CCSD(T) data is usually used as a reference for benchmarking. Due to the high computational cost of coupled cluster methods, only a simplified model of the original reaction can be studied. For this benchmark, a minimum reaction model for dehydroperoxidation of methyl hydroperoxide (MeOOH, the smallest alkyl hydroperoxide) and isopropyl hydroperoxide (*i*PrOOH, the smallest secondary alkyl hydroperoxide) was investigated, involving hydrogen transfer and O-O cleavage as well as hydroperoxide addition via a proton relay mechanism. This is in analogy to the dehydroperoxidation studies which will be presented later in chapter 3.3. CCSD(T)/def2-TZVPP was chosen as the benchmark reference method. Six methods were benchmarked against the CCSD(T) data: BP86/def2-SV(P), which is the level of geometry optimization, BP86/def2-QZVPP, the same method, but with an appropriate basis set and B3LYP/def2-QZVPP as the most widely used hybrid functional. As methods that incorporate dispersion interactions in different ways, PBE0-D3(BJ)/def2-QZVPP was chosen for a dispersion-corrected hybrid functional, M06/def2-QZVPP as a representative meta-GGA and RPA(PBE)/def2-QZVPP, the random phase approximation which had been successfully employed by Philipp N. Plessow in a previous PhD thesis.[80]

A comparison of the reaction paths in Figures 2.3 and 2.4 shows that the more advanced DFT methods (PBE0-D3, M06 and RPA) easily outperform BP86 and B3LYP. At the level of geometry optimization, both barriers are severely underestimated and the general reaction free enthalpy is underestimated by more than 50 kJ·mol^{-1}. BP86 in conjunction with the large def2-QZVPP basis set essentially halves the mean absolute deviation over both reactions (see Table 2.1) and (over)corrects the far too low activation energy for **TS-A2**/**TS-B2**, but generally energies are still quite far off from the CCSD(T) values. B3LYP on average performs slightly better, although the dehydroperoxidation transition states are strongly overestimated in activation energy (deviation of 38.5 kJ·mol^{-1}/42.6 kJ·mol^{-1} relative to CCSD(T)), which would predict the wrong order for the rate-determining step. The overall reaction energy is reproduced relatively well as expected for B3LYP. The M06 functional performs a bit better – although it overestimates the activation energies in all cases by about 10 to 15 kJ·mol^{-1}, it does so systematically and therefore reproduces the qualitatively correct energetic order of transition states from CCSD(T). Still, the mean average deviation over all structures is only slightly better than B3LYP (12.4 kJ·mol^{-1} vs. 15.2 kJ·mol^{-1}). The two best methods in this bench-

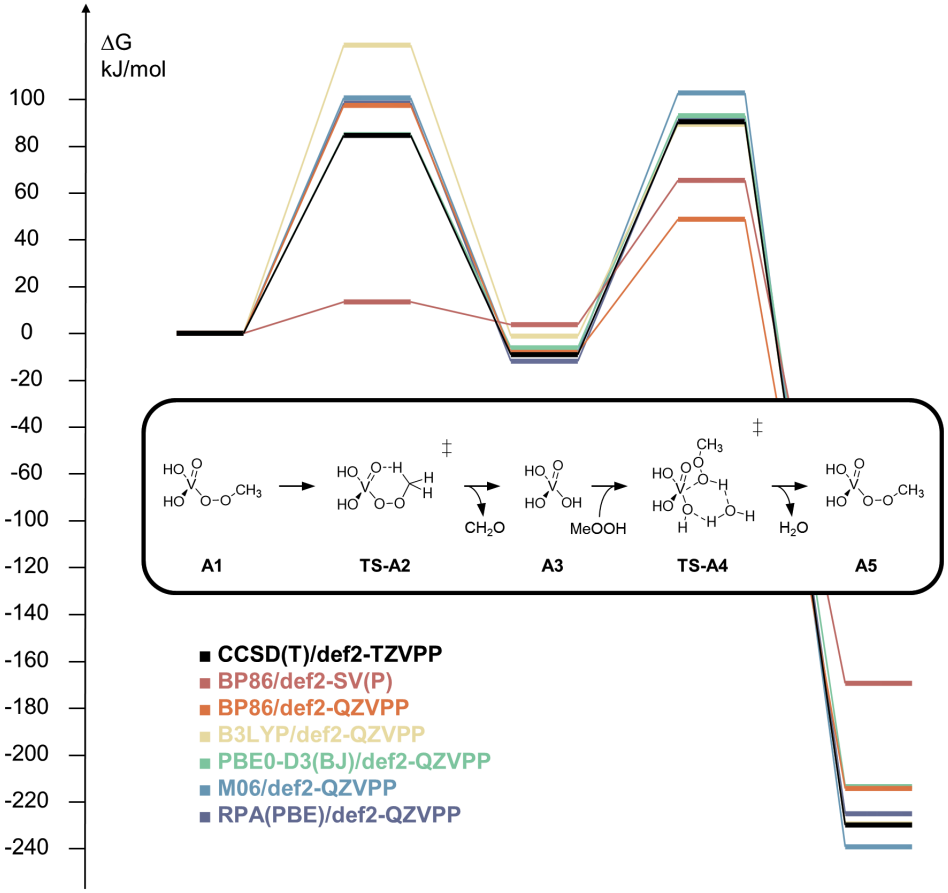

Figure 2.3: Benchmark of various electronic structure methods against CCSD(T)/def2-TZVPP reference for a strongly simplified dehydroperoxidation mechanism with **MeOOH**. Thermodynamic reference for all structures is the vanadium alkylperoxo complex. The geometries have been optimized at BP86/def2-SV(P) level; ZVPEs and thermal corrections at 298.15 K and 1 bar are included at the same level of theory.

mark are RPA and PBE0-D3 with MADs of only 6.4 kJ·mol^{-1} and 5.1 kJ·mol^{-1}. The PBE0-D3 method is in very good agreement with the CCSD(T) profile, with only one larger deviation for the general reaction free enthalpy with MeOOH (**A5**, 16.4 kJ·mol^{-1}); this error is not observed for the more realistic secondary alkyl hydroperoxide *i*PrOOH (**B5**). The catalytic path is quite accurately reproduced with both activation energies being quantitatively correct and showing the right energetic order and deviations smaller than 7 kJ·mol^{-1}. RPA also tends to be very accurate, but overestimates the activation energy for the first transition state in both cases (**TS-A2**/**TS-B2**, deviation of +13.8 kJ·mol^{-1} and +14.3 kJ·mol^{-1}) and therefore gives the wrong energetic order for the two transition states by a small margin. It should be mentioned that no CCSD(T) reference values could be obtained with the quadruple zeta basis set def2-QZVPP; M06/RPA could potentially be more accurate than CCSD(T)/def2-TZVPP.

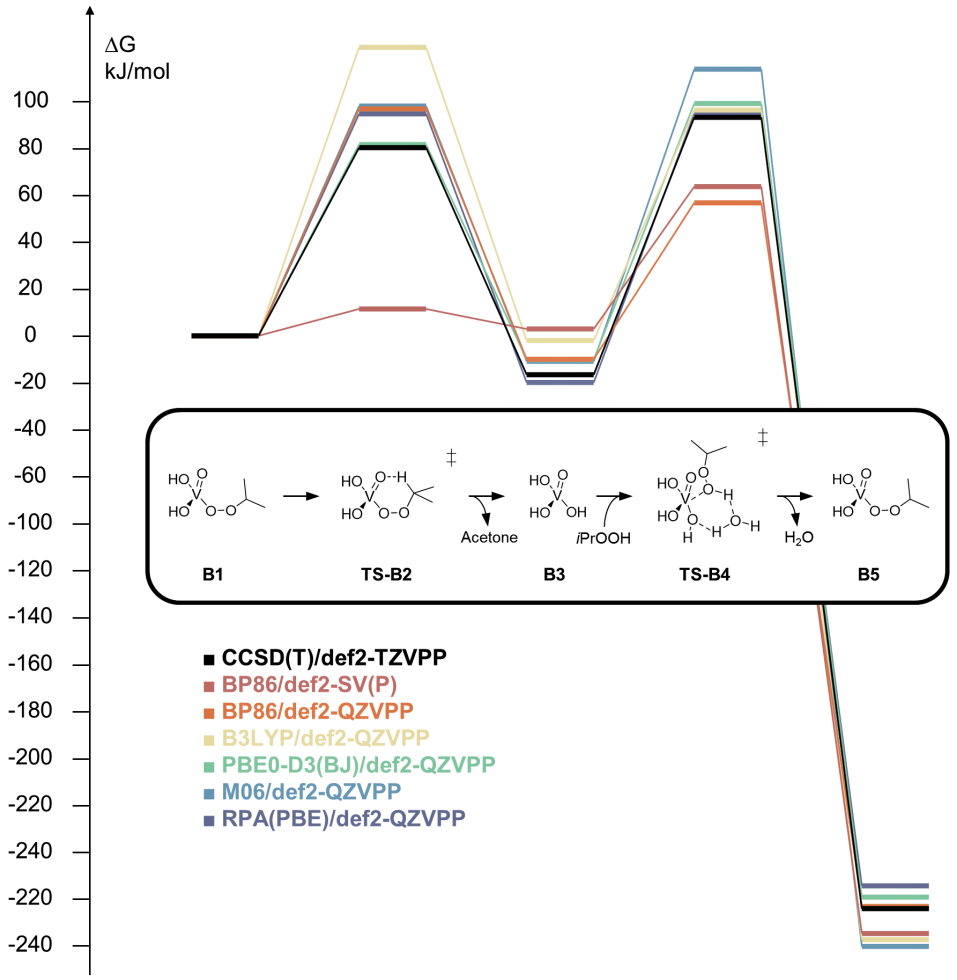

Figure 2.4: Benchmark of various electronic structure methods against CCSD(T)/def2-TZVPP reference for a strongly simplified dehydroperoxidation mechanism with ***i*PrOOH**. Thermodynamic reference for all structures is the vanadium alkylperoxo complex. The geometries have been optimized at BP86/def2-SV(P) level; ZVPEs and thermal corrections at 298.15 K and 1 bar are included at the same level of theory.

Table 2.1: Benchmark summary for model dehydroperoxidation of MeOOH and *i*PrOOH. The reference values at CCSD(T)/def2-TZVPP level are given in the left column (ΔG relative to **A1**/**B1**). The values from the other methods are given as deviations from the CCSD(T)/def2-TZVPP values. BP86* is the level of geometry optimization (BP86/def2-SV(P)). All other methods are calculated with the def2-QZVPP basis set. PBE0-D3 is the dispersion corrected hybrid functional with Becke-Johnson damping. The orbitals for the RPA method were obtained from the PBE functional. The mean average deviation for each method over all structures relative to CCSD(T)/def2-TZVPP is given at the bottom.

Structure	Reference	Tested Methods					
	CCSD(T)	BP86*	BP86	B3LYP	PBE0-D3	M06	RPA
MeOOH							
TS-A2	84.5	-71.1	12.8	38.5	0.2	16.0	13.8
A3	-9.1	12.7	1.0	7.9	2.9	1.2	-2.8
TS-A4	90.3	-25.0	-41.7	-1.2	2.6	12.3	0.6
A5	-209.9	60.5	15.6	0.5	16.4	-9.3	4.8
***i*PrOOH**							
TS-B2	80.1	-68.7	16.4	42.6	1.3	17.7	14.3
B3	-16.6	19.5	6.6	14.6	6.5	5.7	-3.3
TS-B4	93.0	-29.5	-36.4	3.1	5.9	20.6	1.6
B5	-243.9	-10.6	0.8	-13.2	4.9	-16.1	9.6
MAD	-	37.2	16.4	15.2	5.1	12.4	6.4

For the ruthenium-related chemistry a reasonable benchmark is harder to perform since we are interested in differences between enantiomers and the ligand plays a more crucial role. Unfortunately, any meaningful simplified ligands are too large to obtain reliable CCSD(T) data, but there are several reasons to assume that our method of choice (PBE0-D3(BJ)/def2-QZVPP) should give reasonable results. As previously mentioned, in a large benchmark set of prototypic organometallic reactions for $3d/4d$ transition metals Ni/Pd in different oxidations states, which included a variety of bond activation reactions (C-H, N-H, O-H, H-H, C-C, ...) and the corresponding barriers, PBE0-D3 performed the best compared to a large set of tested functionals including meta-GGAs and meta-hybrid functionals as well as other dispersion corrected GGAs and hybrid functionals.[83] In a very recent paper, Grimme and co-workers performed another benchmark against the MOR41 database of organometallic reactions.[84] MOR41 contains even more reactions covering most of the synthetically relevant metals in catalysis ($3d$: Ti, Cr, Mn, Fe, Co, Ni / $4d$: Mo, Ru, Rh, Pd / $5d$: W, Ir, Pt), with a broad range of bonding motifs and transformations. Most importantly, the complexes are realistic in that they are actually used in catalysis (e.g. Grubbs metathesis catalysis, Milstein's pincer ligands, etc.) and have not been simplified. The reference data was obtained from DLPNO-CCSD(T)[85,86] which was recently developed in the group of Neese, and enables CCSD(T) quality calculations on large systems. Among the tested functionals, PBE0-D3(BJ)/def2-

QZVPP again performed very well (MAD of 2.8 kcal/mol) and was only outperformed by ωB97X-V and mPW1B95-D3, but not by the Minnesota meta-hybrids or RPA.[84]

Consequently, PBE0-D3 has been applied in the mechanistic study of transition metal catalyzed reactions in the past years. Examples are a study of the oxidative addition of triflates to palladium complexes by Schoenebeck et al. which highlights the importance of dispersion[87], the rhenium-catalyzed hydrogenation of carbonyl derivatives with PNP ligands which was studied by Sortais et al.,[88] or a study of the Pd-catalyzed Suzuki-Miyaura coupling by Kozuch and Martin.[89,90] For ruthenium catalysis, two examples include Breit et al.'s investigation of the Ruthenocene-phosphine-based anti-Markovnikov hydration of alkynes[91] or the mechanistic study of a decarboxylative C-H alkylation with Ru(II) in the group of Ackermann.[92] Despite all benchmarking and successful applications, it is important to verify that computational results are in accordance with experimental observations where they are available.

3

Oxidation of Cyclohexane with Early Transition Metal Catalysts

3.1 Motivation

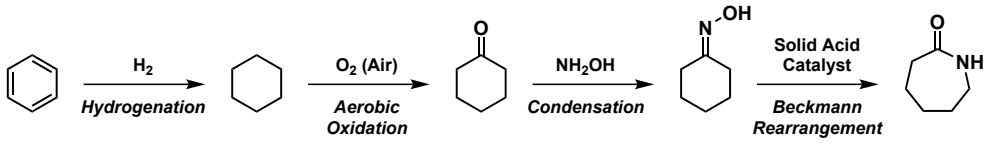

Figure 3.1: Industrial route to ϵ-caprolactam.

The oxidation of cyclohexane to cyclohexanone is of great importance as it is a crucial step in the synthesis of ϵ-caprolactam, the monomer for the production of Nylon-6. Industrial synthesis of ϵ-caprolactan starts from benzene, which is hydrogenated to cyclohexane and oxidized to cyclohexanone, followed by oximation with hydroxyl amine to give cyclohexyl oxime

which can undergo a Beckmann rearrangement to the final lactam (see Figure 3.1).[93] Around seven million tons of cyclohexanol/cyclohexanone (KA oil) are produced annually, mostly through oxidation of cyclohexane with air.[94] The reaction is carried out in liquid-phase, either with cobalt catalysts or uncatalyzed at 140 - 180 °C and 8 - 20 bar. Conversion is kept low to avoid overoxidation of cyclohexane; in most processes conversion is lower than 6 %.[95] The main intermediate in this reaction is cyclohexyl hydroperoxide, which is catalytically decomposed by cobalt into a mixture of cyclohexanone and cyclohexanol, also called KA oil (for **k**etone/**a**lcohol). In the uncatalyzed oxidation, cyclohexyl hydroperoxide is obtained as the main product, which can then be subjected to decomposition in a separate reaction. Different ratios of cyclohexanol to cyclohexanone can be observed depending on the applied metal catalyst. A method to decompose cyclohexyl hydroperoxide only into ketone and water is not known. The KA oil is then separated from cyclohexane which constitutes the bulk of the mixture due to low conversion. Cyclohexane is fed back into the oxidation stream, while the KA oil is split into cyclohexanone and cyclohexanol via distillation. Cyclohexanol can then be dehydrogenated with different catalysts (CrO/Cu, Ni, Zn, $CoCO_3$, ...) to cyclohexanone, which is the desired product for nylon production.[95]

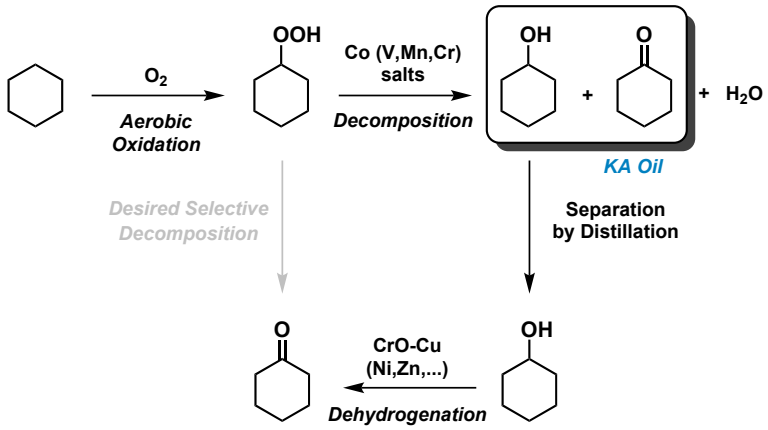

Figure 3.2: Currently applied oxidation of cyclohexane to cyclohexanone.

The problems with this process are obvious:

1. Low general selectivity towards cyclohexanol/cyclohexanone
2. Separation of the KA oil mixture which consumes substantial energy and is not trivial due to azeotrope formation
3. Additional steps are added to the overall synthesis as cyclohexanol has to be dehydrogenated after separation from cyclohexanone so that it can be converted later into the oxime

Preferably, a selective decomposition of cyclohexyl hydroperoxide would yield only the ketone and water, which could be separated easily and would avoid distillation/separation and dehydrogenation steps from the process.

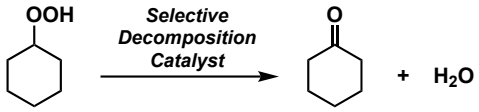

Figure 3.3: Desired dehydroperoxidation to solely cyclohexanone and water.

This was the starting point for research into selective catalysts for the decomposition of cyclohexyl hydroperoxide into cyclohexanone and water. The currently industrially applied systems also allow for some selectivity, giving cyclohexanone:cyclohexanol ratios of up to 4:1 for the aqueous caustic phase process, but in the usually applied Co-catalyzed aerobic oxidation/decomposition process, the ratio favors the alcohol by 7:2.[95] Additionally, the radical dehydroperoxidation suffers from a general selectivity problem: Only about 80% are converted into KA oil, with the rest being carboxylic acids and other ring-opened products. The problem even for a ketone/alcohol ratio of 4:1 is, that this is not sufficient for a change in production as the amount of cyclohexanol that is produced is still to high – a good catalyst will have to provide almost complete selectivity towards the ketone to be of industrial interest.

3.2 Computational Details

Molecular geometries were optimized at BP86/def2-SV(P) level of theory.[35,44,46] Final electronic energies were computed at the PBE0-D3(BJ)/def2-QZVPP[35,54] level using Grimme's dispersion correction[70] with Becke-Johnson damping.[71] Electronic structure calculations were carried out using the TURBOMOLE program[96] using the resolution of the identity approximation[62,97,98] with the corresponding auxiliary basis sets.[36] Thermal corrections and zero-point vibrational energies were computed at the level of geometry optimization (BP86/def2-SV(P)), within the harmonic oscillator/rigid rotor approximation at 298.15 K and 1 bar. All positive vibrational frequencies were used in the vibrational partition function. Free enthalpies of solvation in cyclohexane were calculated for each structure at infinite dilution with the conductor-like screening model for real solvents, COSMO-RS theory[75,76] at the BP86/def-TZVP level using the COSMOtherm program package[78,99] with the corresponding parameter set (Version C3.0, Release 1501, revision 1744).

For each species only the lowest conformer that was found was considered and the conformational partition function was set to 1. In case of cyclohexanol and cyclohexyl hydroperoxide, the equatorial conformers were identified as energetically preferred and used throughout the calculations. For 4-heptyl hydroperoxide, the linear alkyl chain was chosen as the reference in all structures.

For species in the investigation of the chromium chemistry, the calculation of ^{1}H NMR shifts was performed at the B3LYP/def2-TZVPP[44,45,52] level using the DFT-GIAO method[100] as implemented in the TURBOMOLE package with the *chemshift* program from geometries that were optimized at the same level of theory in the gas phase. As usual, tetramethylsilane was selected as reference for the isotropic ^{1}H NMR shifts. NMR shifts for chemically equivalent hydrogen atoms were averaged.

3.3 Vanadium-based Dehydroperoxidation

To enable a selective decomposition of cyclohexyl hydroperoxide to cyclohexanone and water, vanadium complexes had been identified as promising candidates. More specifically, Mimoun et al. had shown that vanadium(V) dipicolinato complexes can form stable alkylperoxo complexes.[101–103] Other examples of alkylperoxo complexes with cobalt[104] and molybdenum[105] had also been demonstrated by Mimoun and coworkers. However, the alkylperoxo complexes they prepared had been obtained from *t*Bu-hydroperoxide, which cannot undergo the desired decomposition, as no corresponding ketone exists. Their focus, however was on reactions of alcohols and alkenes with the alkylperoxo species, with the hydroperoxide serving as an oxidant, not on the fate of the hydroperoxide itself. In further work with vanadium, different reactions of vanadium(V) alkylperoxo complexes were explored, including epoxidations and oxidations of alcohols, but since the hydroperoxide substrate was always *t*Bu-hydroperoxide, only *t*-butanol was obtained. Due to the initial inaccessibility of cyclohexyl hydroperoxide as the desired test substrate, experimental tests for dehydroperoxidation were performed with 4-heptyl hydroperoxide for which a dedicated synthesis had been reported in the literature.[106] The catalyst was prepared from pyridine-2,6-dicarboxylic acid (dipic) and V_2O_5 giving the free hydroxido vanadyl dipicolinato complex **1**.

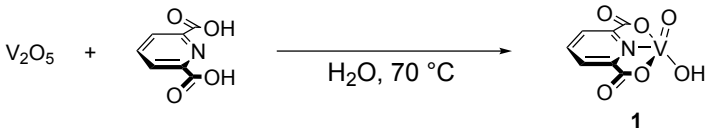

Figure 3.4: Synthesis of vanadium(V) dipicolinato oxido hydroxo catalyst precursor.

Reaction of **1** with alcohols exchanges the hydroxo group and gives the corresponding alkoxido complexes, of which several different species were prepared.

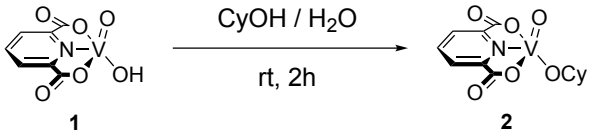

Figure 3.5: Preparation of corresponding cyclohexyl alkoxido complex/catalyst **2** from **1** through addition of the cyclohexanol.

Indeed, 4-heptyl hydroperoxide would undergo dehydroperoxidation when subjected to catalyst **2**, preferably giving the ketone over the alcohol (3.7:1 at room temperature, 2.4:1 at 60 °C).

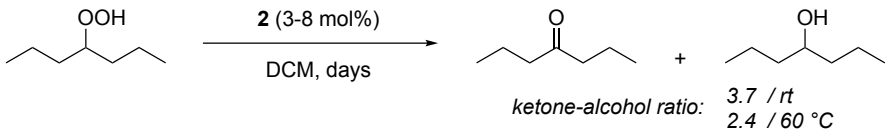

Figure 3.6: Initial dehydroperoxidation experiments with vanadium(V) dipicolinato complexes with 4-heptyl hydroperoxide. Preference of the desired ketone could be observed in ratio of 3.7:1 at room temperature.

These promising results prompted the investigation of cyclohexyl hydroperoxide as the original and industrially relevant substrate. Cyclohexyl hydroperoxide (CyOOH) was obtained via basic extraction from actual KA oil of BASF's cyclohexane oxidation plant. Submitting CyOOH to dehydroperoxidation with complex **2** gave worse selectivities (around 1:1, depending on conditions), but crystals of the cyclohexyl peroxido complex **3** could be obtained as a first example of an alkylperoxido complex derived from a secondary alkyl hydroperoxide.

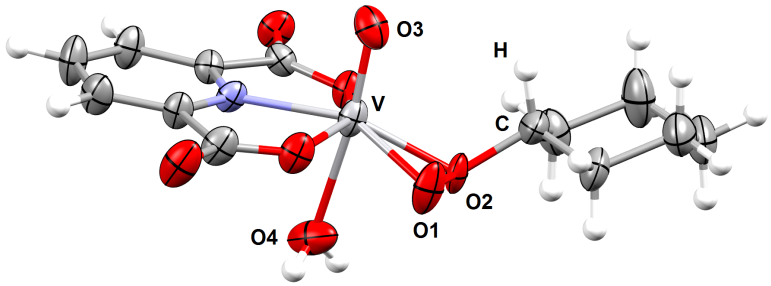

Figure 3.7: Crystal structure of the cyclohexyl peroxide vanadium oxo complex **3** isolated from the reaction of **2** with cyclohexyl hydroperoxide. Bond lengths in Å: V-O1: 1.885(13), V-O2: 2.008(9), V-O3: 1.579(3), V-O4: 2.215(4), O1-O2: 1.438(10), O3-H: 2.742.

In the crystal structure of **3** (figure 3.7), cyclohexyl hydroperoxide is bound to vanadium in an η^2 mode, with V-O bond lengths of 1.89 Å for the primary coordinating oxygen atom and 2.01 Å for the second peroxo oxygen which is bound to the cyclohexyl ring. The O-O bond length is 1.44 Å. Water coordinates *trans* to the oxo group on the vanadium center and the V-O distance for water is 2.21 Å. The distance between the α-hydrogen on the alkylperoxo ligand and the vanadium oxo group is found to be 2.74 Å. This relative proximity already suggests a hydrogen transfer between oxo group and the alkylperoxo substrate, which will be discussed later. We used this structure as a starting point to investigate the reaction computationally. The "regular" radical-based decomposition has been studied extensively by other groups,[107–109] although a full picture of radical decomposition still remains challenging due to reactivity of the species and vastness of the possible reaction network. We were therefore interested whether the selectivity towards ketone and water formation could be due to an underlying non-radical mechanism. This would be a potential entry point for optimization of the reaction to drive the selectivity towards the ketone and improve the overall selectivity.

3.3.1 Thermodynamics

From a purely thermodynamic point of view, the decomposition of cyclohexyl hydroperoxide to ketone and water is strongly exergonic and irreversible. ΔG for this reaction was calculated to be −282.7 kJ·mol^{-1}. This is due to the inherent weakness of the O-O bond; the O-O bond dissociation energy (BDE) in *t*BuOOH is only ~189 kJ·mol^{-1} compared to the C-O BDE in *t*BuOH which is about ~398 kJ·mol^{-1} according to literature.[110] Another factor is the stability of the generated carbonyl group (ΔH = −245.2 kJ·mol^{-1}) as well as the favorable change in entropy (ΔS = 0.157 kJ·mol^{-1}·K^{-1}).

For the radical background decomposition there are several ways how initiation might occur. All are higher in energy then the reactions that will be discussed in the following, but that will not necessarily exclude radical reactions since a small amount of radicals may turnover a relevant fraction of substrate, depending on radical chain length, availability of termination reactions, and general reaction conditions. Homolytic cleavage of the O-O bond in CyOOH was computed to be relatively high in energy with 259.9 kJ·mol^{-1}, similar to the dissociation of the alkylperoxo complex into a vanadium(V) peroxyl and cyclohexyl radical (244.7 kJ·mol^{-1}). In contrast, O-O dissociation in the alkylperoxo complex to a vanadium oxyl and cyclohexyl oxyl radical is much more feasible (146.0 kJ·mol^{-1}). Another possible pathway would be the homolytic cleavage of V-O into a vanadium(IV) oxo complex and cyclohexyl peroxyl radical, which is endergonic by 151.9 kJ·mol^{-1}. In some reactions the formation of VO(dipic)$(H_2O)_2$ was observed, which supports this mode of radical initiation. Radical mechanisms will not be evaluated in this thesis, but the work of Hermans and co-workers should be mentioned once again here, who have performed in-depth experimental and theoretical work on radical autoxidations, and more specifically the oxidation of cyclohexane.[108,109,111–114]

3.3.2 Dehydroperoxidation via H-Transfer to the Oxo Group

In a proposed schematic mechanism (figure 3.8) for the dehydroperoxidation from an initial vanadium(V) alkylperoxido complex, the α-hydrogen on the hydroperoxide is transferred to the oxo group, while the O-O bond is cleaved. This step could be concerted or stepwise. Upon hydrogen transfer the free hydroxido oxido vanadium dipicolinato complex is formed. From this complex, addition of hydroperoxide yields the initial alkylperoxido complex and releases water, which completes the catalytic cycle.

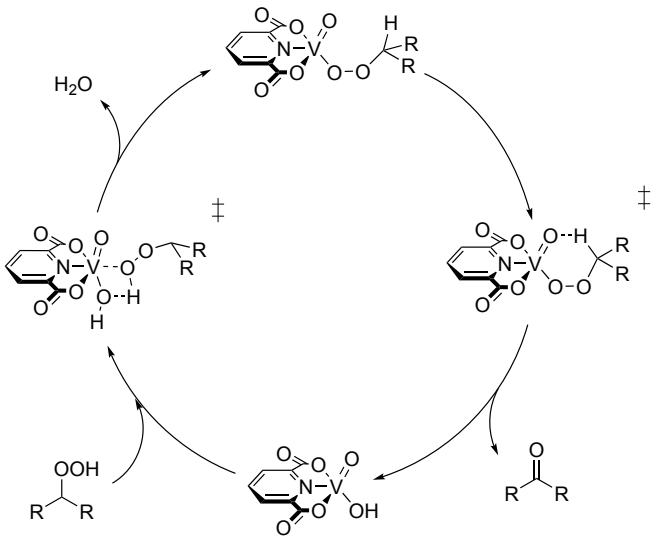

Figure 3.8: Proposed mechanism for the vanadium-catalyzed dehydroperoxidation of cyclohexyl hydroperoxide via intramolecular transfer of the α-hydrogen on the hydroperoxide to the oxo group on the vanadium catalyst with cleavage of the peroxide O-O bond. The decomposition is followed by addition of new substrate under release of water to restore the initial complex.

An overview of the investigated mechanism as a reaction path is depicted in Figure 3.9. The catalytic cycle starts from the cyclohexylperoxo complex **3**, which was isolated and analyzed by X-ray crystallography (see Figure 3.7) and is used as the reference (G = 0 kJ·mol^{-1}) for our mechanism. Decoordination of water from this complex forms the distorted square pyramidal complex **4** in which the peroxide oxygens are still bound in η^2-fashion to the vanadium center. Despite the weak enthalpy of dissociation of only 41.3 kJ·mol^{-1}, formation of this complex is endergonic by 9.0 kJ·mol^{-1} as the gained entropy (ΔS = +0.146 kJ·mol^{-1}·K^{-1}) is countered by release of water into cyclohexane with ΔG_{solv} = +11.1 kJ·mol^{-1}. The water-free complex **4** can then rearrange to the η^1 alkylperoxo complex **5**, which structurally already resembles the following hydrogen transfer transition state and is endergonic by 27.0 kJ·mol^{-1} relative to **3**. From **5**, decomposition of cyclohexyl peroxide occurs through the six-membered transition state **TS6**. The activation energy of this process is 110.1 kJ·mol^{-1} with respect to **3**. The deperoxidation is concerted; the hydrogen transfer to the oxo group occurs simultaneously with the cleavage of the O-O bond.

The transition state structure is shown in Figure 3.10. The O-O bond is already significantly elongated to 1.71 Å, especially when compared to the O-O bond length in the loose η^1 complex **5** (1.40 Å). The two V-O bonds are of similar length in the transition state: 1.63 Å for the V-O double bond about to turn into a new V-OH group with a single bond, while the other V-O peroxo bond length is 1.69 Å, on trajectory to form the new V-O oxo group and double

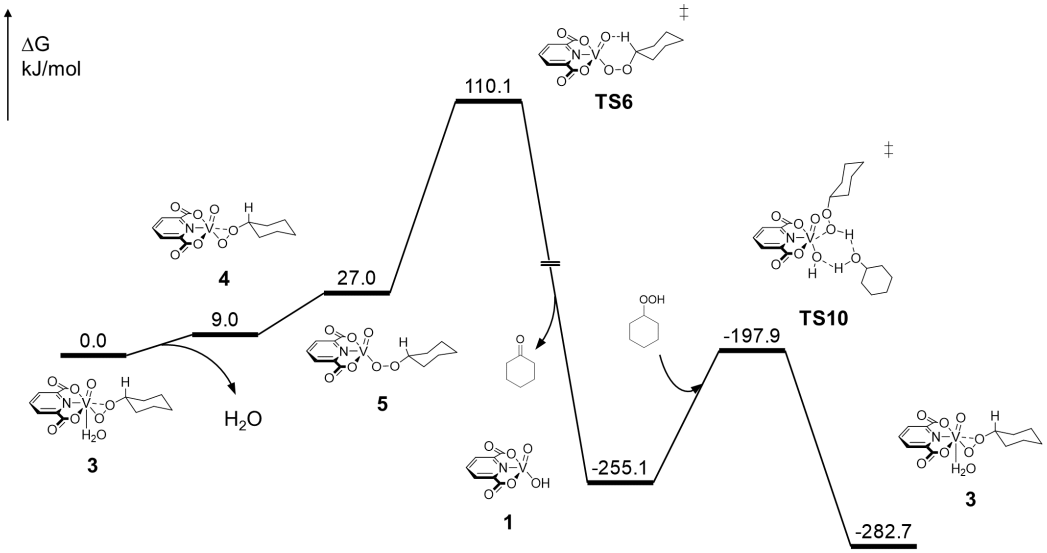

Figure 3.9: Free energy pathway for the vanadium-catalyzed dehydroperoxidation of cyclohexyl hydroperoxide. Energies are given in kJ/mol and are relative to complex **3** which was isolated and characterized by X-ray crystallography. The energy levels after **TS6** have been adjusted in height due to the highly exergonic nature of the reaction.

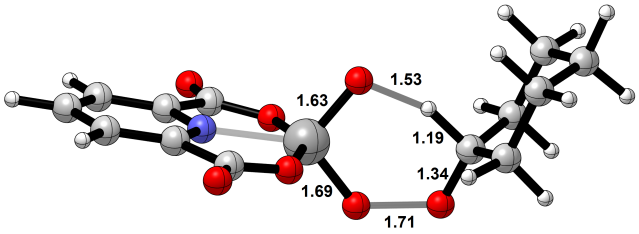

Figure 3.10: Transition state **TS6** in which hydrogen transfer and O-O bond cleavage occur in a concerted mechanism.

bond. The hydrogen to be transferred to the oxo group has a O-H distance of only 1.53 Å and the C-H bond is almost directly pointing at the oxo group. A stepwise mechanism could proceed through the corresponding alkylperoxo species with no α-hydrogen and a protonated oxo group on the vanadium complex, but this is not a stable intermediate. Similarly, the other stepwise mechanism would involve cleavage of the O-O bond before hydrogen transfer into a cyclohexyloxyl radical and the corresponding vanadium oxyl species, but this process is too high in energy (ΔG = 146.0 kJ·mol^{-1}). The formation of cyclohexanone and the vanadium oxo hydroxo species **1** via **TS6** is irreversible as the reverse barrier would be 365.2 kJ·mol^{-1}. Intermediate **1** can then undergo addition of new cyclohexyl hydroperoxide to give the initial cyclohexylperoxo complex **3** and water. This addition is exergonic with respect to **1** by 27.6 kJ·mol^{-1}. Figure 3.11 shows different transition states for the hydroperoxide addition.

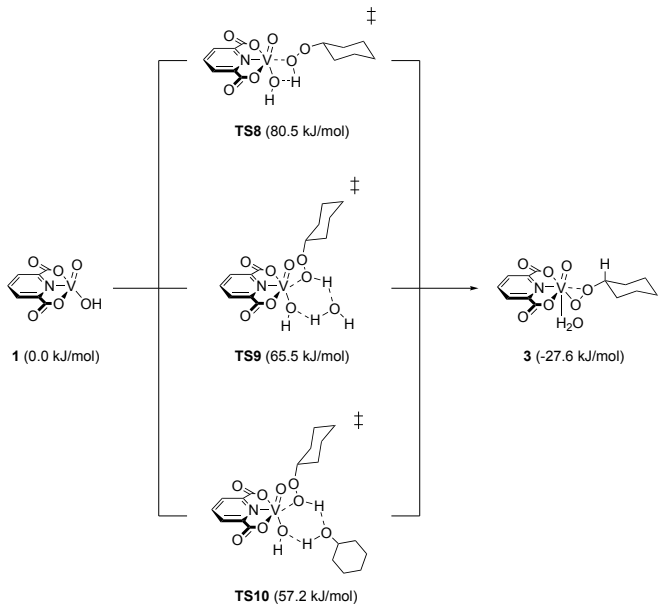

Figure 3.11: Comparison of direct hydroperoxide addition (**TS8**) and proton relay mechanisms for hydroperoxide addition with water (**TS9**) and cyclohexanol (**TS10**).

The direct addition of cyclohexyl hydroperoxide through a four-membered transition state (**TS8**) is relatively high in energy with a barrier of 80.5 kJ·mol^{-1}. However, different proton relay mechanisms are possible: water can act as a proton relay agent and is generated anyway during the reaction as well as cyclohexanol. The proton relay transition states, forming six-membered rings, all have lower barriers than the direct addition: 65.5 kJ·mol^{-1} for **TS9** with water and 57.2 kJ·mol^{-1} for **TS10** with cyclohexanol. Hydrogen transfer and cleavage of the O-O bond in **TS6** (figure 3.9) is therefore the rate-determining step in the overall mechanism with a barrier of 110.1 kJ·mol^{-1}.

3.3.3 Comparison with 4-Heptyl Hydroperoxide

Since higher selectivities towards the dehydroperoxidation into ketone and water were observed for 4-heptyl hydroperoxide, the mechanism was recalculated for this substrate. The reaction path is shown in Figure 3.12. Again, the η^2 alkylperoxo complexes with coordinated water serve as reference. From the alkylperoxo complex **11**, loss of water (**12**) and rearrangement to the η^1 alkylperoxo complex **13** are endergonic by 4.5 kJ·mol^{-1} and 19.2 kJ·mol^{-1}, which is slightly lower than the corresponding changes for cyclohexyl hydroperoxide. Despite both substrates being secondary hydroperoxides, a considerably lower activation energy for the transition state **TS14** is found for 4-heptyl hydroperoxide (91.7 kJ·mol^{-1} vs. 110.1 kJ·mol^{-1} for cyclohexyl hydroperoxide) to give 4-heptanone and oxo hydroxo intermediate **1**. The relative difference $\Delta\Delta G^{\ddagger}$ of 18.4 kJ·mol^{-1} when comparing to cyclohexyl hydroperoxide trans-

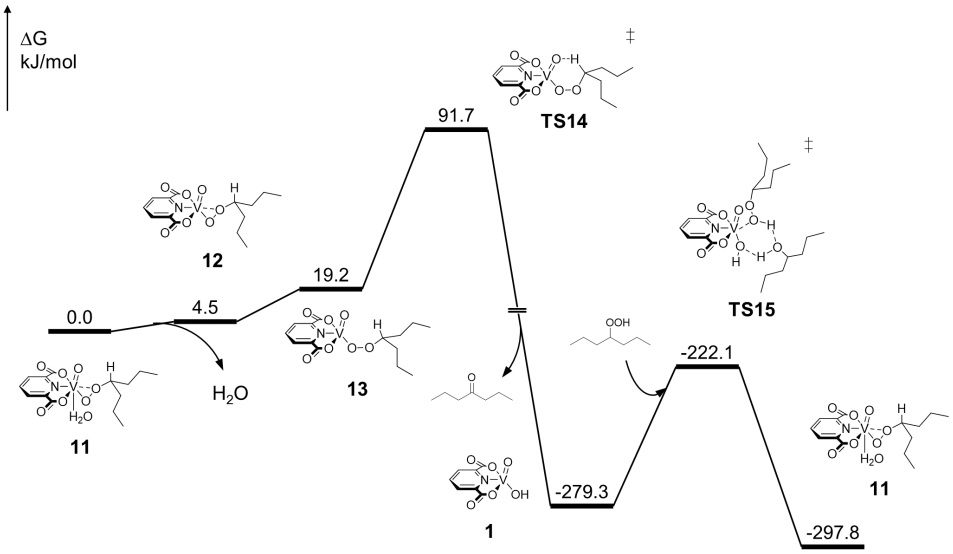

Figure 3.12: Free energy pathway for the vanadium-catalyzed dehydroperoxidation of 4-heptyl hydroperoxide. Energies are given in kJ/mol and are relative to complex **11**. The energy levels after **TS14** have been adjusted in height due to the highly exergonic nature of the reaction.

lates into a ~1600-fold increase in rate, which may explain the observed selectivity difference: For the linear alkyl hydroperoxide, more decomposition through the non-radical based pathway is occurring which leads to formation of ketone and water, rather than decomposition into a mixture of ketone and alcohol which is likely radical-based. The lower activation energy is likely due to better adaption to the transition state structure in the linear alkyl chain. Structural comparison of intermediates **5** and **13**, which preceed the hydrogen transfer transition states **TS6** and **TS14**, show that the change in O-H distance is lower for 4-heptyl hydroperoxide (0.72 Å) than cyclohexyl hydroperoxide (0.89 Å), indicating that the linear alkane is already closer to the transition state in the preceeding intermediate. Addition of new substrate to intermediate **1** proceeds similar to cyclohexyl hydroperoxide. Only the proton relay through 4-heptanol was calculated in analogy to cyclohexanol which had the lowest barrier in the mechanism for CyOOH. For 4-heptyl hydroperoxide, this has process has an activation energy of 57.2 kJ·mol^{-1} via **TS15** and is exergonic by 18.5 kJ·mol^{-1} to yield the initial alkylperoxo complex **11**.

3.3.4 Influence of Water Coordination

In addition to the previous mechanistic studies of cyclohexyl and 4-heptyl hydroperoxide, variants of the mechanism in which water stays coordinated to the complex were also investigated. This is of interest since the obtained crystal structure of **3** had a water molecule coordinating trans to the oxo group, but also because water is generated in the dehydroperoxidation

and therefore abundant during the reaction; furthermore the decoordination of water to **4**/**12** was found to be endergonic in the calculations.

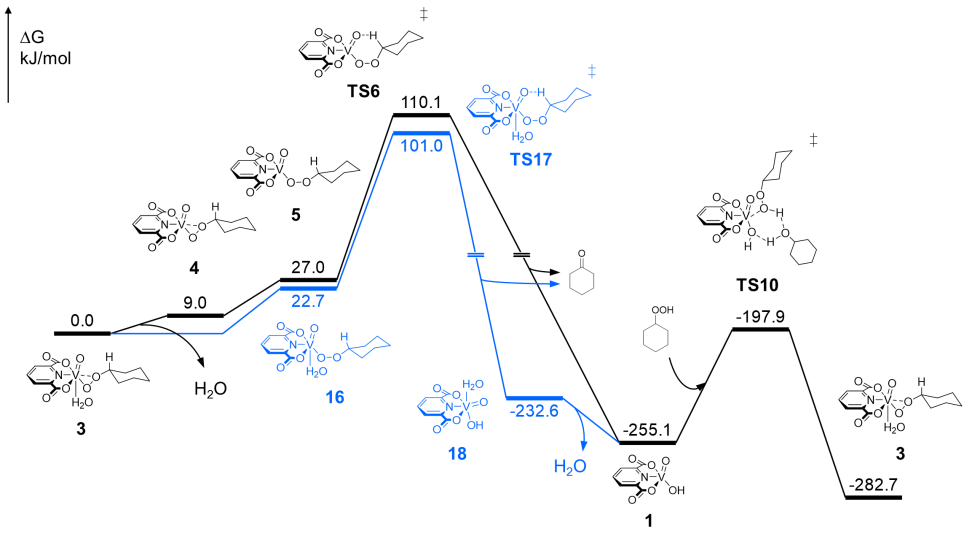

Figure 3.13: Free energy pathway for the vanadium-catalyzed dehydroperoxidation of cyclohexyl hydroperoxide with (blue) and without (black) water coordinating to the catalyst. Energies are given in kJ/mol and are relative to complex **3**. The energy levels after **TS6** and **17** have been adjusted in height due to the highly exergonic nature of the reaction.

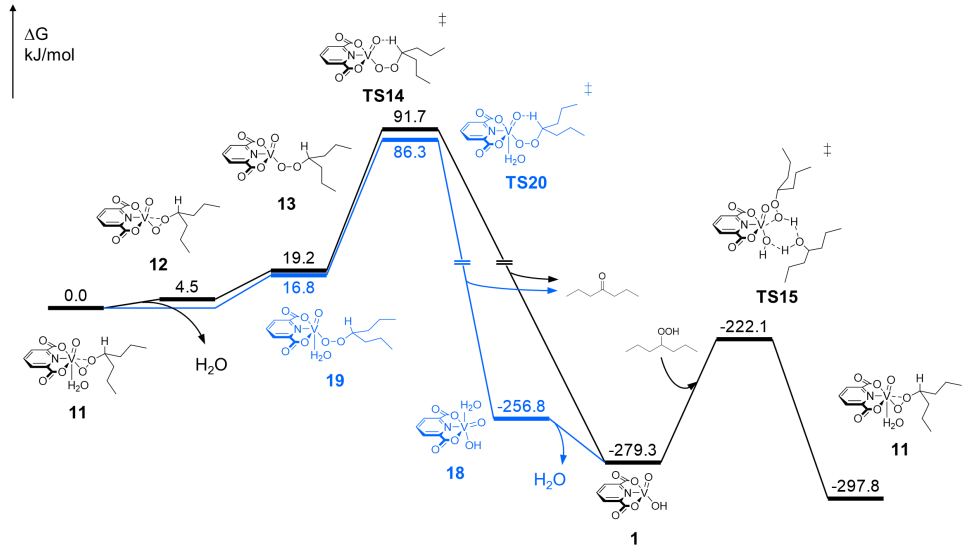

Figure 3.14: Free energy pathway for the vanadium-catalyzed dehydroperoxidation of 4-heptyl hydroperoxide with (blue) and without (black) water coordinating to the catalyst. Energies are given in kJ/mol and are relative to complex **11**. The energy levels after **TS14** and **TS20** have been adjusted in height due to the highly exergonic nature of the reaction.

Figures 3.13 and 3.14 show the water-assisted pathways in comparison with the regular dehydroperoxidation mechanisms. The relative changes are very similar for cyclohexyl and 4-heptyl

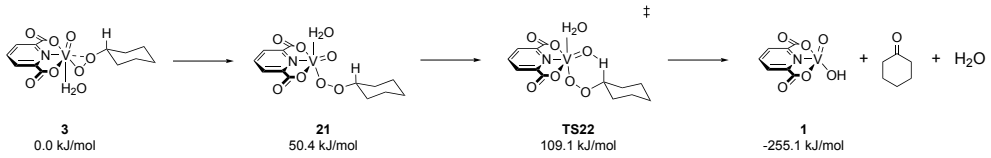

Figure 3.15: Free energy pathway for dehydroperoxidation with water coordinating *cis* to the oxo group during the reaction for cyclohexyl hydroperoxide. Energies are given in kJ/mol and are relative to complex **3**.

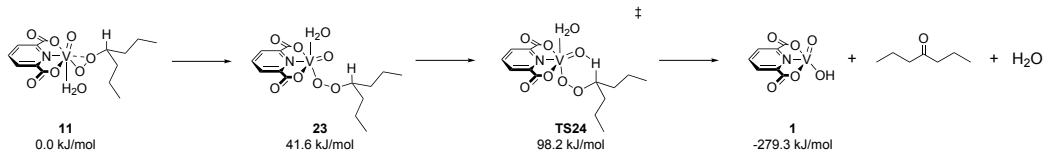

Figure 3.16: Free energy pathway for dehydroperoxidation with water coordinating *cis* to the oxo group during the reaction for 4-heptyl hydroperoxide. Energies are given in kJ/mol and are relative to complex **11**.

hydroperoxide. The loose hydroperoxide without η^2 coordination is slightly more stable with water coordinating in both cases ($4.3\,\mathrm{kJ{\cdot}mol^{-1}}$ for CyOOH, $2.4\,\mathrm{kJ{\cdot}mol^{-1}}$ for HeptOOH). The barrier for dehydroperoxidation is also lowered for both substrates, with $101.0\,\mathrm{kJ{\cdot}mol^{-1}}$ for cyclohexyl hydroperoxide via **TS17** and $86.3\,\mathrm{kJ{\cdot}mol^{-1}}$ for 4-heptyl hydroperoxide via **TS20**. The previously calculated difference remains, as dehydroperoxidation is favored for the linear hydroperoxide by $13.7\,\mathrm{kJ{\cdot}mol^{-1}}$, in agreement with the observation of more selective dehydroperoxidation for 4-heptyl hydroperoxide. While coordination of water is favorable to this point, after dehydroperoxidation, the newly formed oxo group is now in *trans* to the ligand and *cis* to the coordinating water. Due to the oxo groups strong trans effect, decoordination of water from **18** to **1** is now energetically favored by $22.5\,\mathrm{kJ{\cdot}mol^{-1}}$. In summary, the water-assisted pathway is not only feasible but also lower in energy and can therefore likely take place, depending on the reaction conditions.

The water-assisted dehydroperoxidation was also recalculated for water being *cis* to the oxo group during the mechanism, and the correspoding pathways are shown in Figures 3.15 and 3.16. These complexes could potentially be formed from hydroperoxide addition to intermediate **18**. However, the *cis* coordinated loose alkylperoxo complexes **21** and **23** are already substantially higher in energy than their *trans* counterparts: for the cyclohexyl substrate, the corresponding intermediate **21** is $23.4\,\mathrm{kJ{\cdot}mol^{-1}}$ less stable than *trans* complex **5**, for heptyl hydroperoxide the difference between **13** and **23** is lower with $12.4\,\mathrm{kJ{\cdot}mol^{-1}}$, but still favors the *trans* complex. Not surprisingly, the following transition states **TS22** and **24** are also higher in energy, with overall barriers of $109.1\,\mathrm{kJ{\cdot}mol^{-1}}$ for CyOOH and $98.2\,\mathrm{kJ{\cdot}mol^{-1}}$ and HeptOOH,

which render them unlikely compared to the regular water-assisted mechanism.

3.3.5 Proton Relay Mechanisms

Since a significant reduction of the activation energy was found for proton relay mechanisms in the addition of hydroperoxide to the catalyst ($57.2\,\mathrm{kJ{\cdot}mol^{-1}}$ via **TS10** vs. $80.5\,\mathrm{kJ{\cdot}mol^{-1}}$ for **TS8**), a potential proton relay mechanism for the dehydroperoxidation step was also investigated. The difference, however, is that the direct addition in **TS8** proceeds through a four-membered transition state, and the additional entropic contribution of the proton relay mechanisms can be compensated by better orbital overlap in a six-membered transition state, whereas a proton relay mechanism for dehydroperoxidation as in **TS6** does not provide this benefit (six-membered vs. eight-membered transition state).

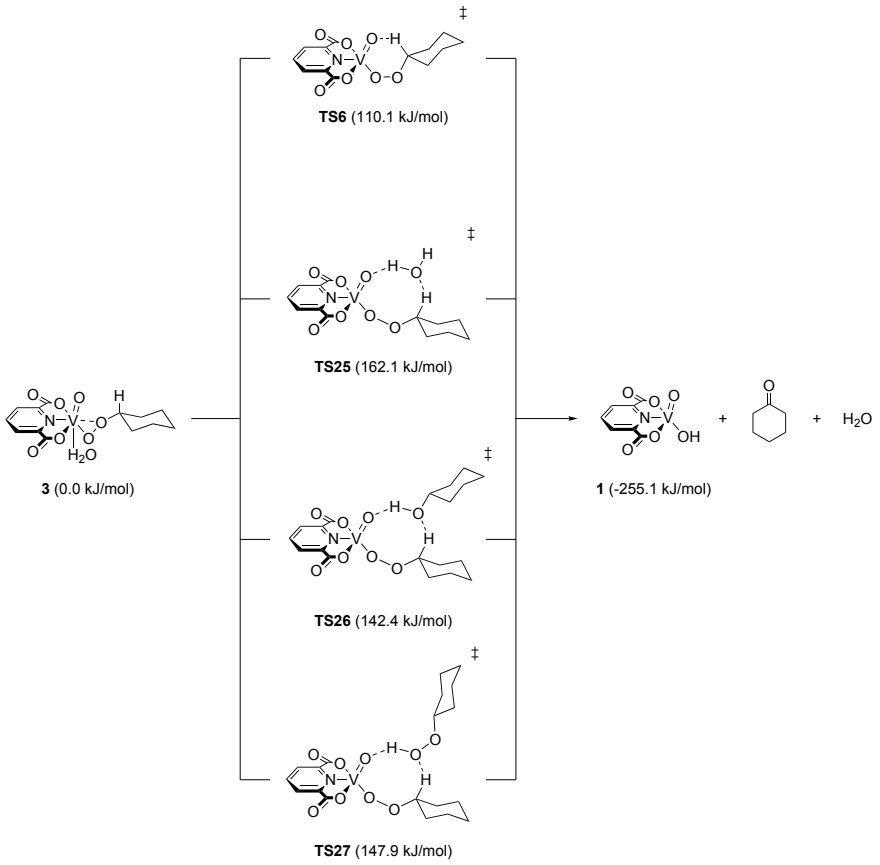

Figure 3.17: Proton relay transfer for the dehydroperoxidation step with water, cyclohexanol and cyclohexyl hydroperoxide, with **TS6** for comparison. Energies are given in kJ/mol and are relative to complex **3**.

As expected, proton relays are therefore not a valid alternative to the regular six-membered transition state: all transition states (see Figure 3.17) are substantially higher in energy. Proton relay through water (**TS25**) is the highest with an overall barrier of $162.1\,\mathrm{kJ{\cdot}mol^{-1}}$ relative

to **3**, the corresponding transition states with cyclohexanol (**TS26**) and cyclohexyl hydroperoxide (**TS27**) are lower with 142.4 kJ·mol^{-1} and 147.9 kJ·mol^{-1}, but still not competitive with the original mechanism (110.1 kJ·mol^{-1}). Hence, participation of proton relay agents in the dehydroperoxidation step is ruled out for this reaction.

3.3.6 Hydrogen Transfer to Carboxyl Group of Dipic

Another open question was whether the ligand participates in the reaction. In a variant of metal-ligand cooperation, the α-hydrogen of CyOOH could be potentially abstracted by a carboxyl group of the ligand, releasing the ketone through O-O bond cleavage and forming a partially protonated dipic vanadium(V) dioxo complex. Carboxylated vanadium(V) dioxo complexes have been known for some time,[115,116] and dioxo vanadium complexes with tridentate Schiff-base ligands, which are structurally related to dipic, have been previously prepared by Plass and Yozgatli.[117] If the ligand were to participate actively in the reaction, changes in the ligand structure could be used to actively engineer the ligand's properties for a more selective dehydroperoxidation.

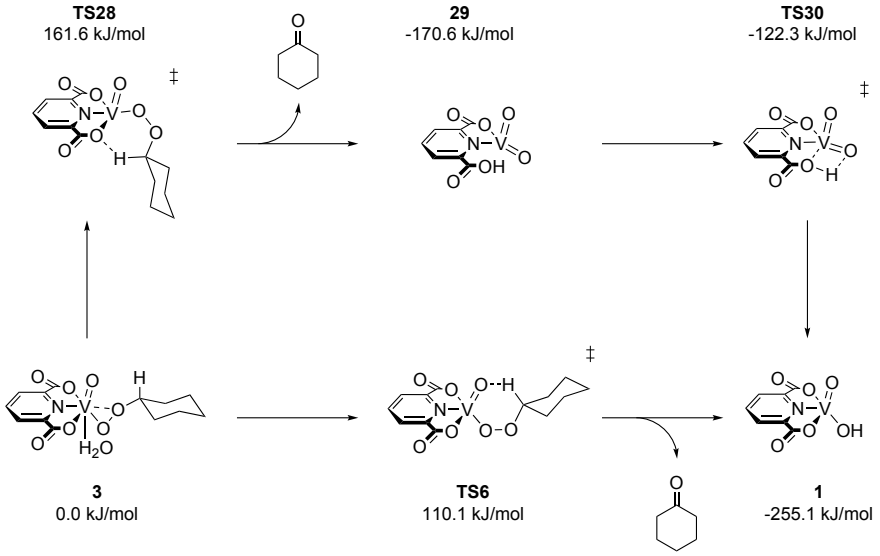

Figure 3.18: Deprotonation through protonation of the carboxyl group of the dipic ligand in comparison with the regular dehydroperoxidation. Energies are given in kJ/mol and are relative to complex **3**.

Figure 3.18 depicts the ligand-assisted pathway in comparison with the regular dehydroperoxidation mechanism, complex **3** serves as reference. The ligand protonation transition state **TS28** cannot be considered feasible with 161.6 kJ·mol^{-1}, which is 51.5 kJ·mol^{-1} higher in energy than **TS6** where the vanadium oxo group is the hydrogen acceptor. Interestingly, if **TS28** was lower in energy, the hypothetical dioxo species **29** could undergo very fast isomerization

back to oxo hydroxo complex **1** with an activation energy of only 48.3 kJ·mol^{-1} through **TS30**. A closer look at the transition state structure reveals that the O-O bond length is very large (1.91 Å) compared to that in the regular pathway (**TS6**, O-O distance: 1.71 Å), which might explain the high energy of this transition state. The O-O bond is essentially already dissociated when hydrogen transfer takes place, costing significant energy. This is due to the V-O bond of the hydrogen acceptor being considerably longer for dipic (2.03 Å in **TS28**) than for the vanadium oxo group in the regular mechanism (1.63 Å in **TS6**). Otherwise, the bond lengths are similar; the α-hydrogen being abstracted from the cyclohexyl hydroperoxide has a C-H distance of 1.21 Å, the O-H distance for the reprotonation of the dipic oxygen is 1.53 Å and the second oxo group on dipic to be formed has an O-V bond length of 1.69 Å (the oxo group that remains untouched in this mechanism has a V-O distance of 1.59 Å).

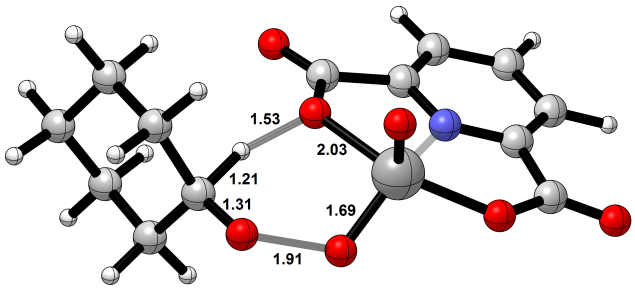

Figure 3.19: Transition state for the ligand-assisted deprotonation via **TS28**, leading to the vanadium(V) dioxo complex **29** with a partially protonated dipic ligand.

3.3.7 Addition of Hydroperoxide through Ligand Protonation

Although participation of the ligand in dehydroperoxidation has been ruled out, the carboxyl group could still be involved in the other crucial step of the reaction mechanism, the addition of hydroperoxide to the complex. Here, the O-H bond of the hydroperoxide formally adds to the V-O bond of the complex to give an alkylperoxo oxo hydroxo vanadium species. The proposed mechanism is shown in Figure 3.20.

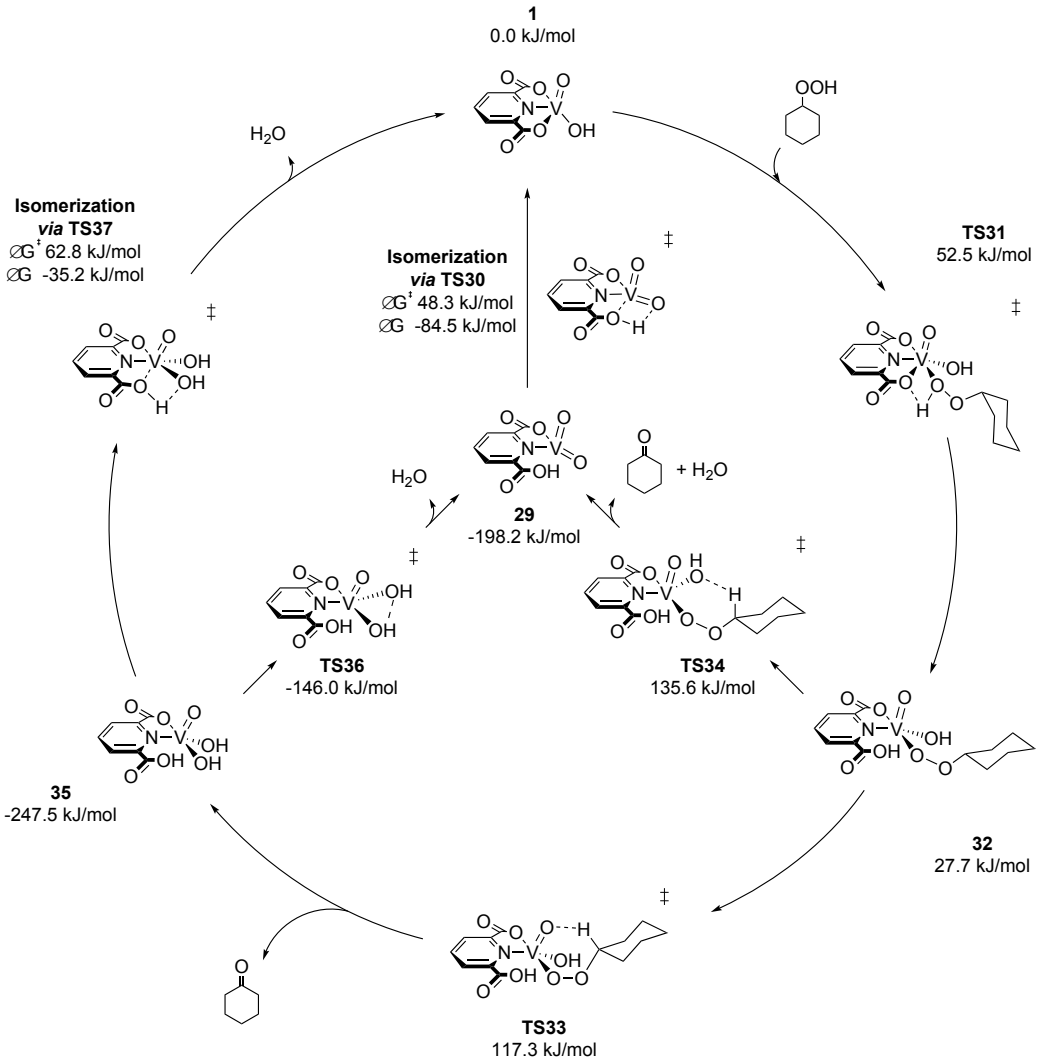

Figure 3.20: Mechanism based on hydroperoxide addition to the carboxyl vanadium V-O bond. Reference is the free oxo hydroxo species **1** where in the regular mechanism hydroperoxide addition occurs to the hydroxo group. Energies are free enthalpies in kJ/mol. From the intermediate **32**, several pathways are possible: hydrogen transfer to the oxo group (**TS33**) or hydroxo group (**TS34**), followed by several isomerization/dehydration reactions to the initial oxo hydroxo vanadium complex **1**.

Direct addition through the four-membered transition state **TS31** on to the ligand-metal bond is in fact feasible with an activation energy of 52.5 kJ·mol^{-1}. This is, surprisingly, a lower bar-

rier than the regular hydroperoxide addition, even when assisted through proton relay agents (**TS10** through cyclohexanol, 57.2 kJ·mol^{-1}). Figure 3.21 shows the transition state for the addition to the carboxyl ligand, with a long V-O bond length (3.51 Å) for the peroxo oxygen to be added onto vanadium due to the formally saturated/closed coordination shell of vanadium. The trajectory shows that this transition state is mostly a deprotonation of the hydroperoxide; the newly formed anion seamlessly transitions into coordination to vanadium to yield the new VO(Hdipic)(OH)(OOCy) complex. Formation of the alkylperoxo oxo hydroxo vanadium complex **32** with a protonated dipic ligand is kinetically favored over the regular oxo alkylperoxo complex **3**, due to the lower activation energy. But contrary to the formation of **3**, which is exergonic by 27.6 kJ·mol^{-1}, reaction to **32** is endergonic by 27.7 kJ·mol^{-1}. The reverse reaction back to **1** therefore only has a barrier of 24.8 kJ·mol^{-1} and will take place rapidly, while addition product **3** is much less likely to undergo such a backreaction ($\Delta G^{\ddagger}$ = 84.8 kJ·mol^{-1}). From **32**, two potential acceptors for the transfer of the α-hydrogen on the peroxide are possible: either to the hydroxo group, which is still available in this pathway, or to the oxo group, similar to the regular mechanism. The former is too high in energy with 135.6 kJ·mol^{-1} via **TS34** to yield the dioxo species **29**. More likely, but still higher in energy than the regular mechanism, is the transfer to the vanadium oxo group through **TS33**, with a barrier of 117.3 kJ·mol^{-1}. Either way, closing the catalytic cycle in both reaction paths seems feasible: Dioxo complex **29** can restore the initial oxo hydroxo complex **1** as already shown through **TS30** with a small activation energy of only 48.3 kJ·mol^{-1}. Oxo dihydroxo species **35** originating from **TS33** can do an internal protonation between the two *cis* hydroxo groups leading to expulsion of water and formation of **29**, from which formation of **1** has just been discussed. This process has a relatively high barrier of 101.5 kJ·mol^{-1}. **35** can also transfer hydrogen from the protonated carboxyl group to the hydroxo group *cis* to go directly to complex **1**, which has a far lower barrier of only 62.8 kJ·mol^{-1} via **TS37**. Nevertheless, the barriers through **TS33** and **TS34** make this pathway not feasible.

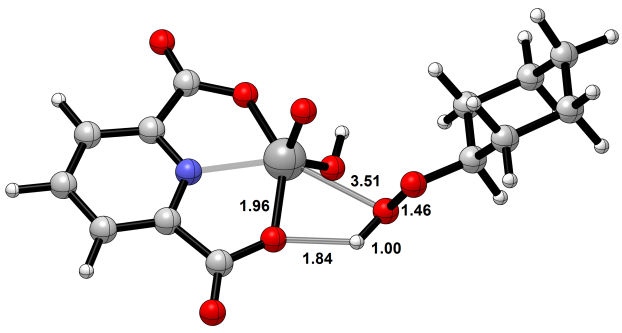

Figure 3.21: Structure of transition state **TS31** for the addition of cyclohexyl hydroperoxide directly to the carboxyl group of the dipic ligand and vanadium.

3.3.8 Hydrogen Transfer to a Peroxide Oxygen Atom

Another conceivable mechanism for dehydroperoxidation from **3** would be the transfer of the α-hydrogen to the peroxide oxygen that is bound to vanadium in the alkylperoxo complex. This would lead to the same intermediate **1** as in our current regular mechanism, although the oxo group on the vanadium center is conserved in this process and the new hydroxo group is formed from the peroxo oxygen. In a direct transfer through a four-membered transition state, two conformational variants are possible, with the hydrogen transfer occurring either *syn* or *anti* to the vanadium oxo group. The direct hydrogen transfers can be excluded as relevant since they are very high in energy. The dehydroperoxidation in *syn* mode has a barrier of 202.0 kJ·mol^{-1}, the *anti* pathway a similar barrier of 203.5 kJ·mol^{-1}, which are far too high to occur at the employed reaction conditions (room temperature to 60 °C).

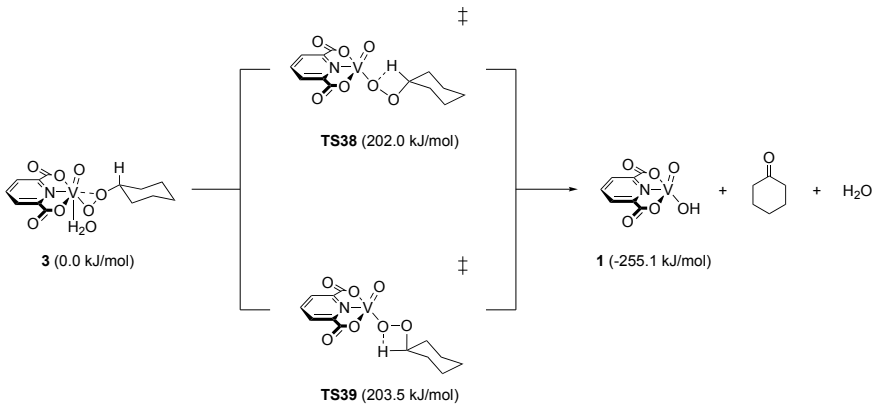

Figure 3.22: Hydrogen transfer to the peroxide oxygen atom in *syn* and *anti* conformation. Energies are free enthalpies in kJ/mol and relative to complex **3**.

Structures of the corresponding transistion states are shown in Figure 3.23. Despite being conformationally different, the structural cores of the transition states are very similar for the *syn* and *anti* dehydroperoxidation, in line with them being almost isoenergetic. The O-O bond lengths in both transition states are very large with 2.02 Å for **TS38** (*syn*) and 2.01 Å for **TS39** (*anti*). For comparison: the O-O distance in the regular dehydroperoxidation transition state **TS6** was only 1.71 Å. Even in the already unfavorable ligand-assisted mechanism via **TS28**, the O-O distance is lower with 1.91 Å. It therefore seems like these transition states resemble an adduct of a cyclohexyloxyl radical and a vanadium(V) oxyl species, and in fact, the dissociation energy into these two separate species is only higher by about ~40 kJ·mol^{-1} (244.7 kJ·mol^{-1}). C-H and C-O distances are equal in both the *syn* and *anti* mode with 1.22 Å and 1.32 Å. It may be argued, that in the case of large O-O bond lengths, increasing biradical character is not very well described by a single reference method, but since the corresponding transition states are > 100 kJ·mol^{-1} higher in energy than our proposed mechanism, these

pathways can still be considered unfeasible despite potential error in the correct description of the electronic structure.

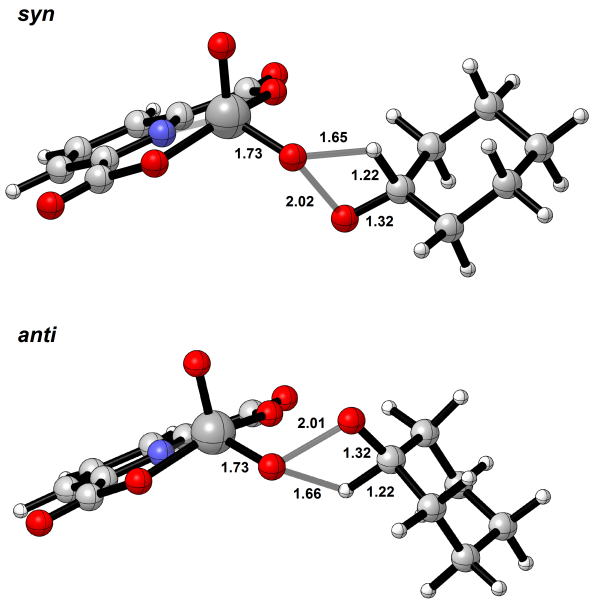

Figure 3.23: Structure of *syn* and *anti* transition states **TS38** and **TS39** for the hydrogen transfer to peroxo oxygen on vanadium.

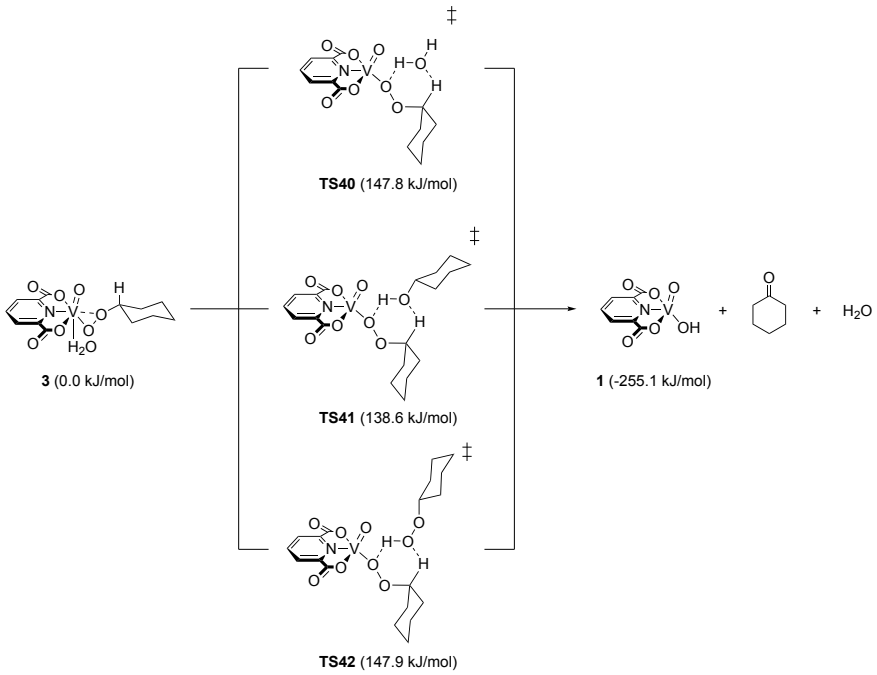

Figure 3.24: Proton relay assisted hydrogen transfer transition states to the peroxide oxygen atom in *syn* and *anti* conformation. Energies are free enthalpies in kJ/mol and relative to complex **3**.

Accordingly, proton relay transfers were also studied for this step and are shown in Figure 3.24. Hydrogen transfer through any proton relay agents reduce the barrier height substantially. For water the overall barrier goes down to 147.8 kJ·mol^{-1} via **TS40**, cyclohexanol as a proton relay agent has a barrier of 138.6 kJ·mol^{-1} and cyclohexyl hydroperoxide shows a similar barrier to that of water with 147.9 kJ·mol^{-1} through transition state **TS42**. Still, even the energetically most feasible pathway via **TS41** is not competitive compared to the original mechanism (**TS6**, 110.1 kJ·mol^{-1}) or the water-assisted analogous pathways which have smaller barriers.

3.3.9 Summary and Conclusion

The radical-free dehydroperoxidation of alkyl hydroperoxides with a vanadium dipicolinato complex has been studied. Results show, that a radical-free mechanism, without change in oxidation state on the vanadium center, is energetically feasible. Depending on conditions, a water-assisted pathway, where water stays coordinated in *trans* position to vanadium during the dehydroperoxidation step, is energetically favored (figures 3.13 and 3.14). A considerable difference is found for the substrates, cyclohexyl hydroperoxide and 4-heptyl hydroperoxide. For cyclohexyl hydroperoxide, overall barriers lie at 110.1 kJ·mol^{-1} (**TS6**) and 101.0 kJ·mol^{-1} (water-assisted, **TS17**), whereas 4-heptyl hydroperoxide has barriers of 91.7 kJ·mol^{-1} (**TS14**) and 86.3 kJ·mol^{-1} (water-assisted, **TS20**). Selective decomposition of the latter is hence favored by ~15 to 18 kJ·mol^{-1}, explaining differences in ketone selectivity, relative to the background radical decomposition that usually produces a 1:1 ratio of ketone and alcohol. In further investigations, many other variants of possible dehydroperoxidation reactions with the vanadium dipicolinato ligand were explored: proton relay mechanisms for the dehydroperoxidation step, hydrogen transfer to the carboxyl group on the dipicolinato ligand, addition of the hydroperoxide to the carboxyl group and the subsequent possible pathways as well as an internal hydrogen transfer to the peroxide oxygen and its proton relay variants. None of these were found to be competitive with the original mechanism. The crucial step for the radical-free dehydroperoxidation is therefore a six-membered transition state in which cleavage of the O-O bond occurs simultaneously with the hydrogen transfer to the vanadium oxo group.

Based on these results, two possible ideas were developed to improve selectivity. The overall goal is to lower the activation energy for the selective, non-radical pathway as studied in this chapter to facilitate more decomposition into ketone and water, rather than a ketone-alcohol mixture.

1. Altering the ligand might potentially give a vanadium oxo group which can serve as a better acceptor, lowering the activation energy for dehydroperoxidation in our pathway.

2. Since the six-membered transition state for dehydroperoxidation is enabled through the neighboring oxo and hydroxo/alkylperoxo motif on the metal, other metal complexes that can exhibit this motif and form stable oxo complexes could potentially act by a similar mechanism and be more suitable for selective dehydroperoxidation.

Following approach 1, several Schiff base ligands were prepared. These contain the same tridentate O-N-O coordination motif as the dipicolinato ligand, but are relatively simple to syn-

thesize. As mentioned earlier, vanadium complexes of Schiff bases had been prepared previously by several groups.[118–120]

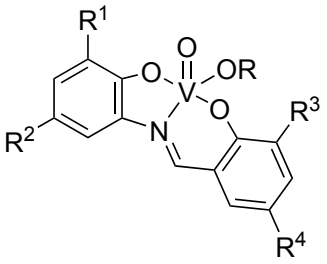

Figure 3.25: Schiff base vanadium complexes that were prepared as catalysts for dehydroperoxidation. The ligands can be synthesized from the corresponding aniline and benzaldehyde. Reaction of the ligand with $VO(OEt)_3$ gives the desired vanadium complexes.

Three different Schiff base ligand complexes were tested in dehydroperoxidation reactions. Groups R^2/R^4 were either *tert*-amyl or *tert*-butyl to increase solubility, whereas R^1/R^3 were varied to make the complexes differently sterically demanding (H/H, H/*t*Bu and *t*Bu/*t*Bu). The first two tended to form μ-oxo bridged dimer complexes (which were nevertheless used in catalysis) while the last and most sterically demanding Schiff base gave a monomeric complex with R = Et. However, all complexes failed to give significantly improved selectivities. The ketone-alcohol ratios were in a range of 0.7 to 1.3, with better stereoselectivities for the sterically less demanding Schiff bases (despite their tendency for dimerization). The search for better ligands was then supplanted by approach 2. Rather than trying to find or test out other ligands for the vanadium-based dehydroperoxidation, new metal-oxo species or metals known to form similar oxo/hydroxo motifs, were tested. A large body of transition metals was screened for catalytic activity and ketone-alcohol selectivity. Most promising were chromium(III) complexes or more specifically, chromium acetylacetonato (acac) complexes.

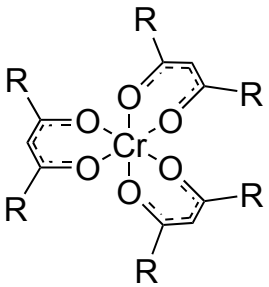

Figure 3.26: Cr(III) acetylacetonato complexes. In the initial screening for dehydroperoxidation, R = Me, *t*Bu, CF_3 and the unsymmetric benzoylacetonate (R = Me/Ph) were tested.

After the regular acetylacetonato complex (R = Me) had shown good selectivity towards the ketone for dehydroperoxidation of cyclohexyl hydroperoxide (90:10), electronically and ster-

ically different acetylacetonato complexes were tested. Regardless of the ligand, the selectivity remained about the same for all complexes: 96:4 for *t*Bu-substituted acac, 91:9 for the electron-poor CF_3 analogue and 88:12 for benzoylacetonate, all at room temperature. Temperature seemed to have a deleterious effect on the selectivity (for *t*Bu-acac, selectivity dropped to 81:19 at 100 °C and 73:27 at 130 °C). The relative independence of selectivity from the ligand hinted at a different active species not bearing acetylacetonate ligands. Rather, different reaction times suggested different time periods for formation of the actual catalyst from the Cr(III) acac-type precursors. This also seemed to make sense since the chromium acetylacetonato complexes do not bear any oxo groups, which a suspected catalyst probably would. Following these first results, Cr(III) and Cr(VI) oxide were tested. Cr(III) oxide performed worse with a ketone-alcohol ratio of 29:71, but CrO_3 showed an excellent selectivity of 98:2 and also reacted much faster (complete conversion within 10 min compared to several days for the acac complexes). The active species is therefore likely a chromium (VI) oxo compound, that was previously just very slowly formed from acac complexes in the oxidative conditions with CyOOH. These findings and observations prompted us to look into the selective decomposition of cyclohexyl hydroperoxide with chromium (VI).

3.4 Chromium-based Dehydroperoxidation

Reproduced in part from [Hamann, J. N.; Hermsen, M.; Schmidt, A.-C.; Krieg, S.; Schießl, J.; Riedel, D.; Teles, J. H.; Schäfer, A.; Comba. P.; Hashmi, A. S. K.; Schaub, T. Selective Decomposition of Cyclohexyl Hydroperoxide using Homogeneous and Heterogeneous Cr(VI) Catalysts: Optimizing the Reaction by Evaluating the Reaction Mechanism. *ChemCatChem* **2018**, *10*, 2755-2767.] Copyright Wiley-VCH Verlag GmbH & Co. KGaA. Reproduced with permission.

3.4.1 Previous Work

The stoichiometric use of chromium in oxidation reactions has been known for some time, and several name reactions are associated with it: the Jones,[121] Sarett[122] and Collins[123] oxidations in which ketones are obtained from alcohols by oxidation with different chromium trioxide (CrO_3) reagents. One of the first patents that mentions use of chromium trioxide in the synthesis of cyclohexanone/cyclohexanol was filed by Stamikarbon, a subsidiary of Dutch State Mines (DSM), as early as 1973.[124] Catalytic applications of chromium trioxide for the oxidation of alcohols were published by Muzart in 1987.[125] Using 5 mol% CrO_3 and 4 eq. of *tert*-butyl hydroperoxide (70%) in dichloromethane (DCM), a series of alcohols could be converted into ketones, with the best selectivities obtained for benzylic alcohols. Muzart also proposed a mechanism involving conservation of the oxidation state of Cr(VI) in which a combined chromic acid ester of alcohol and alkyl peroxide lead to ketone formation. This was later investigated in more detail by Boitsov et al.[126] with nuclear magnetic resonance (NMR) spectroscopy and will be discussed in one of the following subsections (Cooperative Mechanism, 3.4.4). In a study of homogeneous and heterogeneous chromium catalysts for the decomposition of cyclohexyl hydroperoxide, Buijs et al. proposed a different mechanism, which also conserves the oxidation state of +VI at chromium, similar to the previously discussed deperoxidation mechanism for our vanadium catalyst. The mechanistic study included calculations at the B3LYP/6-31G** level which predict such a mechanism to be feasible – we will discuss this in more detail in the subsection on the regular dehydroperoxidation mechanism (3.4.3).

As mentioned, the dehydroperoxidation with chromium(VI) is considerably faster than with vanadium. For example, in initial experiments addition of hydroperoxide to neat CrO_3 in cyclohexane reacted so vigourously that within seconds the solvent started boiling in the NMR tube and conversion was completed after only a few minutes. But even through cooling and using less reactive chromium trioxide precursors (such as the Collins reagent, $CrO_3 \cdot Py_2$), it

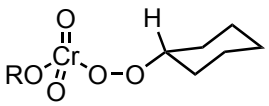

Figure 3.27: Suspected chromium alkylperoxo complex, which would formally be a peroxo ester of chromic acid. Different complexes are possible – the free acid with R=H, but also R=OCy or R=OOCy for the bisalkylperoxo ester.

was not possible to experimentally isolate a suspected chromium alkylperoxo complex, which had been the starting point for our previous investigations with vanadium. To our knowledge, isolation of a chromium alkylperoxo complex has not been reported before in the literature, although the related chromium oxide peroxide (CrO_5) and derivatives of it are known.[127] Instead, the existence of such a proposed intermediate was confirmed indirectly. Cooling a solution of $CrO_3 \cdot Py_2$ in non-coordinating α,α,α-trifluorotoluene to 5 °C and adding a stoichiometric amount of cyclohexyl hydroperoxide triggered a change in the UV/Vis spectrum with a new absorption band appearing at 480 nm. This band has been attributed in the literature to alkylperoxo complexes of chromium with *t*BuOOH.[126] The alkylperoxo complex is, however, not stable and after 48 h the typical UV/Vis spectrum of Cr(VI) without distinct absorption bands is observed. This was also seen in the catalytic reactions, confirming conservation of the +6 oxidation state of chromium. Additionally to the UV/Vis experiments, the formation of alkylperoxo chromium was followed by NMR. To a solution of CyOOH in deuterated toluene, a stoichiometric amount of $CrO_3 \cdot Py_2$ was added at −20 °C. A downfield shift of the peak at 3.72 ppm to 4.09 ppm was observed, which was attributed to the α-hydrogen on cyclohexyl hydroperoxide (free vs. bound to chromium). A new peak appeared at 11.64 ppm with simultaneous disappearance of the hydroperoxide ($CyOO\mathit{H}$) signal at 5.83 ppm.

Table 3.1: Experimental and calculated NMR shifts of free cyclohexyl hydroperoxide and the suspected chromic acid alkylperoxo ester $CrO_2(OH)(OOCy)$.

Proton	Exp. [ppm]	DFT [ppm]
Free CyOOH		
$OO\mathit{H}$	5.83	6.62
$OOC\mathit{H}$	3.72	3.84
$CrO_2(OH)(OOCy)$		
$O\mathit{H}$	11.64	11.82
$OOC\mathit{H}$	4.09	4.19

Comparison with DFT-computed values (table 3.1) confirms that formation of the chromium alkylperoxo complex $CrO_2(OH)(OOCy)$ is likely, which is the product of direct addition of CyOOH to CrO_3. The downfield shift of the α-hydrogen on the hydroperoxide is in agree-

ment with the prediction from DFT ($\Delta\delta_{exp}$ = 0.37 ppm, $\Delta\delta_{DFT}$ = 0.35 ppm) and the new signal at 11.64 ppm seems to correspond to the newly formed O*H* on chromic acid. The OO*H* signal of free CyOOH is predicted to be too far downfield from the experimental value, which is expected due to neglection of interactions for protons that can participate in hydrogen bonding and exchange. Having established that formation of an alkylperoxo species from CrO_3 and cyclohexyl hydroperoxide is very likely occurring, we used this as our starting point for computational investigations into the mechanism of the dehydroperoxidation.

3.4.2 Formation of Chromium Alkoxy and Alkylperoxy Species

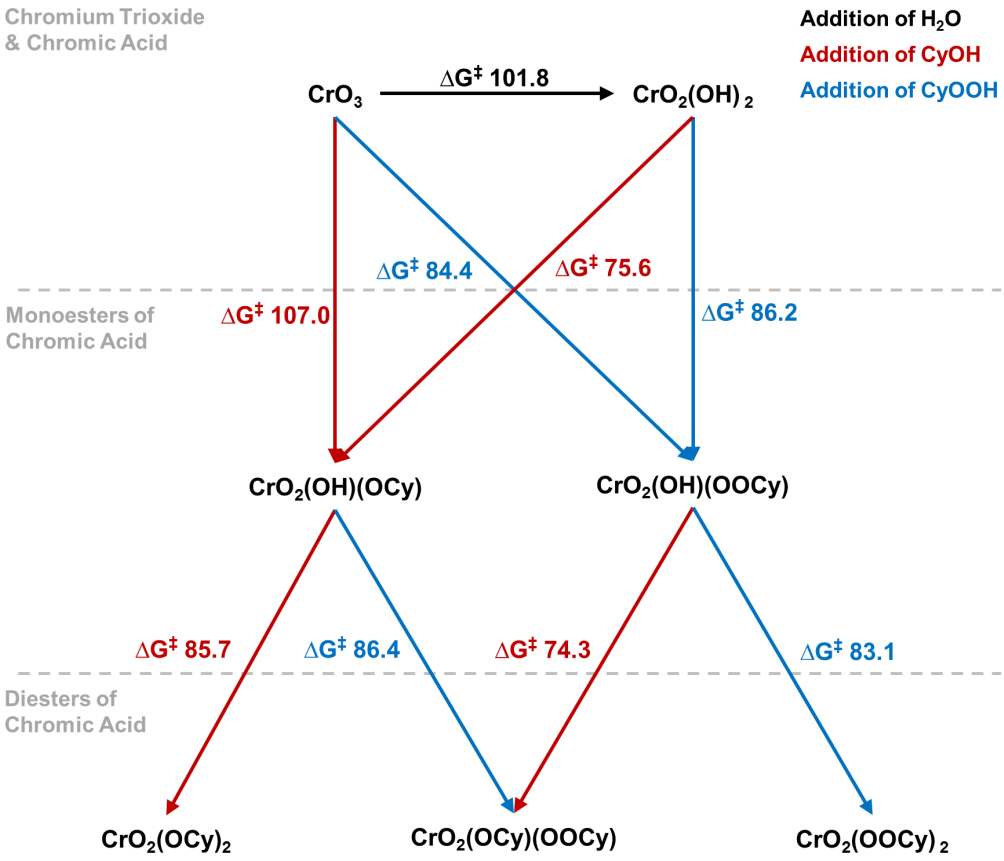

Figure 3.28: Direct additions of water, cyclohexanol and cyclohexyl hydroperoxide to form chromic acid and various chromic acid esters. The $\Delta G^{\ddagger}$ are free enthalpies of activation in kJ/mol in cyclohexane.

Besides $CrO_2(OH)(OOCy)$, different related chromium species can potentially be formed in the reaction mixture. Figure 3.28 shows an overview how mono- and diesters of chromic acid can form from either chromium trioxide or chromic acid. The reactions shown are direct additions: the substrate approaches the corresponding chromium species through a four-

membered transition state in which the OH moiety of H_2O, CyOH or CyOOH formally adds onto a Cr-O double bond or CrO-H single bond (forming either a new Cr-OH group, or releasing water in the latter case). From the calculations with vanadium, the direct addition can be considered an upper limit to the necessary activation energy for substrate addition – proton relay mechanisms are even lower in energy and will be discussed later in section 3.4.3. Generally, even for direct addition, the activation energies are feasible and lie between ~ 75 to 85 $kJ \cdot mol^{-1}$, which would correspond to a half-life of the reaction on the order of a few seconds or minutes, in agreement with the experimentally observed rapid reaction. Direct addition to CrO_3 is higher for water ($101.8\,kJ \cdot mol^{-1}$) to give chromic acid or cyclohexanol to yield the cyclohexyl chromate ester ($107.0\,kJ \cdot mol^{-1}$). However, addition to monomeric CrO_3 should in any case only be considered a rough model, since it is more likely that the addition occurs on a surface of solid CrO_3 or to the Collins reagent $CrO_3 \cdot Py_2$, depending on which precursor is used. Formation of the previously experimentally observed $CrO_2(OH)(OOCy)$ can occur with a barrier of only $84.4\,kJ \cdot mol^{-1}$ from CrO_3. This monoester can potentially react with either CyOH or CyOOH to the mixed chromic acid ester $CrO_2(OCy)(OOCy)$ or the dialkylperoxo complex $CrO_2(OOCy)_2$. Both additions have reasonable barriers of $74.3\,kJ \cdot mol^{-1}$ for CyOH and $83.1\,kJ \cdot mol^{-1}$, respectively for CyOOH. Formation of $CrO_2(OCy)_2$ from $CrO_2(OH)(OCy)$ can also occur with an activation energy of $85.7\,kJ \cdot mol^{-1}$ for the addition of cyclohexanol. Which species is actually dominant depends on the concentrations of water, cyclohexanol and cyclohexyl hydroperoxide which vary during the reaction, and secondary effects such as the phase separation of water and cyclohexane during dehydroperoxidation of the substrate. In all cases, formation of the different alkylperoxo and alkoxy complexes of chromium is energetically feasible. Looking at the thermodynamics of the reaction, substitution of the free chromic acid $CrO_2(OH)_2$ is energetically always favored. The monoesters $CrO_2(OH)(OCy)$ and $CrO_2(OH)(OOCy)$ are more stable by $28.7\,kJ \cdot mol^{-1}$ and $23.1\,kJ \cdot mol^{-1}$ relative to $CrO_2(OH)_2$. For the diesters the reaction is even more favorable, with formation of $CrO_2(OCy)(OOCy)$ being exergonic by $50.1\,kJ \cdot mol^{-1}$ (this species is important for the cooperative mechanism as proposed by Boitsov et al.).[126] The other two species, $CrO_2(OCy)_2$ and $CrO_2(OOCy)_2$, are also exergonic compared with the free chromic acid by $56.5\,kJ \cdot mol^{-1}$ and $42.9\,kJ \cdot mol^{-1}$, respectively. It can be concluded, that any of the above species may qualify for participating in the dehydroperoxidation reaction.

3.4.3 Regular Dehydroperoxidation Mechanism

As in the dehydroperoxidation mechanism of the vanadium complex, a similar mechanism is proposed for the dehydroperoxidation with the chromium catalyst (figure 3.29), where a

concerted hydrogen transfer to the metal oxo group and simultaneous O-O bond cleavage of the alkyl peroxide is the crucial step. The dehydroperoxidation is followed by addition of hydroperoxide to the generated oxo hydroxo chromium species.

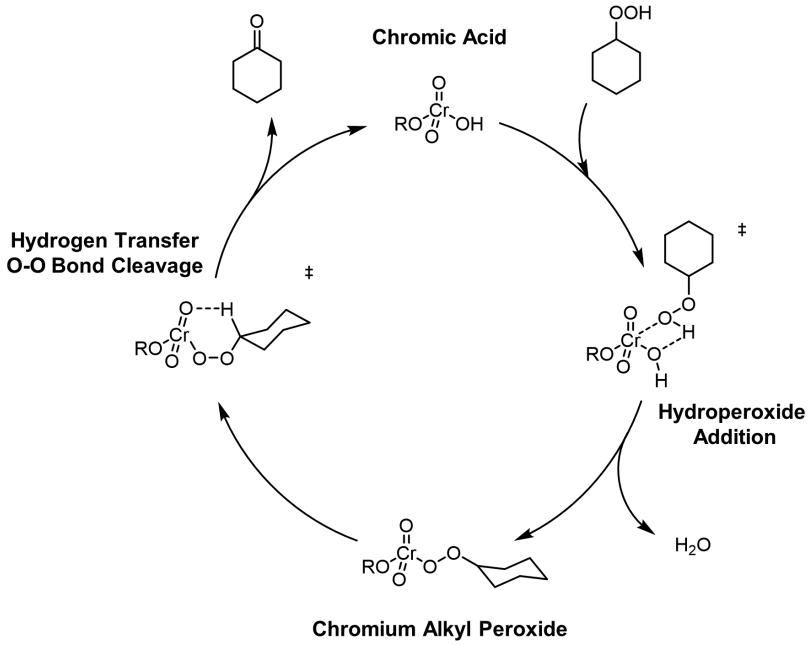

Figure 3.29: Mechanism for the dehydroperoxidation with chromium similar to the vanadium-catalyzed dehydroperoxidation. R may be just -H for the monoester or -OCy/-OOCy for the diesters of chromic acid. The addition can be direct as depicted here, or through a proton relay mechanism.

In this mechanism, the oxidation state of chromium is not altered during the reaction and remains at +6. Buijs and coworkers calculated this reaction for R=H in the gas phase at the B3LYP/6-31G** level and obtained an activation energy of 65.3 kJ·mol^{-1} for the deperoxidation (in their calculation, a water molecule has a loose hydrogen bond to the peroxide, but this should only have a minor effect). Starting from chromic acid **43**, Figure 3.30 shows the addition of cyclohexyl hydroperoxide which can proceed either directly through **TS44** or through proton relays with cyclohexanol (**TS45**) or water (**TS46**). As already shown in Figure 3.28, the direct addition via **TS44** has an activation barrier of 86.2 kJ·mol^{-1}, which is certainly feasible, but relatively high. In the analogous addition to the vanadium complex (**TS8**) this step had an activation energy of 80.5 kJ·mol^{-1}, but was significantly reduced by proton relay agents. The same is found for chromic acid. Addition of the hydroperoxide through transition state **TS45**, where cyclohexanol acts as a proton relay agent only has a barrier of 54.5 kJ·mol^{-1} and is therefore favored by 31.7 kJ·mol^{-1} over the direct addition. Water as a proton relay agent (**TS46**) also lowers the barrier for hydroperoxide addition, although the effect is smaller than

with CyOH ($\Delta G^{\ddagger}$=75.1 kJ·mol^{-1}, 11.1 kJ·mol^{-1} less than **TS44**). All additions lead to the release of water and formation of the chromium alkylperoxo ester **47**, which was experimentally observed *in situ* by NMR and UV/Vis. Formation of **47** is exergonic compared to the free hydroperoxide and chromic acid by 23.1 kJ·mol^{-1}.

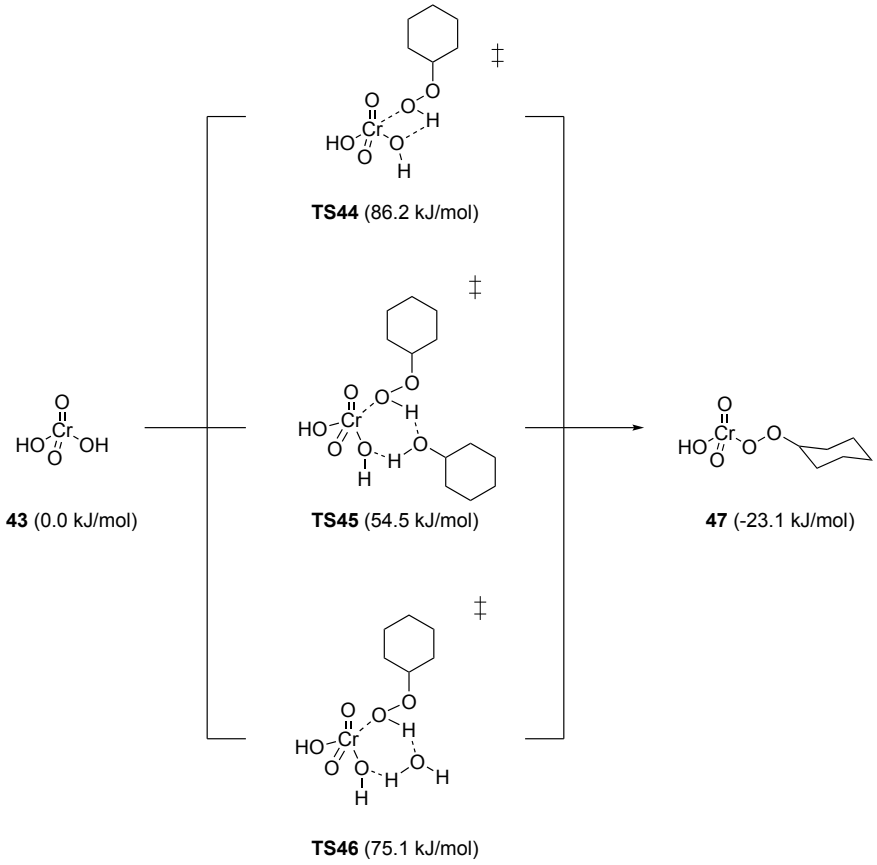

Figure 3.30: Comparison of direct addition of hydroperoxide (**TS44**) with proton relay mechanisms for the hydroperoxide addition through cyclohexanol (**TS45**) and water (**TS46**). Energies are free enthalpies relative to chromic acid **43**.

The alkylperoxo complex **47** can then undergo dehydroperoxidation through six-membered transition state **TS48** (see Figure 3.32 for structure). The α-hydrogen on the hydroperoxide is transferred to the chromium oxo group and the peroxide O-O bond is cleaved to release cyclohexanone. The computed barrier is 83.7 kJ·mol^{-1} for this step which makes it the rate-determining step of the reaction. Structurally, the transition state is very similar to its counterpart with vanadium (**TS6**). The O-O bond distance is marginally smaller 1.69 Å (1.71 Å in **TS6**), but the O-H distance for the oxo group on chromium and the abstracted hydrogen is shorter (1.44 Å vs. 1.53 Å). Formation of cyclohexanone and chromic acid is highly exergonic by 260.6 kJ·mol^{-1} relative to the preceding chromium alkylperoxo complex **47**, making this step irreversible ($\Delta G^{\ddagger}$ for reverse reaction is 344.3 kJ·mol^{-1}). Compared to the value com-

puted by Buijs and co-workers (65.3 kJ·mol^{-1}, B3LYP/6-31G**),[128] the barrier is predicted to be slightly higher than in their calculations. However, considering the small benchmark study in section 2.5.2, B3LYP seems to have a tendency to underestimate this barrier (at least for the similar vanadium chemistry), as the stability of the alkylperoxo species is underestimated. In fact, Buijs et al. report the alkylperoxo complex to be isoenergetic or even slightly endergonic (ΔG = 1.7 kJ·mol^{-1}) relative to $CrO_2(OH)_2$, whereas the calculations in this thesis find a thermodynamic preference of the alkylperoxo complexes on the order of 20 to 30 kJ·mol^{-1} for vanadium and chromium. This tendency, albeit smaller, is also found in the CCSD(T) benchmark for the simplified vanadium complexes. Lastly, experimental observation of the rapid reaction with chromium upon addition of CyOOH and the addition of alcohols and hydroperoxide to vanadium oxo hydroxo complexes also support the relative stability of **47** vs. free chromic acid. Comparing the computed barrier with the corresponding barrier for vanadium, it is found that the activation energy for deperoxidation is significantly lower with chromium (**TS48**: 83.7 kJ·mol^{-1}, for vanadium **TS6**: 110.1 kJ·mol^{-1}). This is in line with the far better ketone/alcohol selectivity obtained with chromium as well as the faster reaction rate. It also explains why isolation of the chromium alkylperoxo species could not be achivied due to the low barrier of dehydroperoxidation, whereas the corresponding vanadium alkylperoxo complexes were stable and could be characterized by X-ray crystallography.

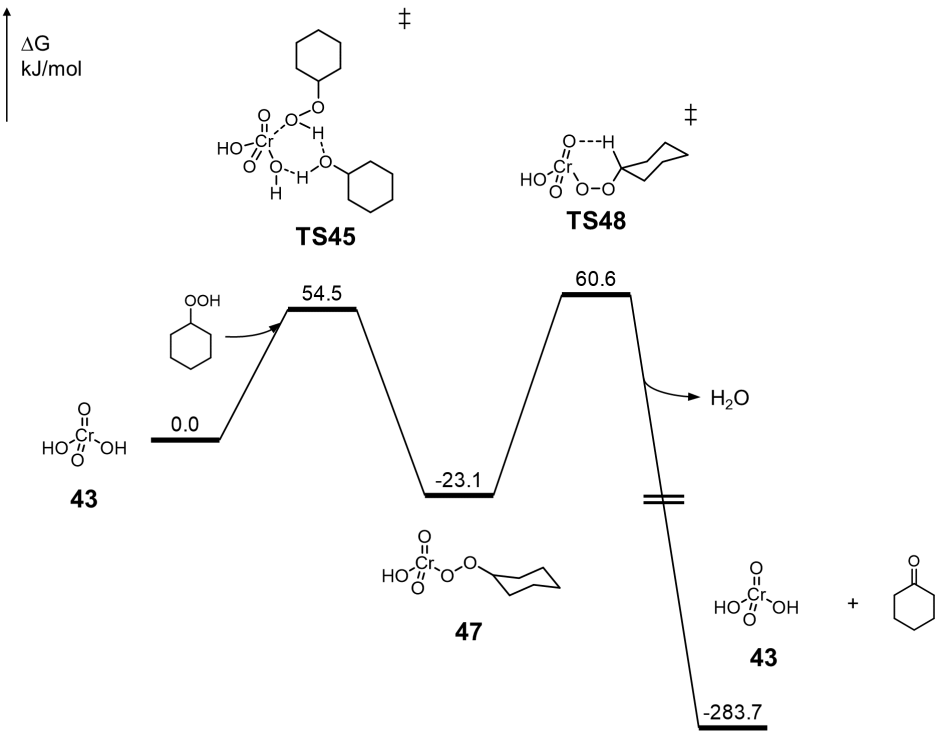

Figure 3.31: Reaction path for the dehydroperoxidation of cyclohexyl hydroperoxide with chromic acid. Energies are free enthalpies in kJ/mol relative to free chromic acid. Only the energetically lowest transition state for addition is shown (**TS45**, proton relay via CyOH). The energy level after **TS48** is adjusted in height due to the high exergonic nature of the reaction.

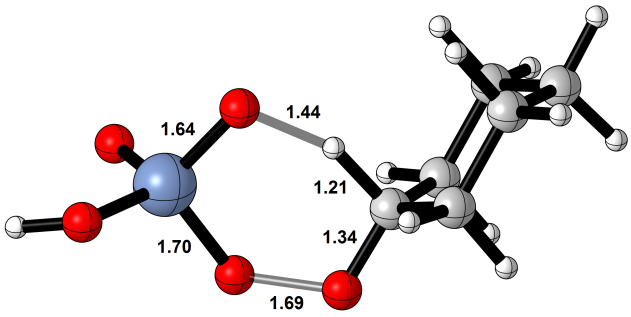

Figure 3.32: Structure of the dehydroperoxidation transition state **TS48** involving hydrogen transfer to the chromium oxo group and simultaneous O-O bond cleavage.

Additionally, the same dehydroperoxidation was also recalculated for the other alkylperoxo species which might be present during the reaction, the cyclohexanol and cyclohexyl hydroperoxide diesters (see Figure 3.33). The differences to the free chromium hydroxo species (mono alkylperoxo ester) are very minor. For $CrO_2(OCy)(OOCy)$ (**49**) the barrier is 85.3 kJ·mol^{-1} via **TS48**, which is only 1.6 kJ·mol^{-1} more than **TS48** in the free chromic acid alkylperoxo

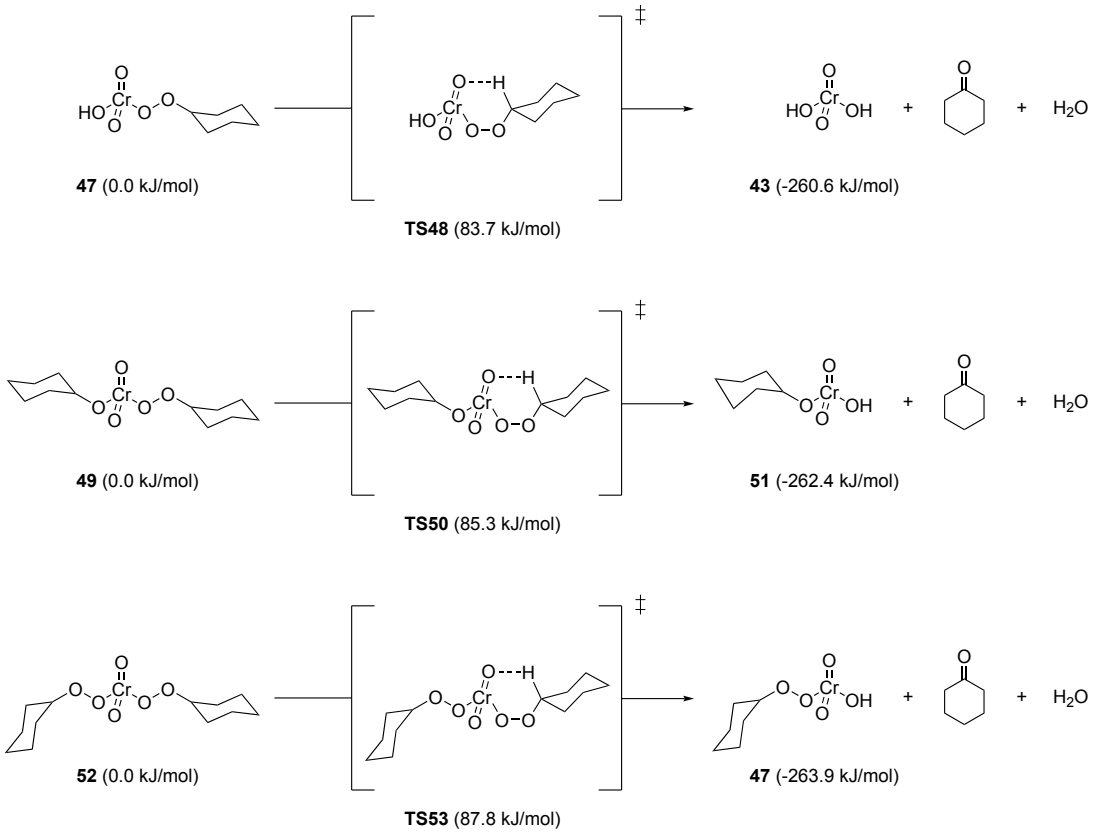

Figure 3.33: Deperoxidation barriers for the related species, which are formally esters of chromic acid with cyclohexanol **49** and cyclohexyl hydroperoxide **52**, through the same six-membered transition state with hydrogen transfer and O-O bond cleavage. The regular mechanism is shown at the top for comparison. Energies are free enthalpies in kJ/mol and relative to the corresponding preceding alkylperoxo complex.

complex. Similarly, for the symmetric dialkylperoxo complex **52**, the barrier is in the same range ($87.8\,\mathrm{kJ{\cdot}mol^{-1}}$ via **TS53**). Thermodynamically, formation of cyclohexanone and water is strongly exergonic in all cases, with also only minor differences ($-262.4\,\mathrm{kJ{\cdot}mol^{-1}}$ from **49** to **51** and $-263.9\,\mathrm{kJ{\cdot}mol^{-1}}$ from **52** to **47**; the original value for the regular dehydroperoxidation of **47** is $260.6\,\mathrm{kJ{\cdot}mol^{-1}}$). It can be concluded, that not only is formation of all species is possible, but dehydroperoxidation can also occur from any of the different alkylperoxo species. The differences in free enthalpy are too low to favor one single path and therefore likely are more subject to the reaction conditions. Experimental evidence for the $CrO_2(OH)(OOCy)$ species **47** suggests that this might be the dominant pathway under the reaction conditions employed in our experiments.

3.4.4 Cooperative Mechanism

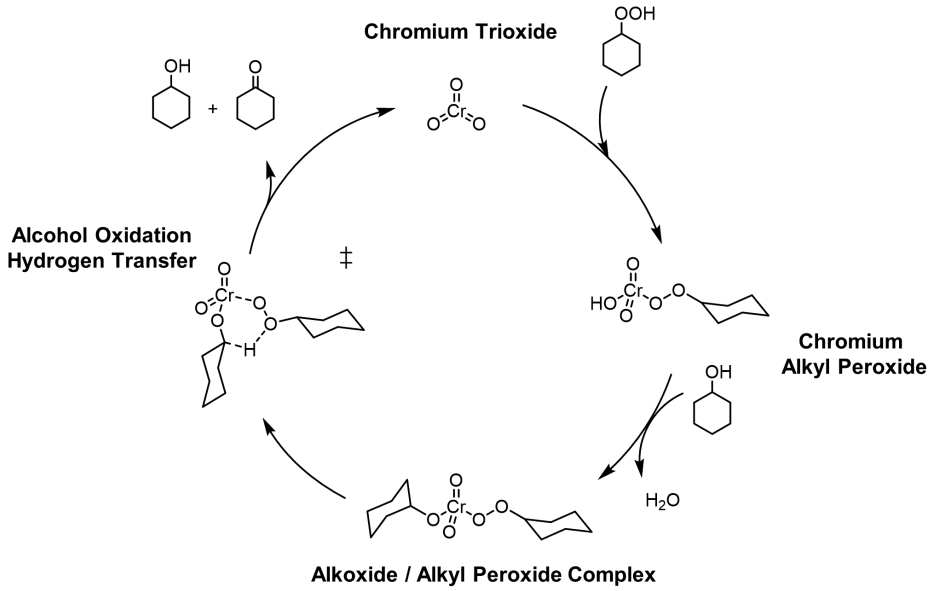

Figure 3.34: Cooperative mechanism in which a mixed alkoxy alkylperoxy chromium complex is needed for the dehydroperoxidation. The key transition state is a transfer of the α-hydrogen on the alkoxy group to the peroxo oxygen on the alkylperoxo ligand to yield chromium trioxide, cyclohexanol and cyclohexanone. Since cyclohexanol is needed for regeneration of the alkoxide / alkylperoxo complex, the net reaction is the same: cyclohexyl hydroperoxide is decomposed to cyclohexanone and water.

An alternative mechanism has been suggested by Boitsov et al. in 2001 on the basis of NMR experiments.[126] They studied the oxidation of secondary alcohols with *t*BuOOH and found NMR evidence for a mixed chromium species, containing both an alkylperoxo ligand from *tert*-butyl hydroperoxide and alkoxy ligand from the secondary alcohol. Based on this observation, it was assumed that this species participates in a cooperative mechanism. Here, the carbon-bound peroxo oxygen would abstract the α-hydrogen on the alkoxy ligand, which would then form the corresponding ketone. The alkylperoxo ligand would release chromium trioxide and the corresponding alcohol. For *t*BuOOH, the corresponding alcohol *tert*-butanol cannot be oxidized to a ketone, but for a secondary hydroperoxide like cyclohexyl hydroperoxide, the generated secondary alcohol could itself be oxidized to the corresponding ketone. Intermediary formed chromium trioxide would immediately coordinate and add new substrate, and thus close the catalytic cycle.

To verify whether this might be a valid alternative to the reaction path with the hydrogen transfer to an oxo group and O-O bond cleavage, we computed the corresponding reaction path (figure 3.35). The trigonal bipyramidal pyridine CyOOH/CyOH complexes **54** and

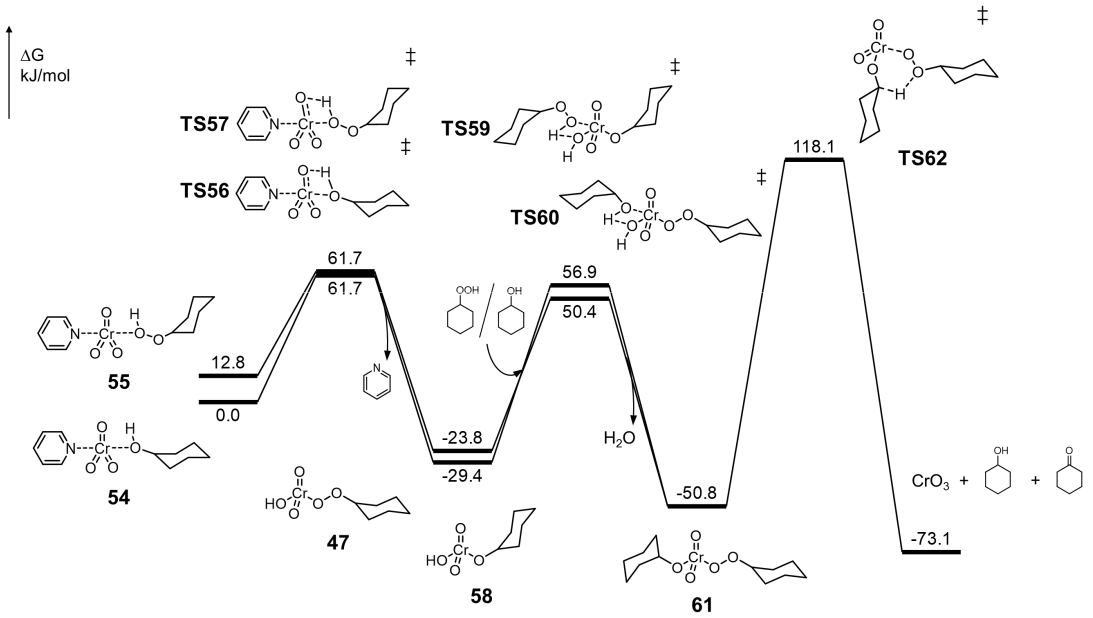

Figure 3.35: Cooperative mechanism in which a mixed alkoxy alkylperoxy chromium complex is needed for the dehydroperoxidation.

55 were chosen as starting points. Fully ligand free chromium trioxide is unlikely to exist in solution (unless formed as a reactive intermediate), but **54**/**55** can be formed through exchange from $CrO_3 \cdot Py_2$. The cyclohexanol complex is slightly more stable by 12.8 kJ·mol^{-1}. From here, both complexes can undergo addition of CyOH/CyOOH via **TS56**/**TS57** and both have the same energy relative to the initial CyOH complex **54**, 61.7 kJ·mol^{-1}. Pyridine is released and either the hydroxo alkylperoxo complex **47** or alkoxy species **58** are formed, which is exergonic by −36.6 kJ·mol^{-1} and −29.4 kJ·mol^{-1}, respectively. To yield the mixed alkoxy/alkylperoxo complex **61**, cyclohexanol must be added in the case of the alkylperoxo complex **47** and cyclohexyl hydroperoxide for the alkoxy complex **58**. Both additions are feasible with activation energies of 86.3 kJ·mol^{-1} for the addition of CyOOH via **TS59** and 74.2 kJ·mol^{-1} for the addition of CyOH via **TS60**. These are direct additions – the proton relay variants are likely to be even lower in energy, as was shown earlier. Formation of the mixed species **61** is therefore kinetically feasible and also exergonic with respect to **54** by 50.8 kJ·mol^{-1}. From this intermediate, the transition state suggested by Boitsov et al. is now accessible. The activation energy for this step, however, is 168.9 kJ·mol^{-1} (**TS62**) and thus far too high in energy to be competitive with the previously studied mechanism. A potential proton relay for this step, through an eight-membered transition state involving water, was also studied, but is even higher in activation energy (258.4 kJ·mol^{-1}). Figure 3.36 shows the structure of transition state **TS62**. Again, the length of the O-O bond is considerable (1.97 Å, which is 0.28 Å longer than in the regular mechanism), that is similar to the O-O distance in

the hydrogen-to-peroxo-oxygen mechanism via **TS38** or **TS39** with vanadium (2.01 Å and 2.02 Å). Also, the peroxo oxygen on the chromium complex has a Cr-O distance of 1.70 Å compared to 1.80 Å in intermediate **61**. This mechanism can be ruled out due to the high barrier, although the generation of chromium trioxide, cyclohexanol and cyclohexanone would be exergonic (by 22.3 kJ·mol^{-1} relative to **61**) and CrO_3 would, as a very reactive intermediate, easily add new substrate or recoordinate pyridine/CyOH/CyOOH. The existence of the mixed species is quite likely as its formation is feasible and thermodynamically favored, but the reaction then does not proceed through the corresponding cooperative mechanism but rather through the regular dehydroperoxidation via **TS50**, which only has an activation energy of 85.3 kJ·mol^{-1}.

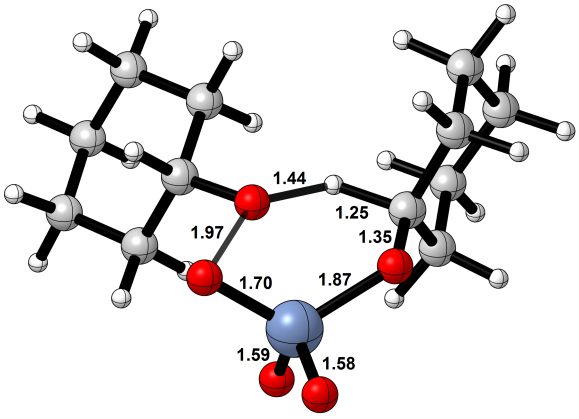

Figure 3.36: Transition state **TS62** for the cooperative dehydroperoxidation via a mixed intermediate containing alkoxy and alkylperoxo ligands that was suggested by Boitsov et al.

3.4.5 Pyridine Pathways

One of the main challenges in the application of chromium catalysts is the high toxicity of chromium(VI). The toxicity of chromium(VI) or chromate stems from its similarity to the sulfate anion, allowing it to enter cells through sulfate channels,[129] where it is reduced to chromium(III) and forms stable complexes with nucleic acids and proteins, exhibiting mutagenic and genotoxic effects.[130–132] As an example for the high safety standards regarding chromium, the German regulations on drinking water set a limit of 0.05 mg·L^{-1} total chromium content, which is around 8 ppb in chromate and similar to the limits for cyanide (0.05 mg·L^{-1}), lead (0.01 mg·L^{-1}) or uranium (0.01 mg·L^{-1}).[133] Especially in a bulk product used for textiles like Nylon-6, which cyclohexanone is ultimately converted to, residual chromium must be kept very low. For this purpose, $CrO_3 \cdot Py_2$ was immobilized with poly(4-vinylpyridine) (PVP). Product solutions from dehydroperoxidation reactions with the Cr-PVP catalyst did not contain chromium higher than the detection limit of 0.1 mg·kg^{-1} by ICP-MS, showing

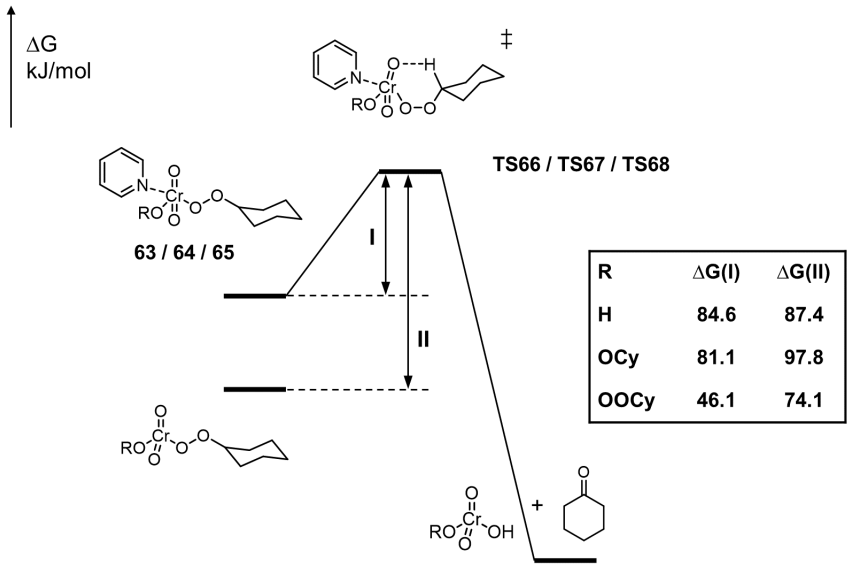

R	ΔG(I)	ΔG(II)
H	84.6	87.4
OCy	81.1	97.8
OOCy	46.1	74.1

Figure 3.37: Barriers for dehydroperoxidation with chromium pyridine complexes. The pyridine molecule coordinates *trans* to the alkylperoxo ligand. Energies are free enthalpies in kJ/mol, relative to the corresponding complex without pyridine.

the success of preventing leaching with PVP. Hence, we were interested in the role of pyridine and whether the previously studied mechanism can still be considered valid for chromium complexes with coordinating pyridine. Pyridine is here both a model for the actual pyridine molecules when using $CrO_3 \cdot Py_2$ as precursor as well as the vinyl pyridine moieties in PVP. The coordination of pyridine to the chromium alkylperoxo complexes is feasible and yields distorted pentagonal bipyramidal chromium complexes in which the pyridine molecule coordinates *trans* to the alkylperoxo ligand. From these complexes (**63**, **64** and **65** depending on the ligand R on chromium, see Figure 3.37) the regular dehydroperoxidation transition states, albeit with coordinating pyridine, are accessible. Barriers compared to the "free" alkylperoxo complexes are relatively similar to the regular mechanism without pyridine: 87.4 kJ·mol^{-1} for the unsubstituted chromic acid via **TS66**, slightly higher for the alkoxy complex **64** through **TS67** (97.8 kJ·mol^{-1}) and lower for the dialkylperoxo species (74.1 kJ·mol^{-1} via **TS68**). Coordination of pyridine is endergonic due to entropic contributions, but this is expected to be different in a polymer like PVP. Generally, the additional entropic and steric effects for chromium on actual PVP are not considered in this model, but dehydroperoxidation for the pentagonal bipyramidal complex should be energetically feasible.

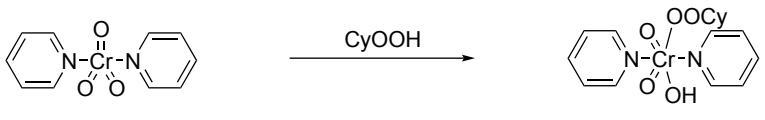

69
0.0 kJ/mol

70
129.7 kJ/mol

Figure 3.38: Formation of hexacoordinate chromium complexes from the Collins' reagent.

Since the Collins' reagent ($CrO_3 \cdot Py_2$, **69**) bears two pyridine ligands in a similar fashion, a hexacoordinate complex upon addition of CyOOH could be potentially formed. Generation of this species is however highly endergonic by 129.7 kJ·mol^{-1} (**70**). Participation of hexacoordinate chromium species or bispyridine complexes in the dehydroperoxidation was therefore ruled out, since the formation of the corresponding complex is thermodynamically disfavored.

3.4.6 Related Chromium(VI) Species

Other alternatives to the dehydroperoxidation catalyzed by chromic acid or the previously discussed derivatives of it, are dichromic acid ($Cr_2O_5(OH)_2$) and the anions of both chromic and dichromic acid, chromated and dichromate. Dichromic acid can be formed depending on the concentration of chromic acid and water,[134] of which the latter is formed from cyclohexyl hydroperoxide during the reaction. The corresponding ions can be generated through deprotonation, for example by pyridine, but even in water dissociation may occur as both chromic and dichromic acid are strong acids.

To test whether these species can also potentially participate in the investigated dehydroperoxidation mechanism, both addition of hydroperoxide and the subsequent deperoxidation through a six-membered transition state similar to **TS48** were computed. The results are shown in Figure 3.39. In the transition state for hydroperoxide addition, the proton relay through cyclohexanol was chosen for better comparison with **TS45**. For the regular mechanism with $CrO_2(OH)_2$, this had been the energetically lowest transition state for addition of substrate with a barrier of 54.5 kJ·mol^{-1}. In the case of dichromic acid and its deprotonated anion, dichromate, addition of cyclohexyl hydroperoxide is very fast with a barrier of only 31.1 kJ·mol^{-1} (**TS72**) and 43.1 kJ·mol^{-1} (**TS80**), respectively. For the chromate anion, however, the addition is significantly higher in energy with an activation barrier of 99.4 kJ·mol^{-1} via **TS76**. At first this seems a bit surprising, since the transition states are structurally similar. However, in the case of the chromate anion, the negative charge is directly at the chromium center where the addition is taking place. This is different for the dichromate anion, where the negative charge is located further away from the center of reaction. Also, the negative charge

is delocalized over the whole chromate anion, instead of being located on the oxygen on the opposite side of the addition. The lowered electrophilicity of chromium therefore hinders the nucleophilic attack of the peroxide oxygen, leading to a higher energy for this transition state. The alkylperoxo chromate **77** could possibly be generated differently: rather than having the energetically unfavored addition to the chromate species in **TS76**, it can be formed from the "regular" chromium species **47** by deprotonation after hydroperoxide addition. Formation of the three different alkylperoxo complexes **72**, **77** and **81** is exergonic ($-23.4\,\mathrm{kJ{\cdot}mol^{-1}}$, $-23.9\,\mathrm{kJ{\cdot}mol^{-1}}$ and $-13.5\,\mathrm{kJ{\cdot}mol^{-1}}$) and similar to that of the free chromic acid alkylperoxo complex **47** ($-23.1\,\mathrm{kJ{\cdot}mol^{-1}}$). Dehydroperoxidation occurs via the known six-membered transition state where hydrogen transfer and O-O bond cleavage are concerted. This step is rate-determining in all cases (considering formation of **77** through deprotonation of **47**) and the energies are close to those observed in the neutral, monomeric chromic acid pathway. For dichromic acid, the barrier to dehydroperoxidation is $85.8\,\mathrm{kJ{\cdot}mol^{-1}}$ via **TS74**, the corresponding anion **81** has a bit lower activation energy for transition state **TS82** of $71.5\,\mathrm{kJ{\cdot}mol^{-1}}$. The chromate anion **77** has an energetic barrier of $89.0\,\mathrm{kJ{\cdot}mol^{-1}}$ for the same reaction. All of the reactions can be considered feasible under our reaction conditions; the anions seem to be a little more active – if they are formed – which is not necessarily supported in cyclohexane.

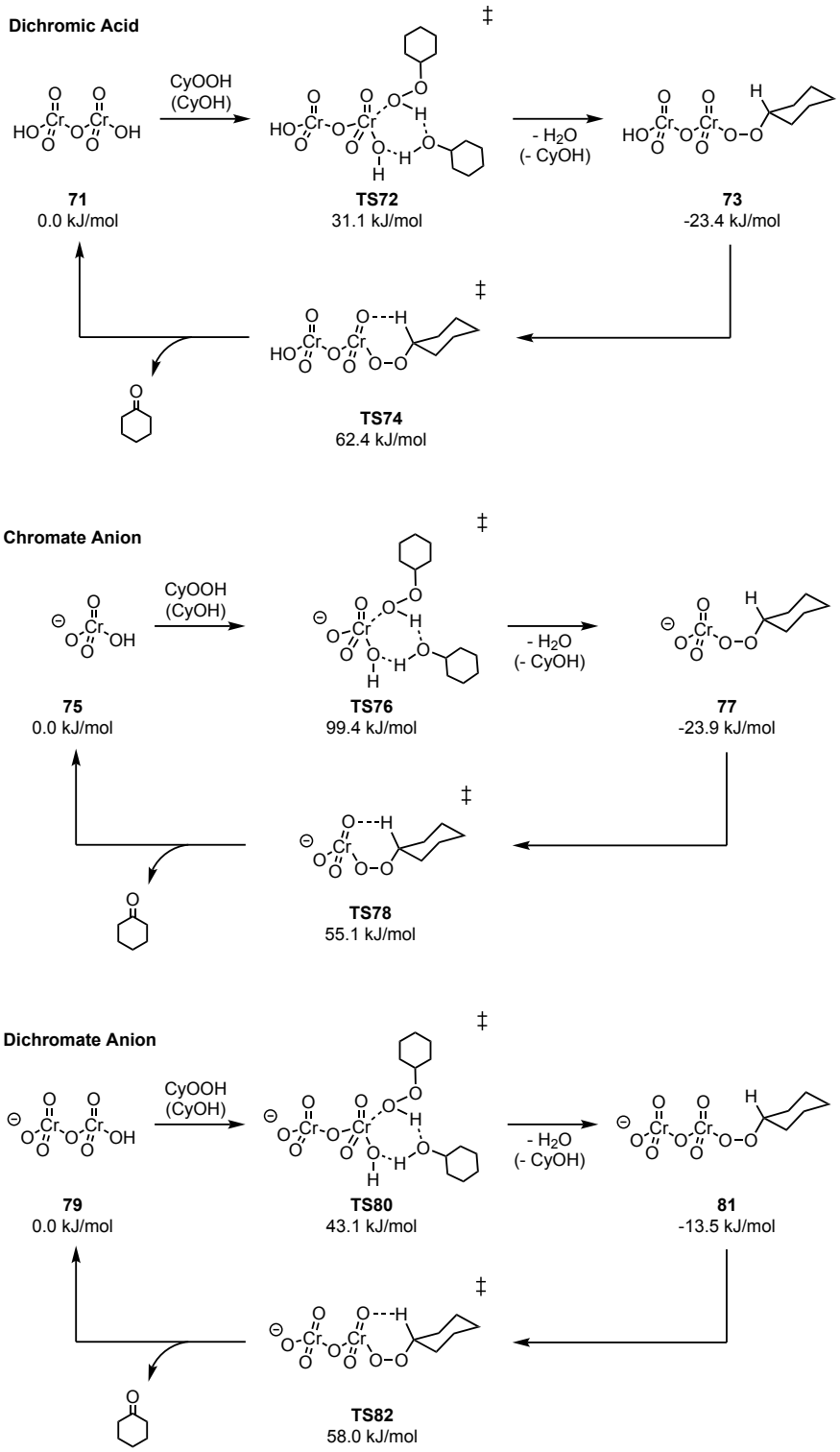

Figure 3.39: Dehydroperoxidation pathways for dichromic acid, and the chromate and dichromate anions. The addition reactions of cyclohexyl hydroperoxide to the initial complexes are with cyclohexanol as a proton relay agent for better comparison with **TS45** in Figure 3.31. Energies are free enthalpies in kJ/mol, relative to the corresponding acid/anion without alkylperoxo ligand.

3.4.7 Summary and Conclusion

The dehydroperoxidation of cyclohexyl hydroperoxide with chromic acid and its derivatives was studied. Through various addition reactions, a multitude of different chromium (alkylperoxo) species can be formed, including the mixed ester of cyclohexanol and cyclohexyl hydroperoxide, $CrO_2(OCy)(OOCy)$. As seen before, addition reactions benefit from proton relay through water or cyclohexanol as they lower the corresponding transition states compared to the direct addition of these substrates. The previously investigated mechanism for the vanadium dipicolinato complex can also act here and we thus confirm the results of Buijs et al. Activation energies are slightly dependent on the substitution pattern of the chromium catalyst, but are generally energetically feasible. Barriers for dehydroperoxidation are lower than those found for vanadium, which is in agreement with the higher selectivity observed for chromium in the dehydroperoxidation of cyclohexyl hydroperoxide to cyclohexanone and water. A mechanism that was suggested by Boitsov et al. was also studied. This mechanism included the formation of the mixed species bearing alkoxy and alkylperoxo ligands on chromium to facilitate dehydroperoxidation by hydrogen abstraction through the peroxo oxygen from the alkoxy ligand. This hypothesis was ruled out as the necessary activation energy is far higher than that of the regular dehydroperoxidation mechanism. Formation of the mixed intermediate of alkoxy/alkylperoxo chromium(VI) is very well feasible, but will then rather undergo dehydroperoxidation through the "regular" mechanism, leaving the alkoxy moiety on the ligand untouched. Which of the many species that can be formed is the most relevant in solution is not certain. Since almost all of the have similar barriers for dehydroperoxidation, this is likely to depend on the exact reaction conditions (solvent, free $CrO_3 \cdot Py_2$ in cyclohexane or chromium(VI) immobilized on poly(4-vinylpyridine), etc.), but comparison of NMR data at low temperatures with computed NMR parameters suggests that the intermediate $CrO_2(OH)(OOCy)$ plays an important role. For this particular complex, the dehydroperoxidation can proceed rapidly with a small barrier of only 83.7 $kJ \cdot mol^{-1}$, i.e. 26.4 $kJ \cdot mol^{-1}$ lower than the analogous reaction with the vanadium complex. We conclude that the selective formation of cyclohexanone is due to an analogous mechanism as in the vanadium system, but favored by lower activation energies with chromium. Some details, such as the specific interaction of PVP with Cr(VI), the formation of a dialkylperoxide in some cases (which was not discussed in this chapter) or radical decomposition and possible ways to prevent them remain interesting and provide potential starting points for future investigations in the chromium(VI) system.

4

Asymmetric Reductive Amination of Aryl-Alkyl Ketones

4.1 Motivation

Chiral amines belong to one of the most important building blocks for pharmaceuticals and agrochemicals.[135] The high abundance of chiral amines in natural products may be owed to amino acids, which are all chiral except for glycine, and make up the building blocks for proteins, which are essential to life. Nonetheless, many non-amino acid derived biologically active compounds exist and many of these are aryl-alkyl substituted chiral amines. Figure 4.1 shows some examples of currently approved chiral amine drugs: Cinacalcet (secondary hyperparathyroidism), Rivastigmine (Parkinson's and Alzheimer's disease), Codeine (pain), Repaglinide (diabetes mellitus), Mefloquine (malaria) and Sertraline (antidepressant). While less of-

ten encountered, chiral amine agrochemicals also exist, with (*S*)-Metolachlor and Dimethenamide-P being two examples of which the former is probably the largest industrially and synthetically produced chiral amine.

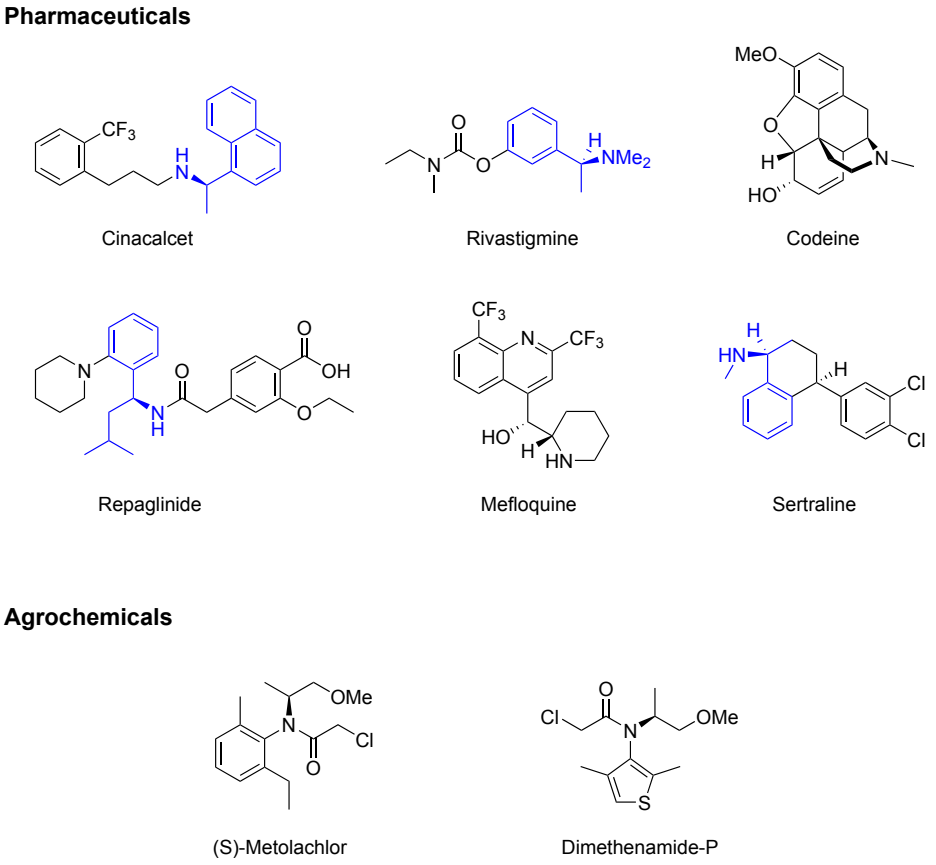

Figure 4.1: Examples for chiral amines in pharmaceuticals and agrochemicals which are not derived from chiral amino acids. Chiral aryl-alkyl amine derivatives are highlighted in blue.

Naturally, a plethora of methods have been developed to synthesize chiral amines:

1. Chiral Resolution of Racemic Amines
   The resolution of racemic amines by conversion into diastereomeric salts is not exactly a chiral synthesis of amines, but it is included nevertheless, since it remains an important way to access chiral amines on an industrial scale even today. Usually chiral carboxylic acids are used for the resolution that can be obtained at low cost and in pure form from natural sources; examples are mandelic, malic or tartaric acid. Obvious disadvantages of these processes are the need for racemization (or in the worst case disposal) of the undesired enantiomer, the stoichiometric amounts of chiral auxiliary for crystallization and the additional steps needed for removal and recycling of the auxiliary to obtain the pure chiral amines.

2. Asymmetric Hydrogenation of Enamides
   In the asymmetric hydrogenation of enamides, a stereoselective hydrogenation of a C-C double bond, substituted by an amine, is carried out, resulting in a chiral amine. Usually, *N*-acetylenamides are hydrogenated. These can be produced from ketones via the oxime and acetylation or through the Blaise reaction of a nitrile with a Grignard reagent and subsequent acetylation with acetic anhydride. In both cases, once the asymmetric hydrogenation has been performed, only a chiral amide is obtained. When the primary amine is desired, additional removal of the acetyl group is necessary.

3. Asymmetric Hydrogenation of Imines and Derivatives
   Asymmetric hydrogenation of C-N bonds also yields chiral amines. Imines are the primary choice as substrate, but oxime ethers and hydrazones can also be hydrogenated asymmetrically. The compounds can be made from ketones/aldehydes and the corresponding amine, hydroxyl amine and alkylating agent, or hydrazine derivative. These work well if the imines are sufficiently substituted, but primary imines, due to their instability, can usually not be reduced to the chiral primary imine. This introduces the need for additional steps to remove protecting groups on the imine.

4. Enzymatic Routes
   Ketones and α-keto acids may be transformed into chiral amines by transamination. A (non-chiral) amine such as isopropyl amine is needed as the nitrogen source and is converted to the corresponding ketone in the reaction. Drawbacks are the instability of some transaminases, separation from product mixtures, access to both *R* and *S* enantiomers and challenges in the engineering of enzymes for new substrates. Another strategy is kinetic resolution of racemic mixtures by enzymes, which can do stereoselective acylations or hydrolysis of amides to separate enantiomers.

5. Asymmetric Reductive Amination
   Reductive aminations (RA) are reactions in which a carbonyl compound is directly converted into an amine with an imine only formed as an intermediate. They are more challenging then hydrogenation of imines since chemoselectivity is also an issue: reduction of the imine has to be favored over the reduction of the carbonyl compound. In principle, reductive aminations are very elegant in that they can proceed within one step from the corresponding carbonyl compound, compared to the other methods. However, especially asymmetric reductive aminations are far less explored due to numerous challenges.

Of the various methods, particular interest has been on the reductive amination due to its po-

tential of yielding amines in one step. Several name reactions can be considered reductive aminations that have existed for some time, albeit being non-asymmetric: the Eschweiler-Clarke reaction,[136,137] the Leuckart-Wallach reaction[138,139] and the Mannich aminomethylation.[140] The Leuckart-Wallach reaction is a simple example for a reductive amination that only needs ammonium formate as both nitrogen source and reductant, releasing only carbon dioxide.

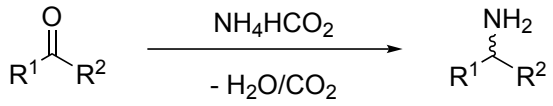

Figure 4.2: Leuckart-Wallach reaction. A ketone or aldehyde is converted to the corresponding primary amine. Ammonium formate serves both as the source of nitrogen and reductant.

In the original Leuckart-Wallach reaction and early applications,[141] high temperatures were necessary (up to 185 °C). Depending on the conditions, not the primary amine is formed, but its formamide or ammonium salt. Of course, all aminations at this point were non-asymmetric.

Despite the early successes of transition metal-based asymmetric catalysis in the 1970s and 1980s pioneered by Knowles[142] and Noyori[143] for hydrogenations and Sharpless in asymmetric oxidations[144–146], which were eventually awarded with the nobel prize, it took some time for the first asymmetric reductive amination to be developed. In 1999, Blaser et al. reported the synthesis of an intermediate for the production of (*S*)-metolachlor with a chiral iridium catalyst[147] that is now widely regarded as the first example of an asymmetric reductive amination.[148]

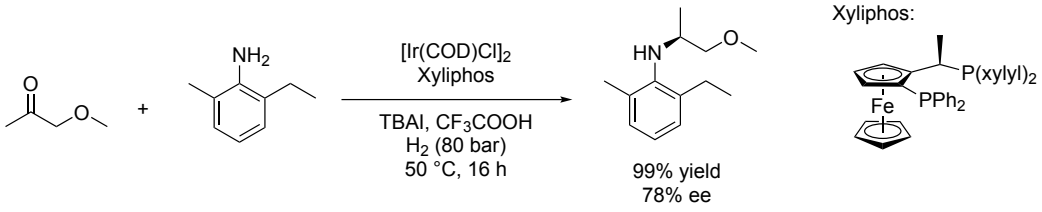

Figure 4.3: Blaser et al.'s 1999 synthesis of the key chiral intermediate for the synthesis of (*S*)-metolachlor.

An enantiomeric excess of 77 % could be achieved using iridium with the Xyliphos ligand from the family of Josiphos ligands developed a couple of years earlier by Togni and coworkers.[149] The new method was patented by Ciba-Geigy and has since been implemented on a >10,000 t/y scale. The ability to produce enantiomerically enriched metolachlor was especially important since only the (*S*)-enantiomer shows biological activity[150] and the patent for racemic (*RS*)-metolachlor had run out. Still, the example by Blaser is an enantioselective *N*-alkylation, not a synthesis of a chiral primary amine. In the following years, several

protocols for asymmetric reductive amination, imine hydrogenation and alcohol amination were published using iridium,[151–155] rhodium,[156,157] palladium[158] and ruthenium[159] catalysts. Most of these also produce secondary or tertiary amines, but some are notably close to primary amines: Kadyrov et al. developed a system based on [((*R*)-tol-binap)$RuCl_2$] with NH_4HCO_2 (as in the Leuckart-Wallach reaction) in NH_3/MeOH and obtained mixtures of amine and formylated amine with good enantiomeric excess (86-98%).[159] Nevertheless, the free amine has to be obtained by removal of the formyl protection group. Another approach by Zhang used an iridium catalyst with the (*S*,*S*)-*f*-binaphane ligand to hydrogenate iminium salts to the corresponding chiral ammonium salts with dihydrogen as the reductant.[152] This is relatively close to the desired free amine, but technically speaking not a reductive amination – the iminium salts have to be prepared separately from alkylation of nitriles with (expensive) Grignard reagents. To summarize the state of the art in 2016, numerous asymmetric reductive amination procedures had been developed from 2000 onward, but none yielded the free, unprotected chiral primary amine in decent yield. Also, the use of ammonium formate as a reductant is not ideal, and in the cases where hydrogen (H_2) had been used for the reduction, the source of nitrogen was expensive as the iminium salts in the chemistry of Zhang had been made from nitriles and organometallic reagents.[152,153,157]

From an industrial perspective, an ideal asymmetric reductive amination for primary amines would have to fulfill the following criteria:

1. Provide high enantioselectivity.
2. Provide high chemoselectivity (vs. ketone hydrogenation).
3. Yield the chiral primary amine, without any protecting groups or intermediary steps directly from the ketone.
4. Employ H_2 as the simplest and cheapest reductant.
5. Employ NH_3 as the simplest and cheapest nitrogen source.

Such a reductive amination would be the simplest and economically most viable route to chiral amines and also the most atom-efficient pathway (producing only water during imine formation as the sole byproduct). There are, however, numerous challenges in the direct asymmetric reductive amination, especially for the synthesis of primary chiral amines directly with NH_3 and H_2. First of all, primary imines, formed from the condensation reaction of ketone and ammonia, are known to be unstable. Only very few examples of *N*-unsubstituted imines,

that could be isolated, exist.[160] As a consequence, the reaction has to be highly chemoselective, since the equilibrium between ketone/ammonia and imine/water favors the ketone. The increasing amount of water left over from hydrogenation of the imine will shift this equilibrium even further. The catalyst must therefore exhibit an intrinsic strong preference for imine hydrogenation over reduction of the ketone. Secondly, for the enantioselectivity, *N*-unsubstituted imines also pose a significant challenge as they lack a third (bulky) substituent on the nitrogen to enhance enantiodiscrimination. Another issue in imine hydrogenation (compared to ketones) is that they exhibit potential *E*/*Z* isomerism, also affecting enantioinduction. Since ammonia, the formed amine but also imines are usually good ligands, catalyst poisining can also be an issue. Lastly, potential overalkylation to secondary and tertiary amines rather than the primary amines has to be controlled.

As no catalyst for this reductive amination existed and none had been reported for the explicit RA with NH_3 and H_2, a new project was developed at CaRLa in search for a suitable catalyst system. The target substrates were aryl-alkyl amines. BASF currently produces a portfolio of chiral amines under the tradename ChiPros, which contains 32 aryl-alkyl amines of which most belong to the group of phenylethylamines (acetophenone-type). These are produced through the lipase-catalyzed enantioselective amidation of racemic amines, followed by separation and deprotection.[135] The basis for the asymmetric reductive amination at CaRLa was a previous project in which the non-asymmetric reductive amination with NH_3/H_2 had been established.[161]

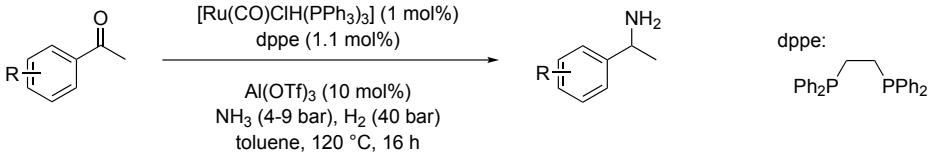

Figure 4.4: Previously developed non-asymmetric reductive amination that only uses NH_3 and H_2 with aryl-alkyl amines as targets.

The protocol uses a ruthenium complex of 1,2-bis(diphenylphosphino)ethane (dppe) to reach yields of up to 99% amine with almost no alcohol formation. It was therefore natural to use a chiral variant of dppe to achieve the same reductive amination with enantioinduction. Chiraphos is such an analogue of dppe and is the same molecule except for two methyl groups on the ligand backbone which make the ligand chiral. Unfortunately, only 26% ee were obtained and a lower yield was also observed. A variety of ligands were screened of which a few showed some enantioselectivity (see Figure 4.5), but the enantiomeric excess did not exceed 32%.

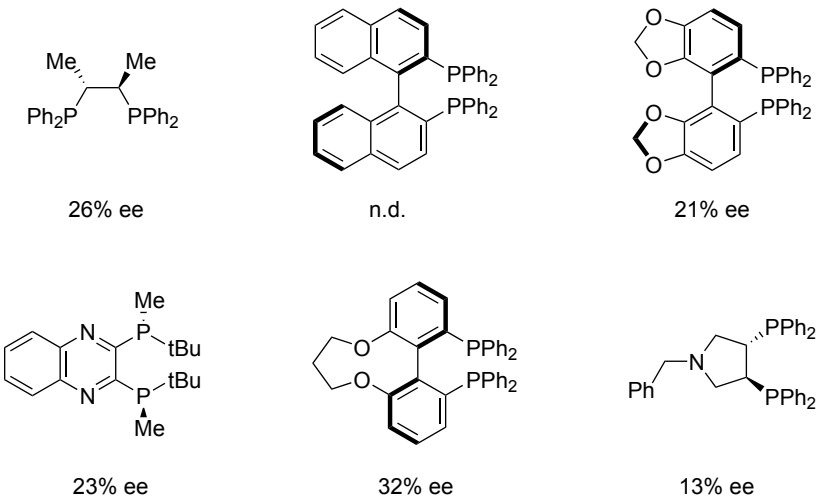

Figure 4.5: Chiral ligands tested for the asymmetric reductive amination which all exhibit not even moderate enantioselectivity. From left to right; top, then bottom row: (*R*,*R*)-Chiraphos, (*R*)-BINAP, (*R*)-SEGPHOS®, (*S*)-QuinoxP®, (*R*)-C_3-TunePhos, (*N*)-benzyl-(3*S*,4*S*)-bis(diphenylphosphino)pyrrolide. In the case of BINAP, the enantiomeric excess was not determined since activity was very low.

After about 20 ligands had been screened unsuccessfully, (*S*,*S*)-*f*-binaphane finally achieved a promising ee of 70%. The ligand was developed in the group of Xumu Zhang, which had used it for the hydrogenation of imines.[151] The enantioselectivity could be further increased using ammonium iodide as an additive and tweaking the reaction parameters to 87% ee. The optimized protocol is shown in Figure 4.6. Since the newly developed reaction was the first example of an asymmetric reductive amination to primary amines directly from NH_3/H_2 with good enantioselectivity, we became interested in studying the reaction mechanism to gain more understanding and potentially improve the system even further. As experimental insights into the mechanism were limited, a computational study became the method of choice, which will be discussed in this chapter.

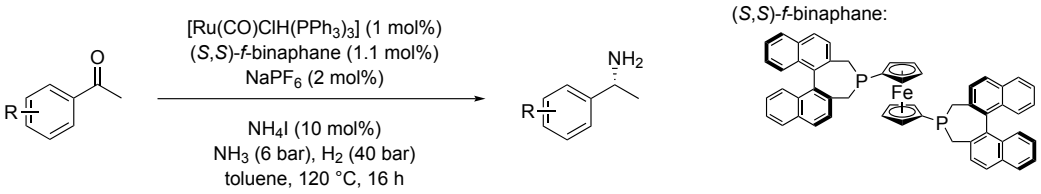

Figure 4.6: Current system for the direct asymmetric reductive amination with NH_3/H_2 using (*S*,*S*)-*f*-binaphane. NH_4I is crucial for a good enantioselectivity (and chemoselectivity).

4.2 Computational Details

All molecular structures were optimized at the BP86/def2-SV(P) level of theory.[35,44,46] Final electronic energies were computed at the PBE0-D3(BJ)/def2-QZVPP[35,54] level using dispersion correction[70] with Becke-Johnson damping.[71] Electronic structure calculations were carried out using the TURBOMOLE program[96] using the resolution of the identity approximation[62,97,98] with the corresponding auxiliary basis sets.[36] Thermal corrections and zero-point vibrational energies were computed at the level of geometry optimization (BP86/def2-SV(P)), within the harmonic oscillator/rigid rotor approximation at 298.15 K and 1 bar. The thermodynamic reference for all species was a molar fraction of $\chi = 0.01$, except for hydrogen ($p = 40$ bar) and ammonia ($p = 6$ bar). All positive vibrational frequencies were used in the vibrational partition function. Free enthalpies of solvation for toluene were calculated for each structure at infinite dilution with COSMO-RS theory[75,76] at the BP86/def-TZVP level using the COSMOtherm program package[78,99] with the corresponding parameter set (Version C3.0, Release 1501, revision 1744).

For each species, only the lowest conformer that was found was considered and the conformational partition function was set to 1, with the exception of substrate conformers, which were investigated in-depth as was necessary for accurate prediction of the enantioselectivity. For the free imine, the *E* isomer was used as reference, which was computed to be favored by 3.1 kJ·mol^{-1} over the *Z* configuration of the double bond.

In the search for some transition states, the single-ended growing string method by Zimmerman[162] and coworkers was applied.

Ab-initio molecular dynamics simulations were performed with the Quickstep[163] module of the CP2K program suite,[164] version 5.0. The calculations were carried out with the Perdew-Burke-Ernzerhof functional[48] and the third generation dispersion correction by Grimme and coworkers.[70] The DZVP-MOLOPT-SR-GTH basis set[165] was used for all atoms in combination with Goedecker-Teter-Hutter pseudopotentials for the core electrons.[166–168] The time step was set to 0.5 fs and the trajectory was recorded every 5 steps. The temperature was set to 330 K and pressure to 1 bar. Each MD simulation contains the respective binaphane complex with the backbone of interest as the type **A** isomer as reference, solvated with 90 toluene molecules. The initial cells were packed with the packmol program.[169] Using an NPT ensemble, MD simulations were performed until the cubic, periodic cell reached equilibrium (cell size only fluctuating around the equilibrium value). An average cell size was calculated from

the last 1000 frames of the NPT ensemble. Then a frame with cell size close to the averaged cell size was taken and used as the initial configuration for a NVT ensemble MD simulation with the same parameters. The bite angle distributions were obtained with the VMD (Visual Molecular Dynamics) program[170] from the trajectory of the NVT ensemble.

4.3 Results and Discussion

4.3.1 General Thermodynamics

In a reductive amination, the intermediary imine is formed by condensation of the ketone with ammonia and then reduced to the corresponding amine. Looking at the plain thermodynamics, the computed Gibbs free energy changes are as follows:

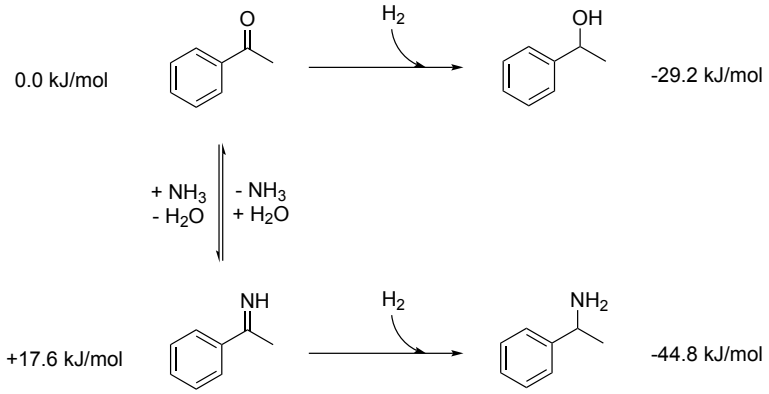

Figure 4.7: Thermodynamics of imine formation and hydrogenation of ketone and imine for acetophenone. Energies given are free enthalpies in kJ/mol and relative to the ketone.

Formation of the imine from the ketone is endergonic by 17.6 kJ·mol^{-1}, which is generally expected as *N*-unsubstituted imines are known to be unstable. Hydrogenation of both ketone and imine are exergonic by 29.2 kJ·mol^{-1} and 62.4 kJ·mol^{-1}. The heat of hydrogenation for the ketone reduction $\Delta_{red}H$ is computed to be −57.7 kJ·mol^{-1}, which is in line with experimentally measured hydrogenation enthalpies, ranging from ~50 to 70 kJ·mol^{-1}.[171]

4.3.2 Catalyst Structure

The very first question in the investigation of the mechanism that had to be addressed was that of the actual catalyst structure. Since we had not been able to obtain a crystal of the active catalyst due to purification and isolation issues, not much was known about the structure. There where some experimental hints for which ligands were of relevance and might be involved:

1. (S,S)-f-Binaphane
   The influence of the ligand on enantio- and chemoselectivity and the signals from ^{31}P NMR clearly indicated that the ligand is coordinating to the catalyst.

2. Iodide
   Similarly, the influence of halide on the reaction outcome suggested that iodide is coordinating to ruthenium in the active catalyst.

3. Hydride

   A hydride ligand on ruthenium seemed necessary to facilitate any type of hydrogenation reaction, and the hydride was also present in our precursor.

4. Carbon monoxide

   The presence of coordinated carbon monoxide on the ligand was deduced from the fact that a CO-free precursor, $[RuH_2(PPh_3)_3]$ did not facilitate the reaction under the same conditions, and due to the general stability of Ru-CO coordination.

With six coordination sites on a typical ruthenium(II) octahedral complex, this would leave one free coordination site for the imine to initiate the reaction. Due to the different modes of conformation possible for the imine, ammonia was chosen as a substitute for a sixth ligand. Since ammonia is also present during the reaction, it is also likely that coordination of ammonia occurs. With this set of ligands, six isomers **A**-**F** were proposed as likely candidates for the active catalyst species.

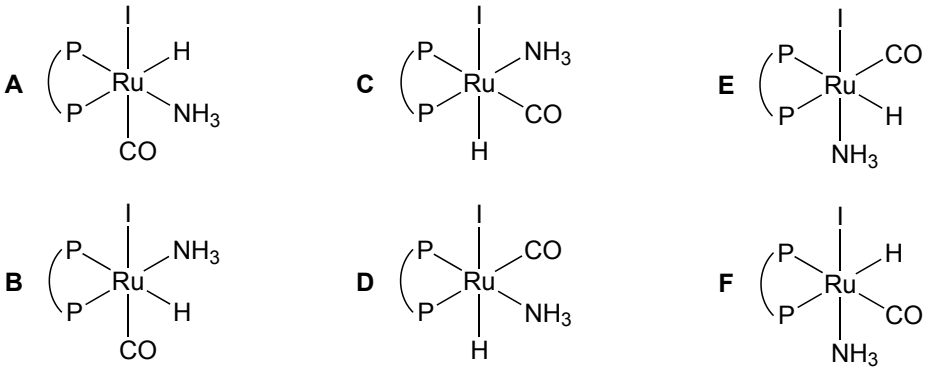

Figure 4.8: Suggested general isomers for the structure of the catalyst in the asymmetric reductive amination. The C_2-symmetric (*S*,*S*)-*f*-binaphane ligand is simplified.

Of the six different isomers, the pairs **A**/**B**, **C**/**D**, and **E**/**F** are, except for the chirality of the ligand, almost mirror images of each other. (*S*,*S*)-*f*-binaphane is C_2-symmetric, but has no mirror plane (hence the chirality). The energetically lowest pair of isomers is **A**/**B**. Complex **B**, in which the hydride is *trans* to the phosphine ligand and on the left when the halide is viewed as being in the upper apical position, is slightly more stable by 4.7 kJ·mol^{-1} than complex **A**. Complex types **C** and **D** are a bit higher in energy with 8.2 kJ·mol^{-1} and 11.0 kJ·mol^{-1} relative to **B**. In these complexes, the hydride is *trans* to the halide and CO coordinates in equatorial position *trans* to the phosphine. Although these complexes are not as stable as **A**/**B**, the energy difference is too low to rule them out for being catalytically active species. To assess whether these are relevant in catalysis, it is necessary to go a step further and look at the necessary η^2-imine complexes which have to be formed for hydride transfer from the catalyst. In

these complexes, ammonia is substituted by the imine (phenylmethyl imine, the imine of the ubiquitous test substrate acetophenone) and the imine coordinates with the π-double bond to the ruthenium center. For a full picture, η^2 complexes of the *R* and *S* prochiral faces of the imine as well as the *E* and *Z* isomers have to be calculated for each isomer type of the complex (**A**/**B**, **C**/**D**). We will go into more detail regarding the isomer/conformer complexity later. Contrary to **A**/**B**, complexes of type **C**/**D** do not have stable η^2 intermediates. Thus, "supposed" η^2 complexes were calculated, with fixed Ru-C and Ru-N bond lenghts taken from the stable intermediates of **A** and **B**. For these complexes, however, the η^2 imine coordination for isomer types **C**/**D** is disfavored: compared with the lowest η^2 intermediate of **A**/**B**, the complexes of **C** and **D** are higher in energy by 18.3 to 50.0 kJ·mol^{-1}. Additionally, these complexes have the C-N double bond more or less in plane with the phosphine ligand in *trans* position. For an actual hydride transfer, they would have to rearrange into an η^2 coordination where the C-N bond is parallel to the apical I-Ru-H axis, so that the electrophilic carbon points toward the hydride – in which case either the phenyl or methyl group points directly into the ligand, rendering them even less realistic in terms of energy. Therefore, complexes **C** and **D** were ruled out for participating in the catalysis. Finally, complexes **E** and **F**, where ammonia (or the substrate binding site) is *trans* to the halide, are very high in energy. Relative to **B**, they are less stable by 73.3 kJ·mol^{-1} and 73.2 kJ·mol^{-1}, which also seemed not competitive with **A**/**B**. As a result, it was proposed that complexes of type **A** or **B** would facilitate the reaction, potentially both, due to the low energy difference.

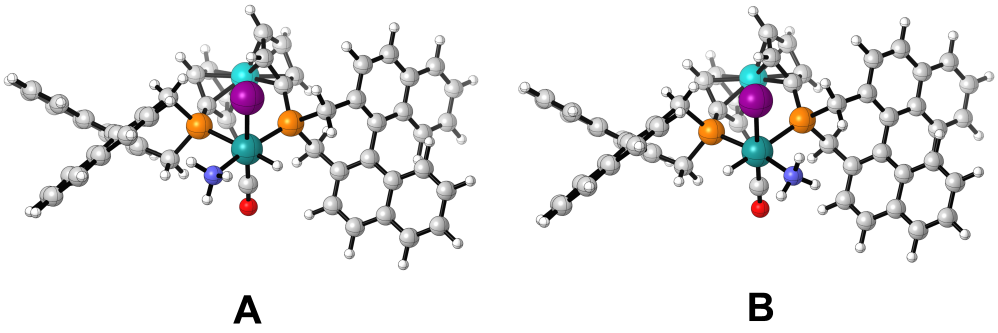

Figure 4.9: Computed structures of catalyst isomers **A** and **B**, which are the relevant species in catalysis. A very distinct feature of (*S*,*S*)-*f*-binaphane as a ligand is already visible: in contrast to many ligands where chirality is located on the backbone, the chiral binaphane "wings" wrap around the metal complex and create a chiral pocket of two parallel naphthyl groups.

The computational proposal was later confirmed by experiment, when a crystal was finally obtained that was suitable for analysis by X-ray crystallography (unfortunately, this was the only time a ruthenium species could be isolated from the reaction mixture and analyzed). Figure 4.10 shows the crystal structure of the pre-catalyst/catalyst resting state that was obtained.

Except for having triphenylphosphine (from the $[Ru(CO)ClH(PPh_3)_3]$ precursor) instead of ammonia, since it is a better ligand, the complex is of proposed type **B**, which was predicted to be the energetically lowest of all species.

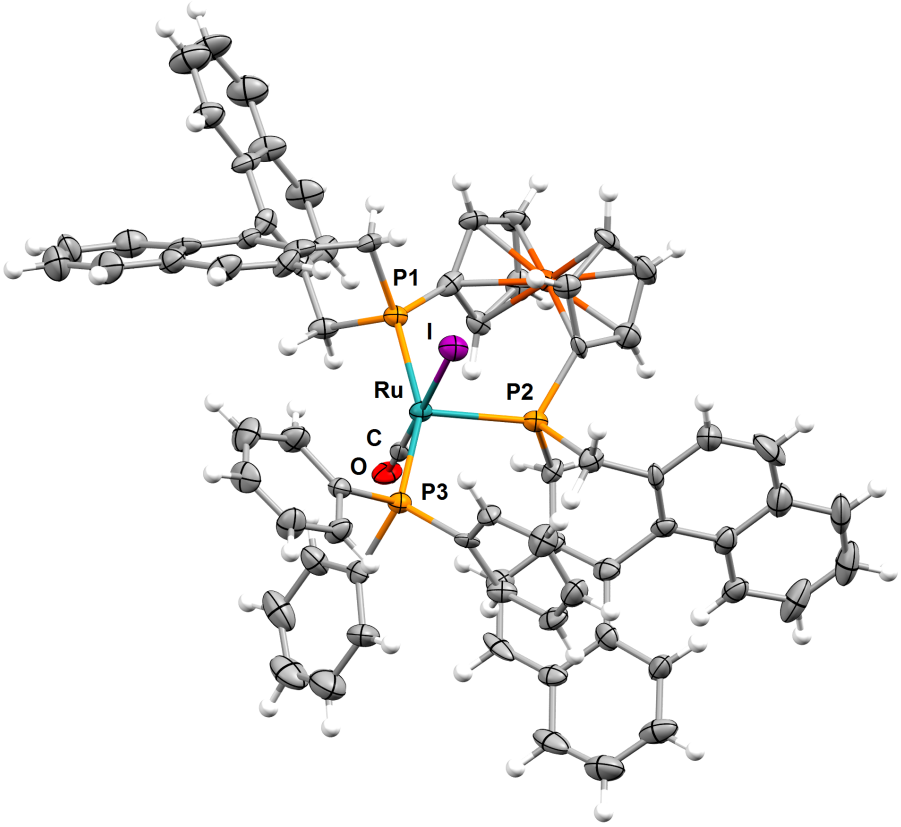

Figure 4.10: Structure of [Ru(I)H(CO)((*S*,*S*)-*f*-binaphane)(PPh_3)] from X-ray crystallography. The hydride cannot be located in the difference electron density map, but charge balance, as well as the overall complex geometry and the elongation of the Ru-P2 distance (2.43 Å) demonstrate that it is present. The NMR signal of the hydride could also be detetced in ^{1}H NMR (δ = -7.86 ppm). The corresponding mass of the hydride complex was confirmed by FD-MS. Selected bond distances (Å) and angles (°): Ru−I: 2.7932(9), Ru−C: 1.834(10), Ru−P1: 2.340(2), Ru−P2: 2.434(3), Ru−P3: 2.404(2), C−O: 1.138(9), I−Ru−C: 179.0(3), P3−Ru−I: 84.59(5), P1-Ru-P2: 100.23(9), P3−Ru−P1: 155.63(2), P2−Ru−C: 90.5(3), Ru−C−O: 175.6(7).

The crystal structure again shows the wing-like geometry of the complex with the binaphtyl groups wrapping around the complex. The ferrocene backbone has its cyclopentadienyl parallel to the backward facing naphtyl groups of the binaphtyl moieties, creating a sandwhich-in-a-sandwhich-like appearance. While the hydride cannot directly be seen, its presence was confirmed by ^{1}H NMR and in FD-MS. The elongation of the *trans* Ru-P2 bond (2.43 Å) due to its strong σ-donation also indicates that the hydride is coordinating *cis* to triphenylphosphine. The other Ru-P bond distance of (*S*,*S*)-*f*-binaphane is considerably shorter with 2.34 Å. The bite angle of the chelate ligand is 100.2°.

4.3.3 Mechanistic Proposal

After initial considerations and several revisions during the investigations, the mechanism shown in Figure 4.11 was proposed:

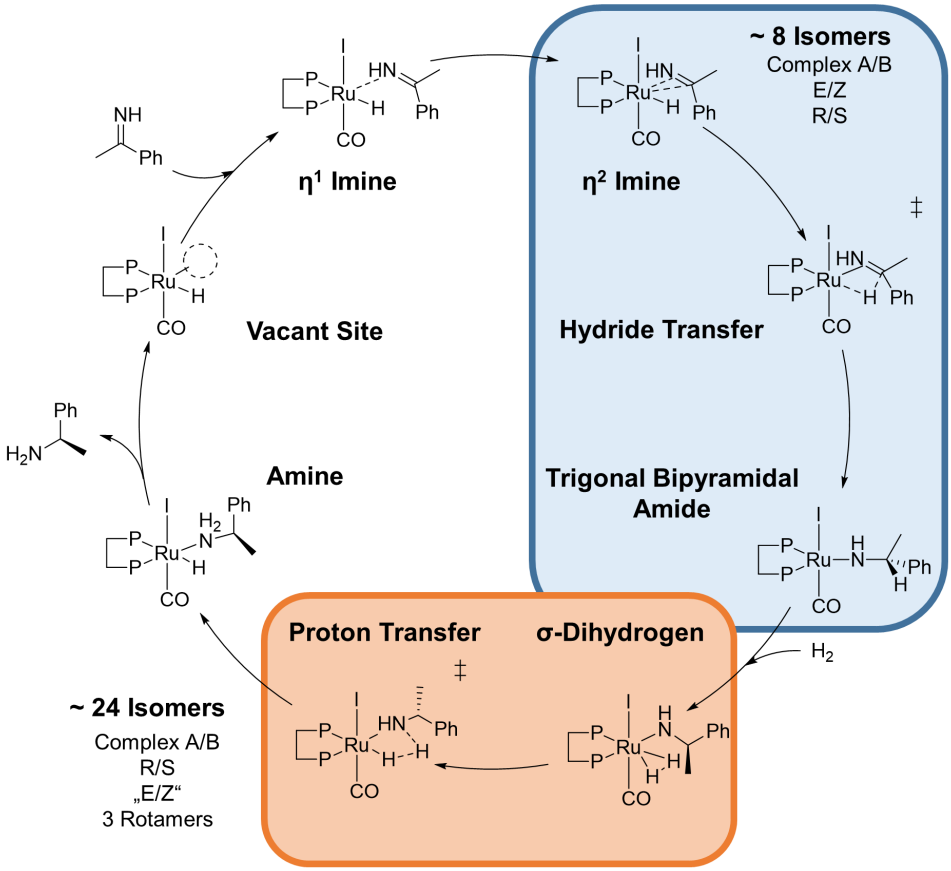

Figure 4.11: Mechanistic proposal for the hydrogenation of the intermediary imine in the asymmetric reductive amination of acetophenone to (*R*)/(*S*)-1-phenylethylamine. The bidentate phosphine ligand is (*S*,*S*)-*f*-binaphane.

In the mechanism, the free imine coordinates to the vacant site on the ruthenium complex of either type **A** or **B** to form the corresponding η^1 imine complex. To initiate hydride transfer, the imine must rearrange from the η^1 mode, where it coordinates with its lone pair, into the η^2 complex where the π-system of the C-N double bond coordinates to ruthenium. From here, hydride transfer can occur and will result in the ruthenium amide complex (as we will later see, an amido complex with agostic C-H-Ru interaction is also possible). Molecular hydrogen can coordinate to the Ru amide complex to form the corresponding σ-dihydrogen complex, which can then undergo heterolytic cleavage of H_2 to facilitate the proton transfer to the amide, restoring the initial hydride and releasing the final amine. This is a very typical pathway for hydride formation when the alternative of oxidative addition to the dihydride is not

feasible. H_2 here acts as an internal acid and numerous examples of ligand protonation from σ-dihydrogen complexes exist, for systems where this behavior could be isolated.[172] This is due to the kinetic acidity of σ-bonded hydrogen being greatly enhanced for the intramolecular protonation since no change in oxidation state or coordination number occurs. Direct pK_a estimates are difficult, but estimates of pK_as as low as -6 have been reported for ruthenium complexes.[173] For the hydride transfer transition state and the η^2 imine, different isomers are possible (highlighted in blue): any combination of either the complex type **A**/**B**, the prochiral faces of the imine for R/S, and the double configuration on the imine (E/Z), should be considered, which can be up to eight potential pathways. Similarly, the same applies to the σ-dihydrogen complexes and the proton transfer. It was also realized, that due to the reduction of the double bond to a single bond in the hydride transfer step, the C-N rotamers have to be considered for this species, giving up to 24 different possibilities for this pathway. We will discuss this later in more detail, but the investigations showed, that a thorough analysis of these isomers/conformers was necessary for reliable results (with respect to enantioselectivity).

Other mechanistic proposals were also considered. The classical Noyori-type hydrogenation mechanism[174] for an outer-sphere hydrogenation was unlikely since no analogous diamine ligand was present. The only similar proton source for a Noyori-type outer sphere mechanism would have been free ammonia, but the formation of an unsubstituted NH_2 amido ligand did not seem realistic, and to our knowledge no reports of such systems exist. It should be mentioned here, that very recent investigations by Dub and Gordon have shed some doubt on the originally established involvement of the amine ligand in Noyori-type hydrogenations.[175,176] An outer-sphere hydrogenation exclusively taking place at ruthenium through a dihydride species was also discarded: since the presence of halide on the ruthenium complex was certain, it would have involved very unusual Ru(III)/Ru(I) redox chemistry, with a tetracoordinated intermediate, but NMR experiments never showed signs of paramagnetic ruthenium species. In fact, experimental observations suggested that the oxidation state of ruthenium remained +2 during catalysis, which also supported our proposal. Finally, we could exclude metal-ligand cooperation as has been proposed for Milstein's pincer-type systems,[177–179] since (*S*,*S*)-*f*-binaphane does not offer the required functionality for a ligand-substrate hydrogen transfer through aromatization/dearomatization. One might argue that the benzylic position on the ligand could be susceptible to this; but the known PNP-pincers work by formation of the corresponding enamide (not some phosphorous ylide).

Our proposed mechanism consists of different intermediates and transition states of many

isomers and conformers that should finally be able to predict our experimental observations, especially the enantioselectivity, and these will be discussed in the following subsections.

4.3.4 Substrate Coordination and η^1 Imine Complexes

In an initial step, the substrate must coordinate to the metal complex for catalysis to begin. With our catalyst, this is the η^1 imine complex which is initially formed. Several other species compete with coordination at the vacant site of the ruthenium hydrido complex: imine, ammonia, molecular hydrogen and triphenyl phosphine from the catalyst precursor. Figure 4.12 shows the relative free enthalpies of the species.

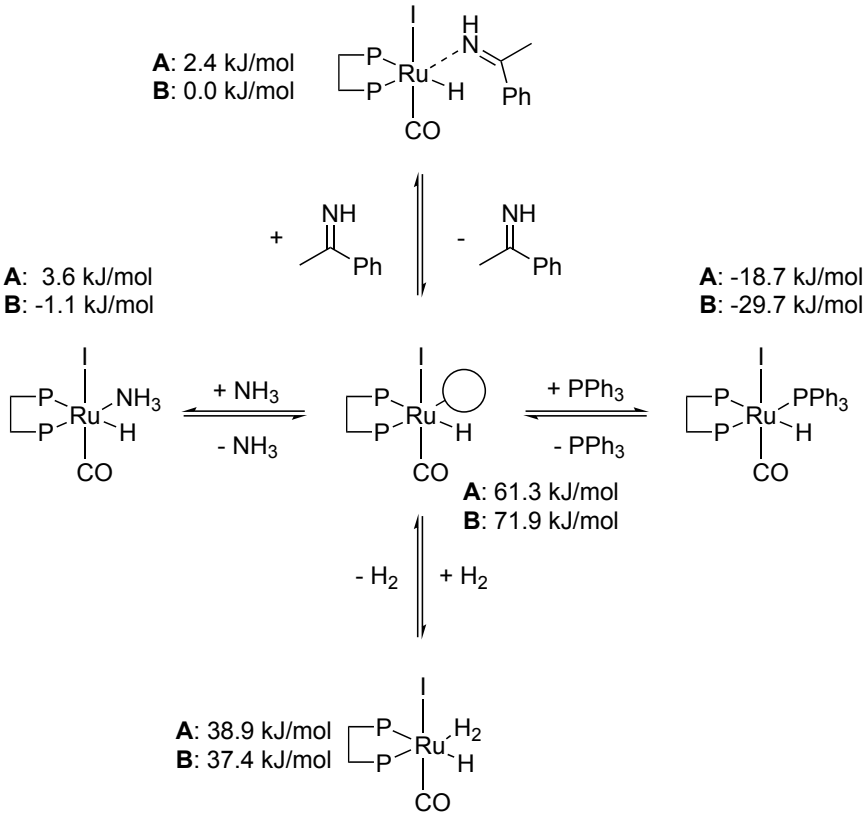

Figure 4.12: Mechanistic proposal for the hydrogenation of the intermediary imine in the asymmetric reductive amination of acetophenone to (*R*)/(*S*)-1-phenylethylamine. The bidentate phosphine ligand is (*S*,*S*)-*f*-binaphane. Energies are in kJ/mol and relative to the most stable η^1 imine complex (which is of complex type **B**). The depicted complexes have the **B**-structure, but values are given for both **A**/**B**.

The energies are given relative to the most stable η^1 imine complex. This is the initial species for the catalysis and will also serve as reference in the upcoming subsections. The most stable η^1 complex is of isomer type **B** (similar to our estimations for the isomer types, **B** is slightly more stable by 2.4 kJ·mol^{-1}) and more precisely has the imine in configuration R/Z. Unsurprisingly, the pentacoordinate species with a vacant site is energetically unfavored (61.3 kJ·mol^{-1}

for **A**, 71.9 kJ·mol^{-1} for **B**). Coordination of NH_3 is energetically very similar to the imine (**A**: 3.6 kJ·mol^{-1}, **B**: −1.1 kJ·mol^{-1}) and it can be assumed that the two ligands can interchange quickly in solution. Triphenyl phosphine is a better ligand than the imine by 21.1 kJ·mol^{-1} and 29.7 kJ·mol^{-1} for isomers **A**/**B**. For PPh_3, the difference between **A** and **B** seems to be more pronounced (11.0 kJ·mol^{-1}), probably due to its bulkiness, which discriminates more strongly between the two sites of the complex. The relative stability also explains why the only crystal that could be obtained in the project was of isomer type **B** with triphenyl phosphine coordinating. Under catalytic conditions, the relative excess of substrate vs. PPh_3 will likely alleviate the better ligand capabilities of the latter. The σ-dihydrogen hydrido complexes were also calculated, and contrary to the fear that they might be resting states (ruthenium complexes of hydrido dihydrogen type have been isolated, for example in the group of Sabo-Etienne),[180] they were endergonic by 38.9 kJ·mol^{-1} (**A**) and 37.4 kJ·mol^{-1} (**B**) relative to the imine complexes. Dihydrogen hydrido complexes are therefore only formed as short-lived intermediates, but do not affect the activity of the catalyst.

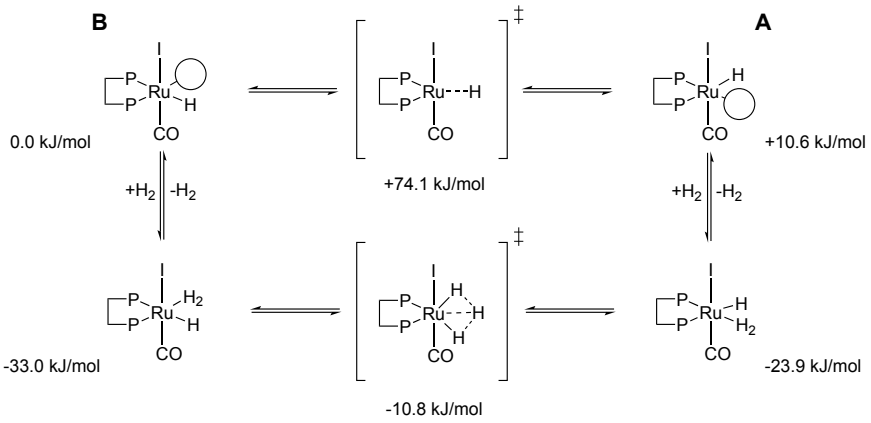

Figure 4.13: Isomerization between complex types **A** and **B**, either by direct transition of the hydride through the trigonal bipyramidal hydride complex or via H_2. Energies are free enthalpies in kJ/mol and relative to the hydride complex with a vacant site of type **B**.

The hydride complex of types **A** and **B** are in a rapid equilibrium, so that the initial configuration is not relevant. The direct interconversion from the hydride complexes with a vacant coordination site has a barrier of 63.5 kJ·mol^{-1} (**A**→**B**) and 74.1 kJ·mol^{-1} (**B**→**A**). Isomerization is accelerated by the formation of the σ-dihydrogen hydride complexes which are exergonic with respect to the pentacoordinated complexes. In these, proton transfer from H_2 to the hydride only has a barrier of 13.1 kJ·mol^{-1} (**A**→**B**) and 22.2 kJ·mol^{-1} (**B**→**A**).

Comment on Nomenclature

As already indicated, several η^1 imine complexes can be formed. Eight isomers/conformers are possible from isomer types **A**/**B**, R/S prochiral faces of the imine and the E/Z isomerism of the imine $(2 \times 2 \times 2)$. To make things easier, we will introduce a systematic nomenclature for complexes throughout this chapter, which is also consistent with the tables in the appendix. The structures are numbered/named according to Figure 4.14 with **TSH** for the hydride transfer transition states and **TSP** for the proton transfer transition states. These will be used in the whole chapter. η^1 complexes will be denoted with **1**, followed by the halide (**I** for the iodide complex, we will discuss other halides in section 4.3.12) and the indicators for complex type, enantiomer and E/Z isomer:

<Structure><Halide>-<Complex Type><Enantiomer><E/Z Isomerism>

For example **1I-ARZ**, which is the η^1 imine complex for the catalyst with iodide as a halide, in complex type **A**, where the imine coordinates with the *R* face and is in *Z* configuration.

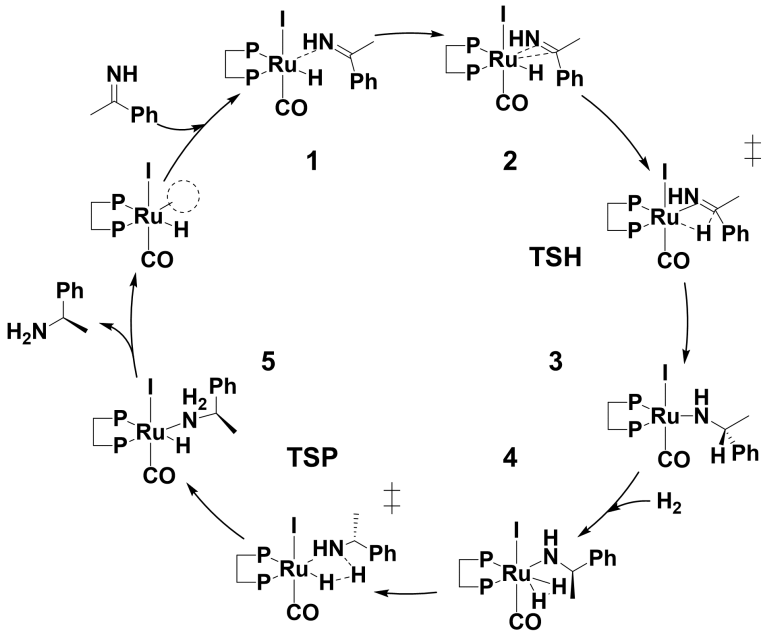

Figure 4.14: Numbering/names for the structures in the mechanism of the asymmetric reductive amination. Each structure has many subvariants which are indicated by suffixes in the nomenclature.

All eight variants of the η^1 imine complex are shown in Table 4.1. The most stable η^1 imine complex is **1I-ARZ**, which will be used for reference throughout this chapter. Complexes **1I-BRZ** and **1I-BSZ** are only slightly higher in energy with 2.4 kJ·mol^{-1} and 5.1 kJ·mol^{-1}. Generally, no very clear trend for the energetic order of the complexes can be seen. This is because they are the η^1 complexes preceding the following η^2 complexes. These have a much more defined structure due to the C-N double bond being in plane with the Ru-P bonds, creating a well-defined, rigid geometry with respect to the other substituents. The η^1 complexes in contrast only loosely correspond to that coordination as they are more loosely coordinated to the ruthenium center. The definition of *R* and *S* is also less pronounced since each prochiral face is only weakly facing either toward or away from the complex, whereas in η^2 coordination, the *R*/*S* determination is obvious. Nevertheless, some weak trends may be identified: the *Z* complexes have lower energies than the corresponding imines in *E* configuration, albeit the latter being more stable for the free imine. This can be explained as a steric effect: since in the η^1 coordination, ruthenium can be considered as a formally forth substituent on the C-N double bond (the other three being N-H, C-Me and C-Ph), having the smaller methyl group on the side of ruthenium leads to lower steric repulsion with the hydride bound to ruthenium. Also, the imine complexes of type **B** are energetically preferred relative to the corresponding complexes of type **A** (with the exception of **1I-ARZ**/**1I-BRZ**), a trend that has already been found for the complexes in Figure 4.12 and reflects the intrinsic discrimination of left- and right-hand side on the complex due to the chirality of the ligand. Speaking of left and right, we will always view the complex having the halide on top and viewed with the bidentate ligand in the back – thus complex **A** has the hydride on the right and substrate on the left and vice versa for complex type **B**.

Table 4.1: Free enthalpies of the eight η^1 complexes in kJ/mol, relative to the most stable complex **1I-ARZ** (0.0 kJ·mol^{-1}).

Relative Energies of η^1 complexes [kJ/mol]		
Complex	*E*	*Z*
AR	35.2	0.0
AS	16.3	7.3
BR	11.2	2.4
BS	10.5	5.1

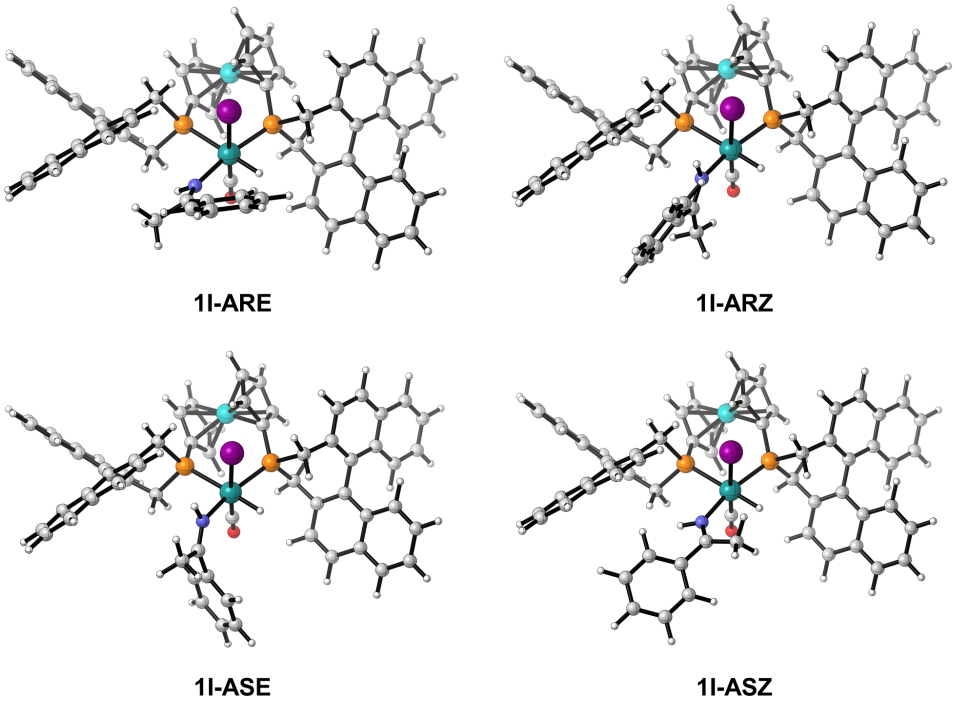

Figure 4.15: Molecular structures of η^1 imine complexes of type **A**. In type **A**, the imine is coordinating on the left side of the complex. The complex in the lower right, **1I-ARZ**, is the most stable of all complexes (see Table 4.1) and serves as reference for all species in this chapter.

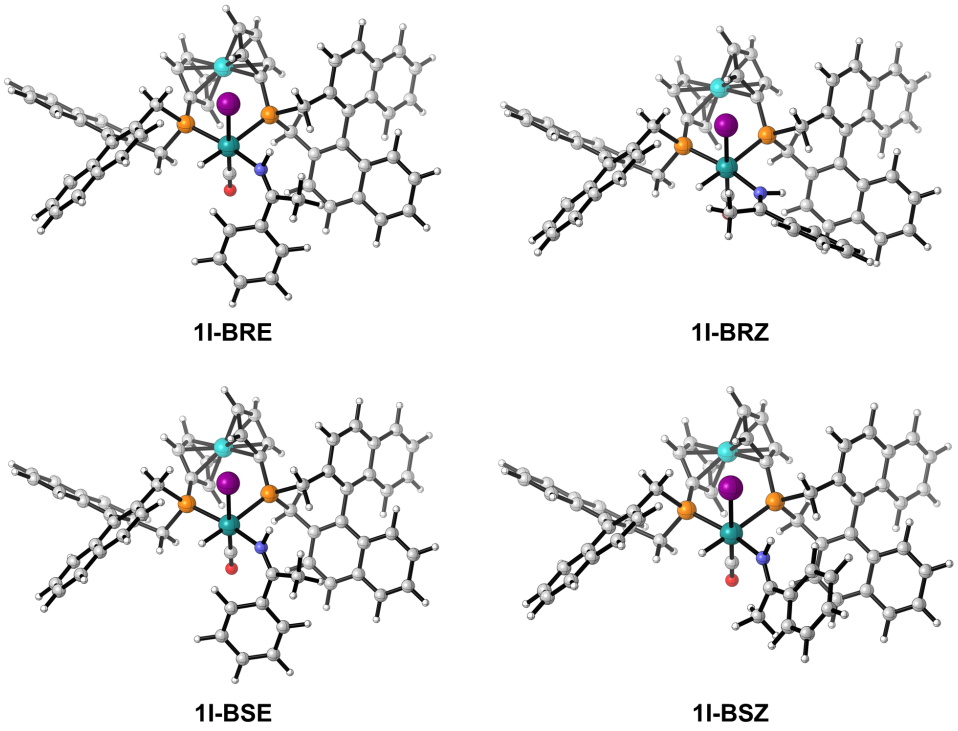

Figure 4.16: Molecular structures of η^1 imine complexes of type **B**. In type **B**, the imine is coordinating on the left side of the complex.

4.3.5 η^2 Imine Complexes

1I **2I**

Figure 4.17: Rearrangement of η^1 complexes **1I** to the η^2-bound imine complexes **2I**

η^2 complexes are the precursors to the following transition state for the hydride transfer and as just mentioned have a much more defined geometry that the η^1 complexes. The corresponding energies are considerably higher than the η^1 complexes. Rearrangement into the η^2 complex is endergonic by 42.4 to 63.3 kJ·mol^{-1}, and the most stable for complexes for the pathway to the *R* and *S* enantiomers are **2I-ASE** and **2I-BRE** which are endergonic by 53.5 kJ·mol^{-1} and 54.9 kJ·mol^{-1} relative to **1I-ARZ**. Two η^2 complexes could not be located. **2I-ASZ** and **2I-BSE** seem to go from the η^1 complexes directly into the respective hydride transfer transition states without a having an η^2 intermediate as a minimum in between. The relative energy difference to the η^1 imine complexes and the fact that some could not be found shows that these are likely only very short lived intermediates in the reaction. This is in agreement with the fact that so far no complexes of imines (even *N*-substituted ones) in η^2 coordination mode have been isolated in the literature, contrary to the examples for C-C double bond η^2 complexes with transition metals.[181,182]

Table 4.2: Free enthalpies of the eight η^1 complexes in kJ/mol, relative to **1I-ARZ**.

Relative Energies of η^2 complexes [kJ/mol]		
Complex	*E*	*Z*
AR	77.6	63.3
AS	53.5	-
BR	54.9	64.3
BS	-	67.0

What explains the relative stability of intermediates **2I-ASE** and **2I-BRE** compared to the others? When looking at the structures in comparison (figure 4.18), several features become obvious for the two complexes:

1. The imine is in its naturally lowest configuration, *E*.
2. The imine hydrogen N-H is pointing toward the halide.

3. The phenyl group is in the hemisphere of the carbonyl group.

All of these factors are stabilizing: as was mentioned earlier, the *E* configuration of the imine, where the hydrogen is on the side of the smaller methyl group is more stable by 3.1 kJ·mol^{-1} for the free imine. Having the N-H bond pointing toward the halide stabilizes the η^2 complex through a hydrogen bond-like interaction to the iodide ligand. The magnitude of stabilization ΔG_{HB} may be estimated by comparing complexes that are identical with regard to the spatial arrangement of the imine except for the orientation of the N-H bond, and subtracting the E/Z energy difference of the imine:

$$\Delta G_{HB} = G_{wHB} - G_{nHB} \pm \Delta G_{E/Z} \tag{4.1}$$

G_{wHB} is the free enthalpy of the complex with hydrogen bond, G_{nHB} the free enthalpy corresponding complex without hydrogen bond, and $\Delta G_{E/Z}$ the correction for the energy difference of the imine. Complexes **2I-ARE** and **2I-ARZ**, as well as **2I-BRE** and **2I-BRZ** can be used for this comparison. Using equation 4.1, ΔG_{HB} can be calculated by comparison of **2I-ARE**/**2I-ARZ** and **2I-BRE**/**2I-BRZ**. The estimate for the stabilization ΔG_{HB} is then in the range of 6.3 to 17.4 kJ·mol^{-1}. It should be mentioned, that there is an additional difference in the two structures with N-H$\cdots$I interaction: due to the ligands chirality, **2I-ARZ** has a more unhindered hydrogen bond since the methylene group of the ligand is pointing away from the complex core (NH-H_2C distance: 3.54 Å), whereas for **2I-BRE**, the closest methylene group is pointing inwards and the NH-H_2C distance is smaller (2.43 Å). The increase in the neighboring N-Ru-P angle from 82.6 to 84.7° also indicates steric repulsion by the methylene group. As a last comment, the NH-I interaction may also be influenced by a weak interaction between NH and the π-system of the naphthyl group, which coincides with the orientation of the methylene group. It is therefore difficult to estimate the actual stabilization through the hydrogen-to-halide bond, as separation from (steric) ligand interactions due to chirality is not trivial. Literature examples are scarce, but Eisenstein and Crabtree estimated a hydrogen bond strength of NH_2-I-Ir of < 7.5 kJ·mol^{-1},[183] although for a different complex (iridium with iodide trans to halide, and the NH being an amine on a pyridine ring). We will revisit this for the hydride transfer, where we can compare all four possible combinations for the transition state. Finally, we may do a similar comparison for the arrangement of the phenyl group. For the phenyl group facing the halide, complexes are a bit less stable, by 9.8 kJ·mol^{-1} for **2I-ARZ** vs. **2I-ASE** and 12.1 kJ·mol^{-1} for **2I-BSZ** vs. **2I-BRE**. A reason could be the unfavorable anion-π interaction, which is known to be repulsive for aromatic systems that are not electron-deficient.[184] In the same way as with the NH interactions, slight differences in steric interaction with the ligand may also influence the energetic order.

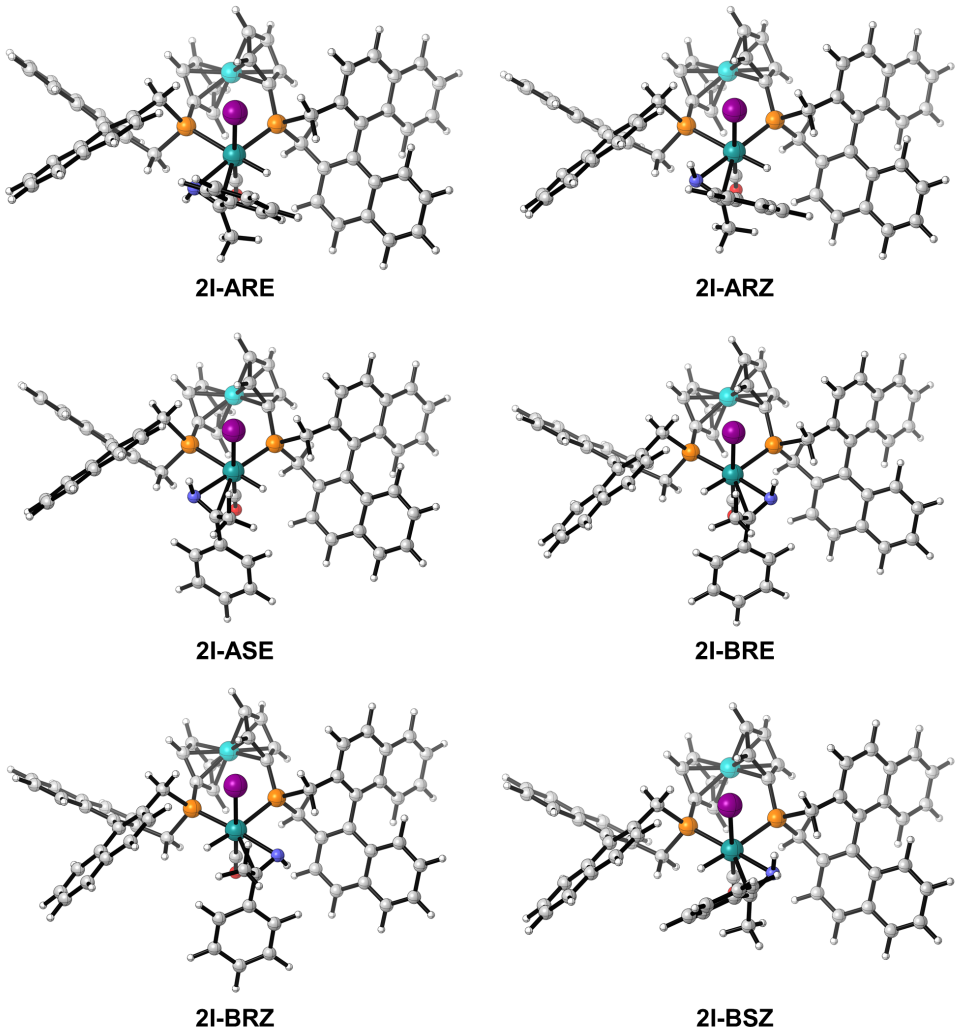

Figure 4.18: Molecular structures of η^2 imine complexes. **2I-ASE** and **2I-BRE** are the most stable complexes. The complexes for **2I-ASZ** and **2I-BSE** could not be located, for these species the corresponding η^2 imine seems to be no minimum on the PES.

4.3.6 Hydride Transfer

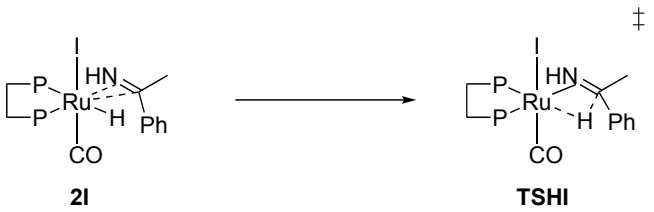

Figure 4.19: Hydride transfer transition states **TSHI**, which follow the η^2 coordinated complexes **2I**.

For the hydride transfer transition states, all eight possible combinations could be located. The structures can be seen in Figure 4.20. The free enthalpy barriers are given in Table 4.3. Structurally, the transition states are very close to their preceding η^2 intermediates. Comparison shows that only a small tilt of the electrophilic carbon on the imine and the hydride on ruthenium distinguish the hydride transfer transition states from their η^2 precursors. Since the geometric change is only minor, the energies are also only moderately higher. The lowest transition state leading to the *R* enantiomer is **TSHI-BRE** with a barrier of 70.2 kJ·mol^{-1}. For the *S* enantiomer, the lowest transition state is **TSHI-ASE** and the barrier is 71.5 kJ·mol^{-1}. From these barrier differences alone, the enantiomeric excess would be estimated to be only around ~ 26%, which is somewhat lower than what is experimentally observed (~ 87%). We will later see, that the hydride transfer is reversible and that the proton transfer is the rate-determining and also enantio-discriminating step, hence the prediction of ee from the hydride transfer transition state difference is not reliable. Also attention should be directed toward two other transition states. While **TSHI-ASE** and **TSHI-BRE** are the overall lowest hydride transfer transition states, this is only true for the respective combination of **A**/*S* and **B**/*R*. The lowest energy TS for *R* and *S* with the respective other complex type are **TSHI-ARZ** and **TSHI-BSZ** with barriers of 77.8 kJ·mol^{-1} and 81.9 kJ·mol^{-1}. These are also of importance since the energetic order of the hydride transfer transition states is not necessarily the same as for that of the complexes facilitating the proton transfer. Coming back to the stabilizing effects that were observed for the η^2 complexes, the same trend is also found for the hydride transfer transition states. The lowest barriers have *E* configuration, show the NH-I interaction and have the phenyl group in the carbonyl hemisphere of the complex. Since for these TS all eight combinations were found, the relative trend seems to be that the strength of NH-I interaction (together with contributions from steric/ligand effects) is greater than that of the repulsive anion-π interaction from phenyl group and iodide.

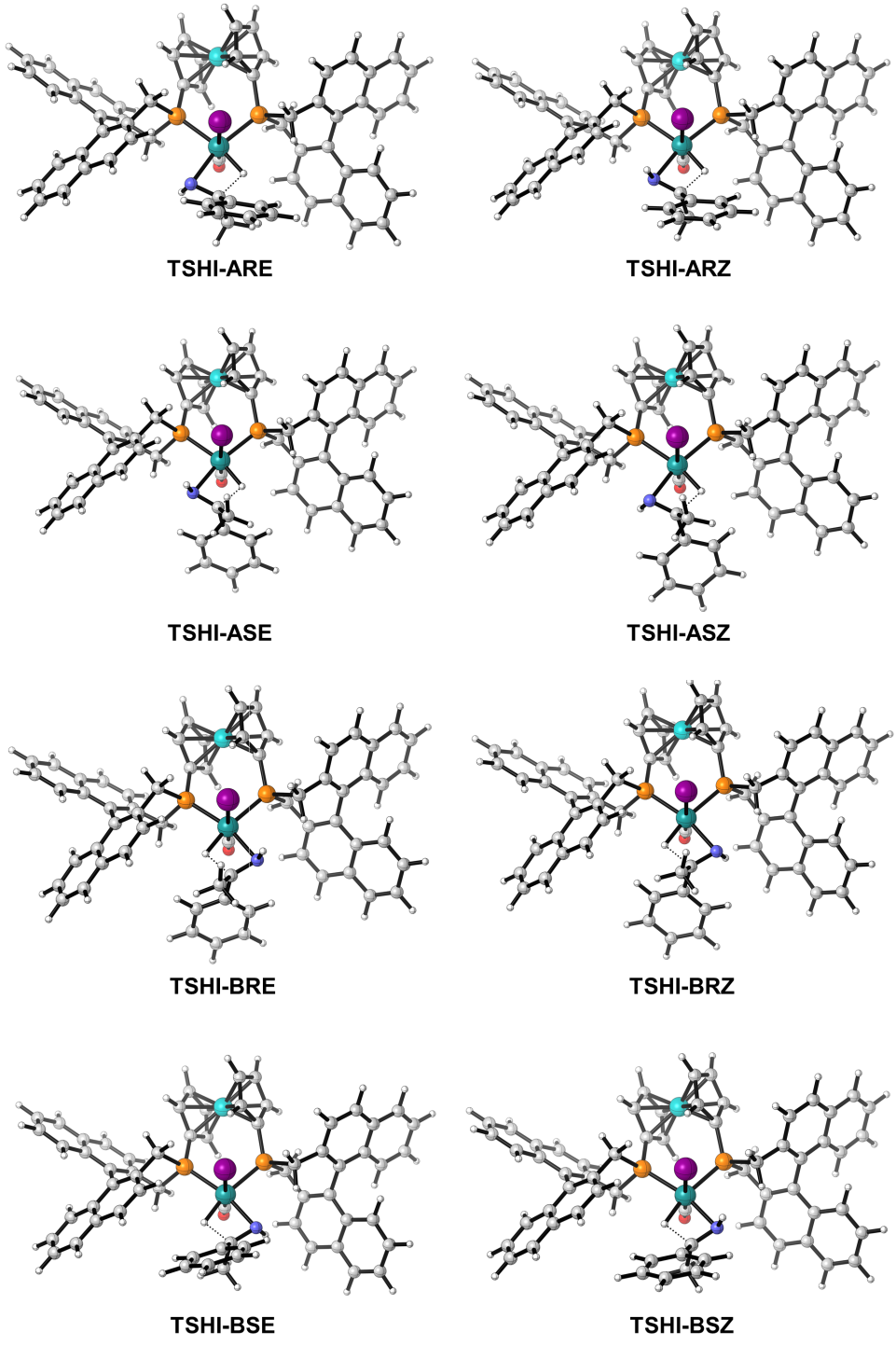

Figure 4.20: Overview of transition state structures for the hydride transfer. **TSHI-ASE** and **TSHI-BRE** have the lowest barriers to the *R* and *S* enantiomers.

This becomes evident from the energetical "grouping" of structures: **TSHI-ASE**/**TSHI-BRE** have both interactions in favorable orientation ($71.5\,\mathrm{kJ{\cdot}mol^{-1}}$/$70.2\,\mathrm{kJ{\cdot}mol^{-1}}$), followed by **TSHI-ARZ**/**TSHI-BSZ** which are identical except for the different phenyl-iodide interaction

(77.8 kJ·mol^{-1}/81.9 kJ·mol^{-1}). **TSHI-ASZ** and **TSHI-BRZ** have no attractive NH-I orientation, but avoid the repulsive anion-π interaction (99.3 kJ·mol^{-1}/85.9 kJ·mol^{-1}), and **TSHI-ARE** and **TSHI-BSE** (96.4 kJ·mol^{-1} and 89.2 kJ·mol^{-1}) with both interactions in the less favorable orientation, although the order for the latter two is not so clear. We may also apply our estimate for the NH-I interaction strength here again and obtain four values from pair comparisons: 18.6 kJ·mol^{-1} (**TSHI-ARE**/**TSHI-ARZ**), 27.8 kJ·mol^{-1} (**TSHI-ASE**/**TSHI-ASZ**), 15.7 kJ·mol^{-1} (**TSHI-BRE**/**TSHI-BRZ**), and 7.3 kJ·mol^{-1} (**TSHI-BSE**/**TSHI-BSZ**). The spread already indicates that the NH-I interaction is not isolated from an additional effect due to interaction with the methylene groups and potentially the naphthyl π-system. This also explains the difference between the highest and lowest value. In **TSHI-ASE**, the NH-I hydrogen bond comes together with a favorable orientation with respect to the ligand methylene group compared to **TSHI-ASZ**, giving an especially high stabilization of 27.8 kJ·mol^{-1}, while exactly the opposite is the case for **TSHI-BSZ** vs. **TSHI-BSE**, reducing the stabilization to only 7.3 kJ·mol^{-1}. The effect seems to be less pronounced though with the other two remaining pairs, so the phenyl group orientation still plays some role. Averaging over these pairs should eliminate the NH-ligand effects, and we arrive at an estimate of about 17.4 kJ·mol^{-1} for the stabilization of the NH-I interaction and around ~10 kJ·mol^{-1} for the residual ligand interaction. As mentioned previously, η^2 complexes and the hydride transfer transition states are structurally very close. One might therefore expect a systematic energy difference between them, and this is indeed true in our calculations. The hydride transfer transition states are higher by about 15 to 21 kJ·mol^{-1}, a relatively narrow bandwidth, as expected.

Table 4.3: Barriers for the hydride transfer to the imine. Energies are free enthalpies in kJ/mol relative to **1I-ARZ**.

Barriers for hydride transfer [kJ/mol]		
Complex	*E*	*Z*
AR	96.4	77.8
AS	71.5	99.3
BR	70.2	85.9
BS	89.2	81.9

To examine the structure of the transition states in more detail for the lowest two TS, **TSHI-ASE** and **TSHI-BRE**, the inner structures are shown in Figure 4.21. Since both are structures are mirror images of each other (except for the chirality of the ligand) the structural parameters are very similar. The C-N double bond is elongated from 1.34 Å in the η^2 complex to 1.38 Å and the C-H distance for the incoming hydride is 1.54 Å. At the same time, the Ru-N bond distance decreases as the new amido bond is about to be formed from 2.28 Å to 2.18 Å/2.19 Å in the hydride transfer transition state, while the dissociating Ru-H hydride bond distance increases from 1.64 Å in the η^2 complex to 1.74 Å/1.73 Å in the TS. Since electron density is shifted from the (former) hydride ligand to the amide which is being formed, the Ru-P distances also change: the elongated Ru-P *trans* to the hydride has a bond distance of 2.48 Å for the η^2 complex (compared to 2.34 Å for the other Ru-P bond), but in the hydride transfer transition state, the two Ru-P bonds are almost equidistant, with only a slightly longer bond for the Ru-P *trans* to the hydride (2.39 Å vs. 2.36 Å).

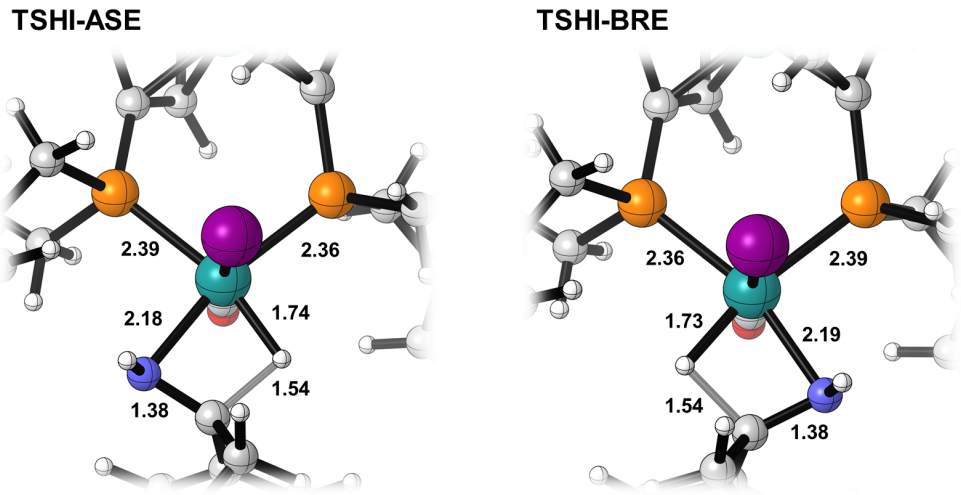

Figure 4.21: Core of the transition states **TSHI-ASE** and **TSHI-BRE** with selected bond distances in Å. The two TS are the lowest transition states for hydride transfer. The structures are mirror images of each other except for the ligand's chirality and bonding is very similar.

In summary, the hydride transfer transition states are structurally close to their η^2 counterparts and energetic differences may be explained through arrangement/orientation of the NH moiety and the substituents on the imine with respect to the complex and its ligand. Energetically, hydride transfer is definitely feasible, with the lowest barriers being 70.2 kJ·mol^{-1} and 71.5 kJ·mol^{-1} for *R* and *S* (relative to our initial reference, **1I-ARZ**).

4.3.7 Trigonal Bipyramidal and Agostic Amide Complexes

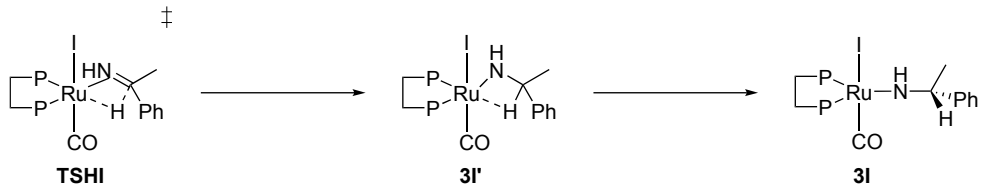

Figure 4.22: Formation of the agostic amide complexes **3I'** and the more stable trigonal bipyramidal amide complexes **3I** upon hydride transfer via **TSHI**.

Upon hydride transfer the corresponding agostic amide complexes are formed. These are structurally very similar to the **TSHI** hydride transfer transition states, although the new Ru-N bond is now fully formed and a weak agostic interaction of the new hydrogen on the amide occupies the former hydride coordination site. Agostic amides will be denoted **3I'** as rearrangement to the trigonal bipyramidal amides (**3I**) is energetically favored. This was realized when looking at the free enthalpies for the agostic amides (table 4.4). The energies are within a few kJ/mol of those of the corresponding hydride transfer transition states and sometimes even slightly higher. The reason for this is that the geometry is almost the same as in the hydride transfer TS, and the thermal contributions are higher due to an additional entry in the vibrational partition function (compared to one imaginary frequency in the TS that is not included).

Table 4.4: Energies of the agostic amide complexes **3I'**. Energies are free enthalpies in kJ/mol.

Agostic amide complexes [kJ/mol]		
Complex	*E*	*Z*
AR	92.4	78.8
AS	72.6	97.3
BR	71.2	84.4
BS	88.4	85.7

Not all structures will be shown here, but exemplarily the agostic amide complexes of **3I'-ASE** and **3I'-BRE** will be discussed, which are the energetically the lowest for *R*/*S* and allow for comparison with the TS structures in Figure 4.21. The inner structures of **3I'-ASE** and **3I'-BRE** are shown in Figure 4.23. Distances for the agostic CH-Ru interaction are 1.90 Å for **3I'-ASE** and 1.85 Å for **3I'-BRE**. The longer Ru-P bond is now *trans* to the amide in both cases (2.39 Å/2.38 Å). Ru-N bond distances and the C-N bond only show minor changes, whereas the new C-H bond is now distinctly visible with a bond length of 1.26 Å and 1.29 Å.

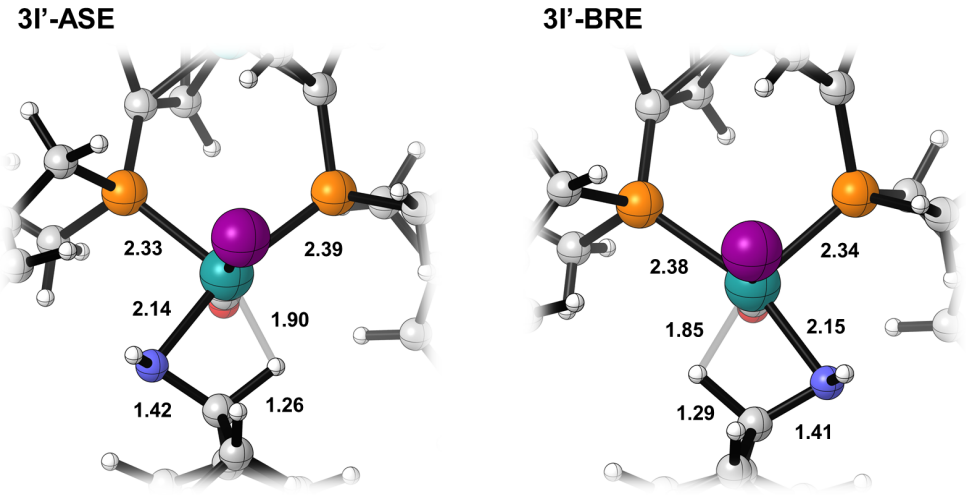

Figure 4.23: Inner structure of agostic amide complexes **3I'-ASE** and **3I'-BRE**. Bond distances are given in Å.

As previously mentioned, these are relatively unstable intermediates that will rearrange to the more stable trigonal bipyramidal amide complexes **3I**, with loss of the agostic CH-Ru interaction. This introduces a new conformational degree of freedom, since the double bond is lost and the new C-N bond may rotate freely, also *E*/*Z* isomerism does not exist anymore. For the trigonal bipyramidal amides the differentiation between **A**/**B** is also lost, since the geometry has no left/right coordination on the complex with a vacant site, but the amide is coordinating in the middle between the former two positions. Hence, we use the following nomeclature:

3I-<*Enantiomer*><*NH Orientation*><*Conformer*>

This way, all isomers/conformers may be systematically described. "NH Orientation" is described by the ligand that the NH group is pointing toward (**I** or **CO**), and "Conformer" indicates which substituent on the amide (hydrogen, methyl or phenyl) is *anti* to the amide hydrogen with respect to the C-N bond (e.g. **H**, **Me** or **Ph**). As an example, **3I-RCOMe** refers to the trigonal bipyramidal amide complex with iodide as a halide in which the amide is the *R* enantiomer, has the NH group pointing toward the carbonyl ligand on ruthenium, and the methyl group is *anti* to the amide hydrogen. While the **3I'** complexes technically also only have a C-N single bond, the old nomenclature may be used for them, since the agostic interaction determines the position of the amide and its substituents just like in the η^2 complexes and the hydride transfer transition states. We may now have a look at which trigonal bipyramidal complexes are formed.

Table 4.5 shows the energies of the different possible trigonal bipyramidal amide complexes. Some do not exist as they immediately rotate into one of the other isomer/conformer com-

Table 4.5: Energies of the trigonal bipyramidal amide complexes **3I**. Energies are free enthalpies in kJ/mol.

Trigonal bipyramidal amide complexes [kJ/mol]			
Conformer	H	Me	Ph
RCO	64.3	95.9	82.6
RI	45.4	50.9	-
SCO	62.8	-	-
SI	48.4	48.1	-

binations (**3I-RIPh** → **3I-RIH**, **3I-SCOMe** → **3I-SCOH**, **3I-SCOPh** → **3I-SCOH** and **3I-SIPh** → **3I-SIH**). For the others, two things can be noticed: They are considerably more stable than the agostic amides, by up to 25.8 kJ·mol^{-1}, when comparing the most stable agostic amide (**3I'-BRE**) and trigonal bipyramidal amide (**3I-RIH**). Also, within one set of enantiomer and NH orientation, the energy differences for different conformers can be quite large (31.6 kJ·mol^{-1} for **3I-RCOH** vs. **3I-RCOMe**). This will be important for the proton transfer, since the amide now has a higher steric demand compared to the previously planar imine, increasing energetic differentiation with respect to the chiral ligand. It is also found that the amide complexes where NH is pointing toward the iodide ligand are again more stable, in line with our previous observations. More important for now is that the hydride transfer is still endergonic with respect to the initial η^1 imine complex (by at least 45.4 kJ·mol^{-1}, **3I-RIH**) and that the hydride transfer is reversible. With a reverse barrier of only 24.8 kJ·mol^{-1} for the *R* enantiomer (**3I-RIH** via **TSHI-BRE**) and 23.4 kJ·mol^{-1} (**3I-SIMe** via **TSHI-ASE**), racemization is still possible and the trigonal bipyramidal amides are only short-lived intermediates. Figure 4.24 shows the structures of the lowest two isomers/conformers for the *R* and *S* enantiomers, **3I-RIH** and **3I-SIMe**. The two complexes are almost identical, and the exchange of hydrogen and methyl group seems to be the only difference, which also sets the different chirality on each amide. Ru-N amide bond distances are 1.95 Å (*R*) and 1.96 Å (*S*). The trigonal bipyramidal arrangement of the amide and the chelating diphosphine can be seen very well. Another interesting feature is the orientation of the phenyl group. In both complexes, the phenyl group on the ligand is engaging in a π-π interaction with the naphtyl group on the (*S*,*S*)-*f*-binaphane ligand in the T-shaped motif. The angle is tilted and the distance is a little larger (~5.9 Å for *R*, ~6.1 Å for *S*) than in the typical T-shaped benzene dimer (~4.9 Å),[185] but the alignment of the phenyl group is clearly visible. As with the many other interactions that play a role, this one is also small, but might add up in combination. For the benzene dimer, Jaffe and Smith calculated the interaction to be stabilizing by about 12 kJ·mol^{-1} at the MP2/6-311G(2*d*,2*p*) level. Finally, it can be seen that the **A**/**B** distinction is lost in this step, as the trigonal bipyramidal amide has no clear preference – both N-Ru-P angles are more or less

identical (130.2°/132.5° in **3I-RIH**, and 126.6°/135.1° for **3I-SIMe**). The latter may seem to exhibit a preference, but it is still far from the hexacoordinate complexes with clear **A**/**B** isomers (where for example the H-Ru-P or N-Ru-P angles are around 80° and 90°).

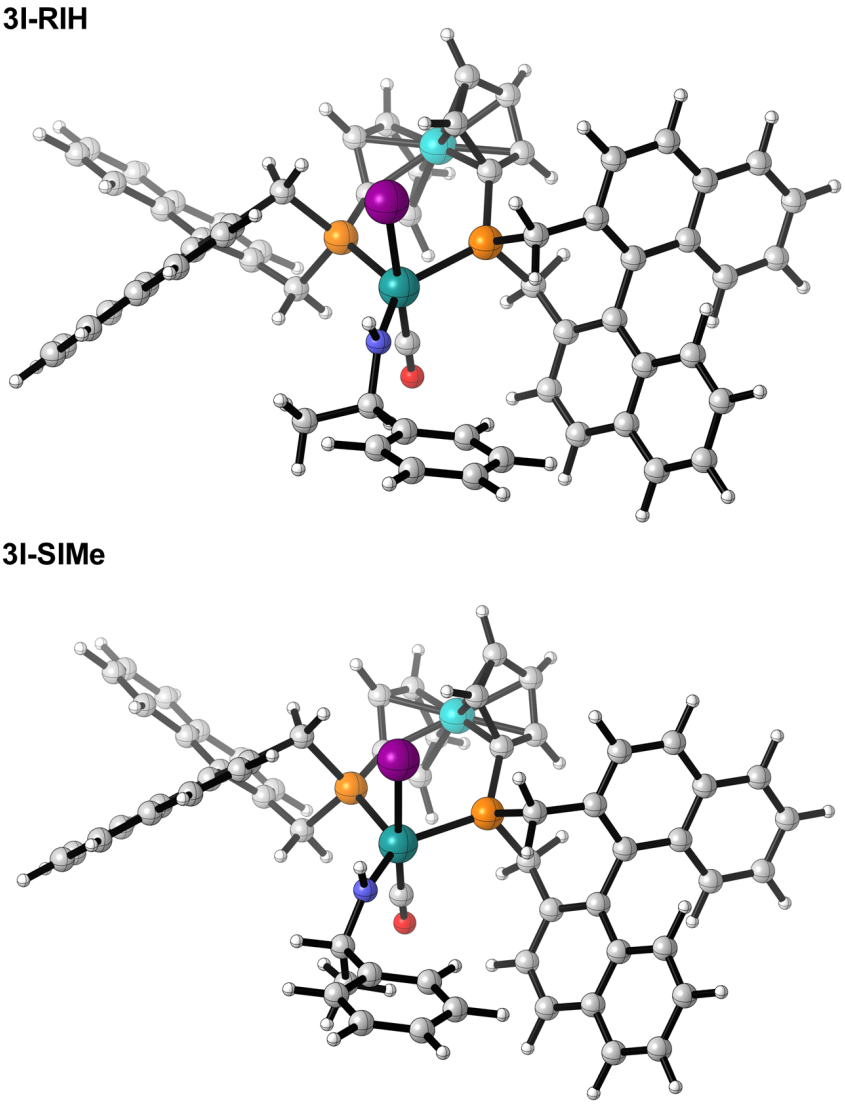

Figure 4.24: Structure of the energetically lowest trigonal bipyramidal amides for enantiomers *R* and *S* (**3I-RIH** and **3I-SIMe**). The complexes are structurally very similar, with hydrogen and methyl group exchanged on the amide for both complexes. The phenyl group forms a long-distance T-shaped π-π interaction with the naphthyl group in both complexes.

4.3.8 Coordination of Molecular Hydrogen

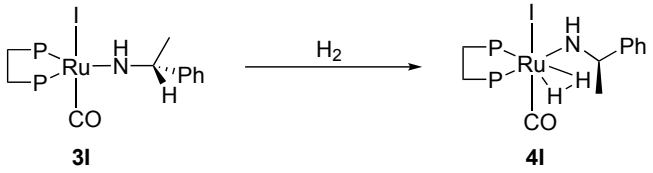

3I **4I**

Figure 4.25: Addition of molecular hydrogen to the trigonal bipyramidal amides **3I** to form the σ-dihydrogen complexes **4I**.

In our mechanism, the next step is now coordination of molecular hydrogen to form the corresponding σ-dihydrogen complexes which allow for proton transfer to finally liberate the amine. Coordination of H_2 again creates a hexacoordinate octahedral complex and restores the **A**/**B**-type isomerism. Since addition may occur from both sides to form either the **A** or **B** complex, this marks another point for isomerization between the two types, together with isomerization prior to coordination of the imine in the beginning. This means, that the hydride transfer could potentially occur through a complex of type **A**, but then be followed by proton transfer by a complex of type **B**. When we studied the coordination of H_2 to the ruthenium hydrido complex, it was already observed that the coordination of dihydrogen was much more endergonic compared to the other species (imine, ammonia, etc.). We find the same for this step, where addition of H_2 is endergonic relative to the trigonal bipyramidal amide complexes. The nomenclature for complexes is slightly adapted to include the two types **A**/**B** again:

4I-<*Complex Type*><*Enantiomer*><*NH Orientation*><*Conformer*>

So **4I-ARIH**, for example, would be the σ-dihydrogen complex with iodide as the halide, of complex type **A** (where H_2 is coordinating on the right side of the complex), with the amide being in *R* configuration, having the NH pointing toward the halide and hydrogen *anti* to the amide hydrogen. This way, up to 24 isomers/conformers can potentially be formed. The energies for the σ-dihydrogen complexes are given in Table 4.6. For some structures no corresponding σ-dihydrogen seems to exist, as the amide will undergo a conformational change to accomodate the new ligand on the complex (**4I-ARCOPh**, **4I-ASIH** and **4I-BRCOMe**). Most complexes, however, could be located. Energies for the coordination of dihydrogen range from 67.9 to 110.1 kJ·mol^{-1}, meaning that the formation of σ-dihydrogen complexes is at least endergonic by 22.5 kJ·mol^{-1} for *R* and 27.7 kJ·mol^{-1} for *S*. Unsurprisingly, the complexes with the NH orientation to iodide, so that a favorable NH-I hydrogen bond is kept, are mostly lower in energy than the NH-CO complexes. They therefore also include the energetically most stable complexes for *R*/*S*, **4I-ARIH** (67.9 kJ·mol^{-1}) and **4I-ASIPh** (75.8 kJ·mol^{-1}).

We will only exemplarily discuss the complexes **4I-ARIPh** and **4I-BSIH**, because these are the precursors to the lowest proton transfer transition states to *R*/*S* as we will see in the next section. The structures of **4I-ARIPh** and **4I-BSIH** are given in Figure 4.26. If we dismiss the ligands chirality, the two complexes with their arrangement of ligands are almost mirror images of each other, which makes them suitable for comparison. **4I-ARIPh** has the amide hydrogen in the hemisphere of the iodide ligand, but in contrast to the **4I-BSIH**, the N-H bond is not aligned with Ru-I as was usually observed before for the NH-I interaction. Instead, the amide hydrogen points towards the naphthyl group and is hence stabilized by the NH-π interaction. The same arrangement is not realizable for **4I-BSIH**, as the orientation of the naphthyl group is different on the right side of the complex due to its chirality. The rotation of NH from iodide toward the naphthyl group in **4I-ARIPh** is likely in anticipation of the incoming proton from H_2. This is supported by the fact that the N-H_2 distance is lower for **4I-ARIPh** (2.32 Å) than for **4I-BSIH** (2.46 Å), so that the former is already closer to the following proton transfer transition state. This is also in line with the Ru-H_2 distance being longer for **4I-ARIPh** with 1.85 Å than in the *S* complex (1.79 Å), accompanied by a shorter Ru-P bond *trans* to the σ-dihydrogen ligand (2.36 Å vs. 2.40 Å). The longer Ru-P bond in both cases is, of course, the phosphine *trans* to the amide ligand (2.44 Å for *R* and 2.43 Å in the *S* complex), which is expected and has been seen before for the strong σ-donor ligands.

Table 4.6: Energies of the σ-dihydrogen complexes **4I**. Energies are free enthalpies in kJ/mol.

σ-Dihydrogen complexes [kJ/mol]						
NH orientation	CO			I		
Conformer	H	Me	Ph	H	Me	Ph
AR	99.6	110.1	-	67.9	84.3	78.1
AS	84.9	102.9	107.1	-	89.5	75.8
BR	81.8	-	94.8	92.5	98.3	92.5
BS	88.6	104.9	90.7	76.0	87.9	-

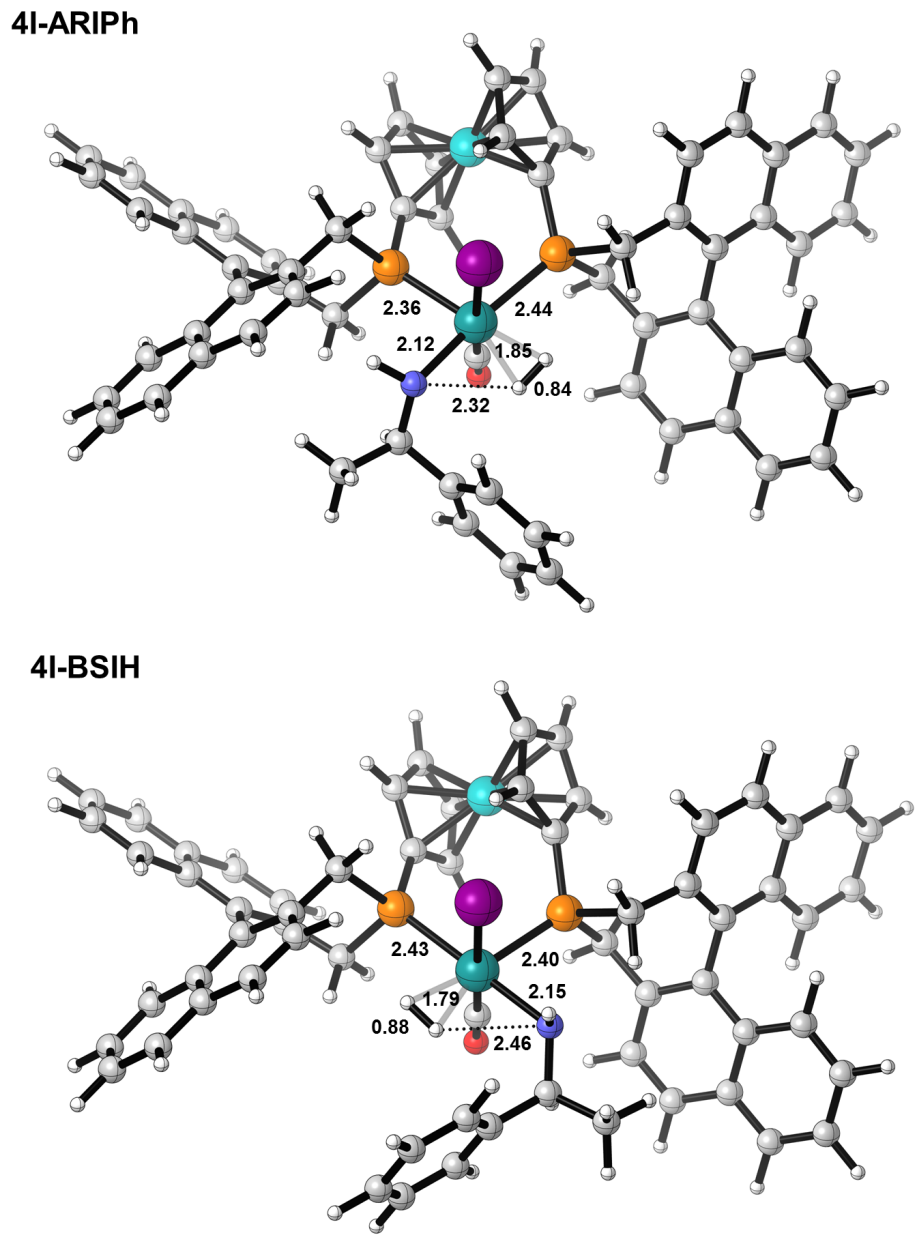

Figure 4.26: Structures of **4I-ARIPh** and **4I-BSIH**, which are the preceding complexes to the lowest proton transfer transition states for *R* and *S*. Selected distances in Å.

4.3.9 Proton Transfer

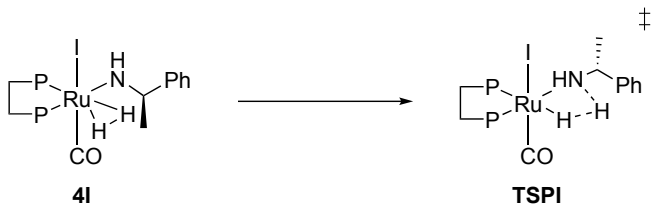

Figure 4.27: Proton transfer transition states **TSPI**, following the σ-dihydrogen complexes **4I**.

The σ-dihydrogen complexes **4I** can finally undergo heterolytic cleavage to protonate the amide and restore the hydride via the proton transfer transition states **TSPI**. Of the 24 possible combinations for the proton transfer, not all transition states exist, since some would require very unfavorable orientation of the substituents on the amide (e.g. phenyl group pointing into the naphthyl wings of the ligand), whereas others just seem to have no barrier for rotation into one of the other isomer/conformer combinations. The barriers for the proton transfer transition states in Table 4.7 clearly indicate that this is the rate-determining step as even the lowest barrier ($93.2\,\mathrm{kJ{\cdot}mol^{-1}}$, via **TSPI-ARIPh**) is higher in energy than that of the corresponding hydride transfer ($70.2\,\mathrm{kJ{\cdot}mol^{-1}}$, via **TSHI-BRE**). Since hydride transfer is reversible for all intermediate species between **TSHI** and **TSPI**, and proton transfer is rate-determining, enantiodiscrimination is occuring in this very step. Whether enantioselectivity is correctly predicted by our mechanism is of high relevance for a successful description of the catalysis. The predicted enantiomeric excess may be calculated from the barriers in Table 4.7. Either by only comparing the lowest two transition states leading to *R* and *S*

$$ee = \frac{1 - e^{-\frac{\Delta\Delta G^{\ddagger}}{RT}}}{1 + e^{-\frac{\Delta\Delta G^{\ddagger}}{RT}}} \quad \text{with} \quad \Delta\Delta G^{\ddagger} = \Delta G^{\ddagger}_{R} - \Delta G^{\ddagger}_{S} \tag{4.2}$$

which is commonly used in the literature, or by Boltzmann-averaging over all *R* and *S* transition states:

$$ee = \frac{\sum_i e^{-\frac{\Delta G^{\ddagger}_{R,i}}{RT}} - \sum_j e^{-\frac{\Delta G^{\ddagger}_{S,j}}{RT}}}{\sum_i e^{-\frac{\Delta G^{\ddagger}_{R,i}}{RT}} + \sum_j e^{-\frac{\Delta G^{\ddagger}_{S,j}}{RT}}} \tag{4.3}$$

Experimentally, the (*S*,*S*)-*f*-binaphane ruthenium system achieved an enantiomeric excess of 84% of the *R* enantiomer for the direct asymmetric reductive amination of acetophenone. Comparing only the lowest two *R*/*S* transition states, we computationally predict an enantiomeric excess of 77% for the *R* enantiomer, which is both qualitatively and magnitude-wise

very close to the experimental value, especially considering limitations in computational accuracy and the general difficulty of predicting enantiomeric excesses in the 0-90% range, where $\Delta\Delta G^{\ddagger}$ is < 5.7 kJ·mol^{-1}. Computing the ee from Boltzmann-averaging over all transition states gives a very similar, albeit slightly lower estimate of 67%ee, which is still very close to the experimental value.

Table 4.7: Barriers for the proton transfers from H_2 to the amide to form the final amine and restore the initial hydride complex. Energies are free enthalpies in kJ/mol.

Proton transfer transition states [kJ/mol]						
NH orientation	CO			I		
Conformer	H	Me	Ph	H	Me	Ph
AR	117.5	148.0	-	97.0	-	93.2
AS	113.2	-	161.3	100.6	121.0	-
BR	110.0	-	108.0	104.2	122.8	127.2
BS	111.9	141.3	-	98.3	110.8	100.0

A look at the relative Boltzmann weights in Table 4.8 shows that many TS have almost no contribution (< 0.001), but several have weights of > 0.01. By weight, the population of any species relative to the energetically lowest species is meant, which in this case is **TSPI-ARIPh**. Initially guessing which of all these transition states might be relevant or energetically preferred (or may be the lowest leading to *R* and *S* enantiomers) just from structural considerations or intuition is almost impossible, and only a thorough analysis of all pathways results in accurate description of the reaction's enantioselectivity. This was realized when initially only a subset of these transition states were investigated less systematically and first predictions of enantioselectivity were far off from the experimental values. This catalysis therefore seems to be a case where an in-depth analysis of substrate conformers is really needed to get both qualitatively and quantitatively correct results. Contrary to, for example, the quadrant model[186] which has been widely used to explain enantioselectivity in asymmetric hydrogenations.[187–191] In our case, quadrants would not only be hard to define for the catalyst, but since the enantioselectivity is not dependent on the step of η^2 coordination of the double bond that is hydrogenated, even when we had defined quadrants, the model would not be applicable. Investigating the results in more detail, we again find that the NH-I interaction, or atleast complex geometries where the amide hydrogen faces the halide, is dominant. The six most energetically viable transition states are of this geometry (**TSPI-ARIPh**, **TSPI-ARIH**, **TSPI-BSIH**, **TSPI-BSIPh**, **TSPI-ASIH**, and **TSPI-BRIH**, see Table 4.7). Furthermore, the energetically lowest complex with NH facing the carbonyl group is **TSPI-BRCOPh**, which is 14.8 kJ·mol^{-1} higher than the overall lowest proton transfer TS, resulting in only ~ 0.2% of product formation through this pathway (table 4.9). The sum of all transition states with the

NH orientation toward CO is still less than < 1%, which makes their overall contribution to enantioselectivity negligible. Within the NH-I variants for the proton transfer, the picture is more diverse with several complexes having contributions to the final product outcome of > 1%. Clearly the dominant pathways are through **TSPI-ARIPh** and **TSPI-ARIH** accounting for 67.8% and 14.6% of product formation directed towards the *R* enantiomer. On the other hand, **TSPI-BSIH** and **TSPI-BSIPh** are the transition states that are mostly responsible for the formation of the *S* enantiomer, with shares of 8.7% and 4.4% in the overall chiral amine formation. When comparing the two complex types **A** and **B**, we see that they do not equally contribute to the enantioselectivity. Rather, complex type **A** favors formation of the *R* enantiomer, while complex type **B** drives formation of the *S* enantiomer, but is slightly less active, resulting in the enantiodescrimination toward *R*.

Table 4.8: Relative Boltzmann weights of the **TSPI** proton transfer transition states, with the lowest proton transfer via **TSPI-ARIPh** as reference (= 1).

Relative Boltzmann Weights of **TSPI** structures						
NH orientation	CO			I		
Conformer	H	Me	Ph	H	Me	Ph
AR	< 0.001	< 0.001	-	0.216	-	**1**
AS	< 0.001	-	< 0.001	0.051	< 0.001	-
BR	0.001	-	0.003	0.012	< 0.001	< 0.001
BS	0.001	< 0.001	-	0.128	0.001	0.064

Table 4.9: Normalized contribution of the **TSPI** proton transfer transition states, with the sum of all pathways equal to 1.

Normalized contribution of **TSPI** structures [%]						
NH orientation	CO			I		
Conformer	H	Me	Ph	H	Me	Ph
AR	< 0.1	< 0.1	-	14.6	-	67.8
AS	< 0.1	-	< 0.1	3.4	< 0.1	-
BR	< 0.1	-	0.2	0.8	< 0.1	< 0.1
BS	< 0.1	< 0.1	-	8.7	0.1	4.4

A discussion of all transition states would be too extensive, especially since many of them have only very minor contribution to the enantioselectivity. We will take a more in-depth look at the four just mentioned transition states which are the most important TS for the observed enantioselectivity. The structures are shown in Figure 4.28 (*R*) and 4.29 (*S*). All four structures share some similarities. The **AR** and **BS** complexes are mirror images of each other except for the respective neighboring binaphthyl "wing", since those are chiral on the ligand.

Also the arrangement for the **H**/**Ph** complexes is quite similar even though different groups are *anti* to the amide hydrogen. The reason is, that it is rather the orientation of the amide hydrogen that changes than the orientation of the substituents on the amide (with the rest of the catalyst as reference). If we now go back to the fact that the two sides of the complex have different chiral environments, this shows how discrimination between the two enantiomers takes place: in case of **TSPI-ARIPh**, the phenyl-*anti* conformer is favored over **TSPI-ARIH** as the former is stabilized through a NH-π interaction with the naphthyl group. On the other side of the complex, the methylene group is facing the NH moiety, which reverses the energetic order. **TSPI-BSIPh** is now less stable than **TSPI-BSIH**, since no attractive π-interaction is possible and the short NH-CH distance (2.28 Å) is likely repulsive. Otherwise, when we compare the complexes without tilting of the N-H bond (**TSPI-ARIH** and **TSPI-BSIH**) these are mirror images with very similar energies ($\Delta\Delta G^{\ddagger}$ = 1.3 kJ·mol^{-1}), which would not result in significant enantioselectivity (ee ~ 25%). The inner structural parameters of the transition states differ between the two conformer types, but are very similar for the "mirror"-TS of each enantiomer (**TSPI-ARIH**/**TSPI-BSIH** and **TSPI-ARIPh**/**TSPI-BSIPh**). In all TS, judging from the Ru-P bond length *trans* to either the forming hydride or amide that is being protonated, the negative charge is relatively evenly distributed as the difference in *trans* effect between hydride/amide is low. There seems to be, however, a qualitative difference: in **TSPI-ARIH**/**TSPI-BSIH**, the phosphine *trans* to the amide has a shorter bond (2.38 Å/2.37 Å vs. 2.40 Å/2.40 Å), suggesting that the TS are closer to the product side of hydride and amine than dihydrogen and amide. In line with this trend are the longer H-H distance in dihydrogen (0.98 Å) and shorter N-H distance for the incoming proton (1.70 Å). For transition states **TSPI-ARIPh** and **TSPI-BSIPh**, the tendency is the opposite. Ru-P bonds are longer for the amide being *trans*, the H-H dihydrogen distance is shorter (0.88 Å/0.90 Å, close to the H-H distance in the σ-dihydrogen complexes **4I**) and the N-H distance is longer. Overall these are relatively small and fine details; structurally all TS resemble each other which is represented in the small energy differences.

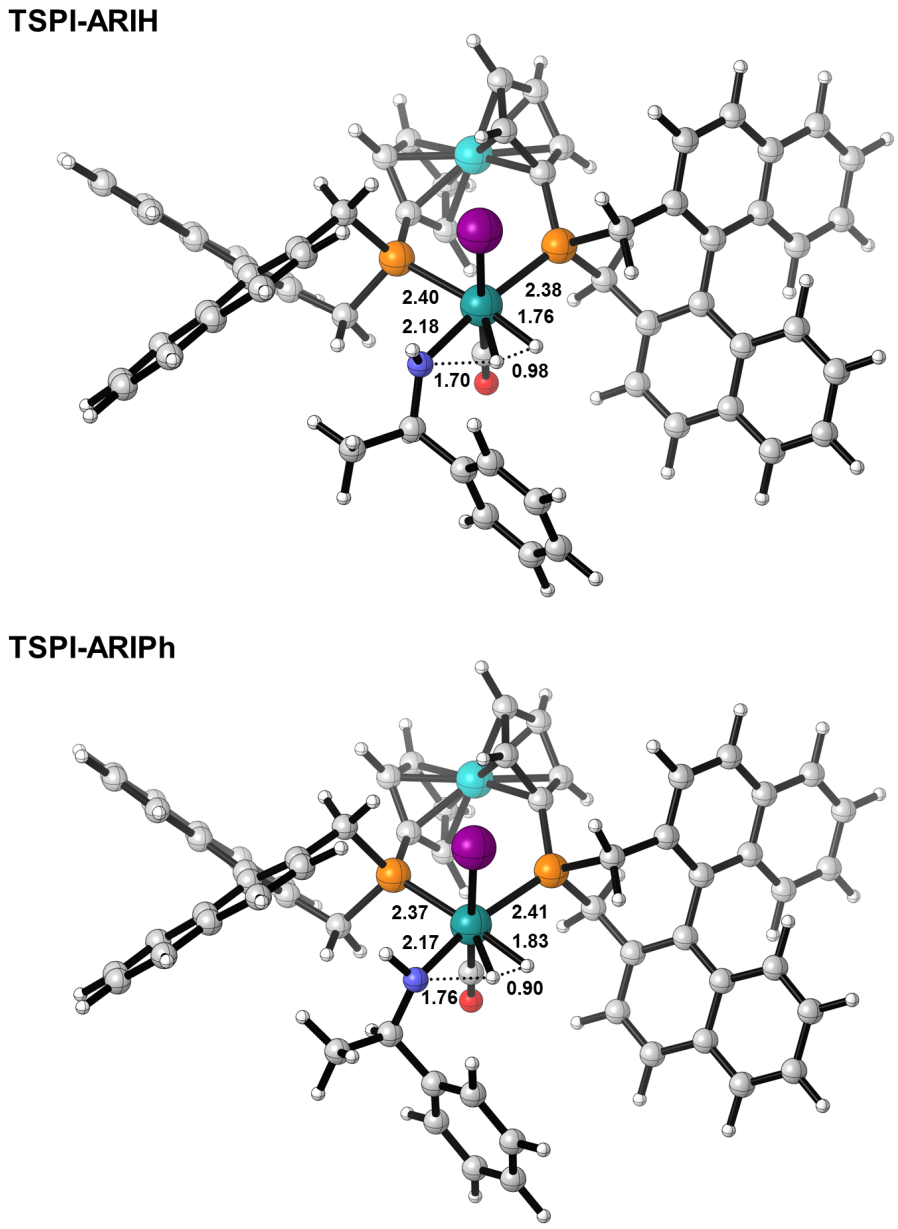

Figure 4.28: Proton transfer transition states **TSPI-ARIH** and **TSPI-ARIPh**, the lowest two transition states which lead to formation of the *R* amine.

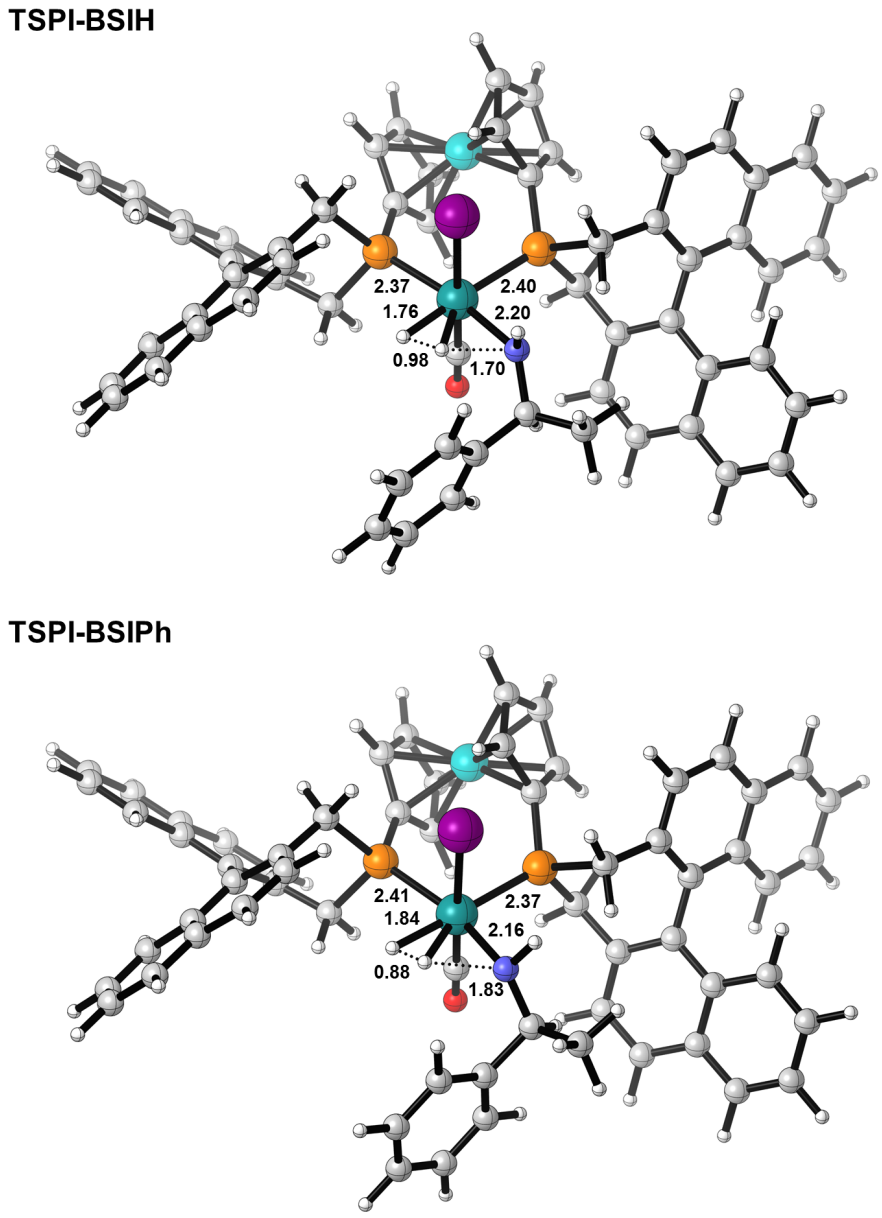

Figure 4.29: Proton transfer transition states **TSPI-BSIH** and **TSPI-BSIPh**, the lowest two transition states which lead to formation of the *S* amine.

4.3.10 Release of Amine

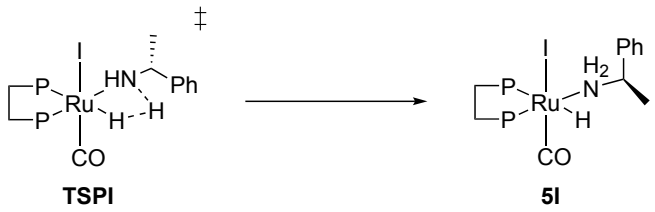

Figure 4.30: Final formation of the chiral amine **5I** on the ruthenium catalyst after proton transfer from H_2 via **TSPI**.

Finally, upon proton transfer to the amide, the chiral amine is formed and the initial hydride is restored. Only the amine hydrido complexes for the combinations **A**/**B** and *R*/*S* following the respective lowest proton transfer transition states were calculated. While the amine also has different conformational arrangements, this is of less relevance since they do not play any further role in the course of the reaction. This is also the most important information: protonation of the amide to liberate the amine is irreversible. Formation of the amino hydrido complexes is exergonic by 54.5 to 62.2 kJ·mol^{-1} with respect to the initial η^1 imine complex **1I-ARZ**, and the lowest reverse barriers are therefore 155.4 kJ·mol^{-1} for the *R* enantiomer and 152.8 kJ·mol^{-1} for the *S* enantiomer. These are too high in energy to be feasible, making the reaction irreversible. Not only does this then definitely determine proton transfer as the finally enantioselectivity determining step, but it also means that the catalyst does not racemize any already formed chiral amine. Figure 4.31 shows the two final amine complexes **5I-AR** and **5I-BS** (since *R* is mostly formed through the corresponding **A** complexes, and *S* via type **B**).

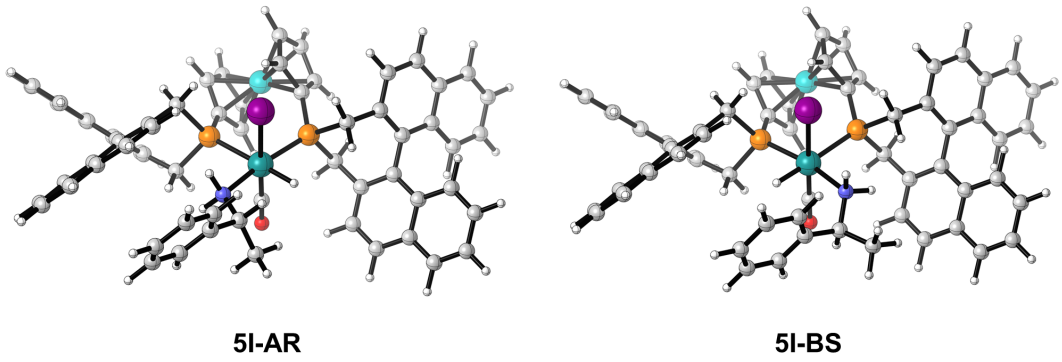

Figure 4.31: Final formation of the chiral amine **5I** on the ruthenium catalyst after proton transfer from H_2 via **TSPI**.

To complete the catalytic cycle, the amine must decoordinate and exchange with an imine molecule to form the η^1 imine complex that the catalyst initially started with. This is very well

feasible, and the imine is in fact a slightly better ligand than the amine, making the exchange of product and substrate thermodynamically favored by 3.3 kJ·mol^{-1} and 5.8 kJ·mol^{-1} (*R* and *S*).

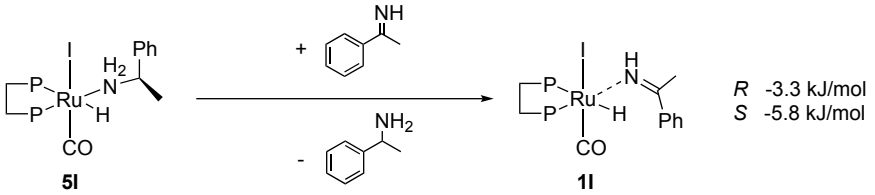

Figure 4.32: Exchange of amine with imine to continue asymmetric reductive amination. Energies are free enthalpies in kJ/mol, and relative to the corresponding *R*/*S* amine complex.

4.3.11 Mechanistic Summary

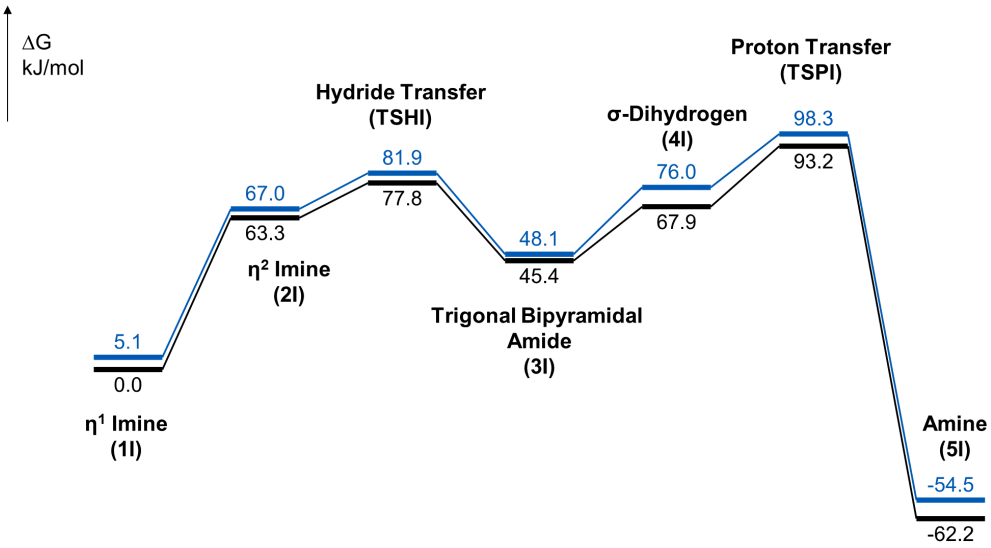

Figure 4.33: Summary of the asymmetric hydrogenation. Only the lowest paths leading to formation of *R* (black) and *S* (blue) enantiomers of 1-phenylethylamine are shown. Energies are free enthalpies in kJ/mol. The most stable η^1 complex serves as reference (**1I-ARZ**). The formation of the *R* enantiomer mostly proceeds through the complex type **A**, whereas the *S* enantiomer is formed by type **B** complexes.

The mechanism of the asymmetric hydrogenation will be briefly summed up. The Gibbs free energy profile of the reaction pathway is shown in Figure 4.33, with the *R* pathway in black and *S* pathway in blue. Only the lowest isomer/conformers for each step in the reaction are shown for better clarity. Initial formation of imine is endergonic by 17.6 kJ·mol^{-1}. Catalysis starts through coordination of the imine substrate to the catalyst, giving the η^1 imine complexes **1I**. The lowest complex, **1I-ARZ** will serve as energetic reference throughout the mechanism. From the η^1 imine complex, rearrangement into the η^2 coordination with π-coordination of the C-N double bond to ruthenium is necessary for hydride transfer. The η^2 complexes are endergonic by 63.3 kJ·mol^{-1} for *R* and 67.0 kJ·mol^{-1} for *S*. Hydride transfer follows through **TSHI-ARZ** and **TSHI-BSZ** with barriers of 77.8 kJ·mol^{-1} and 81.9 kJ·mol^{-1}, to give agostic amides that will rearrange into the more stable trigonal bipyramidal amides **3I**. Up to this point, configuration of the double bond, *R* and *S* face and complex types **A**/**B** allow for different combinations, but especially the orientation of the N-H bond toward the halide is favored due to a hydrogen bond type stabilization. The formation of trigonal bipyramidal complexes **3I-RIH** and **3I-SIH** is still endergonic by 45.4 kJ·mol^{-1} and 48.4 kJ·mol^{-1} making the hydride transfer potentially reversible with only a small barrier of ~ 24 kJ·mol^{-1}. Hydrogen can coordinate to the pentacoordinate trigonal bipyramidal amide complexes and

restores the octahedral geometry. Now, up to 24 isomer/conformer combination potentially exist. In any case, coordination of H_2 to form the σ-dihydrogen complexes is endergonic by 22.5 kJ·mol^{-1} and 27.9 kJ·mol^{-1} to form the complexes **4I-ARIH** and **4I-BSIH**. These can finally undergo heterolytic cleavage of the H-H bond to protonate the amide and form a hydride ligand via the proton transfer transition states **TSPI-ARIPh** and **TSPI-BSIH** (as the lowest TS for *R* and *S*). With an overall barrier of at least 93.2 kJ·mol^{-1} for the *R* enantiomer and 98.3 kJ·mol^{-1} for the *S* enantiomer, this step is rate-determining. The formation of the amine (**5I**) from the **TSPI** transition states is now very exergonic 155.4 kJ·mol^{-1}/152.8 kJ·mol^{-1} for *R*/*S* rendering this step irreversible. Proton transfer therefore determines the overall enantioselectivity. The predicted enantiomeric excess is 67-77% for *R*, which is very close to the experimental value of 84%. This, and the energetical feasibility of the mechanism, support the mechanistic proposal. Finally, decoordination of amine and coordination of new substrate (imine in η^1 coordination) is thermodynamically possible and favored by a small margin of 3.3 kJ·mol^{-1}/5.8 kJ·mol^{-1}, closing the catalytic cycle.

The energy differences between the pathways are governed by many different and small contributions, depending on the orientation of the substrate and the chiral features of the ligand, which ultimately lead to enantioselectivity in the observed way. The fact that so many arrangements and orientations, isomers and conformers are ultimately involved, shows that a detailed and systematic look at this is necessary to finally give a correct prediction of the enantioselectivity in which very minor energy differences are of high importance.

4.3.12 Enantioselectivity in the Halide Series

As mentioned in the very beginning of the chapter, good enantioselectivities were obtained with iodide on the ruthenium catalyst. This behavior was further examined experimentally by varying the type of ammonium halide under otherwise exactly the same conditions as the "regular" direct asymmetric reductive amination. The results are shown in Figure 4.34. The best enantioselectivity was obtained with iodide as the halide (ee 84%), and a drop in ee is observed when going to smaller halides (77% for bromide, 74% for chloride) until fluoride gives the lowest enantioselectivity in the series (41%ee).

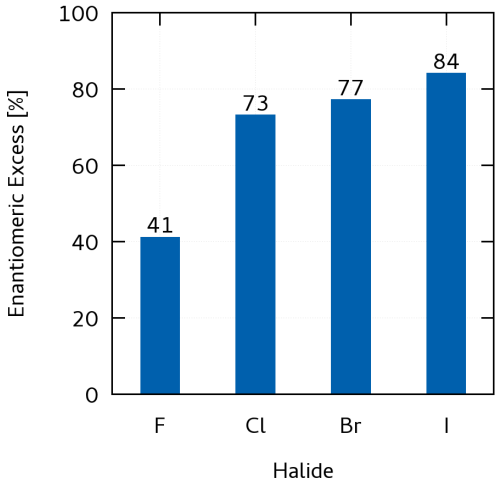

Figure 4.34: Observed enantioselectivity for different halides. 100 mol% of NH_4X were added to the standard asymmetric reductive amination protocol under the same conditions. Within the halide series, enantioselectivity increases when going down the periodic table. The amination with fluoride shows a particularly low enantioselectivity.

This "halide effect" has been previously reported on in the literature with varying magnitude. One of the first examples (in asymmetric hydrogenation) is again the synthesis of (*S*)-metolachlor by Blaser et al., who discovered that addition of tetrabutyl ammonium iodide to the iridium catalyst would increase the ee to from 58% to 70%.[192] Kutney and coworkers reported a similar increase in enantioselectivity for the Rh-catalyzed asymmetric hydrogenation of imines when addition of potassium bromide to the chloride-containing rhodium catalyst (precursor: $[Rh(NBD)Cl]_2$) would increase the ee from 60% to 72%, with a further increase to 91% when KBr was substituted by KI.[193] An extensive review of the halide effect in transition metal catalysis, including enantioselective effects, has been published by Fagnou and Lautens.[194]

Table 4.10: Barriers for the hydride transfer to the imine, with bromide in the apical position of the catalyst. Energies are free enthalpies in kJ/mol.

Hydride transfer – Bromide [kJ/mol]		
Complex	*E*	*Z*
AR	90.7	74.6
AS	65.5	94.7
BR	67.9	82.4
BS	84.3	81.5

Table 4.11: Barriers for the hydride transfer to the imine, with chloride in the apical position of the catalyst. Energies are free enthalpies in kJ/mol.

Hydride Transfer – Chloride [kJ/mol]		
Complex	*E*	*Z*
AR	86.3	70.8
AS	59.6	90.5
BR	52.8	75.3
BS	79.5	77.0

Table 4.12: Barriers for the hydride transfer to the imine, with fluoride in the apical position of the catalyst. Energies are free enthalpies in kJ/mol.

Hydride Transfer – Fluoride [kJ/mol]		
Complex	*E*	*Z*
AR	77.8	63.4
AS	55.2	81.2
BR	58.0	71.2
BS	74.9	73.7

To check whether our computationally investigated mechanism reproduces this trend correctly, the full mechanism was recalculated for the three other halides (F, Cl, Br) in the apical position of the catalyst. Rather than a lengthy discussion about all steps in the reaction mechanism for all of the halides, we will discuss the hydride transfer and proton transfer transition states, which are the critical points in the reaction pathway. The relative order of the other intermediates stayed the same and is therefore of minor interest, they were nevertheless calculated to assure that any potentially unusual behavior for any of the halides may be captured in our investigation. Hence we will start with the hydride transfer transition states which are given in Tables 4.10, 4.11 and 4.12. For comparison with the calculations where iodide is coordinating to the catalyst, the same energetic reference was chosen (the energetically lowest

respective η^1 imine complex, which were: **1Br-BSZ**, **1Cl-ARZ** and **1F-BSZ**). The relative energetic order is very similar for all halides, with the **ASE** and **BRZ** being the lowest transition states to *R* and *S* in all cases, as was already found for the iodide catalyst. The lowest barrier to hydride transfer is lower for the smaller halides – for the iodide-containing catalyst that barrier was 70.2 kJ·mol^{-1}, for Br the lowest TS has a barrier of 65.5 kJ·mol^{-1} and Cl and F have even lower barriers (52.8 kJ·mol^{-1} and 55.2 kJ·mol^{-1}). This is of less relevance as the hydride transfer is not rate-determining for any of the halides, which will be shown when we have a look at the proton transfer transition states. In the iodide pathway, these were the relevant transition states to determine the final enantioselectivity and the same is true for the other halides.

Table 4.13: Barriers for the proton transfers with bromide in the apical position of the catalyst. Energies are free enthalpies in kJ/mol.

Proton transfer – Bromide [kJ/mol]						
NH orientation	CO			Br		
Complex	H	Me	Ph	H	Me	Ph
AR	116.3	142.3	153.5	95.9	-	92.7
AS	111.4	-	-	98.4	118.3	-
BR	107.1	-	103.2	103.9	120.4	126.8
BS	107.9	131.9	-	96.5	108.9	97.4

Table 4.14: Barriers for the proton transfers with chloride in the apical position of the catalyst. Energies are free enthalpies in kJ/mol.

Proton transfer – Chloride [kJ/mol]						
NH orientation	CO			Cl		
Complex	H	Me	Ph	H	Me	Ph
AR	114.4	138.0	-	93.3	-	89.8
AS	107.5	130.9	-	95.4	114.3	-
BR	101.3	-	96.9	-	115.3	121.3
BS	104.8	127.1	-	93.2	104.5	93.3

Table 4.15: Barriers for the proton transfers with fluoride in the apical position of the catalyst. Energies are free enthalpies in kJ/mol.

Proton transfer – Fluoride [kJ/mol]						
NH orientation	CO			F		
Complex	H	Me	Ph	H	Me	Ph
AR	111.9	134.3	145.9	95.5	-	90.5
AS	109.6	-	-	94.7	110.0	96.0
BR	97.7	-	93.2	99.8	109.0	114.5
BS	100.4	120.9	-	93.4	101.5	91.6

Tables 4.13, 4.14 and 4.15 show the energies for all isomer/conformer combinations in the proton transfer of the different halides. Several trends are visible: With X being the respective halide, the **ARXPh** and **BSXH** transition states are the lowest pathways to *R* and *S*, except for fluoride, where **TSPF-BSFPh** is slightly lower in energy than **TSPF-BSFH** ($91.6\,\mathrm{kJ{\cdot}mol^{-1}}$ vs. $93.4\,\mathrm{kJ{\cdot}mol^{-1}}$). The strong discrimination between transition states with NH orientation towards halide X and those pointing toward the carbonyl ligand also fades with the smaller halides – for I the difference between the lowest **I**/**CO** isomers had been $14.8\,\mathrm{kJ{\cdot}mol^{-1}}$, but for bromide that decreases to $10.5\,\mathrm{kJ{\cdot}mol^{-1}}$, and even more so for chloride ($7.1\,\mathrm{kJ{\cdot}mol^{-1}}$) and fluoride ($2.7\,\mathrm{kJ{\cdot}mol^{-1}}$). In the latter two cases, especially for fluoride, the **CO**-type transition states therefore have non-negligible contribution to the overall enantioselectivity, which is different from the iodide catalyst. Complex types **A**/**B** keep different preferences for the enantiomers, with **A** predominantly producing the *R* enantiomer and **B** preferring the *S* enantiomer. The most interesting aspect is of course the prediction of enantioselectivity, and a comparison of computed and experimental enantiomeric excess is shown in Figure 4.35.

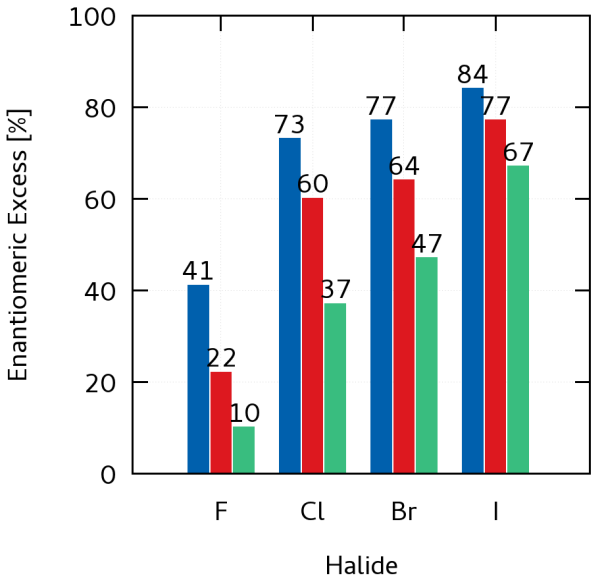

Figure 4.35: Comparison of experimentally observed enantiomeric excess (blue) and computationally predicted ee (red: lowest *R*/*S* transition states only, green: Boltzmann-averaging over all proton transfer transition states). Computed enantioselectivity is slightly lower than the actually observed enantioselectivity, but the trend and magnitude are generally very well reproduced.

The calculations predict the correct enantioselectivity for the *R* enantiomer and although predicting slightly lower enantiomeric excess, the trend is very accurately reproduced, with the highest ee for iodide, a minor drop in enantioselectivity for Br/Cl and a more significant loss of ee when the halide is exchanged for fluoride. As previously, the Boltzmann-averaging pre-

dicts lower enantioselectivities than the comparison of just the lowest R/S transition states. The good agreement of theory and experiment again support our mechanism and also raise the question of what may be the origin of the difference in ee for the halides. To measure the steric effect of each halide, the cone angle θ for each halide was calculated according to 4.4 from the computationally obtained Ru-X distance r_{Ru-X} and the ionic radius of each halide, r_X, which were taken from the literature compiled by Shannon.[195]

$$\theta = 2 \cdot \sin^{-1}\left(\frac{r_{Ru-X}}{r_X}\right) \tag{4.4}$$

Table 4.16 shows that the cone angles increase with increasing halide size; fluoride has a substantially smaller cone angle (81.5°) than the other three halides, with Cl/Br being relatively close (97.0° and 100.7°) and iodide being again larger (107.7°). That is in line with the steep drop in enantioselectivity and the relative similarity regarding enantiodiscrimination for Cl/Br. Plotting the experimental enantiomeric excess against the cone angles in Table 4.16 shows the correlation between size/sterics of the halide and the resulting ee (figure 4.36). This relationship is also supported by an experiment in which thiocyanate, a pseudohalide, gave a relatively similar ee as iodide (81% vs. 84%), while having a similar ionic radius of ~2.15 Å,[196] although the concept of a ionic radius is not well defined for a polyatomic ion.

Table 4.16: Cone angles for the different halides in the Ru-(*S*,*S*)-*f*-binaphane catalyst.

Halide	r_X [pm]	r_{Ru-X} [pm]	θ [°]
F	203.7	133	81.5
Cl	241.6	181	97.0
Br	254.5	196	100.7
I	272.5	220	107.7

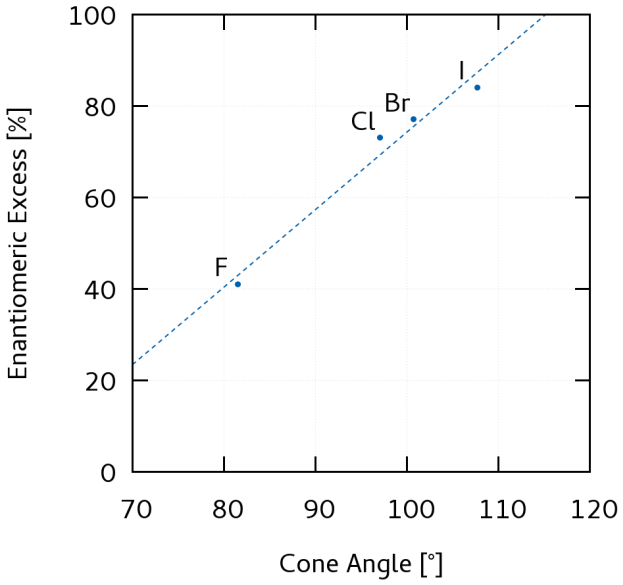

Figure 4.36: Correlation of the halide cone angle, a typical steric parameter, with the observed enantiomeric excess.

As for electronic effects, the electron density at the metal is usually considered. Although electronegativity clearly decreases within the halide series from fluoride to iodide, the varying size and therefore d-orbital overlap including strength of σ- and π-donation make it unclear which halide is more effective at providing or withdrawing electron density. A good and therefore often used probe is the Tolman Electronic Parameter,[197] using the carbonyl stretching frequency as a measure of electron density on the metal (originally in $Ni(CO)_3L$-type complexes). With increasing electron density on the metal, backbonding into the π^*-orbital on CO increases and the wavenumber $\tilde{\nu}$ of the corresponding vibration decreases due to the weakening of the bond. The experimental value for $\tilde{\nu}_{CO}$ was measured for the [Ru((*S*,*S*)-*f*-binaphane)HCOI(PPh_3)] complex by FT-IR: 1935 cm^{-1}. The calculated value for the same complex is $\tilde{\nu}_{CO}$ = 1934 cm^{-1}, which indicates that the computationally obtained values are sufficiently accurate. For a systematic comparison, the CO stretching frequencies were calculated for the same complex type **B**, with ammonia as a ligand for all halides (table 4.17).

Table 4.17: Carbonyl stretching frequencies for complex type **B** with different halides.

Halide	$\tilde{\nu}_{CO}$ [cm^{-1}]
F	1931.9
Cl	1934.6
Br	1934.4
I	1932.6

All $\tilde{\nu}_{CO}$ are within a narrow range of only ~3 cm^{-1}, with no visible trend between the halides. We therefore think that the electron density on the ruthenium center is not significantly altered for different halide ligands – indicating that the electronic effect within the halide series probably only plays a minor role in its influence on the enantioselectivity.

4.3.13 Chemoselectivity

Finally, the last interesting aspect is the chemoselectivity of the reaction. Three questions may be addressed here:

1. Why is no overalkylation to secondary amines observed?

2. Why is the hydrogenation of the imine favored over that of the ketone?

3. Why is the chemoselectivity different in the case of fluoride?

Overalkylation is regularly a challenge in redutive amination. This involves reductive amination of the ketone with a primary amine that has been obtained from an initial reductive amination of the ketone with ammonia. In fact, the formation of the *N*-substituted imine from 1-phenylethylamine and acetophenone is favored over the primary imine formation through condensation of acetophenone and NH_3 by 6.2 kJ·mol^{-1}. Formation of both imines is, however, still endergonic (11.4 kJ·mol^{-1} for the substituted imine and 17.6 kJ·mol^{-1} for the unsubstituted imine). This means that after formation of an initial amount of chiral amine, undesired secondary amine could be formed. The reason why hydrogenation of the *N*-substituted imine is not occurring lies in the catalyst's structure: since the binaphane wings engulf the metal center, the steric demand of the substituted imine is simply to large. When looking at the initial η^1 and η^2 imine structures in Figures 4.15, 4.16 and 4.18, it becomes obvious that coordination of the substrate is impossible with a large substituent like 1,1-methylphenyl instead of just hydrogen on the imine. No complex of the substituted imine with the catalyst could be optimized. Therefore overalkylation is not observed due to sterics – while the necessary imine can be formed as an intermediate, it is to bulky to be hydrogenated. Since its formation is also endergonic, neither the substituted imine, nor the secondary amine are formed.

To understand the excellent chemoselectivity, the hydrogenation of the ketone was also calculated. For the discussion we will focus on the hydride and proton transfer as the important steps. Structures are denoted with an additional **K** for ketone, otherwise the nomenclature remains the same (e.g. **TSHKI** for the hydride transfer and **TSPKI** for the proton transfer transition states in ketone hydrogenation). Since ketones do not have *E*/*Z* isomerism, this combinatorial option can be omitted, and four hydride transfer transition states exist. The energies are given in Table 4.18.

Table 4.18: Barriers for the hydride transfer to the ketone with the iodide-containing catalyst. Energies are free enthalpies in kJ/mol, relative to the same reference as the imine hydrogenation.

Hydride transfer TSHKI [kJ/mol]		
Complex	*R*	*S*
A	105.3	100.8
B	95.1	105.7

The barriers for hydride transfer are higher for the ketone than for the imine: for the ketone, the lowest hydride transfer transition state is **TSHKI-BR** with a barrier of 95.1 kJ·mol^{-1}, which is 24.9 kJ·mol^{-1} higher in energy than the lowest hydride transfer to the amide (**TSHI-BRZ**, 70.2 kJ·mol^{-1}). Ketone hydrogenation is therefore already disfavored in the hydride transfer step. Since proton transfer is rate-determining, this step is of higher importance. The energies for the proton transfer to the corresponding alkoxide complexes are given in 4.19. Proton transfer to the alkoxide species is also higher than for the amide, with the energetically favored pathway via **TSPKI-BRCOPh** having a barrier 125.8 kJ·mol^{-1}. This would be the rate-determining step in ketone hydrogenation and is 32.6 kJ·mol^{-1} higher in energy than the corresponding proton transfer for liberation of the amide (**TSPI-ARIPh**, 93.2 kJ·mol^{-1}). The large gap between hydrogenation of ketone and imine explains why almost only hydrogenation of the imine is experimentally observed (~99% yield of the amine in the reductive asymmetric amination).

Table 4.19: Barriers for the proton transfers to the alkoxide for the iodide-containing catalyst. Energies are free enthalpies in kJ/mol.

Proton transfer TSPKI [kJ/mol]						
Ru-O hemisphere	CO			I		
Complex	H	Me	Ph	H	Me	Ph
AR	149.8	129.8	-	167.6	-	128.7
AS	158.2	132.1	-	-	132.8	-
BR	155.7	-	125.8	164.5	135.6	-
BS	-	130.2	-	166.0	-	131.8

Our last question of concern was then the chemoselectivity with the fluoride catalyst. While the preference of amine over alcohol generally decreases in the halide series, a particular change is observed for the fluoride catalyst: here, hydrogenation of the ketone is favored, by about 4:1. Recalculating the hydrogenation pathway with fluoride in the apical position of the complex and ketone as the substrate gave no satisfying explanation: in this mechanism hydrogenation of imine was still favored. The corresponding energies of the hydride and proton transfer transition states are shown in Tables 4.20 and 4.21.

Table 4.20: Barriers for the hydride transfer to the ketone with the fluoride-containing catalyst. Energies are free enthalpies in kJ/mol, relative to the same reference as the imine hydrogenation.

Hydride transfer TSHKF [kJ/mol]		
Complex	*R*	*S*
A	86.1	81.7
B	76.4	83.9

Table 4.21: Barriers for the proton transfers to the alkoxide for the fluoride-containing catalyst. Energies are free enthalpies in kJ/mol.

Proton transfer TSPKF [kJ/mol]						
Ru-O hemisphere	CO			F		
Complex	H	Me	Ph	H	Me	Ph
AR	137.3	124.3	-	158.3	-	120.3
AS	143.5	122.5	-	-	125.4	-
BR	-	-	118.8	147.2	115.5	-
BS	-	118.4	-	146.4	-	114.2

Imine hydrogenation is favored as the pathway to the alcohol has a barrier of 114.2 kJ·mol^{-1} (**TSPKF-BSFPh**), compared to 90.5 kJ·mol^{-1} for the imine (**TSPF-ARFPh**), which is a lower preference than for the iodide pathway, but still a considerable gap preferring the amine over the alcohol. The reason for the change in chemoselectivity must there be somewhere else. We propose an alternative pathway in which catalytic amounts of hydrogen fluoride are responsible for the formation of the alcohol. In our synthetic protocol, the halide is added as an ammonium salt (NH_4X) in excess (100 mol%). Ammonium fluoride is known to dissociate into ammonia and HF when heated,[198] which makes presence of HF under the applied conditions likely.

It is also more likely to be present in contrast to HI, due to the stark difference in pK_a, with both dissociation constants different by about 13 orders of magnitude (3.2 vs. ~ -10). Initially it was thought that HF might form a similar σ-HF complex which would alter the proton transfer step. It does, however, seem that HF is not forming any intermediate similar to the σ-dihydrogen complexes. Instead, upon further investigations, proton transfer with HF seems to be barrierless. Figures 4.37 and 4.38, show an example of the potential energy surface for the addition of HF to the amide and alkoxide complex. For liberation of both amine and alcohol, the process is barrierless and leads to formation of the difluoride amine/alcohol complex.

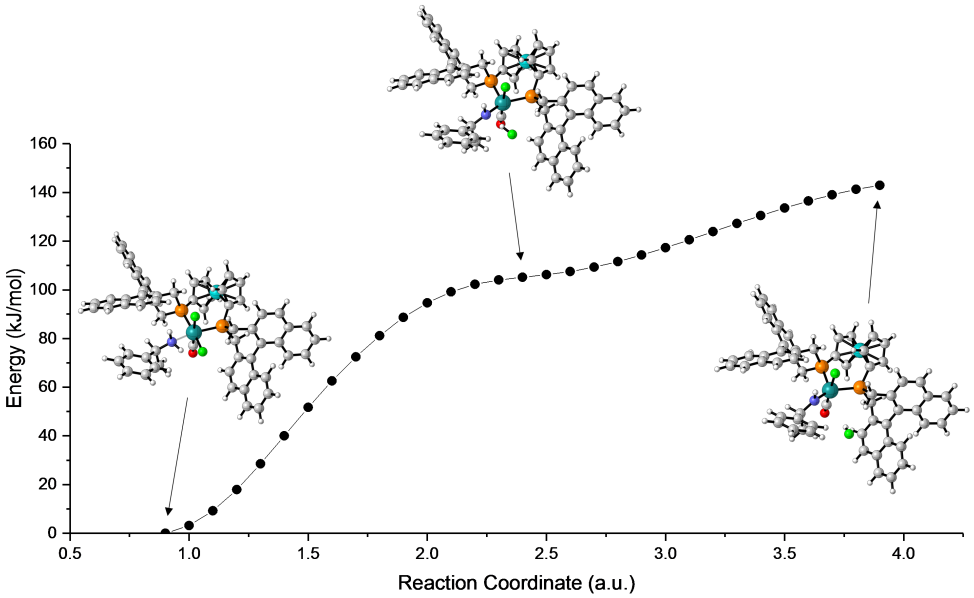

Figure 4.37: Potential energy surface at the BP86/def2-SV(P) level for the addition of HF to the amide complex. HF does not form a σ-complex, but instead protonates the amide and forms a difluoride complex without any barrier. The energetically favored product (amine) is on the left.

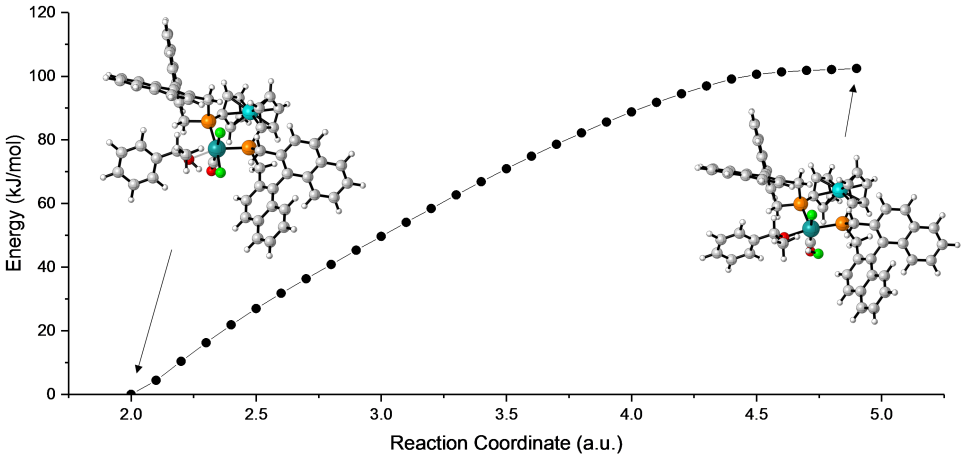

Figure 4.38: Potential energy surface at the BP86/def2-SV(P) level for the addition of HF to the alkoxide complex. HF does not form a σ-complex, but instead protonates the alkoxide and forms a difluoride complex without any barrier. The energetically favored product (alcohol) is on the left.

Due to the absence of the proton transfer in presence of HF, hydride transfer probably becomes the rate-determining step. Here, the hydride transfer to the imine is lower in energy, but is countered by the abundance of ketone vs. imine and the endergonic formation of imine from ketone and ammonia, which could tip chemoselectivity toward the alcohol. The resulting difluoride complex is also no catalytic resting state, but can regenerate the initial hydride

complex by addition of H_2 to give the σ-dihydrogen difluoride complexes **FRA**/**FRB**, followed by proton transfer via **TSFRA**/**TSFRB** to restore the hydride/fluoride complex with decoordination of HF. This regeneration is very feasible since the corresponding barriers are small with 40.1 kJ·mol^{-1}/36.8 kJ·mol^{-1} for **TSFRA**/**TSFRB**, closing the catalytic cycle of this pathway.

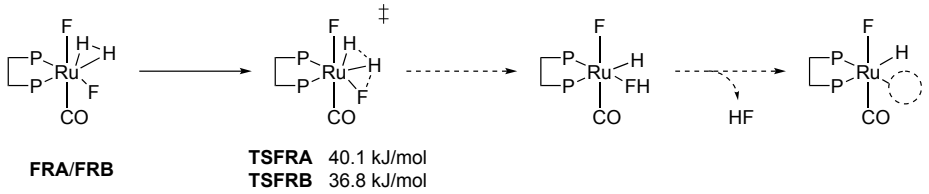

Figure 4.39: Regeneration of the initial hydride through proton transfer from H_2.

Still, more investigations would be needed to fully explain chemoselectivity toward the alcohol in the case of the fluoride catalyst; it cannot be ruled out that other species or intermediates are involved in the formation of 1-phenylethanol, potentially through a different mechanism – it would certainly be of interest to isolate the catalytically active species in the case of fluoride, which has not been achieved so far.

4.3.14 Summary and Conclusion

The asymmetric reductive amination with a [Ru(I)H(CO)((*S*,*S*)-*f*-binaphane)] catalyst was investigated. The computational studies show that our proposed mechanism is energetically feasible and accurately predicts the enantioselectivity that has been observed experimentally. The most likely structure of the catalyst was predicted by our calculations and later confirmed to be a reasonable structure through X-ray crystallography of a corresponding crystal. From there, the mechanism proceeds through coordination of the imine, rearrangement into η^2 coordination and hydride transfer to yield the amide complex. Hydrogen coordinates to form the corresponding σ-complex and then undergoes heterolytic cleavage in a proton transfer to the amide, giving the final amine and the initial hydride complex. Proton transfer from H_2 is the rate-determining step of the reaction and controls enantioselectivity. An in-depth analysis of substrate conformers, complex types, *E*/*Z* and finally prochiral faces of the substrate *R*/*S* is crucial to predict the correct enantioselectivity. The energy differences finally leading to the two enantiomers are governed by several small interactions, including NH hydrogen bonding with the iodide or the π-system of the binaphthyl groups, steric interactions of the substate substituents with the ligand or the configuration of the imine. The investigations were expanded to the full series of halides and the trend in enantioselectivity is also here reproduced correctly, by taking all relevant isomer/conformer combinations of the rate-determining step into account. It is suggested that the steric demand of the halides plays the dominant role for the effect on selectivity, based on correlation of the halide ligand cone angle with the enantiomeric excess. The electronic effect is deemed to be small, as the halide has only minor effect on the metal electron density, probed by the sensitive CO carbonyl vibrational frequency. Chemoselectivity was investigated in the end and the gap between ketone and imine hydrogenation explains the selectivity for the regular protocol with iodide. It is suggested in the case of fluoride that in-situ formed HF is responsible for the change in chemoselectivity, but more investigations in the future may be needed to fully explain the observed selectivity.

In conclusion, the mechanistic studies provide a good picture of the asymmetric reductive amination that is in agreement with our experimental observations. These studies may be used for rational optimization of the system toward higher enantioselectivities.

4.4 Ligand Search

With the newly gained insights into the mechanism, we were interested, whether a new ligand could be found or designed that performs even better and achieves higher enantioselectivities. The motivation for this was two-fold: First, the current system was remarkable in that it provided unprecedented enantiomeric excess for the direct asymmetric reductive amination that had so far not been achieved. But the enantiomeric excess was still in the range of 80-90% and for most applications an ee of greater than 95 or 99% would probably be desired (the currently applied lipase route in BASF achieves enantiomeric excesses of 99+%). Secondly, the enantioselectivity was worse for alkyl-alkyl ketones, another very important target class of molecules. For example, in the asymmetric reductive amination of 2-heptanone under the same protocol, only 14% ee was achieved. As a computational example, the enantioselectivity for the asymmetric reductive amination cyclohexyl methyl ketone was calculated. This substrate is the aliphatic analogon of our test aryl-alkyl test substrate acetophenone and was preferred over 2-heptanone due to the smaller conformational space (see appendix 6.2.5). From the energy differences of the proton transfer transition states, an enantiomeric excess of 30% was estimated for the *R* enantiomer (8% using Boltzmann averaging). This is lower than the experimental and computational enantioselectivity for the aryl-alkyl substrate and in line with the low experimental selectivity for 2-heptanone. Cyclohexyl methyl ketone was then subjected to our experimental protocol and an enantiomeric excess of 45% was measured, in accordance with our expectations for alkyl-alkyl ketones and the calculations on this substrate.

It is assumed, that a catalyst that performs even better in the asymmetric reductive amination of aryl-alkyl ketones will likely also be a promising candidate for alkyl-alkyl ketones as substrates. Since the current catalyst has only limited room for optimization (typical reaction conditions have already been optimized, e.g. solvent, temperature, NH_3/H_2 pressure, additives, etc.), the most promising approach is the search for a better ligand. As mentioned in the introduction of this chapter, many different ligands have already been tested, with only (*S*,*S*)-*f*-binaphane resulting in satisfying enantioselectivity. Predicting or suggesting a totally new ligand from scratch therefore does not seem particularly promising. Instead, a modification of (*S*,*S*)-*f*-binaphane is likely more promising. In this ligand, the unique feature is the "wrapping" of the metal complex in the ligand's binaphthyl groups, creating a chiral pocket for the substrate. This feature should be kept and enhanced to yield higher enantioselectivities. By keeping the general motif of the ligand, it is also relatively reasonable to assume that the mechanism (within boundaries) stays the same. Just suggesting trial-and-error modifications to (*S*,*S*)-*f*-binaphane are undesirable as the synthesis of derivatives can be compli-

cated: the original route requires synthesis of the chiral dichloromethyl binaphthyl fragments and diphosphanoferrocene, which are then coupled.[151] Obviously, the capability of synthesizing many binaphane-type ligands depends on whether the corresponding halides and phosphanes are available, and synthesis of many derivatives can quickly become very demanding. We therefore wanted to follow a different approach. The most intuitive and logical modification to this ligand seems a change in bite angle of P-Ru-P by introducing a different linker, while keeping the binaphthyl wings as they are which induce the enantioselectivity in the chiral pocket.

As we have identified the enantiodetermining step of the reaction computationally, two questions were of particular interest:

1. Will a modification of the bite angle result in higher enantioselectivities?
2. Which linkers instead of ferrocene will produce the desired bite angle?

The first question may be answered by using the gained computational insights to build a model that predicts the dependency of the enantioselectivity on the bite angle of the binaphane ligand. Answering this question is also relevant for the next question – if no or no significant improvement is predicted for other bite angles, it may be futile to attempt ligand modification in this way. Otherwise, if a change in bite angle is predicted to yield better enantioselectivities, the next question is which linkers can be introduced into (*S*,*S*)-*f*-binaphane to achieve the desired bite angle while preserving the general catalyst structure and chiral environment.

4.4.1 Model for Enantioselectivity

The mechanistic investigations have shown that the enantioselectivity depends on the relative energy differences for the proton transfer transition states **TSPI**. For a model of the enantiomeric excess depending on the bite angle, it makes sense to calculate the relative energy differences for all involved proton transfer transition states for different bite angles. In a simplified model the binaphane wings are disconnected and a scan of P-Ru-P bite angles is performed under constraints to keep the ligand geometry of a linked binaphane ligand. These constraints are the fixed bite angle for each step of the scan, a dihedral H-P-P-H angle of 0° to keep the parallel geometry of the binaphthyl wings (this is necessary since no linker is present anymore) and fixing the core of the transition state as in the originally optimized structures in the mechanistic studies. The latter is necessary to avoid a dedicated transition state search for each step of the scan for every isomer/conformer variant. The deviations due to this were probed by explicitly running TS searches for some of the constraint geometries, but seem to be very small, which makes this an acceptable constraint.

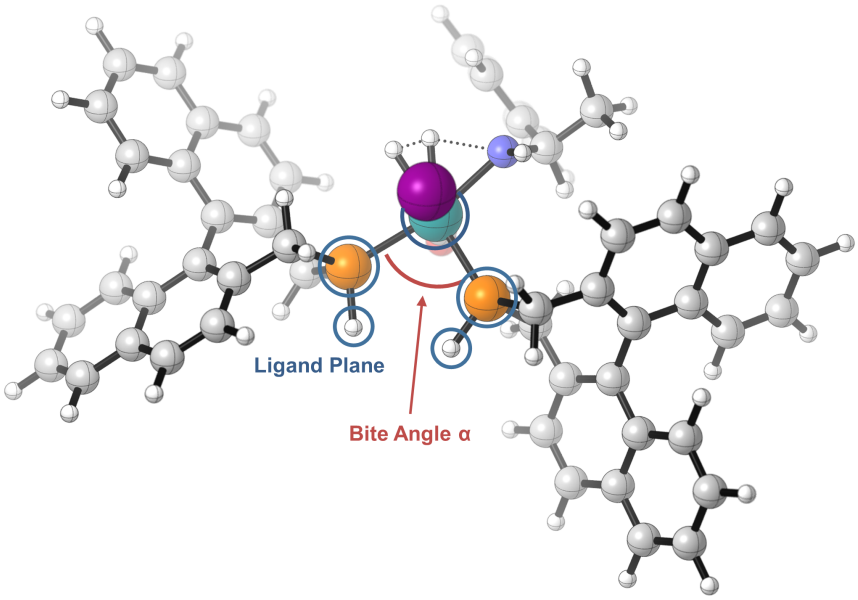

Figure 4.40: Model for the systematic scan of bite angle-dependency of the enantioselectivity. The disconnected binaphane has hydrogen atoms in place of the linker (formerly ferrocene). The H-P-P-H dihedral, bite angle α and the TS are kept fixed and geometries are then optimized for bite angles from 80 to 120° in steps of 2°. This is repeated for each proton transfer TS.

Figure 4.40 shows an example of the disconnected binaphane. The ligand plane is fixed by the H-P-P-H dihedral and the TS is fixed by the N-H, Ru-H and Ru-N distances. Then, the bite angle is varied from 80 to 120° in steps of 2° and a geometry optimization is performed. This

range was chosen since the original (*S*,*S*)-*f*-binaphane ligand has a bite angle of around ~100° and ± 20° is likely a useful range, where 120° is the limit for a trigonal bipyramidal complex geometry. The absolute energies calculated in the scan can only to some extent be interpreted since for small bite angles the repulsion of the phosphine hydrogens becomes dominant. This, however, is not really a problem since we are interested in relative energy differences anyway, where the errors from constraining the complexes to a certain geometry are cancelling. From the scans, curves are obtained that show the energy of a transition state in dependency of the bite angle. These curves have a shape similar to a harmonic potential and we use a simple cubic polynomial fit to account for some skewness. This way, a continuos function $E_i(\alpha)$ is obtained for each transition state i, that describes the energy of the transition state as a function of the bite angle. As an example, Figure 4.41 shows the energy profiles for the two isomer/conformer combinations **ARIPh** and **BSIH** (relative to an arbitrary reference point). The curves have a minimum between 90 to 95° and the form of a harmonic potential is clearly visible. The skew of the curve is well reproduced by the cubic polynomial fit. As a tendency, the energy increases faster from the minimum for smaller bite angles, which is likely induced by the repulsion between the two phosphine hydrogens. The relative difference between the two curves is also not constant, which already shows that the enantioselectivity may vary with the bite angle of the ligand; this will be investigated in the following in more detail.

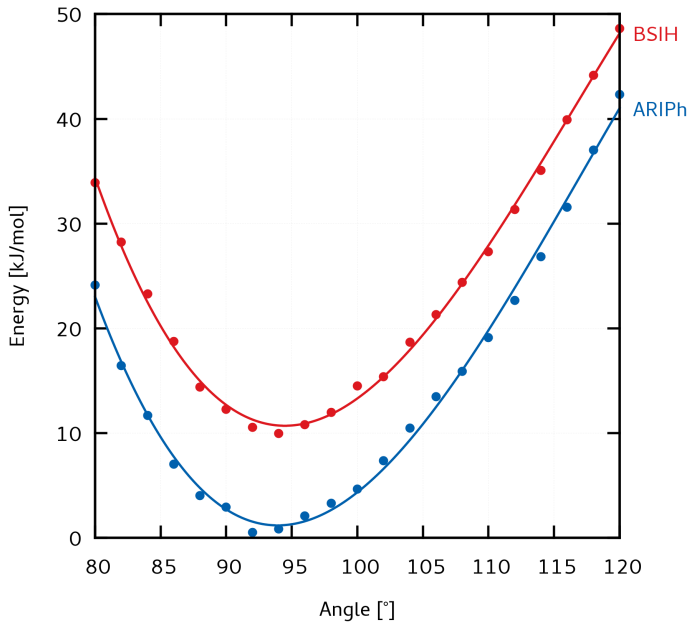

Figure 4.41: Example of bite angle dependency of the energies of proton transfer transition states **ARIPh** and **BSIH**. Data points are the energies obtained from the scan, the lines are the cubic polynomial fit to obtain a continous function $E(\alpha)$. The general harmonic form with a small skew toward larger bite angles can be seen.

Before we continue with looking at the full scans for all transition states, the limitations of this model will briefly be discussed. For one, the electronics on the phosphine deviate from the original ferrocene-linked binaphane, since this substituent is missing on the disconnected binaphane. Also, the bite angle range has to be considered with caution. Whether the catalyst still follows our investigated mechanism for the upper and lower limit of the bite angle interval, may be questioned. Another issue is that of vibrational contributions to the partition function: since we artificially impose constraints on the geometry, thermal corrections fluctuate due to different numbers of imaginary frequencies and low frequency vibrations. We circumvent this problem by averaging the thermal contributions of all 21 bite angle data points and using the averaged value for all structures, but this is certainly not ideal. Finally, the model only predicts the expected enantioselectivity with respect to the bite angle of a binaphane-type ligand. No statement is made about the chemoselectivity and, more importantly, the activity of the catalyst, which is known to be influenced greatly by the bisphosphine bite angle.[199,200] Of the possible isomer/conformer combinations, two could not be found at all: **ARCOPh** and **BSCOPh** – these seem to be not stable under any circumstances. All others were found, three of them tend to "switch" into a more stable isomer/conformer for very small or large

bite angles (**ARIH**, **ARIMe** and **BRCOMe**). In these cases, the fit was only performed on the data that had the correct conformational orientation and was then extrapolated to 80 to 120°.

In Figure 4.42, the energies of all transition states are plotted against the bite angle for a complete picture. Blue lines belong to transition states that lead to the *R* enantiomer, red lines show transition states leading to the *S* enantiomer. We will discuss the relative energy differences in a simplified version of this graph in the next paragraph, but some trends can already be identified here. First of all, the lowest curves are always blue, from which a general preference for the *R* enantiomer can be deduced (which, unsurprisingly, has also always been the observed enantiomer in our experiments). We can also see, that the lowest red and blue curve are closer together when going to small bite angles. This means that as a trend one would expect less enantiodiscrimination for smaller bite angles which seems intuitive: If the P-Ru-P bite angle becomes smaller, the chiral pocket opens up and substrate-ligand interaction is reduced – which in theory should lower energy differences between the enantiodiscriminating transition states. It is also visible that most of the transition states do not play any significant role for the enantioselectivity since they are far too high in energy. Lastly, the different transition states share the same general shape, but have different minima with respect to the bite angle (varying mostly in the 90 to 100° range) and also react differently to changes in the bite angle (for some TS, the TS energies increase faster for larger bite angles than for others).

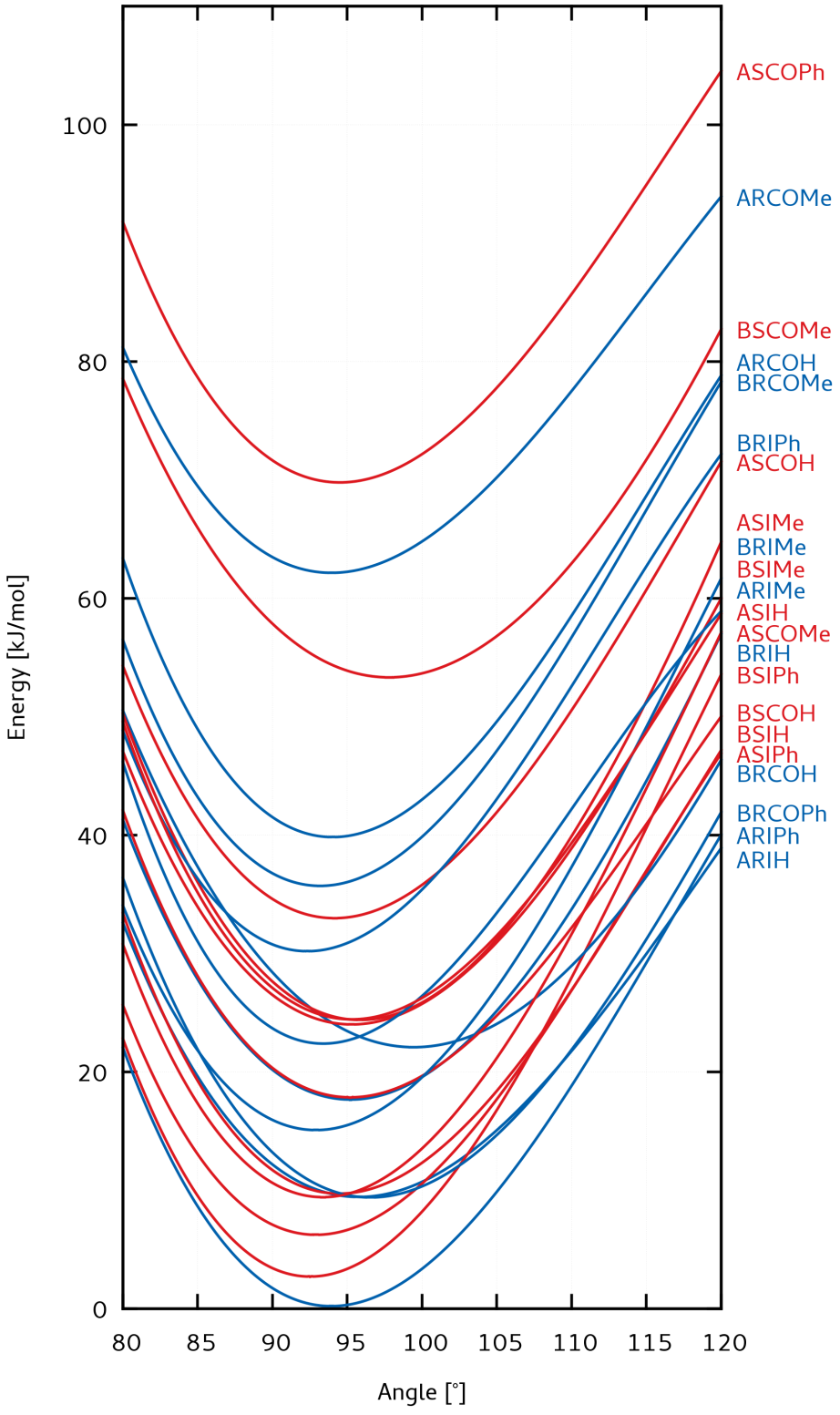

Figure 4.42: Relative energies of all 22 isomer/conformer combinations of proton transfer transition states as a function of the bite angle. Transition states leading to the formation of the *R* enantiomer are shown in blue, TS leading to the *S* enaniomer are shown in red. The energy reference has been set to the lowest minimum of all curves.

As we are interested in the relative energy differences, the main problem with the absolute curves as in Figure 4.42 is that they are not very easy to read. Figure 4.43 therefore shows an adapted variant of the transition state curves, where only the lowest 15 kJ·mol^{-1} are shown and the curves are plotted against a constant reference, namely the transition state which is the lowest TS at any point (reminding of the Tanabe-Sugano diagram, in which the ground state is used as a constant reference). The first prominent feature is therefore the cusp at around ~117°, caused by a change in the lowest transition state from **ARIPh** to **ARIH**. Starting from smaller bite angles, the energy difference between *R* and *S* is relatively low – the lowest TS for *R* is **ARIPh**, while **BSIPh** is responsible for the formation of the *S* enantiomer. **ARIPh** stays as the overall lowest transition state for most of the 80-120° bite angle interval, and is only superseded by **ARIH** for very large bite angles. In contrast, the relative energy of **BSIPh** rises with increasing bite angle. Looking back at the structure of the analogous transition state **TSPI-BSIPh** that was discussed earlier in Figure 4.29, we see that this is probably due to increasing repulsion between the ligand methylene group and the NH functionality on the amide, since for larger bite angles, the two come into close contact.

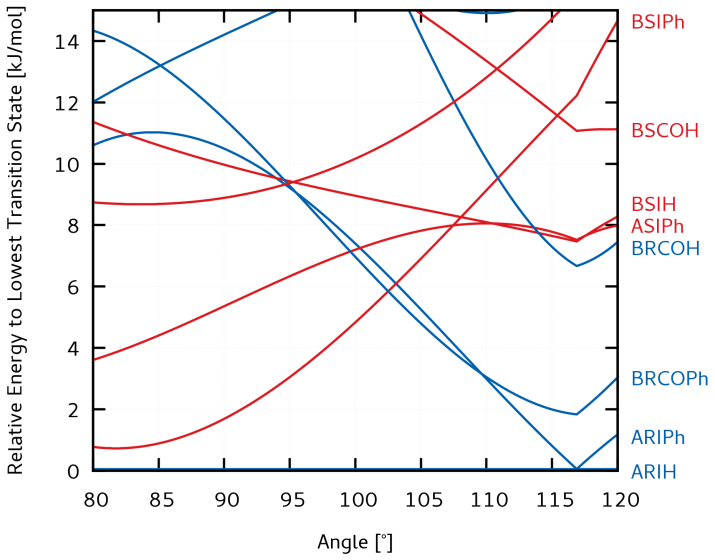

Figure 4.43: Relative energies of proton transfer transition states as a function of the bite angle, against a constant reference (the lowest transition state). Transition states leading to the formation of the *R* enantiomer are shown in blue, TS leading to the *S* enaniomer are shown in red. The lowest TS is **ARIPh** until around ~117°, at which point **ARIH** is the lowest TS and reference.

Following this section of the bite angle window, at around ~103 to 110° two things change: the *R*-producing transition states **ARIH** and **BRCOPh** become lower in energy than the energetically lowest pathway to *S* (**BSIPh**), and **BSIH** and **ASIPh** supersede **BSIPh** as the lowest transition state to the *S* enantiomer. In the limit of very large bite angles, **ARIH** finally be-

comes the new reference as it falls below **ARIPh**, while the initially most feasible TS to *S*, **BSIPh** is already very high in energy and plays almost no role anymore.

The most relevant information is of course not the various shapes and trajectories of the transition states' energy-bite angle dependency, but the predicted enantioselectivity as a function of the bite angle that can be distilled from these curves. Each curve is the transition state energy as a function of the bite angle α, either toward *R* ($E_{i_R}(\alpha)$) or toward *S* ($E_{i_S}(\alpha)$). From these, we may calculate the cumulative Boltzmann weights for *R* and *S*, $\omega_R(\alpha)$ and $\omega_S(\alpha)$, defined as

$$\omega_R(\alpha) = \sum_{i_R} e^{-\frac{E_{i_R}(\alpha)}{RT}} \tag{4.5}$$

$$\omega_S(\alpha) = \sum_{i_S} e^{-\frac{E_{i_S}(\alpha)}{RT}} \tag{4.6}$$

The weights can then be used to define the enantiomeric ratio $er(\alpha)$ as a function of the bite angle:

$$er(\alpha) = \frac{\omega_R(\alpha)}{\omega_S(\alpha)} \tag{4.7}$$

It then follows that the enantiomeric excess $ee(\alpha)$ is:

$$ee(\alpha) = \frac{er(\alpha) - 1}{er(\alpha) + 1} \tag{4.8}$$

Plotting $ee(\alpha)$ therefore gives us a real impression of how the enantiomeric excess is expected to change with the bite angle α. The corresponding graph is shown in Figure 4.44. A clear trend is visibile showing that for lower bite angles enantioselectivity is very low, but then increases gradually with a larger bite angle. As a first test, the model should at least reproduce the enantiomeric excess of (*S*,*S*)-*f*-binaphane, for which we have experimental data and which is partially incorporated into the model since we used the previous calculations on that system for our model. (*S*,*S*)-*f*-binaphane has an experimental bite angle of 100.2° (obtained from X-ray crystallography of the [Ru(I)H(CO)((*S*,*S*)-*f*-binaphane)(PPh_3)] complex), and the computed bite angle is around 101.9° (based on the general complex types **A**/**B**). Thus, $ee(\alpha)$ predicts an enantiomeric excess of ~65 to 75 %, which is again not too far off from the experimental value (~84% ee). A small underestimation of the ee had also been previously shown up in our regular mechanistic investigation.

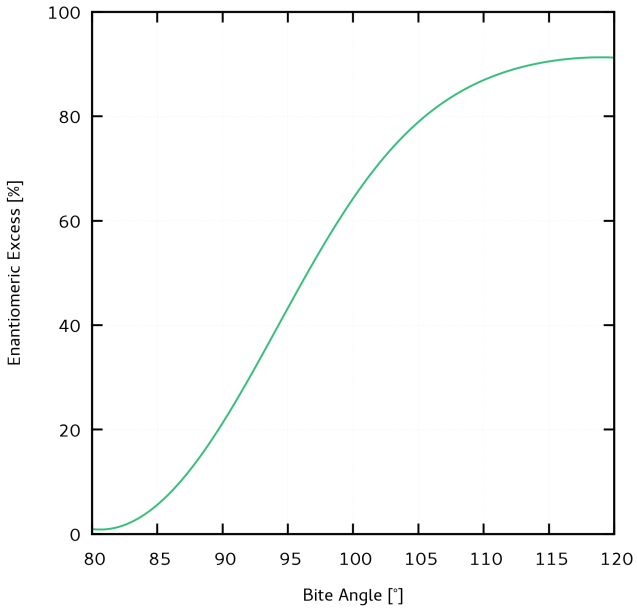

Figure 4.44: Predicted enantiomeric excess of binaphane-type ligands as a function of the bite angle, based on our model.

Another way to view the change of enantioselectivity with the bite angle is the averaged $\Delta\Delta G^{\ddagger}$, which is the energy difference between *R* and *S* pathways if only two pathways existed:

$$\Delta\Delta G^{\ddagger} = -\ln\left(\frac{1}{er(\alpha)}\right) \cdot RT \tag{4.9}$$

The resulting graph is shown in Figure 4.45.

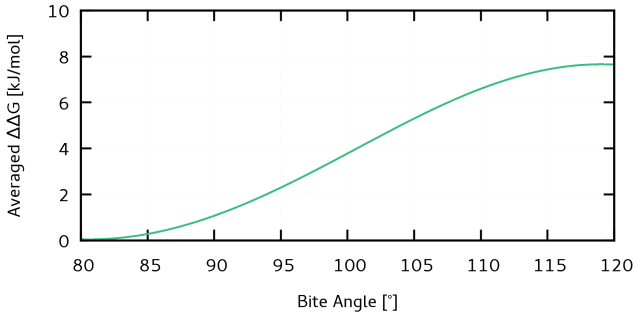

Figure 4.45: Predicted averaged $\Delta\Delta G^{\ddagger}$ of binaphane-type ligands as a function of the bite angle, based on our model.

Either way, the main conclusion to be drawn from our model is, that it suggests potential for improvement of the enantiomeric excess into the 90-95% range or even higher when considering that our calculations tend to be a conservative estimate of the enantioselectivity. Improvements are expected for a ligand that has a higher bite angle, which again makes sense from a

mechanistic standpoint: with a larger bite angle, more steric pressure is exerted on the chiral pocket, increasing enantiodiscrimination. The next question therefore is how we can find reasonable linkers that push the bite angle towards favorable terrain, into a range of 100-120°.

In a first approach to tackle this problem, the idea was to come up with typical, synthetically accessible linkers, optimize the corresponding hypothetical complexes computationally and then estimate the enantiomeric excess with our $ee(\alpha)$ function from our model. It was quickly realized, that many linkers (especially alkyl chains) tend to be more flexible than the ferrocene backbone, and can also potentially have conformational isomers. These problems could be addressed by performing molecular dynamics simulations on the hypothetical catalysts: The vibrational flexibility or rigidity of the ligand can this way be captured over time (also an interesting information) and an average of conformers can be recorded. From the MD simulations, a bite angle probability density $\rho(\alpha)$ can then be obtained and we may calculate an expected enantiomeric excess $\aleph$ from the bite angle probability weighted integral of $ee(\alpha)$:

$$\aleph = \int ee(\alpha) \cdot \rho(\alpha) d\alpha \tag{4.10}$$

Unfortunately, it turned out that conformational changes could not be captured by the MD simulations – the necessary time scales to observe conformational changes are far too long. The bite angle distribution within one type of conformer, however, can be obtained and gives at least some information on the rigidity of the ligand. We therefore resorted to a second approach. Since just coming up with "reasonable" ligand linkers and performing MD simulations on them is also limited by our chemical intuition, it was instead decided to search the database of the Cambridge Crystallographic Data Centre (CCDC), the Cambridge Structural Database (CSD) for suitable ligand backbones to achieve higher enantioselectivity. This approach will be discussed in the next section, followed by some final remarks on the results of the MD simulations.

4.4.2 CSD Search

As of 2018, the CSD contains more than 900,000 crystal structures,[201] which have been recorded over the last 45 years. The search within the CSD for ligand backbones/linkers was motivated by the fact that many more ligand motifs have already been discovered than are accessible by chemical intuition, and that the desired property, the bite angle of ligands can instantly be accessed from the crystal structure data. For known linker molecules, it is also much more likely that a synthetic route to the ligand substructure already exists.

For the search within the CSD, three criteria were applied:

1. Ru, Rh, Ir, Os as metal centers
   The metal should be preferably ruthenium or one of the three related metals for which similar phosphine complexes are known, namely rhodium, iridium or osmium.

2. Bidentate Phosphines
   The ligand should be a true bidentate phosphine ligand – not tridentate or just two unconnected phosphines on the same metal.

3. Bite Angle of > 100°
   (*S*,*S*)-*f*-binaphane is our benchmark ligand with a bite angle of just around ~100°. Since we expect higher enantioselectivity for larger bite angles, only ligands with a P-M-P angle greater than 100° should be listed.

The raw search of the database was carried out by Dr. Frank Rominger at the Institute for Organic Chemistry at the University of Heidelberg and identified 1,075 phosphine complexes (including a few duplicates and some entries from the local crystal structure database, that are not listed in the CSD). The search program within the CSD can only partially differentiate bidentate phosphines from tridentate phosphines, and thus the structures have to be reviewed manually to filter for "true" bidentate ligands. During this review it was discovered that in a few rare cases, the connectivity entered in the CSD does not seem to be correct when compared to the actual bonding situation in the three-dimensional structure, but this should not affect the overall results of the structural search. After review, 212 structures were identified which meet all of the above criteria, including the criterion for bidenticity. Some of the structures appear as duplicates, in many cases there are groups where several derivatives of the same ligand have been published, and some complexes contain several slightly different P-M-P bite angles in one unit cell (as there are several complexes present). The full list can be found in the appendix, section 6.2.4. For clarity, the ligands have been grouped by similarity and the ligand groups will be discussed in the following.

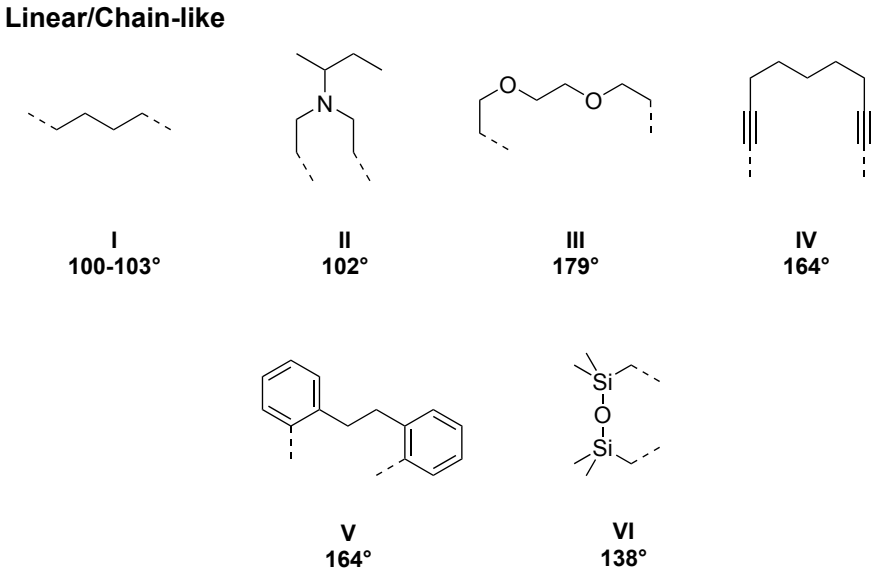

Figure 4.46: Linear or (alkyl) chain-like family of bisphosphines. Bite angle ranges are given when several complexes with different bite angles for the same ligand type where in the dataset.

The first group of ligands is shown in Figure 4.46, encompassing ligands that have a linear or chain-like backbone. These generally do not seem to be very promising candidates as bite angles are either too low (butyl linker **I**, amine backbone **II**) or too large (**III**-**VI**), which means that these are *trans*-coordinating ligands.

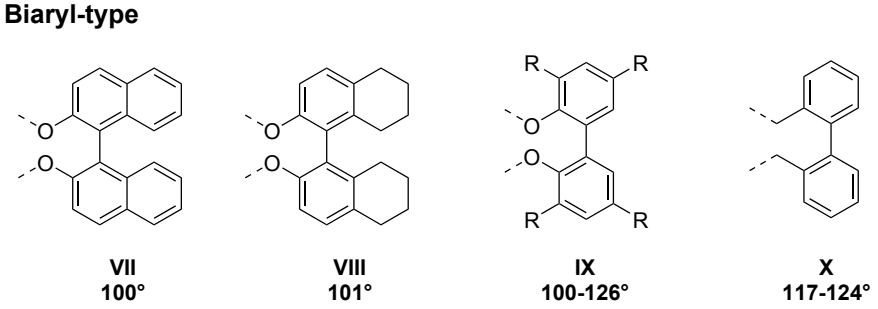

Figure 4.47: Biaryl-type family of bisphosphines. Bite angle ranges are given when several complexes with different bite angles for the same ligand type where in the dataset.

The next group of biaryl-type ligands seems more promising. The binaphthyl phosphites **VII** and **VIII** also have bite angles close to only 100°, but the biphenyl motifs **IX** and **X** exhibit bite angles in the desired range of 110-120°, making them promising candidates. **IX** and **X** are both related as **IX** is the phosphite variant of the methylene-bridge ligand **X**. The latter is preferred as we are using phosphines, not phosphites. Ligand **X** with diphenylphosphino substituents is known as BISBI (2,2'-bis(diphenylphosphinomethyl)-1,1'-biphenyl).

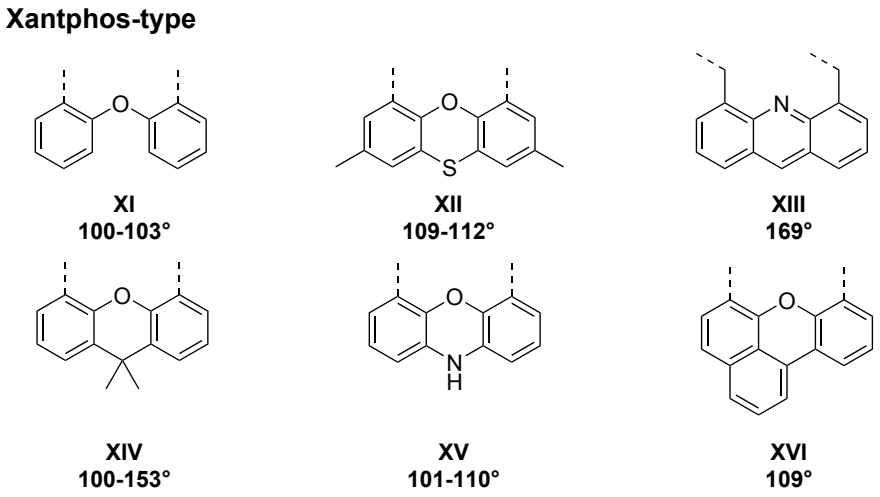

Figure 4.48: Xantphos-like family of bisphosphines. Bite angle ranges are given when several complexes with different bite angles for the same ligand type where in the dataset.

The Xantphos-like family of ligands contains Xantphos itself (**XIV**), but also related condensed tricyclic and/or diphenylether-based structures. Diphenylether (**XI**) has a too small of bite angle to be interesting; similarly, the acridine ligand (**XIII**) is a *trans* coordinating ligand and hence not a suitable backbone. The other ligands are also promising candidates, especially the Xantphos backbone (**XIV**) and phenoxathiin-type ligands (**XII**) with a bite angle of 109-112°. Phenoxazine-type ligands (**XV**) also have the bite angle in the desired range (101-110°), but the amino functionality is more likely to interfere with the reaction, and one would thus prefere **XIV** and **XII** which have the same structural motif.

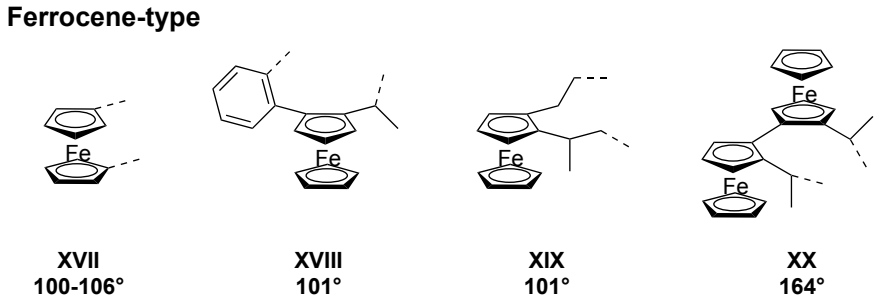

Figure 4.49: Ferrocene-type family of bisphosphines. Bite angle ranges are given when several complexes with different bite angles for the same ligand type where in the dataset.

Ferrocene-type ligands also include our own current ligand, (*S*,*S*)-*f*-binaphane and the CSD shows that other phosphine-type ligands of **XVII** also have bite angles very close to 100°. Variants **XVIII** and **XIX**, where both phosphines are linked on one cyclopentadienyl ring of the ferrocene, also do not provide larger bite angles. The bisferrocenyl-type backbone is *trans*-coordinating (164°), and therefore also ruled out as a possible candidate.

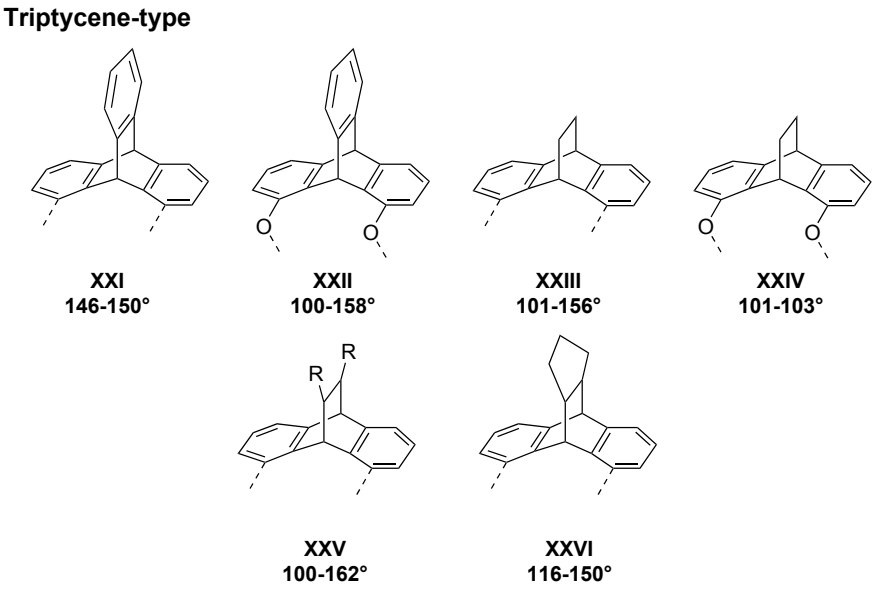

Figure 4.50: Triptycene-like family of bisphosphines. Bite angle ranges are given when several complexes with different bite angles for the same ligand type where in the dataset.

The triptycene-like family of ligands is somewhat related to the Xantphos-type ligands, with a bridged anthracene structure. Both phosphites (**XXII**, **XXIV**) and phosphines (**XXI**, **XXIII**, **XXV**, **XXVI**) exist. A number of these ligands have been prepared in the group of Hofmann and applied in nickel-catalyzed isomerization and hydrocyanation reactions,[202,203] as well as rhodium-catalyzed hydroformylations[204,205] which have been developed in collaboration with CaRLa. Unfortunately, they are unlikely to be useful backbones due to their three-dimensional, bulky structure: The two binaphthyl groups on the binaphane ligand form a parallel pocket of two naphthyl wings, which for symmetry reason is also present on the backside of the complex, where the backbone resides. Ferrocene arranges itself parallel to these wings, the BISBI-type ligand will likely have an axial orientation parallel to the I-Ru-CO axis and Xantphos-like molecules are flat so that they can also fit parallel between the naphthyl wings. A large bulky structure like a triptycene will very likely distort the geometry to fit into the corresponding complex.

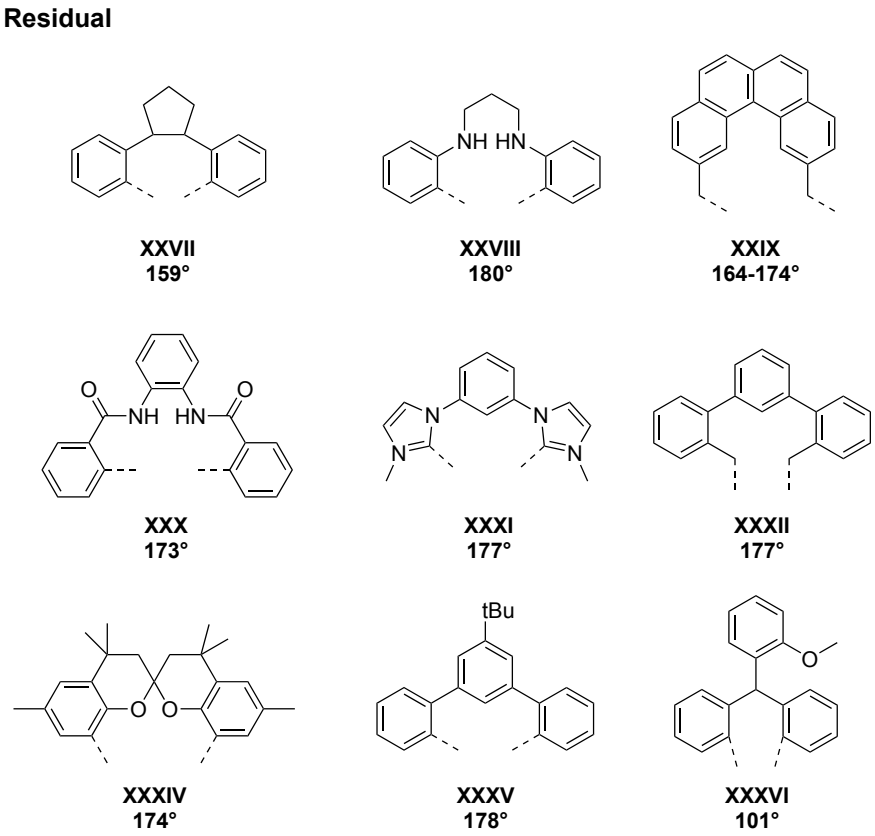

Figure 4.51: Residual bisphosphines. Bite angle ranges are given when several complexes with different bite angles for the same ligand type where in the dataset.

The last, residual category contains different linkers comprised of connected aromatic rings. Except for **XXXVI**, which has a bite angle of < 110°, all ligands exhibit very large bite angles and coordinate *trans* on the metal, which makes them uninteresting for our purpose as a backbone.

Therefore, the two most promising candidates from our search in the CSD are Xantphos-type ligands, especially the phenoxathiin backbone, and the BISBI-like biaryl ligand. Both Xantphos and BISBI have been widely employed in the hydroformylation with rhodium.[206,207] To assess how suitable they might be as ligand backbones, the corresponding structures of the complexes with Xanthphos, phenoxathiin and BISBI backbones were calculated. As with the original model complexes **A**/**B**, ammonia was put on the vacant site of the complex as a small, neutral ligand. We will discuss the Xantphos and phenoxathiin structures first, which are shown in Figures 4.52 and 4.53 and are closely related to each other. Both complexes have large bite angles as desired, with 110.0° for the Xantphos backbone and 108.7° for phenoxathiin. Since both backbones consist of two aromatic rings connected by an ether bridge and either a dimethylmethylene or thioether group, the backbones are bent toward the carbonyl group. Oxygen is not coordinating in both structures. Several features, however, indi-

cate that the ligands might be problematic in catalysis: Due to the bulky tricyclic backbone structure, the binaphthyl wings experience steric pressure and loose the previous parallel arrangement (in Figures 4.52 and 4.53, the left binapthyl group snaps downward). This almost certainly interferes with the enantiodiscrimination exerted by the chiral pocket between the previously parallel binaphthyl groups. Also, the ligands seem to be under stress due to the large P-P distance and the rigidity of the ligand – the Ru-P bond *trans* to the hydride is substantially elongated (2.55 Å, Xantphos and 2.53 Å, phenoxathiin) compared to 2.46 Å for (*S*,*S*)-*f*-binaphane.

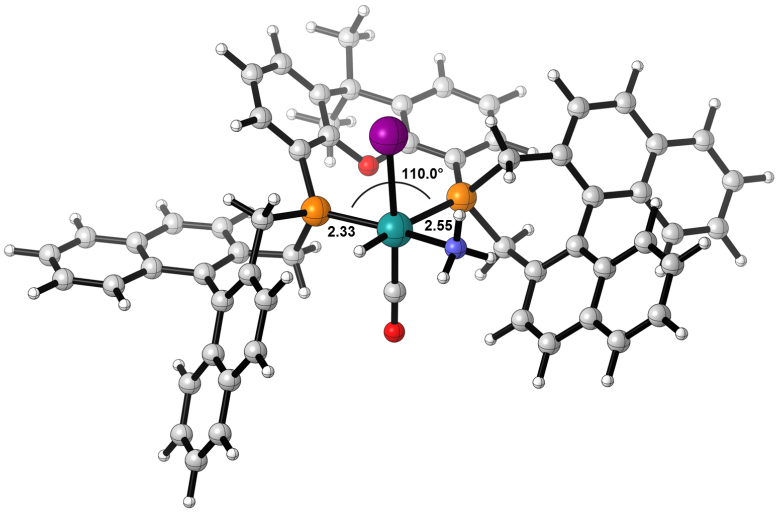

Figure 4.52: Computed structure of a Xantphos-backbone binaphane on the ruthenium catalyst for asymmetric reductive amination. The ligand backbone is bent due to the sp^3-hybridization on the atoms connecting the two aromatic rings.

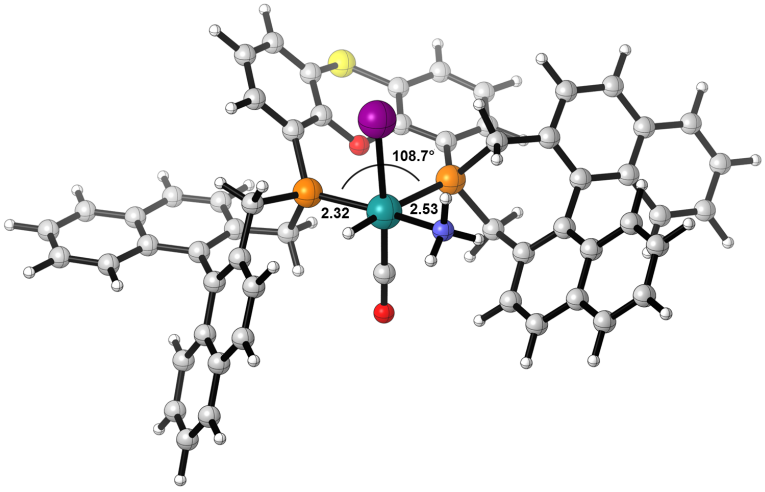

Figure 4.53: Computed structure of a phenoxathiin-backbone binaphane on the ruthenium catalyst for asymmetric reductive amination. The ligand backbone is bent due to the sp^3-hybridization on the atoms connecting the two aromatic rings.

The biggest issue, however, has not been mentioned yet: Both structures show the "regular" structure of the ferrocene-based ligand with a different backbone, but there is a structural variant of both complexes that is slightly lower in energy (2.2 $kJ \cdot mol^{-1}$ and 2.4 $kJ \cdot mol^{-1}$), which has a very different "side-on" geometry. The different coordination allows the backbone to reduce steric interactions with the large binaphthyl groups. In this structure, the previously unique feature of having the binaphane wrap around the ligand for a chiral pocket is completely lost (see Figure 4.54 for the "side-on" coordination: ammonia and the hydride are not covered at all by the binaphane ligand) and it is thus likely that these are not effective for enantiodiscrimination in the reaction.

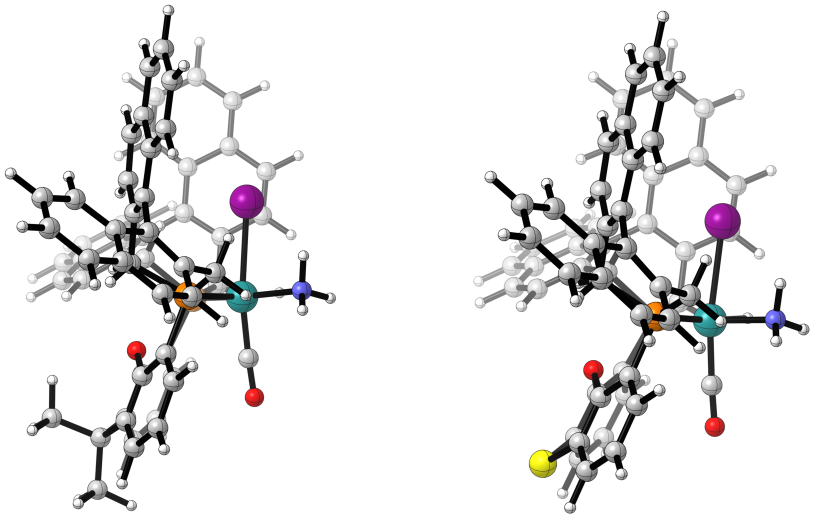

Figure 4.54: "Side-on" coordination for Xantphos (left) and phenoxathiin (right) backbones. The side view shows that the coordination sites for substrate and hydride are not interacting with the ligand like before, since the binaphane wings do not wrap around these sites anymore in this coordination mode.

Besides these two coordination motifs, another one exists where the structure is similar to Figures 4.52 and 4.53, with the convex side of the tricyclic backbone pointing toward the halide instead than the carbonyl group, but this was found to be energetically disfavored by 2.9 $kJ \cdot mol^{-1}$ and 11.0 $kJ \cdot mol^{-1}$.

The BISBI motif seems to be a more suitable candidate when examining the complex geometry (see Figure 4.55). Contrary to the Xantphos-type backbones, the biaryl axis of BISBI avoids steric repulsion with the binaphthyl rings since it has two methylene bridges connecting to the phosphine and fits in between the parallel geometry of the binaphthyl groups. The bite angle is pleasingly large with 111.8°. Coordination of the phosphine seems to be "normal" – the Ru-P bonds are very similar to the original (*S*,*S*)-*f*-binaphane ligand (2.33 Å/2.32 Å for the Ru-P

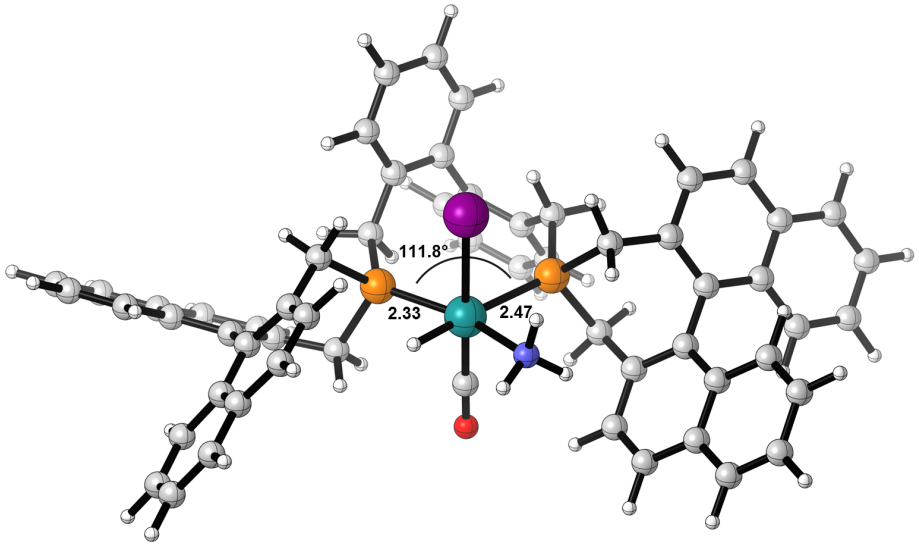

Figure 4.55: Computed structure of a BISBI-backbone binaphane on the ruthenium catalyst for asymmetric reductive amination.

bond *trans* to ammonia, 2.47 Å/2.46 Å for the Ru-P bond *trans* to the hydride ligand). The parallel pocket of the binaphane is also similar to the original binaphane with a small distortion (but not as large as in the Xantphos-type ligands). A "side-on" coordination is disfavored for the BISBI backbone by at least 10.0 kJ·mol^{-1}. In theory, biaryls like BISBI can be chiral – the unaltered BISBI ligand, however, does not exhibit atropisomerism. A binaphane-type BISBI ligand might be chiral in its backbone, either through a high enough rotational barrier or by forming stereoisomeric complexes with ruthenium. The structure shown in 4.55 is the Λ-atropisomer; the Δ-atropisomer is 6.1 kJ·mol^{-1} higher in energy, and has a slightly larger bite angle of 112.7°, but is otherwise structurally very similar. That all makes the BISBI backbone a promising candidate for a new binaphane-type ligand in asymmetric reductive amination.

4.4.3 Molecular Dynamics Simulations

To round off the investigations, the initially planned molecular dynamics simulations were conducted with several binaphane candidates: the regular (*S*,*S*)-*f*-binaphane ligand, which serves as a benchmark, the ethyl- and phenyl-bridged derivatives, which were synthesized in the lab so far, and the BISBI-type backbone. The bite angle trajectories were used to construct the corresponding histograms, both which can be found for all four complexes in the appendix, section 6.2.6. A normal distribution was fitted to the histogram, which reproduces the shape satisfactorily. At first, kernel density estimation[208,209] (KDE) seemed to be a better choice for estimation of the probability density function of the bite angle distribution, as these are potentially able to capture arbitrary distributions. Tests with several kernels (Gaussian, Exponential, and Epanechnikov) were performed using different bandwidths, but the ambiguity in bandwidth and kernel selection and the tendency for overfitting for small bandwidths led us to resort to the normal distribution fit. A KDE might be more suitable for larger sample sizes with less noise. The bite angle distributions are shown in Figure 4.56 and the parameters of the corresponding normal distributions in Table 4.22.

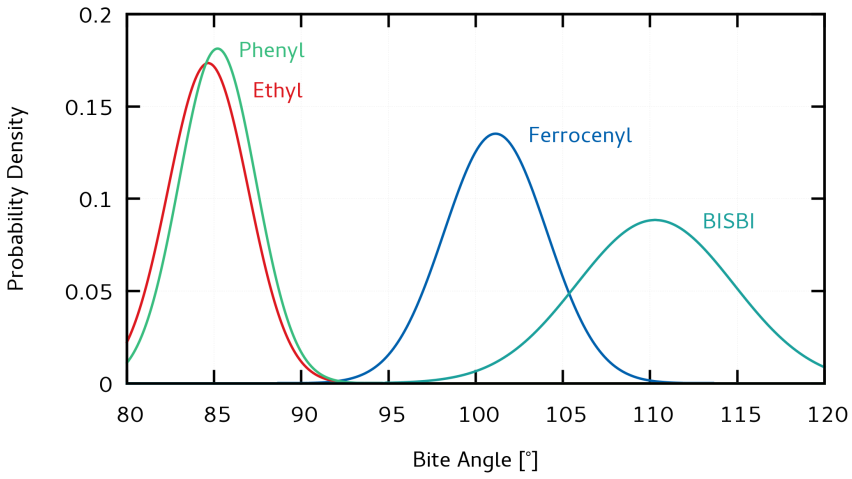

Figure 4.56: Bite angle distributions of binaphane ligands with different backbones: ferrocenyl, phenyl, ethyl, and BISBI.

The original ferrocenyl backbone (*S*,*S*)-*f*-binaphane ligand with a mean bite angle of ~101.1° is clearly superior to ethyl (~84.7°) and phenyl (~85.2°) as backbones. Using the standard deviation σ (or "width" of the distribution) as a measure for the rigidity of the backbone, it is found that the ferrocene backbone seems to be considerably more flexible (σ = 2.95°) than ethyl or phenyl. This may be an effect of the low barrier for internal rotation in ferrocene (~3.8 kJ·mol^{-1}).[210] Interestingly, ethyl and phenyl as backbones show very similar bite angle properties, with much narrower distributions. While both are similar in that they from a

Table 4.22: Parameters of the normal distributions fitted to the bite angle histograms of the four different binaphane-type ligands.

Backbone	μ [°]	σ [°]
Ferrocenyl	101.14	2.95
Ethyl	84.66	2.30
Phenyl	85.20	2.20
BISBI	110.29	4.51

Backbone	ee [%]
Ferrocenyl	67.2
Ethyl	6.3
Phenyl	7.3
BISBI	85.4

Table 4.23: Computed enantiomeric excess from integration of $ee(\alpha)$ weighted with the bite angle distribution $\rho(\alpha)$ obtained from MD simulations.

five-membered ring with ruthenium mediated by a C-C bridge, the difference between the aromatic bond and single bond in the backbone seems to be subtle. As one might expect, the phenyl backbone is slightly more rigid with σ = 2.30° vs. 2.20°. The BISBI-type backbone has the largest σ of 4.25°, indicating that the biaryl moiety is relatively flexible. BISBI also shows the largest mean bite angle of ~112.2°, which is promising as larger bite angles should induce higher enantioselectivity.

The normal distributions $\rho(\alpha)$ of the bite angles were then renormalized on the interval of 80 to 120°, so that

$$\int_{80}^{120} \rho(\alpha) d\alpha = 1 \tag{4.11}$$

since we want to calculate the expected enantiomeric excess from the integral over the product of the $ee(\alpha)$ function and $\rho(\alpha)$ as in equation 4.10. The effect of normalization is not very large, since the integral even for ethyl and phenyl outside of the interval is < 0.05 (see appendix, 6.2.6). With the normalized $ee(\alpha)$ function, the expected enantiomeric excess is calculated. The results are shown in Table 4.23.

According to our model, the regular ligand with a ferrocene backbone therefore should result in an enantiomeric excess of around ~67%, which reproduces the value obtained in our mechanistic studies (77% by lowest TS comparison, 67% from Boltzmann averaging, which is also implemented in the model). This indicates that the deviation introduced by the dis-

connection and fixing of the ligand sphere does at least not negatively influence our model in the bite angle range for which the original mechanistic studies were performed. Going on to the ethyl and phenyl backbone, a low enantiomeric excess of < 10% ee is predicted. For BISBI as a backbone, a higher enantiomeric excess of 85.4% is estimated, which would suggest an advantage over (*S*,*S*)-*f*-binaphane.

4.4.4 Summary and Conclusion

In this section, a model for estimation of enantioselectivity for binaphane-type ligands of varying bite angles was presented. The model is based on bite angle scans of the previously obtained proton transfer transition states in our mechanistic studies of the [Ru(I)H(CO)((*S*,*S*)-*f*-binaphane)(PPh_3)] catalyst. Such bite angle differences would be achieved by incorporating different linkers/backbones into the binaphane. The bite angle scans result in curves that represent the energy of a TS as a function of the ligand bite angle. These can be Boltzmann weighted to give a general function of the expected enantiomeric excess with regard to the bite angle. The bite angle dependency shows that larger bite angles should result in higher ee, which gives reason to believe that our ligand backbone can be improved for higher enantioselectivity. Two methods were proposed to identify new suitable ligands: molecular dynamics simulations of suggested backbones and a search of the CSD for chelating bisphosphine ligands. Problems with the MD simulations were that conformational backbone changes could not be captured as the computationally accessible time scales are too short and that the suggested ligands are limited by intuition. We therefore focused on a search of the CSD database to get a more comprehensive picture of ligand backbones that might be applied to the asymmetric reductive amination. After initial filtering of the database search results, Xantphos and BISBI-type backbones were identified as promising candidates from more than 200 structures. A more detailed look at the computed structures casts doubt on the feasibility of Xantphos-type ligands as they are too bulky for a backbone, distort the unique parallel-shaped geometry and seem to be under stress with a long Ru-P bond to the metal. Also, a side-on coordination is favored for these complexes which would completely remove the chiral pocket of the ligand that is assumed to be crucial for enantioselectivity. BISBI as a backbone, however, does not have these issues, it preserves the general catalyst structure while having a very large bite angle of 111.8°, even larger than the Xantphos backbone.

To conclude, we think that a BISBI-backbone binaphane ligand is a promising candidate for asymmetric reductive amination. A compation of the full catalytic cycle might reveal more insights on this ligand. BISBI's potential to be chiral itself through atropisomerism might be an issue, but that has to be investigated more thoroughly. It is suggested that the BISBI-backbone binaphane should be explored in more detail by synthesis of the corresponding ligand/catalyst and testing in catalysis as it has the potential of achieving high enantioselectivities.

5

Conclusion & Outlook

In this thesis, the aim was to gain new insights into two industrially relevant chemical reactions: the dehydroperoxidation of cyclohexyl hydroperoxide to cyclohexanone and the direct asymmetric reductive amination of ketones into chiral primary amines. The results, and a short outlook with suggestions for the future, will be presented briefly in this chapter. For the dehydroperoxidation, the investigations into the initial vanadium catalyst will be summarized, followed by the approach that led us to our work on the more selective chromium catalysis. In the section on the asymmetric reductive amination, we will discuss the research on the mechanism of the hydrogenation and the follow-up idea for a better future ligand.

5.1 Dehydroperoxidation

The research on the dehydroperoxidation of cyclohexyl hydroperoxide is motivated by the aim to achieve a high ketone-to-alcohol ratio, which is desired due to the higher value of cyclohexanone as a precursor in the synthesis of ϵ-caprolactam, the monomer of Nylon-6. In theory, cyclohexyl hydroperoxide can be decomposed into the ketone with water as the sole byproduct. This could avoid costly steps for separation of KA oil into ketone and alcohol, as well as the necessary dehydrogenation of alcohol to yield the ketone. However, in the industri-

ally applied dehydroperoxidation, selectivity is low in the radical-based dehydroperoxidation, and KA oil mixtures with varying ketone-to-alcohol ratios are obtained.

Vanadium dipicolinato complexes that showed promising selectivities with a test substrate, 4-heptyl hydroperoxide, sparked our interest in the computational study of these to obtain more knowledge on the mechanism. We were especially interested, whether a radical-free mechanism is acting here, as this was suggested by experimental data. In fact, our calculations showed that such a radical-free mechanism is feasible and can also proceed without change of the oxidation state of vanadium. The dehydroperoxidation takes place by a hydrogen transfer of the α-hydrogen on the alkylperoxide bound to vanadium to the vanadium oxo group, while the O-O bond of the alkylperoxo ligand is simultaneously cleaved. This step is rate-determining. The resulting oxo hydroxo vanadium species can then undergo addition of a new alkyl hydroperoxide substrate molecule. The hydroperoxide addition is supported by proton relay agents such as water (which is formed through the reaction) or cyclohexanol. The coordination of water *trans* to the vanadium oxo group acting as a hydrogen acceptor lowers the barrier for dehydroperoxidation. More importantly, we find that the dehydroperoxidation of cyclohexyl hydroperoxide has a higher barrier compared to that of 4-heptyl hydroperoxide by 15 to 18 $kJ \cdot mol^{-1}$, which is in good agreement with the better ketone selectivities observed with 4-heptyl hydroperoxide. Besides this central mechanism, we were able to rule out other potential mechanisms of dehydroperoxidation such as hydrogen transfer to the ligand, the direct insertion of the α-hydrogen into the O-O bond, substrate addition to the carboxyl group or variants of these mechanisms with proton relay agents. As our mechanism showed that the *cis* oxo alkylperoxo/hydroxo motif on vanadium is crucial for the dehydroperoxidation with the key step being the six-membered TS with hydrogen transfer and O-O bond cleavage, we started to investigate other metals that are known to form stable oxo complexes of a similar type.

After a screening of different metal (oxo) species, we arrived at chromium trioxide and derivatives (e.g. CrO_3 on polyvinyl pyridine) as suitable dehydroperoxidation catalysts. The quantum chemical studies show that a very similar mechanism acts here, with a concerted hydrogen transfer and O-O bond cleavage being the rate-determining step, while preserving the oxidation state of +6 on chromium. The main difference to our previous system with the vanadium catalyst is the lower activation energy, which explains the better selectivities – the Cr(VI) catalyst achieves very high ketone selectivities and is much more active than the vanadium dipicolinato complex. The findings confirm the results of Buijs et al. who studied this reaction previously. A mechanism that was proposed by Boitsov et al., involving an intermolecular hy-

drogen transfer from alcohol to hydroperoxide in a mixed $CrO_2(OCy)(OOCy)$ complex, was also studied. While formation of this intermediate is feasible, the suggested dehydroperoxidation is energetically disfavored and can therefore be ruled out.

The mechanistic studies on the hydroperoxidation have shed light on how both vanadium and chromium can perform as dehydroperoxidation catalysts in a radical-free pathway that does not change the oxidation state of the catalyst. The investigated mechanisms are energetically feasible and explain why chromium(VI) is more active than vanadium(V) or why 4-heptyl hydroperoxide tends to have better ketone-to-alcohol ratios with vanadium(V). For future studies of the topic, questions remain that have not been the focus of this work. To gain more understanding that will be helpful in the application and optimization of the chromium-based dehydroperoxidation, a study of radical initiations and means to prevent these would be advantageous. The interaction of PVP with the chromium catalyst was also only studied in a simple pyridine-coordinating model. Since immobilization of Cr with PVP is crucial to industrial application (due to the toxicity of Cr(VI)), more in-depth studies to understand the CrO_3-PVP system may be very interesting.

5.2 Asymmetric Reductive Amination

The direct asymmetric reductive amination of ketones to primary chiral amines, using only ammonia and hydrogen is of special interest as it is one of the most elegant, affordable, and atom-efficient ways to access primary chiral amines. The aim in this project was to understand the structure of the complex and the mechanism behind the asymmetric hydrogenation, as our experimental insights were limited and mechanistic understanding would be beneficial for improvement of the catalyst system. Until today, the protocol developed at CaRLa is the only system achieving high, albeit not very high, enantioselectivities directly from ketones with only NH_3/H_2 and a chiral ruthenium catalyst.

The starting point for the investigations were experimental observations that hinted at the catalyst structure, but did not allow for a precise statement on what the catalyst structure exactly looks like. Using the experimental evidence, several possible catalyst structures were evaluated of which only two — complex types **A** and **B** — seemed reasonable from an energetic perspective or the ability to engage in hydride transfer. The suggested structure was later confirmed by X-ray crystallography. Based on these complexes, an energetically feasible mechanism was proposed. The mechanism starts from the η^1-coordinated imine, which goes into η^2 coordination and then receives a hydride transfer from the catalyst onto the electrophilic

carbon of the imine. This step, however, is reversible as the following agostic amide or trigonal bipyramidal amide complexes are endergonic with respect to the initial imine. Coordination of dihydrogen forms the σ-dihydrogen complexes. The following heterolytic H-H cleavage to protonate the amide is the rate-determining step and is responsible for the enantioselectivity. The proton transfer transition state irreversibly leads to the amine, which through decoordination and coordination of new substrate closes the catalytic cycle. Throughout the whole reaction pathways and especially for the proton transfer transition state, it is important to investigate the possible isomer/conformer combinations in detail. These arise from the complex having two general isomeric structures, the configuration of the imine double bond, the two chiral faces of the imine and the orientation and conformation of the amide after the hydride transfer. Taking all of these species and variants into account, the mechanism predicts the observed enantioselectivity accurately. The mechanistic studies were then extended to the full series of halides for the ruthenium catalyst and both trend and magnitude of the ee could be reproduced by the computation. Additionally, the chemoselectivity is predicted correctly with the hydrogenation of the ketone being disfavored over the imine for the iodide-based catalyst. In the case of fluoride, we suspect that formation of HF can replace the protonation from H_2 and thus leads to formation of alcohol, although more studies might be needed to explain the change in chemoselectivity for this catalyst.

In the second part of the chapter on the asymmetric reductive amination, the gained mechanistic insights were applied to find potential candidates that improve enantioselectivity. This is desirable as enantioselectivity in the 90-99% range has not been achieved yet, and also due to alkyl-alkyl ketones still giving lower enantioselectivities than their aryl-alkyl counterparts. Since the employed binaphane ligand is unique in that it is the only ligand so far giving any considerable enantioselectivity, the idea was to keep the binaphane motif and enhance it, rather than trying to find a completely new ligand from scratch. Altering the bite angle seemed to be the most straightforward way of optimizing the ligand. Therefore, a model was built that uses the proton transfer transition states from the previous mechanistic investigation and probes the energy dependence of the transition states with respect to the bite angle. This way, the expected enantioselectivity as a function of the bite angle was obtained. The model predicts that for larger P-Ru-P bite angles, higher enantioselectivities should be possible to achieve. With this general prediction, the CSD was screened for potential backbone candidates to replace the ferrocenyl linker on the binaphane ligand and get a larger bite angle. Out of about 200 candidates, Xantphos- and BISBI-like linkers appeared to be the most promising. The corresponding structures were calculated and revealed that Xantphos-like backbones might be sterically too demanding and result in a distorted structure likely unable to improve enantios-

electivity. The BISBI-type complex, however, largely preserved the original structural motif while having a considerably larger bite angle, making it a very interesting candidate to now test experimentally.

The quantum chemical investigations on the asymmetric reductive amination enabled us to correctly predict the catalyst's structure, followed by a mechanistic study that shows how enantioselectivity is primarily determined by the proton transfer transition state, for which an in-depth analysis of isomers and conformers is crucial. Treating these in detail, the enantioselectivity could be successfully predicted for the catalyst system and the corresponding series of halides in both trend and magnitude. The origin of chemoselectivity lies in the preference of imine hydrogenation over ketone hydrogenation, which is established for our catalyst, but not entirely clear for the inverted chemoselectivity with fluoride as a ligand on ruthenium. Using these results, a model was built that predicts better enantioselectivities for larger binaphane bite angles. Upon search in the CSD, evaluation of possible candidates and MD simulations, BISBI is suggested as a promising backbone for a future binaphane. In this large area of research, many questions still remain. It would be interesting to study the cause of alcohol formation for the fluoride-containing catalyst in more detail. Regarding the prediction of new ligands, a BISBI-linked binaphane should be synthesized and tested. The bite angle model also has room for optimization. It does for example not take into account that activity and chemoselectivity might change. While we expect better enantioselectivity for larger bite angles, we do not know in what bite angle range the model is accurate (it might well be less than 80 to 120°). A full computation of the mechanism with the proposed ligand would therefore be useful. Other issues are the treatment of vibrations for the fixed structures or the influence of replacing the linker by just hydrogen atoms. Another very interesting project for the future would also be an automated generation of backbone molecules: both the own chemical intuition and the CSD are limited and the linkers we found are relatively concentrated into small bite angle ranges. Such an algorithm would also be potentially very useful for many other applications.

6 Appendix

6.1 Dehydroperoxidation

6.1.1 Coordinates

Due to the large number of calculated structures, coordinates are not included in the appendix, but can be accessed for all structures from this chapter on the attached DVD, in the file

coord-dehydroperoxidation.txt

The naming is consistent with the numbering or nomenclature throughout the thesis or the tables with the respective energies in the appendix. For smaller compounds, trivial names or the molecular formula may have been used. The coordinates are given in atomic units a_0.

6.1.2 Energies

Total free enthalpies of all structures computed in the investigation of the vanadium-catalyzed dehydroperoxidation can be found in the following table. In addition, the eletronic energies at the level of optimization (BP86/def2-SV(P)), final electronic energies (PBE0-D3(BJ)/def2-QZVPP), corrections to the thermodynamic reference (ΔG_{gas}), the zero-point vibrational energy and the solvent corrections in cyclohexane from COSMO-RS (ΔG_{solv}) are given.

Structure	Total G [kJ/mol]	BP86 def2-SV(P) [E_h]	PBE0-D3(BJ) def2-QZVPP [E_h]	ΔG_{gas} [kJ/mol]	ZPVE [kJ/mol]	ΔG_{solv} [kJ/mol]
H2O	-200535.60	-76.345030	-76.385784	5.93	52.49	9.3
H2O2	-397656.44	-151.423878	-151.465972	6.59	65.50	10.8
Hydroxy Radical	-198616.24	-75.652579	-75.646023	-22.37	20.53	14.7
Cyclohexanone	-812744.92	-309.655383	-309.669874	304.20	384.30	-11.0
CyOH	-815850.70	-310.844917	-310.876412	364.23	444.10	-9.0
CyOOH	-1012997.83	-385.929257	-385.966017	366.62	452.00	-10.8
Cyclohexyl Radical	-616755.99	-235.023690	-235.030136	319.24	395.90	-3.7
Cyclohexyloxyl-Radical	-814121.71	-310.184783	-310.204400	330.00	409.40	-10.2
Cyclohexylhydroperoxyl Radical	-1011358.56	-385.304764	-385.330540	337.74	422.60	-11.1
4-Hydroperoxyheptane	-1119164.01	-426.399127	-426.441226	469.44	571.40	-12.2
4-Heptanone	-918926.19	-350.131552	-350.150047	404.41	503.30	-11.8
4-Heptanol	-922020.08	-351.318220	-351.353481	468.50	563.90	-10.1
V-Dipic-Oxo Radical	-4313481.41	-1643.170698	-1642.968414	156.27	255.50	-24.7
V-Dipic-Oxo-O Radical	-4510724.14	-1718.321068	-1718.089368	153.43	258.00	-34.6
V-Dipic-Oxo-OO Radical	-4707991.10	-1793.444724	-1793.228570	159.13	271.20	-29.3
1	-4512528.94	-1718.995206	-1718.792835	186.64	290.70	-25.6
3	-5525554.40	-2104.951011	-2104.787175	612.98	748.80	-49.5
4	-5325009.78	-2028.580394	-2028.382959	556.55	686.50	-47.6
5	-5324991.83	-2028.577445	-2028.374875	553.00	685.60	-47.4
TS6	-5324908.68	-2028.556195	-2028.340153	545.15	675.30	-47.5
TS8	-5525446.26	-2104.922284	-2104.743104	605.00	740.70	-49.0
TS9	-5725996.89	-2181.295339	-2181.151162	662.13	804.40	-47.5
TS10	-6341320.30	-2415.793154	-2415.646142	1023.94	1190.00	-66.2
11	-5631711.44	-2145.418892	-2145.260234	717.31	868.20	-48.8
12	-5431171.32	-2069.049851	-2068.858075	661.63	806.10	-46.9
13	-5431156.60	-2069.047238	-2068.850535	656.87	805.30	-47.2
TS14	-5431084.17	-2069.029320	-2068.819731	647.94	794.90	-46.7
TS15	-6553655.84	-2496.734346	-2496.598576	1227.55	1427.00	-64.8
16	-5525531.72	-2104.945490	-2104.776165	606.67	746.90	-49.4
TS17	-5525453.41	-2104.924421	-2104.742300	595.59	736.20	-48.9
18	-4713042.07	-1795.353064	-1795.183562	238.89	352.10	-27.2
19	-5631694.66	-2145.415038	-2145.251431	710.28	866.40	-48.1
TS20	-5631625.10	-2145.397475	-2145.221592	700.96	855.80	-47.6
21	-5525504.03	-2104.934792	-2104.765224	605.36	746.60	-49.1
TS22	-5525445.30	-2104.919037	-2104.737792	593.16	735.40	-50.2
23	-5631669.84	-2145.404798	-2145.240990	707.35	866.00	-47.8
TS24	-5631613.22	-2145.391961	-2145.217208	702.35	856.90	-48.6
TS25	-5525392.33	-2104.912921	-2104.719917	599.54	737.00	-50.5
TS26	-6140727.13	-2339.404362	-2339.214164	943.42	1106.00	-64.7
TS27	-6337844.59	-2414.487019	-2414.298638	960.47	1128.00	-64.9
TS28	-5324857.21	-2028.538472	-2028.317963	541.81	670.80	-51.0

Structure	Total G [kJ/mol]	BP86 def2-SV(P) [E_h]	PBE0-D3(BJ) def2-QZVPP [E_h]	ΔG_{gas} [kJ/mol]	ZPVE [kJ/mol]	ΔG_{solv} [kJ/mol]
29	-4512444.44	-1718.965153	-1718.759070	187.04	293.40	-30.2
TS30	-4512396.17	-1718.946389	-1718.736845	178.20	281.20	-31.4
TS31	-5525474.29	-2104.924901	-2104.754472	605.06	740.60	-47.3
32	-5525499.06	-2104.932886	-2104.763702	603.91	746.30	-46.7
TS33	-5525409.51	-2104.905106	-2104.724019	588.41	733.00	-45.8
TS34	-5525391.20	-2104.907139	-2104.718458	597.86	735.10	-51.6
35	-4713029.35	-1795.352332	-1795.180289	242.54	354.20	-26.7
TS36	-4712927.85	-1795.315325	-1795.136585	233.06	343.60	-30.5
TS37	-4712966.54	-1795.330996	-1795.153685	238.41	347.40	-29.6
TS38	-5324816.80	-2028.520730	-2028.299798	531.89	665.30	-48.3
TS39	-5324815.27	-2028.518755	-2028.298224	531.57	665.30	-50.6
TS40	-5525406.57	-2104.920781	-2104.727741	604.61	738.30	-49.3
TS41	-6140730.88	-2339.413636	-2339.222540	961.68	1122.00	-64.7
TS42	-6337868.70	-2414.497882	-2414.304564	959.32	1130.00	-72.3

Total free enthalpies of all structures computed in the investigation of the chromium-catalyzed dehydroperoxidation can be found in the following table. In addition, the eletronic energies at the level of optimization (BP86/def2-SV(P)), final electronic energies (PBE0-D3(BJ)/def2-QZVPP), corrections to the thermodynamic reference (ΔG_{gas}), the zero-point vibrational energy and the solvent corrections in cyclohexane from COSMO-RS (ΔG_{solv}) are given.

Structure	Total G [kJ/mol]	BP86 def2-SV(P) [E_h]	PBE0-D3(BJ) def2-QZVPP [E_h]	ΔG_{gas} [kJ/mol]	ZPVE [kJ/mol]	ΔG_{solv} [kJ/mol]
H2O	-200537.33	-76.345028	-76.385784	4.20	52.48	9.3
CyO	-812745.07	-309.655376	-309.669875	304.00	384.20	-10.9
Cy-O Radical	-814102.67	-310.183878	-310.196433	326.93	406.50	-9.0
CyOH	-815849.96	-310.844999	-310.876230	364.23	444.20	-8.8
CyOOH	-1012998.71	-385.929208	-385.966018	365.76	451.40	-10.8
Pyridine	-651227.54	-248.106138	-248.095920	154.04	226.30	-5.8
43	-3534627.03	-1346.494018	-1346.273334	9.72	87.08	3.4
TS44	-4547539.52	-1732.416164	-1732.217771	423.03	536.40	-25.4
TS45	-5363421.16	-2043.287991	-2043.120051	835.48	982.30	-45.7
TS46	-4748088.00	-1808.790767	-1808.624061	479.63	596.90	-25.8
47	-4347111.54	-1656.082786	-1655.862931	374.04	480.70	-18.1
TS48	-4347027.84	-1656.060099	-1655.827377	365.25	468.40	-18.9
49	-4962451.11	-1890.583499	-1890.361033	730.38	866.20	-39.3
TS50	-4962365.79	-1890.560724	-1890.325216	723.21	854.60	-40.9
51	-4149968.39	-1580.996376	-1580.772990	368.83	472.60	-18.3
52	-5159592.68	-1965.670122	-1965.451132	738.53	874.70	-40.0
TS53	-5159504.96	-1965.645776	-1965.414007	730.24	862.10	-41.5
54	-4801166.48	-1829.101344	-1828.871681	580.92	707.90	-45.5
55	-4998302.43	-1904.181608	-1903.955294	578.18	714.60	-46.7
TS56	-4801104.82	-1829.080571	-1828.843937	569.37	693.70	-45.1
TS57	-4998253.55	-1904.168157	-1903.932511	569.41	702.10	-48.9
58	-4149968.39	-1580.996376	-1580.772990	368.83	472.60	-18.3
TS59	-5162880.75	-1966.921576	-1966.719073	784.39	912.20	-45.0
TS60	-5162887.22	-1966.918373	-1966.719936	781.93	919.60	-46.7
61	-4962451.11	-1890.583499	-1890.361033	730.38	866.20	-39.3
TS62	-4962282.21	-1890.532787	-1890.291415	726.10	851.10	-48.9
63	-4998336.35	-1904.199554	-1903.971230	584.70	714.40	-45.3
64	-5613661.96	-2138.695181	-2138.465680	938.90	1096.00	-60.0
65	-5810792.22	-2213.779193	-2213.552144	951.15	1107.00	-63.1
TS66	-4998251.71	-1904.171423	-1903.933977	571.86	697.20	-45.6
TS67	-5613580.90	-2138.674612	-2138.433086	933.92	1084.00	-59.6
TS68	-5810746.15	-2213.764542	-2213.531672	941.13	1092.00	-60.7
69	-4636574.55	-1766.370508	-1766.103114	371.86	489.90	-43.4
70	-5649443.54	-2152.281466	-2152.040127	797.26	945.00	-60.3
71	-6868737.57	-2616.638437	-2616.165552	9.03	116.70	-4.9
TS72	-8697555.17	-3313.449857	-3313.027348	845.55	1013.00	-48.7
73	-7681222.37	-2926.228838	-2925.756037	376.61	510.70	-27.6
TS74	-7681136.56	-2926.206832	-2925.720969	371.72	498.80	-29.0
75	-3533438.33	-1345.975718	-1345.753569	-18.09	58.99	-144.8
TS76	-5362187.65	-2042.773763	-2042.596793	814.96	954.80	-165.5
77	-4345923.62	-1655.569180	-1655.344675	347.54	452.70	-164.4
TS78	-4345844.64	-1655.547890	-1655.308627	339.13	440.60	-171.6
79	-6867578.68	-2616.151950	-2615.670899	-16.99	89.29	-118.7

Structure	Total G [kJ/mol]	BP86 def2-SV(P) [E_h]	PBE0-D3(BJ) def2-QZVPP [E_h]	ΔG_{gas} [kJ/mol]	ZPVE [kJ/mol]	ΔG_{solv} [kJ/mol]
TS80	-8696384.22	-3312.960950	-3312.526848	814.82	983.00	-161.1
81	-7680053.56	-2925.736667	-2925.255455	346.51	482.60	-143.0
TS82	-7679982.07	-2925.716829	-2925.222179	345.90	471.70	-158.3

6.1.3 NMR Chemical Shifts

Calculated isotropic and anisotropic NMR shifts for cyclohexyl hydroperoxide, the cyclohexyl peroxo ester of chromic acid $CrO_2(OH)(OOCy)$ and tetramethyl silane (reference) are given in the following tables. For tetramethyl silane, the T_d-symmetric structure provided by TURBOMOLE was used, the other species are of C_1 symmetry and shifts of chemically equivalent hydrogen atoms in these have been averaged. The values provided in the thesis are relative to the standard of tetramethyl silane. Atom numbers correspond to the numbering of atoms as in the provided coordinates.

Atom No.	Element	Multiplicity	Isotropic Shift [ppm]	Anisotropic Shift [ppm]
1	Si	1	315.62193120	0.00000934
2	C	4	183.93844547	9.10203904
3	H	12	31.69529446	9.18176902

Table 6.3: Calculated NMR data for tetramethyl silane.

Atom No.	Element	Multiplicity	Isotropic Shift [ppm]	Anisotropic Shift [ppm]
1	C	1	155.08393899	14.66414481
2	C	1	148.64125398	24.38099767
3	C	1	153.41855280	5.76578908
4	H	1	29.90758710	10.25670085
5	H	1	30.42316257	8.51211610
6	C	1	153.93851644	13.44363738
7	H	1	30.58032555	8.52058135
8	H	1	30.06312191	9.87552198
9	C	1	94.09414423	70.37157890
10	H	1	30.75681197	6.94279216
11	H	1	29.23503101	7.88005895
12	C	1	149.90343982	12.89865390
13	H	1	30.35436392	8.56368566
14	H	1	29.90586673	10.26637179
15	H	1	29.90686411	8.86645105
16	H	1	30.75200298	6.90090923
17	H	1	27.85081838	4.57676614
18	O	1	33.18665858	392.17864956
19	O	1	83.23197557	409.88161438
20	H	1	25.07658107	13.41300769

Table 6.4: Calculated NMR data for cyclohexyl hydroperoxide.

Atom No.	Element	Multiplicity	Isotropic Shift [ppm]	Anisotropic Shift [ppm]
1	Cr	1	-3181.83128458	504.78744480
2	O	1	-75.92971255	759.02520991
3	O	1	-395.99626925	712.47469654
4	O	1	-1174.16765281	1144.02880548
5	O	1	-1171.81404070	1415.82929073
6	O	1	-81.95619564	300.18059426
7	C	1	93.41163629	72.45127902
8	C	1	149.53343244	10.49320622
9	C	1	148.45324528	17.92649131
10	H	1	27.50671844	5.93699573
11	C	1	155.13543912	15.44186285
12	H	1	29.58730839	9.75153894
13	H	1	30.53291876	7.56288882
14	C	1	154.04938427	15.10682971
15	C	1	153.99455526	6.80659833
16	H	1	30.43142362	9.00021651
17	H	1	29.90260879	10.06151938
18	H	1	30.02722015	9.45560930
19	H	1	30.52993772	8.30337174
20	H	1	29.77221433	9.83820282
21	H	1	30.21319173	8.88345253
22	H	1	30.33275781	7.42989915
23	H	1	29.48237453	10.35072697
24	H	1	19.87283408	18.56051415

Table 6.5: Calculated NMR data for $CrO_2(OH)(OOCy)$.

6.2 Asymmetric Reductive Amination

6.2.1 Coordinates

Due to the large number of calculated structures, coordinates are not included in the appendix, but can be accessed for all structures from this chapter on the attached DVD, in the file

coord-reductiveamination.txt

The naming is consistent with the numbering and nomenclature throughout the thesis or the tables with the respective energies in the appendix. For smaller compounds, trivial names or the molecular formula may be used. The coordinates are given in atomic units a_0.

6.2.2 Energies

Total free enthalpies of all structures computed in the investigation of the reductive asymmetric amination can be found in the following table. In addition, the eletronic energies at the level of optimization (BP86/def2-SV(P)), final electronic energies (PBE0-D3(BJ)/def2-QZVPP), corrections to the thermodynamic reference (ΔG_{gas}), the zero-point vibrational energy and the solvent corrections in cyclohexane from COSMO-RS (ΔG_{solv}) are given.

Structure	Total G [kJ/mol]	BP86 def2-SV(P) [E_h]	PBE0-D3(BJ) def2-QZVPP [E_h]	ΔG_{gas} [kJ/mol]	ZPVE [kJ/mol]	ΔG_{solv} [kJ/mol]
Hydrogen	-3066.09	-1.169999	-1.168772	-6.62	25.51	18.5
Ammonia	-148352.45	-56.496108	-56.519883	36.04	86.33	8.3
Water	-200552.03	-76.345030	-76.385784	4.21	52.49	6.0
HF	-263621.21	-100.344742	-100.399730	-20.90	22.37	10.6
Fluoride Anion	-262390.88	-99.690006	-99.791328	-37.20	0.00	-340.2
Chloride Anion	-1208376.74	-460.129166	-460.138936	-39.53	0.00	-231.2
Bromide Anion	-6758268.42	-2574.188148	-2573.988324	-42.55	0.00	-209.1
Iodide Anion	-782145.80	-297.928845	-297.811392	-44.27	0.00	-186.4
Acetophenone	-1009569.31	-384.616382	-384.614162	265.49	351.70	-19.0
Alcohol	-1012664.55	-385.798004	-385.814674	322.08	410.00	-18.9
Methylphenylimine E	-957352.09	-364.742648	-364.738232	298.14	384.10	-18.7
Methylphenylimine Z	-957349.04	-364.740178	-364.736522	296.22	383.30	-18.2
Triphenylphosphine	-2718648.58	-1035.732500	-1035.674906	575.64	698.30	-48.7
(S,S)-f-Binaphane	-10569867.82	-4026.848521	-4026.461736	1764.67	1976.00	-147.3
Phenylethaneamine	-960480.58	-365.943916	-365.952293	354.76	443.10	-16.3
Secondary Imine	-1769486.46	-674.187818	-674.174185	610.40	731.90	-41.4
Catalyst Complex Type A	-12048580.06	-4590.280831	-4589.721057	1897.37	2130.00	-155.1
Catalyst Complex Type B	-12048584.77	-4590.282302	-4589.723100	1899.13	2130.00	-156.2
Catalyst Complex Type C	-12048576.60	-4590.276266	-4589.718787	1898.11	2129.00	-158.4
Catalyst Complex Type D	-12048573.77	-4590.274984	-4589.717063	1897.14	2129.00	-159.1
Catalyst Complex Type E	-12048511.44	-4590.252078	-4589.689900	1894.62	2128.00	-165.6
Catalyst Complex Type F	-12048511.53	-4590.251224	-4589.689995	1894.05	2127.00	-164.8
1I-ARE	-12857548.12	-4898.509767	-4897.937336	2163.58	2420.00	-167.7
1I-ARZ	-12857583.31	-4898.523002	-4897.948071	2158.81	2419.00	-169.9
1I-ASE	-12857566.98	-4898.516456	-4897.942516	2160.36	2419.00	-169.7
1I-ASZ	-12857575.99	-4898.518651	-4897.946512	2163.47	2419.00	-171.3
1I-BRE	-12857572.06	-4898.518412	-4897.945938	2162.80	2419.00	-168.2
1I-BRZ	-12857580.94	-4898.519835	-4897.948454	2163.71	2419.00	-171.4
1I-BSE	-12857572.79	-4898.518333	-4897.946123	2162.43	2419.00	-168.1
1I-BSZ	-12857578.20	-4898.521889	-4897.945433	2158.46	2419.00	-171.4
2I-ARE	-12857505.73	-4898.487215	-4897.918880	2157.98	2417.00	-168.1
2I-ARZ	-12857519.99	-4898.495224	-4897.927232	2164.84	2418.00	-167.3
2I-ASE	-12857529.78	-4898.498547	-4897.931217	2163.19	2417.00	-165.0
2I-BRE	-12857528.44	-4898.496255	-4897.929695	2161.04	2417.00	-165.5
2I-BRZ	-12857519.03	-4898.491369	-4897.924446	2160.09	2417.00	-168.9
2I-BSZ	-12857516.26	-4898.492865	-4897.925743	2161.87	2418.00	-164.5
TSHI-ARE	-12857486.93	-4898.479180	-4897.914128	2161.17	2413.00	-165.0
TSHI-ARZ	-12857505.48	-4898.486677	-4897.921261	2163.13	2414.00	-166.8
TSHI-ASE	-12857511.78	-4898.489035	-4897.924398	2163.95	2414.00	-165.7
TSHI-ASZ	-12857484.04	-4898.477319	-4897.911855	2161.57	2414.00	-168.5
TSHI-BRE	-12857513.10	-4898.488754	-4897.924793	2163.23	2414.00	-165.2

Structure	Total G [kJ/mol]	BP86 def2-SV(P) [E_h]	PBE0-D3(BJ) def2-QZVPP [E_h]	ΔG_{gas} [kJ/mol]	ZPVE [kJ/mol]	ΔG_{solv} [kJ/mol]
TSHI-BRZ	-12857497.42	-4898.482316	-4897.917875	2163.10	2414.00	-167.6
TSHI-BSE	-12857494.06	-4898.481916	-4897.917611	2164.26	2414.00	-166.1
TSHI-BSZ	-12857501.36	-4898.483825	-4897.918810	2162.27	2414.00	-168.2
3I'-ARE	-12857490.88	-4898.482172	-4897.917017	2167.10	2421.00	-167.3
3I'-ARZ	-12857504.50	-4898.488633	-4897.922632	2168.61	2421.00	-167.7
3I'-ASE	-12857510.67	-4898.490833	-4897.926179	2169.70	2421.00	-165.6
3I'-ASZ	-12857486.01	-4898.481287	-4897.915371	2167.54	2421.00	-167.2
3I'-BRE	-12857512.14	-4898.489893	-4897.926030	2168.49	2420.00	-166.3
3I'-BRZ	-12857498.88	-4898.485616	-4897.919894	2168.32	2421.00	-169.0
3I'-BSE	-12857494.88	-4898.485116	-4897.919784	2169.67	2421.00	-166.6
3I'-BSZ	-12857497.58	-4898.485760	-4897.919698	2168.41	2421.00	-168.3
3I-RCOH	-12857519.05	-4898.500114	-4897.929064	2168.35	2428.00	-165.1
3I-RCOMe	-12857487.45	-4898.488960	-4897.918419	2173.49	2429.00	-166.6
3I-RCOPh	-12857500.68	-4898.489543	-4897.924692	2175.05	2428.00	-164.9
3I-RIH	-12857537.92	-4898.506808	-4897.935529	2170.00	2428.00	-168.6
3I-RIMe	-12857532.42	-4898.503929	-4897.933669	2172.51	2428.00	-170.5
3I-SCOH	-12857520.51	-4898.501741	-4897.929907	2169.88	2428.00	-165.9
3I-SIH	-12857534.86	-4898.506410	-4897.933950	2166.11	2427.00	-165.8
3I-SIMe	-12857535.24	-4898.504537	-4897.933324	2169.43	2428.00	-171.2
4I-ARCOH	-12860549.76	-4899.658469	-4899.098384	2212.51	2468.00	-169.9
4I-ARCOMe	-12860539.28	-4899.656056	-4899.095396	2210.55	2468.00	-165.3
4I-ARIH	-12860581.46	-4899.670451	-4899.111004	2211.04	2468.00	-167.0
4I-ARIMe	-12860565.06	-4899.663677	-4899.102923	2208.88	2467.00	-169.7
4I-ARIPh	-12860571.30	-4899.663158	-4899.105038	2210.08	2466.00	-171.6
4I-ASCOH	-12860564.48	-4899.666304	-4899.105576	2212.58	2468.00	-165.8
4I-ASCOMe	-12860546.46	-4899.657846	-4899.096496	2211.59	2468.00	-170.6
4I-ASCOPh	-12860542.30	-4899.657250	-4899.096102	2211.27	2468.00	-167.2
4I-ASIMe	-12860559.85	-4899.665108	-4899.103879	2212.66	2469.00	-165.7
4I-ASIPh	-12860573.57	-4899.665586	-4899.106096	2207.64	2466.00	-168.6
4I-BRCOH	-12860567.56	-4899.667388	-4899.105573	2210.27	2467.00	-166.6
4I-BRCOPh	-12860554.56	-4899.659273	-4899.099928	2208.30	2466.00	-166.4
4I-BRIH	-12860556.93	-4899.662322	-4899.100572	2211.19	2468.00	-170.0
4I-BRIMe	-12860551.08	-4899.661663	-4899.100446	2212.15	2468.00	-165.5
4I-BRIPh	-12860556.89	-4899.662847	-4899.101975	2211.35	2468.00	-166.4
4I-BSCOH	-12860560.81	-4899.661602	-4899.100619	2206.18	2466.00	-168.8
4I-BSCOMe	-12860544.47	-4899.659757	-4899.097921	2212.54	2468.00	-165.9
4I-BSCOPh	-12860558.74	-4899.661998	-4899.102159	2212.09	2467.00	-168.6
4I-BSIH	-12860573.37	-4899.669415	-4899.108953	2212.55	2468.00	-165.8
4I-BSIMe	-12860561.49	-4899.663279	-4899.101932	2211.42	2468.00	-171.2
TSPI-ARCOH	-12860531.88	-4899.651196	-4899.090429	2208.78	2464.00	-169.2
TSPI-ARCOMe	-12860501.35	-4899.644049	-4899.080212	2208.51	2464.00	-165.2
TSPI-ARIH	-12860552.39	-4899.659535	-4899.096947	2204.36	2463.00	-168.2
TSPI-ARIPh	-12860556.20	-4899.659567	-4899.099657	2210.61	2465.00	-171.1
TSPI-ASCOH	-12860536.15	-4899.654813	-4899.092019	2206.55	2463.00	-167.1
TSPI-ASCOPh	-12860488.08	-4899.636142	-4899.073803	2205.32	2462.00	-165.6
TSPI-ASIH	-12860548.81	-4899.656413	-4899.096896	2207.04	2464.00	-167.4
TSPI-ASIMe	-12860528.43	-4899.654397	-4899.089806	2207.30	2464.00	-165.9
TSPI-BRCOH	-12860539.42	-4899.655607	-4899.092410	2204.58	2463.00	-167.3
TSPI-BRCOPh	-12860541.37	-4899.652895	-4899.093614	2206.90	2463.00	-168.4
TSPI-BRIH	-12860545.21	-4899.656080	-4899.093534	2205.58	2463.00	-171.2
TSPI-BRIMe	-12860526.57	-4899.653337	-4899.088817	2206.81	2464.00	-166.1

Structure	Total G [kJ/mol]	BP86 def2-SV(P) [E_h]	PBE0-D3(BJ) def2-QZVPP [E_h]	ΔG_{gas} [kJ/mol]	ZPVE [kJ/mol]	ΔG_{solv} [kJ/mol]
TSPI-BRIPh	-12860522.17	-4899.650243	-4899.087525	2207.48	2464.00	-165.8
TSPI-BSCOH	-12860537.52	-4899.652387	-4899.091351	2204.97	2463.00	-168.6
TSPI-BSCOMe	-12860508.05	-4899.645964	-4899.080996	2203.37	2462.00	-164.7
TSPI-BSIH	-12860551.13	-4899.660256	-4899.097274	2205.31	2463.00	-167.0
TSPI-BSIMe	-12860538.64	-4899.654009	-4899.091623	2206.27	2463.00	-170.3
TSPI-BSIPh	-12860549.34	-4899.658217	-4899.097512	2209.79	2465.00	-169.1
5I-AR	-12860711.56	-4899.723709	-4899.163618	2221.45	2482.00	-169.4
5I-AS	-12860708.13	-4899.721968	-4899.164612	2225.17	2482.00	-167.1
5I-BR	-12860707.67	-4899.723107	-4899.164188	2223.32	2482.00	-165.9
5I-BS	-12860703.93	-4899.720741	-4899.162609	2222.88	2481.00	-165.8
TSHF-ARE	-12337755.70	-4700.382702	-4699.963570	2167.79	2417.00	-159.5
TSHF-ARZ	-12337770.10	-4700.389022	-4699.968707	2168.57	2417.00	-161.2
TSHF-ASE	-12337778.37	-4700.391618	-4699.971904	2169.15	2417.00	-161.7
TSHF-ASZ	-12337752.32	-4700.383384	-4699.961952	2167.72	2417.00	-160.3
TSHF-BRE	-12337775.52	-4700.391389	-4699.971256	2169.76	2418.00	-161.1
TSHF-BRZ	-12337762.37	-4700.387437	-4699.966054	2169.56	2417.00	-161.4
TSHF-BSE	-12337758.67	-4700.385123	-4699.964907	2169.08	2417.00	-160.3
TSHF-BSZ	-12337759.83	-4700.387974	-4699.966273	2172.58	2419.00	-161.3
TSHCl-ARE	-13283731.33	-5060.742283	-5060.265412	2166.91	2415.00	-161.9
TSHCl-ARZ	-13283746.80	-5060.749484	-5060.271936	2169.09	2416.00	-162.4
TSHCl-ASE	-13283758.01	-5060.752273	-5060.276101	2168.30	2415.00	-161.9
TSHCl-ASZ	-13283727.18	-5060.741704	-5060.264072	2167.76	2416.00	-162.1
TSHCl-BRE	-13283764.80	-5060.752128	-5060.279728	2170.43	2417.00	-161.3
TSHCl-BRZ	-13283742.36	-5060.746224	-5060.269135	2167.38	2416.00	-163.6
TSHCl-BSE	-13283738.12	-5060.744869	-5060.268322	2169.42	2416.00	-163.6
TSHCl-BSZ	-13283740.68	-5060.746464	-5060.269061	2168.54	2416.00	-163.3
TSHBr-ARE	-18833619.40	-7174.768357	-7174.103942	2163.20	2414.00	-164.0
TSHBr-ARZ	-18833635.54	-7174.775829	-7174.110881	2165.26	2415.00	-164.0
TSHBr-ASE	-18833644.60	-7174.778512	-7174.114609	2165.36	2414.00	-163.4
TSHBr-ASZ	-18833615.43	-7174.767311	-7174.102408	2163.68	2414.00	-164.5
TSHBr-BRE	-18833642.26	-7174.778342	-7174.114688	2166.97	2416.00	-162.4
TSHBr-BRZ	-18833627.77	-7174.772034	-7174.107885	2165.74	2415.00	-164.6
TSHBr-BSE	-18833625.86	-7174.771020	-7174.107208	2166.11	2414.00	-164.8
TSHBr-BSZ	-18833628.59	-7174.772986	-7174.108254	2166.11	2415.00	-164.8
TSPF-ARCOH	-12340787.75	-4701.552184	-4701.135000	2216.03	2468.00	-164.2
TSPF-ARCOMe	-12340765.31	-4701.546571	-4701.129117	2218.30	2468.00	-159.5
TSPF-ARCOPh	-12340753.76	-4701.540077	-4701.121112	2212.88	2466.00	-163.5
TSPF-ARFH	-12340804.11	-4701.557823	-4701.139948	2209.87	2466.00	-161.4
TSPF-ARFPh	-12340809.17	-4701.559157	-4701.143953	2215.59	2467.00	-161.7
TSPF-ASCOH	-12340789.99	-4701.555589	-4701.138133	2217.54	2468.00	-159.7
TSPF-ASFH	-12340804.93	-4701.556397	-4701.143112	2217.41	2467.00	-161.5
TSPF-ASFMe	-12340789.60	-4701.554351	-4701.135199	2212.02	2467.00	-161.5
TSPF-ASFPh	-12340803.65	-4701.556000	-4701.140791	2212.05	2466.00	-160.9
TSPF-BRCOH	-12340801.97	-4701.558440	-4701.141048	2215.19	2467.00	-161.7
TSPF-BRCOPh	-12340806.40	-4701.557001	-4701.142360	2216.25	2467.00	-163.8
TSPF-BRFH	-12340799.81	-4701.557386	-4701.139552	2214.29	2467.00	-162.6
TSPF-BRFMe	-12340790.64	-4701.556645	-4701.137720	2215.84	2467.00	-159.8
TSPF-BRFPh	-12340785.12	-4701.553315	-4701.135461	2216.09	2467.00	-160.4
TSPF-BSCOH	-12340799.18	-4701.557138	-4701.139949	2215.16	2467.00	-161.8
TSPF-BSCOMe	-12340778.69	-4701.551454	-4701.131889	2213.89	2466.00	-161.2
TSPF-BSFH	-12340806.27	-4701.560348	-4701.141828	2211.30	2466.00	-160.1

Structure	Total G [kJ/mol]	BP86 def2-SV(P) [E_h]	PBE0-D3(BJ) def2-QZVPP [E_h]	ΔG_{gas} [kJ/mol]	ZPVE [kJ/mol]	ΔG_{solv} [kJ/mol]
TSPF-BSFMe	-12340798.10	-4701.557228	-4701.139318	2216.09	2467.00	-163.3
TSPF-BSFPh	-12340808.05	-4701.559834	-4701.144360	2217.35	2468.00	-161.2
TSPCl-ARCOH	-13286769.29	-5061.912477	-5061.439916	2215.21	2466.00	-164.5
TSPCl-ARCOMe	-13286745.73	-5061.905959	-5061.431320	2213.43	2466.00	-161.7
TSPCl-ARClH	-13286790.41	-5061.920026	-5061.446201	2210.43	2465.00	-164.3
TSPCl-ARClPh	-13286793.92	-5061.920601	-5061.449330	2215.59	2466.00	-164.8
TSPCl-ASCOH	-13286776.20	-5061.916488	-5061.442425	2213.69	2466.00	-163.3
TSPCl-ASCOMe	-13286752.81	-5061.906810	-5061.431884	2212.37	2465.00	-166.3
TSPCl-ASClH	-13286788.29	-5061.917334	-5061.446618	2212.68	2466.00	-163.4
TSPCl-ASClMe	-13286769.39	-5061.915941	-5061.440242	2214.48	2466.00	-163.0
TSPCl-BRCOH	-13286782.43	-5061.918368	-5061.443996	2211.82	2465.00	-163.6
TSPCl-BRCOPh	-13286786.84	-5061.916380	-5061.445648	2214.47	2466.00	-166.3
TSPCl-BRClMe	-13286768.38	-5061.916249	-5061.440141	2213.41	2466.00	-161.2
TSPCl-BRClPh	-13286762.47	-5061.912770	-5061.438448	2215.00	2466.00	-161.3
TSPCl-BSCOH	-13286778.93	-5061.915703	-5061.442622	2211.81	2465.00	-163.6
TSPCl-BSCOMe	-13286756.57	-5061.909915	-5061.434213	2211.76	2465.00	-163.3
TSPCl-BSClH	-13286790.55	-5061.921736	-5061.447376	2212.01	2465.00	-163.0
TSPCl-BSClMe	-13286779.27	-5061.916865	-5061.442756	2215.02	2466.00	-166.8
TSPCl-BSClPh	-13286790.37	-5061.920109	-5061.448233	2215.10	2466.00	-163.6
TSPBr-ARCOH	-18836659.97	-7175.939380	-7175.279307	2211.38	2465.00	-166.8
TSPBr-ARCOMe	-18836633.89	-7175.932659	-7175.270064	2209.63	2464.00	-163.3
TSPBr-ARCOPh	-18836622.73	-7175.926368	-7175.263817	2206.17	2462.00	-165.1
TSPBr-ARBrH	-18836680.34	-7175.947269	-7175.285771	2206.94	2463.00	-165.8
TSPBr-ARBrPh	-18836683.48	-7175.947578	-7175.288574	2212.35	2465.00	-167.0
TSPBr-ASCOH	-18836664.85	-7175.943243	-7175.281522	2209.87	2464.00	-164.4
TSPBr-ASBrH	-18836677.80	-7175.944390	-7175.285867	2209.20	2464.00	-165.3
TSPBr-ASBrMe	-18836657.88	-7175.942788	-7175.279162	2209.75	2464.00	-163.5
TSPBr-BRCOH	-18836669.17	-7175.944624	-7175.282344	2207.60	2464.00	-164.3
TSPBr-BRCOPh	-18836673.00	-7175.942308	-7175.283822	2210.42	2464.00	-167.0
TSPBr-BRBrH	-18836672.37	-7175.944682	-7175.282990	2210.19	2465.00	-168.4
TSPBr-BRBrMe	-18836655.84	-7175.942484	-7175.278714	2210.19	2465.00	-163.1
TSPBr-BRBrPh	-18836649.46	-7175.939190	-7175.277152	2211.82	2465.00	-162.4
TSPBr-BSCOH	-18836668.33	-7175.941666	-7175.281285	2206.39	2464.00	-165.0
TSPBr-BSCOMe	-18836644.30	-7175.935588	-7175.272660	2206.55	2463.00	-163.8
TSPBr-BSBrH	-18836679.68	-7175.948547	-7175.286609	2207.87	2464.00	-163.9
TSPBr-BSBrMe	-18836667.37	-7175.943135	-7175.281483	2211.05	2465.00	-168.2
TSPBr-BSBrPh	-18836678.82	-7175.946713	-7175.287136	2211.33	2465.00	-165.1
TSHKF-AR	-12389964.64	-4720.254347	-4719.835148	2133.34	2384.00	-161.2
TSHKF-AS	-12389969.04	-4720.256863	-4719.837107	2134.51	2384.00	-161.6
TSHKF-BR	-12389974.39	-4720.258375	-4719.839334	2135.30	2384.00	-161.9
TSHKF-BS	-12389966.81	-4720.256589	-4719.836793	2136.78	2385.00	-162.5
TSHKI-AR	-12909695.23	-4918.351565	-4917.786319	2128.74	2381.00	-166.4
TSHKI-AS	-12909699.68	-4918.352901	-4917.788166	2129.83	2381.00	-167.1
TSHKI-BR	-12909705.38	-4918.353997	-4917.790425	2130.22	2381.00	-167.3
TSHKI-BS	-12909694.83	-4918.351519	-4917.786462	2129.99	2381.00	-166.9
TSPKF-ARCOH	-12392979.56	-4721.417183	-4721.005031	2189.41	2438.00	-160.6
TSPKF-ARCOMe	-12392992.59	-4721.423365	-4721.006604	2181.81	2435.00	-161.9
TSPKF-ARFH	-12392958.53	-4721.413464	-4720.995612	2187.92	2437.00	-162.8
TSPKF-ARFPh	-12392996.49	-4721.422472	-4721.006233	2182.82	2436.00	-167.8
TSPKF-ASCOH	-12392973.36	-4721.417255	-4720.997554	2180.01	2436.00	-164.7
TSPKF-ASCOMe	-12392994.34	-4721.422611	-4721.009135	2186.41	2437.00	-161.6

Structure	Total G [kJ/mol]	BP86 def2-SV(P) [E_h]	PBE0-D3(BJ) def2-QZVPP [E_h]	ΔG_{gas} [kJ/mol]	ZPVE [kJ/mol]	ΔG_{solv} [kJ/mol]
TSPKF-ASFMe	-12392991.41	-4721.423271	-4721.005583	2183.00	2436.00	-164.6
TSPKF-BRCOPh	-12392998.07	-4721.425430	-4721.008814	2182.82	2435.00	-162.6
TSPKF-BRFH	-12392969.62	-4721.415808	-4721.000259	2187.84	2438.00	-161.7
TSPKF-BRFMe	-12393000.94	-4721.426592	-4721.009900	2185.24	2437.00	-165.1
TSPKF-BSCOMe	-12392998.43	-4721.426598	-4721.009625	2183.89	2436.00	-161.9
TSPKF-BSFH	-12392970.40	-4721.415352	-4720.997555	2184.93	2437.00	-166.6
TSPKF-BSFPh	-12393002.59	-4721.425956	-4721.010689	2185.41	2437.00	-164.8
TSPKI-ARCOH	-12912716.83	-4919.514743	-4918.957295	2183.44	2434.00	-168.3
TSPKI-ARCOMe	-12912736.80	-4919.523147	-4918.960671	2175.70	2432.00	-171.7
TSPKI-ARIH	-12912699.01	-4919.509872	-4918.948970	2178.16	2432.00	-167.1
TSPKI-ARIPh	-12912737.87	-4919.519892	-4918.961020	2174.72	2432.00	-170.9
TSPKI-ASCOH	-12912708.42	-4919.515481	-4918.950677	2176.11	2433.00	-170.0
TSPKI-ASCOMe	-12912734.55	-4919.520734	-4918.962499	2178.79	2433.00	-167.7
TSPKI-ASIMe	-12912733.77	-4919.522221	-4918.960292	2176.09	2432.00	-170.1
TSPKI-BRCOH	-12912710.89	-4919.515122	-4918.950946	2175.06	2432.00	-170.7
TSPKI-BRCOPh	-12912740.81	-4919.522081	-4918.960413	2172.90	2431.00	-173.6
TSPKI-BRIH	-12912702.07	-4919.508618	-4918.951856	2181.32	2433.00	-165.7
TSPKI-BRIMe	-12912730.96	-4919.521784	-4918.959321	2175.18	2432.00	-168.9
TSPKI-BSCOMe	-12912736.38	-4919.524441	-4918.961575	2176.60	2432.00	-169.8
TSPKI-BSIH	-12912700.60	-4919.510422	-4918.949089	2177.29	2433.00	-167.5
TSPKI-BSIPh	-12912734.80	-4919.519293	-4918.959649	2171.79	2432.00	-168.5
FRA	-11644020.36	-4436.009104	-4435.610066	1835.16	2059.00	-151.6
FRB	-11644022.32	-4436.009053	-4435.610486	1835.45	2059.00	-152.7
TSFRA	-11643980.28	-4435.994679	-4435.593315	1831.88	2055.00	-152.2
TSFRB	-11643985.50	-4435.997408	-4435.595678	1833.09	2056.00	-152.4

6.2.3 Parameters of the Enantioselectivity Model

The parameters to reproduce the curves which show the change of transition state energy with respect to the bite angle x are given in the table below. The form of the polynomial fit is

$$f(x) = a_3x^3 + a_2x^2 + a_1x + a_0 \tag{6.1}$$

Since zero is arbitrarily chosen in this fit, only the differences between transition states for a_0 are relevant, not the absolute values. The a_0 here are chosen so that the lowest curve has its minimum around zero.

Table 6.7: Parameters for the cubic polynomial fits of transition state energies depending on the bite angle.

Transition State	a_3	a_2	a_1	a_0
ARIPh	-0.001349200	0.473921	-53.3187	1945.21
ARIH	-0.001071280	0.383953	-44.0656	1649.01
BSIH	-0.001388240	0.486384	-54.7296	2009.68
BSIPh	-0.001527090	0.533096	-59.4266	2146.98
ASIPh	-0.001527870	0.522607	-57.5428	2066.63
BRIH	-0.000952173	0.359573	-42.5760	1633.60
BRCOPh	-0.000981905	0.366631	-43.3371	1659.62
BRCOH	-0.000440706	0.198039	-26.3143	1113.85
BSIMe	-0.000987189	0.365620	-42.7902	1635.75
BSCOH	-0.001312540	0.459742	-51.8486	1919.62
ASCOH	-0.001219240	0.433567	-49.2170	1841.06
ARCOH	-0.001548280	0.534710	-59.4878	2192.95
ASIMe	-0.000837647	0.330403	-40.2534	1584.80
BRIMe	-0.001258780	0.448426	-50.7276	1866.81
BRIPh	-0.001687010	0.568817	-61.8938	2223.60
BSCOMe	-0.000500074	0.217448	-28.1825	1197.50
ARCOMe	-0.001275350	0.439495	-48.8094	1826.13
ASCOPh	-0.001278680	0.448560	-50.5214	1917.38
ARIMe	-0.002024830	0.672745	-72.6754	2591.31
ASCOMe	-0.001308360	0.468539	-53.2750	1963.99
ASIH	-0.001278880	0.453359	-51.5652	1928.05
BRCOMe	-0.001505760	0.520552	-57.7899	2119.08

6.2.4 Reviewed Crystal Structure List

The table below shows all finally reviewed metal complexes of ruthenium, rhodium, iridium and osmium with a true bidentate chelating phosphine ligand that have a P-M-P bite angle of > 100°. Some of the structures refer to crystals which have been measured at the chemistry department of Heidelberg University; they cannot be found in the web database of the CCDC. "Occurence" in the table refers to how many P-M-P bite angles are present in the crystal structure (for example when several complexes are in one unit cell), all bite angles are given in these cases. The list contains a few duplicates, as some of the complexes have been published twice; usually indicated by the same CSD ID with just "10" appended to it.

ID or CSD #	Metal	Occurence	Bite angle(s) [°]	
AGO022	Rh	1	154.275	
AGO024	Rh	1	155.299	
AGOZEC	Ru	1	101.903	
AGOZEC01	Ru	1	101.886	
ALUXAG	Ru	1	100.64	
AZIVAH	Ru	2	101.019	102.337
B00031	Rh	1	155.082	
BARDEE	Ru	1	151.147	
BARDII	Ru	1	100.298	
BESGEM	Ru	1	100.249	
BIQKIV	Ir	1	124.229	
BUPIRC10	Ir	1	164.147	
CACWEI	Rh	1	103.712	
CERMAN	Ru	1	100.624	
CIGTIV	Rh	2	103.308	103.483
CIGTIV10	Rh	2	103.308	103.483
CIGTOB	Rh	2	104.972	104.591
CIGTOB10	Rh	2	104.972	104.591
CL20	Rh	1	150.891	
CL23	Rh	1	150.311	
CL30	Rh	1	114.585	
CL32	Rh	1	113.81	
CL33	Rh	1	106.872	
CUDZEG	Rh	1	100.245	
DADDUK	Rh	1	100.704	
DEQGEM	Ir	1	100.285	
DEQGIQ	Ir	1	103.027	
DEQGOW	Ir	1	100.006	
DEQGUC	Ir	1	102.272	
DEQHAJ	Ir	1	101.056	
DIHSOD	Rh	1	100.708	
DIHSUJ	Rh	1	101.203	
DIHTAQ	Rh	2	100.705	100.969
DW0004	Rh	1	146.058	
DW0005	Rh	1	146.093	
DW0013	Rh	1	147.292	
DW0017	Rh	1	116.838	
DW0021	Rh	1	151.088	

ID or CSD #	Metal	Occurence	Bite angle(s) [°]	
DW0033	Rh	1	151.925	
DW0034	Rh	1	148.887	
EFUPOM	Rh	1	102.646	
EFUPUS	Rh	1	100.348	
EJUDIX	Ru	1	100.911	
EJUDOD	Ru	2	101.825	102.427
EJUDUJ	Ru	1	101.793	
FAJDAX	Rh	1	153.134	
FEWWIO	Rh	1	162.075	
GA0008	Ir	1	111.482	
GA0009	Ir	1	110.709	
GA0010	Ir	1	107.781	
GA0011	Ir	1	157.277	
GA0012	Ir	1	109.08	
GA0013	Ir	1	105.8	
GA0014	Ir	1	105.45	
GA15	Ir	1	100.995	
GA16	Ir	1	110.173	
GA18	Ir	2	158.257	160.02
GA19	Ir	1	107.049	
GA25	Ir	1	102.915	
GA26	Ir	1	100.617	
GA27	Ir	1	100.565	
GA28	Ir	1	101.24	
GA29	Ir	1	110.145	
GA6	Ir	1	157.05	
GASHUF	Rh	1	104.487	
GESBAI	Rh	1	100.372	
GORZUI	Ir	1	102.131	
GOSBAR	Ir	1	104.82	
HETHET	Ru	1	102.166	
HISZUF	Rh	1	100.312	
HOMHEW	Rh	1	109.309	
HOMHIA	Rh	1	111.724	
HOXLRH	Rh	2	102.232	106.109
INICUD	Rh	1	147.193	
INIDAK	Rh	1	149.559	
INIDOY	Ru	1	103.11	
INIDUE	Ru	1	101.322	
IPIVAF	Ir	1	176.983	
IRAKIW	Ir	1	100.579	
ISUHEK	Ru	1	101.159	
IXIZEV	Ir	1	101.214	
IYUVON	Rh	1	149.401	
JA1	Rh	1	102.801	
JAM10	Rh	2	106.817	107.549
JAM11	Rh	1	100.264	
JAM8	Rh	1	126.24	
JANNOB	Rh	1	179.537	
JANTEA	Os	1	109.462	
JAWLOJ	Ru	1	100.499	
JAXHIZ	Ru	1	164.065	
JGD3	Ru	1	100.018	

ID or CSD #	Metal	Occurence	Bite angle(s) [°]			
JGD4	Ru	1	100.225			
JOPJIJ	Rh	1	103.745			
JUDZOX	Rh	1	124.789			
JUDZUD	Ir	1	117.95			
JUNPOZ	Rh	1	100.294			
KIRYAN	Ru	1	100.172			
LECTOC	Rh	1	164.438			
LECTOC01	Rh	1	164.438			
LEVLED	Ru	1	118.997			
LIRTIR	Rh	1	101.558			
LIRTOX	Rh	1	101.488			
MRO007	Rh	1	152.651			
MRO008	Rh	1	152.334			
MRO011	Rh	1	156.842			
MRO012	Rh	2	149.76	151.01		
MRO014	Rh	1	156.202			
MRO016	Rh	2	149.718	150.913		
MT0011	Rh	1	159.416			
MURWAZ	Rh	2	110.885	114.64		
NALGUD	Rh	1	173.439			
NEPTEJ	Rh	2	117.179	117.985		
NESCUJ	Ru	1	100.275			
NEYTUI	Rh	1	176.797			
NIPRAG	Rh	1	101.185			
NIPREK	Rh	1	100.276			
NISKOQ	Os	1	105.886			
NITMEJ	Rh	1	171.373			
NOMYUJ	Ir	1	102.489			
NUVZOT	Ir	1	118.194			
OJOGIF	Rh	2	100.199	101.643		
PAQBAL	Ru	1	103.073			
PAQBEP	Ru	1	102.492			
PEWBIE	Ir	1	105.451			
PEWBOK	Rh	1	101.448			
PMBZRH20	Rh	1	174.691			
POXORH	Rh	1	178.517			
POYQAW	Ir	1	106.488			
PUQQUP	Rh	1	126.226			
QEWGOO	Rh	1	110.197			
QEWGUU	Rh	1	109.174			
QOHWOA	Rh	1	100.129			
QONSIW	Ru	1	102.762			
QONSOC	Ru	1	102.198			
QONSUI	Ru	1	101.795			
QONVUL	Rh	1	173.216			
RADCAD	Rh	4	177.9	178.57	178.613	178.797
REJGIW	Rh	1	100.922			
RERCUO	Rh	4	100.819	101.034	101.049	101.746
RIYTEA	Ru	1	168.929			
RT0004	Rh	1	149.51			
RT0006	Rh	1	113.552			
RT10	Rh	2	105.904	107.615		
RT11	Rh	1	111.249			

ID or CSD #	Metal	Occurence	Bite angle(s) [°]	
RT12	Rh	1	112.865	
RT13	Rh	1	116.505	
RT7	Rh	1	105.25	
RT8	Rh	1	147.065	
RT9	Rh	1	111.365	
RUGZUP	Rh	1	163.765	
RUNCPP10	Ru	1	167.722	
RURMIC	Ir	1	100.97	
SAKXEI	Ru	1	105.372	
SAMJUM	Ru	1	100.625	
SBN002	Rh	1	149.816	
SBN13	Rh	1	125.219	
SBN14	Rh	1	153.019	
SBN17	Rh	1	119.228	
SBN18	Rh	1	149.093	
SBN2	Rh	1	149.799	
SBN20	Rh	1	116.233	
SBN22	Rh	1	116.354	
SBN3	Rh	1	149.516	
SBN4	Rh	1	148.477	
SES003	Rh	1	113.076	
SF0001	Rh	1	116.694	
SIGDET	Ir	1	101.512	
SIGDOD	Ir	1	101.469	
SIGFAR	Ir	2	110.245	111.296
SIGVAH	Ru	1	162.927	
SUZGOL	Ir	1	100.806	
SUZTIS	Ir	2	102.191	102.536
SUZVAM	Ir	2	102.102	102.14
SUZVEQ	Ir	1	100.318	
TAFTOL	Os	1	138.351	
TCIRPP10	Ir	1	170.639	
TEWSUK	Rh	1	149.794	
TEWXOJ	Ru	2	100.357	100.855
TIBYUA	Ru	2	103.568	105.325
TIQVIA	Ir	2	105.227	105.552
TIZJOB	Ru	1	102.148	
TK0017	Rh	1	146.27	
TK0019	Rh	1	123.741	
TK0022	Rh	1	148.599	
TK0028	Rh	2	145.454	145.574
TRO15	Rh	2	104.738	119.425
TRO17	Rh	1	106.962	
TRO21	Rh	1	125.492	
TRO23	Rh	1	101.375	
TRO25	Rh	1	102.187	
UGANEX	Ru	1	103.179	
VIKQEM	Ru	1	101.795	
VUCBUR	Ru	1	103.318	
VUCCAY	Ru	1	102.678	
VUCCEC	Ru	1	100.481	
VUCCIG	Ru	1	103.316	
WAYPUJ	Rh	1	103.778	

ID or CSD #	Metal	Occurence	Bite angle(s) [°]	
XASDEB	Rh	1	173.793	
XIGGOJ	Ru	1	100.51	
XIPSUK	Rh	1	102.196	
XIPTAR	Rh	2	100.186	105.118
XOQQUR	Rh	1	100.291	
XOQRAY	Rh	1	102.051	
XOQREC	Rh	1	113.079	
XY0003	Ru	1	168.926	
YAVDUW	Rh	1	109.662	
YUDPET	Ru	1	107.559	
ZABHUF	Rh	1	115.95	
ZABHUF10	Rh	1	115.95	
ZIBYUG	Ir	2	109.119	110.496
ZISPAS	Rh	2	161.027	161.514
ZZZBJY10	Ir	1	173.95	

6.2.5 Enantioselectivity with Cyclohexyl Methyl Ketone

For the estimation of enantioselectivity with cyclohexyl methyl ketone, the proton transfer transition states were recalculated for the regular catalyst with iodide in the apical position. The structures are named similar to the **TSPI** transition states, but are supplemented by -H, -Me, -NH, to indicate which group is *anti* to the α-hydrogen of the cyclohexyl group, which adds additional rotamers to the possible isomer/conformer combinations.

Structure	Total G [kJ/mol]	BP86 def2-SV(P) [E_h]	PBE0-D3(BJ) def2-QZVPP [E_h]	ΔG_{gas} [kJ/mol]	ZPVE [kJ/mol]	ΔG_{solv} [kJ/mol]
ARCOH-H	-12869870.62	-4903.253970	-4902.715311	2383.59	2641.00	-165.6
ARCOH-Me	-12869874.39	-4903.255949	-4902.715702	2380.83	2640.00	-165.6
ARCOH-NH	-12869869.46	-4903.253605	-4902.714120	2383.50	2641.00	-167.5
ARCOMe-H	-12869844.33	-4903.246673	-4902.701751	2377.32	2639.00	-168.7
ARIH-H	-12869878.22	-4903.258822	-4902.715692	2381.73	2641.00	-170.3
ARIH-Me	-12869877.43	-4903.257774	-4902.715285	2381.04	2641.00	-169.9
ARIH-NH	-12869881.31	-4903.258897	-4902.717607	2381.64	2641.00	-168.3
ARIPh-H	-12869885.34	-4903.255630	-4902.717376	2380.45	2640.00	-171.8
ARIPh-Me	-12869890.41	-4903.261548	-4902.722205	2386.02	2642.00	-169.7
ARIPh-NH	-12869885.95	-4903.257395	-4902.719237	2383.12	2641.00	-170.2
ASCOH-Me	-12869877.54	-4903.257933	-4902.716895	2382.26	2640.00	-167.0
ASCOH-NH	-12869868.49	-4903.251508	-4902.712086	2381.02	2640.00	-169.4
ASCOPh-H	-12869836.06	-4903.243369	-4902.701428	2382.80	2640.00	-166.7
ASCOPh-NH	-12869827.78	-4903.239086	-4902.696551	2377.39	2638.00	-165.8
ASIH-H	-12869886.12	-4903.258274	-4902.719660	2381.05	2641.00	-167.1
ASIH-Me	-12869884.53	-4903.260549	-4902.719703	2383.27	2642.00	-167.7
ASIH-NH	-12869885.26	-4903.258740	-4902.720981	2384.95	2641.00	-166.7
ASIMe-H	-12869874.42	-4903.259267	-4902.715340	2381.71	2641.00	-167.4
ASIMe-Me	-12869888.89	-4903.261127	-4902.721440	2384.84	2642.00	-169.0
ASIMe-NH	-12869886.87	-4903.258399	-4902.721003	2386.20	2641.00	-169.5
BRCOH-H	-12869866.83	-4903.250630	-4902.713102	2384.07	2641.00	-168.1
BRCOPh-Me	-12869879.58	-4903.256068	-4902.717458	2383.77	2641.00	-169.1
BRIH-H	-12869884.49	-4903.259615	-4902.719276	2382.47	2641.00	-167.9
BRIH-Me	-12869884.01	-4903.261131	-4902.720216	2384.22	2642.00	-166.7
BRIH-NH	-12869882.61	-4903.259884	-4902.719108	2384.82	2641.00	-168.9
BRIMe-H	-12869867.98	-4903.258052	-4902.713748	2384.20	2642.00	-167.7
BRIMe-NH	-12869871.93	-4903.256376	-4902.714071	2379.57	2641.00	-166.2
BRIPh-Me	-12869863.33	-4903.253336	-4902.710966	2380.52	2641.00	-166.7
BRIPh-NH	-12869845.14	-4903.248544	-4902.706494	2385.41	2642.00	-165.1
BSCOH-H	-12869865.65	-4903.253982	-4902.711908	2380.29	2641.00	-166.3
BSCOH-Me	-12869872.34	-4903.257035	-4902.715352	2384.58	2642.00	-168.2
BSCOH-NH	-12869873.46	-4903.254695	-4902.715612	2381.67	2640.00	-165.7
BSCOMe-H	-12869851.72	-4903.249817	-4902.705040	2377.08	2639.00	-167.2
BSIH-H	-12869878.45	-4903.257721	-4902.715495	2378.70	2640.00	-168.1
BSIH-Me	-12869885.25	-4903.262518	-4902.720023	2383.32	2642.00	-167.6
BSIH-NH	-12869876.96	-4903.258475	-4902.716550	2382.00	2641.00	-167.1
BSIMe-H	-12869870.09	-4903.257532	-4902.715167	2385.63	2642.00	-167.5
BSIMe-Me	-12869877.27	-4903.257312	-4902.715557	2381.37	2641.00	-169.4
BSIMe-NH	-12869869.66	-4903.257276	-4902.714702	2385.31	2643.00	-168.0

6.2.6 Molecular Dynamics Simulation

Cell Equilibration

Equilibrated cell lengths for NVT ensemble simulations were obtained from NPT simulations by averaging over the last 1,000 frames (5,000 steps, 2,500 fs). Since most of the cell is filled with toluene (each cell contains one catalyst molecule and 90 toluene molecules for solvation), the differences in cell lengths are very small between the different backbones. These cells were then used to perform NVT simulations from which bite angle distributions were extracted using VMD.[170] The corresponding trajectories can be found on the attached DVD in

md-trajectory-<backbone>.xyz

The corresponding bite angles obtained from VMD are given in the files

md-biteangle-<backbone>.txt

Only every 5th step of the original NVT simulation is saved as a frame in the .xyz-trajectory, the time step between consecutive frames is 2.5 fs. Each trajectory is atleast 8,000 frames long (40,000 MD steps or 20 ps) long.

Table 6.10: Equilibrated cell lengths for NVT molecular dynamics simulations.

Backbone	Cell Length $[a_0]$	Cell Length [Å]
Ferrocenyl	48.54	25.69
Ethyl	48.97	25.91
Phenyl	48.57	25.70
BISBI	48.59	25.71

Bite Angle Trajectories

The graphs below show the fluctuations in bite angle over time from which the corresponding histograms and gaussian fits were derived. Each frame is over five MD simulation steps of 0.5 fs each, the time step between frames is therefore 2.5 ps.

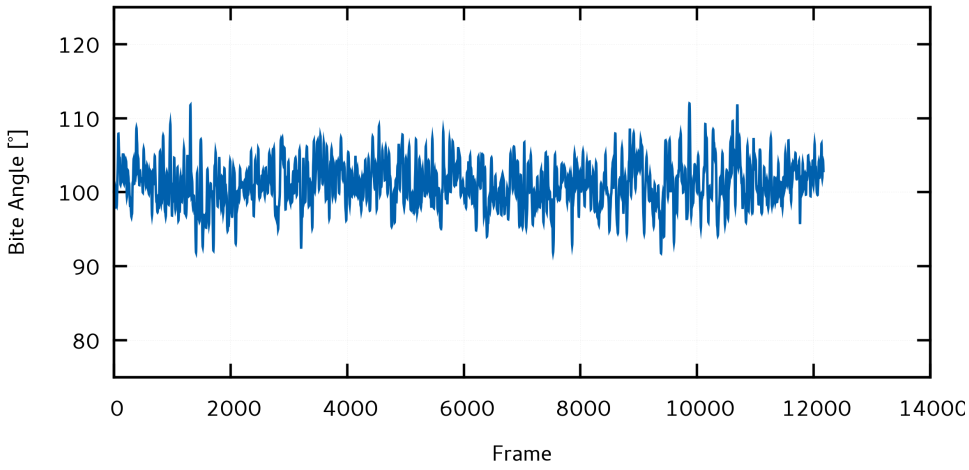

Figure 6.1: Bite angle fluctuations of the ferrocenyl backbone binaphane ligand from NVT MD simulation.

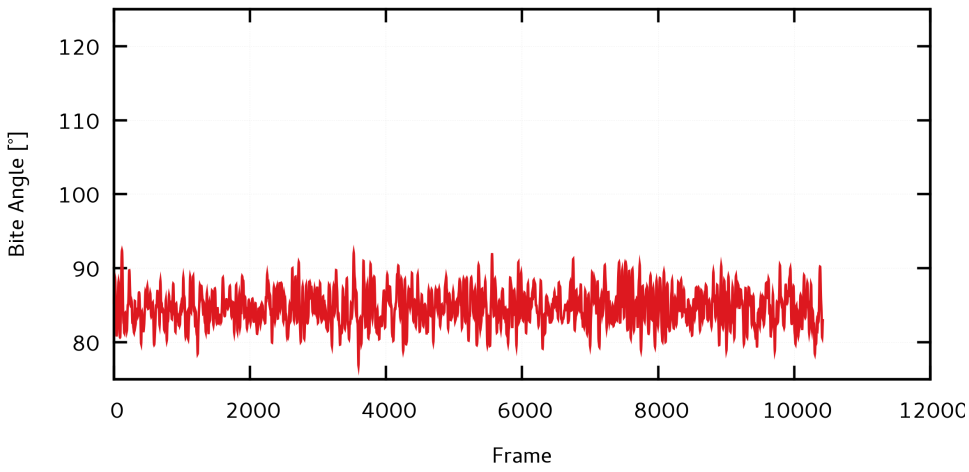

Figure 6.2: Bite angle fluctuations of the ethyl backbone binaphane ligand from NVT MD simulation.

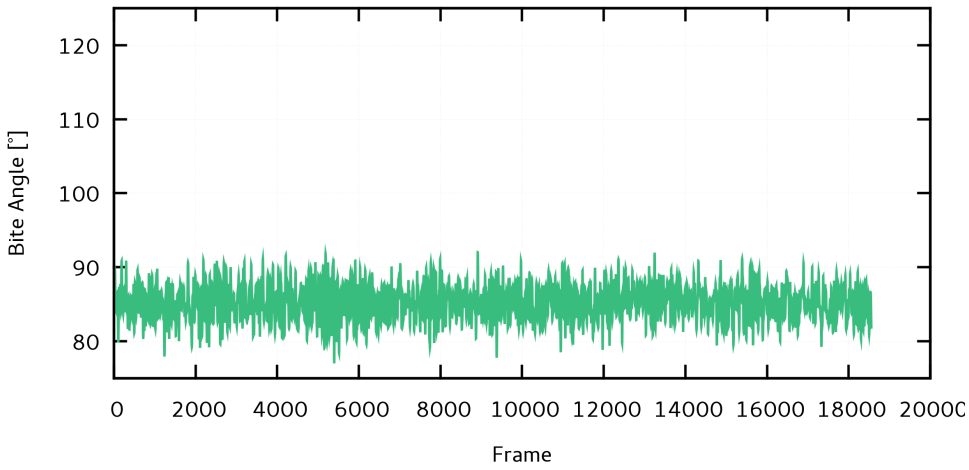

Figure 6.3: Bite angle fluctuations of the phenyl backbone binaphane ligand from NVT MD simulation.

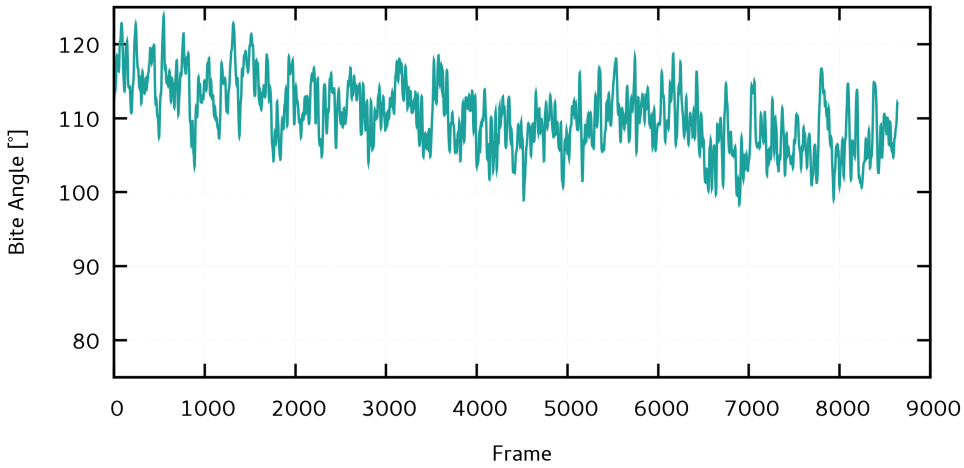

Figure 6.4: Bite angle fluctuations of the BISBI backbone binaphane ligand from NVT MD simulation.

References

[1] Schrödinger, E. An undulatory theory of the mechanics of atoms and molecules. *Physical Review* **1926**, *28*, 1049–1070.

[2] Hartree, D. R. The Wave Mechanics of an Atom with a Non-Coulomb Central Field. Part I. Theory and Methods. *Mathematical Proceedings of the Cambridge Philosophical Society* **1928**, *24*, 89–110.

[3] Fock, V. Näherungsmethode zur Lösung des quantenmechanischen Mehrkörperproblems. *Zeitschrift für Physik* **1930**, *61*, 126–148.

[4] Roothaan, C. C. J. New developments in molecular orbital theory. *Reviews of Modern Physics* **1951**, *23*, 69–89.

[5] Hall, G. G. The Molecular Orbital Theory of Chemical Valency. VIII. A Method of Calculating Ionization Potentials. *Proceedings of the Royal Society A: Mathematical, Physical and Engineering Sciences* **1951**, *205*, 541–552.

[6] Hückel, E. Quantentheoretische Beiträge zum Benzolproblem. I. Die Elektronenkonfiguration des Benzols und verwandter Verbindungen. *Zeitschrift für Physik* **1931**, *70*, 204–286.

[7] Hückel, E. Quantentheoretische Beiträge zum Benzolproblem. II. Quantentheorie der induzierten Polaritäten. *Zeitschrift für Physik* **1931**, *72*, 310–337.

[8] Hückel, E. Quantentheoretische Beiträge zum Problem der aromatischen und ungesättigten Verbindungen. III. *Zeitschrift für Physik* **1932**, *76*, 628–648.

[9] Hückel, E. Die freien Radikale der organischen Chemie. Quantentheoretische Beiträge zum Problem der aromatischen und ungesättigten Verbindungen. IV. *Zeitschrift für Physik* **1933**, *83*, 632–668.

[10] Woodward, R. B.; Hoffmann, R. Stereochemistry of Electrocyclic Reactions. *Journal of the American Chemical Society* **1965**, *87*, 395–397.

[11] Hohenberg, P.; Kohn, W. Inhomogeneous electron gas. *Physical Review* **1964**, *136*, B864–B871.

[12] Kohn, W.; Sham, L. J. Self-consistent equations including exchange and correlation effects. *Physical Review* **1965**, *140*, A1133–AA1138.

[13] Evans, M. G.; Polanyi, M. Some applications of the transition state method to the calculation of reaction velocities, especially in solution. *Transactions of the Faraday Society* **1935**, *31*, 875–894.

[14] Hylleraas, E. A. Neue Berechnung der Energie des Heliums im Grundzustande, sowie des tiefsten Terms von Ortho-Helium. *Zeitschrift für Physik* **1929**, *54*, 347–366.

[15] Schwartz, C. Experiment and Theory in Computations of the Helium Atom Ground State. *International Journal of Modern Physics E* **2006**, *15*, 877–888.

[16] Nakashima, H.; Nakatsuji, H. Solving the Schrodinger equation for helium atom and its isoelectronic ions with the free iterative complement interaction (ICI) method. *Journal of Chemical Physics* **2007**, *127*, 224104.

[17] Pauli, W. Über den Zusammenhang des Abschlusses der Elektronengruppen im Atom mit der Komplexstruktur der Spektren. *Zeitschrift für Physik* **1925**, *31*, 765–783.

[18] Pauli, W. The connection between spin and statistics. *Physical Review* **1940**, *58*, 716–722.

[19] Slater, J. C. The theory of complex spectra. *Physical Review* **1929**, *34*, 1293–1322.

[20] Ritz, W. Über eine neue Methode zur Lösung gewisser Variationsprobleme der mathematischen Physik. *Journal für die reine und angewandte Mathematik* **1909**, *135*, 1–61.

[21] Löwdin, P. O. Quantum theory of many-particle systems. III. Extension of the Hartree-Fock scheme to include degenerate systems and correlation effects. *Physical Review* **1955**, *97*, 1509–1520.

[22] Slater, J. C. Atomic shielding constants. *Physical Review* **1930**, *36*, 57–64.

[23] Kato, T. On the eigenfunctions of many-particle systems in quantum mechanics. *Communications on Pure and Applied Mathematics* **1957**, *10*, 151–177.

[24] March, N. H. Spatially dependent generalization of Kato's theorem for atomic closed shells in a bare Coulomb field. *Physical Review A* **1986**, *33*, 88–89.

[25] Boys, S. F. Electronic Wave Functions. I. A General Method of Calculation for the Stationary States of Any Molecular System. *Proceedings of the Royal Society A: Mathematical, Physical and Engineering Sciences* **1950**, *200*, 542–554.

[26] Hehre, W. J.; Stewart, R. F.; Pople, J. A. Self-consistent molecular-orbital methods. I. Use of gaussian expansions of slater-type atomic orbitals. *Journal of Chemical Physics* **1969**, *51*, 2657–2664.

[27] Hehre, W. J.; Ditchfield, K.; Pople, J. A. Self-consistent molecular orbital methods. XII. Further extensions of gaussian-type basis sets for use in molecular orbital studies of organic molecules. *Journal of Chemical Physics* **1972**, *56*, 2257–2261.

[28] Binkley, J. S.; Pople, J. A.; Hehre, W. J. Self-Consistent Molecular-Orbital Methods. 21. Small Split-Valence Basis-Sets for First-Row Elements. *Journal of the American Chemical Society* **1980**, *102*, 939–947.

[29] Krishnan, R.; Binkley, J. S.; Seeger, R.; Pople, J. A. Self-consistent molecular orbital methods. XX. A basis set for correlated wave functions. *Journal of Chemical Physics* **1980**, *72*, 650–654.

[30] Francl, M. M.; Pietro, W. J.; Hehre, W. J.; Binkley, J. S.; Gordon, M. S.; DeFrees, D. J.; Pople, J. A. Self-consistent molecular orbital methods. XXIII. A polarization-type basis set for second-row elements. *Journal of Chemical Physics* **1982**, *77*, 3654–3665.

[31] Frisch, M. J.; Pople, J. A.; Binkley, J. S. Self-consistent molecular orbital methods 25. Supplementary functions for Gaussian basis sets. *Journal of Chemical Physics* **1984**, *80*, 3265–3269.

[32] Dunning, T. H. Gaussian basis sets for use in correlated molecular calculations. I. The atoms boron through neon and hydrogen. *Journal of Chemical Physics* **1989**, *90*, 1007–1023.

[33] Schäfer, A.; Horn, H.; Ahlrichs, R. Fully optimized contracted Gaussian basis sets for atoms Li to Kr. *Journal of Chemical Physics* **1992**, *97*, 2571–2577.

[34] Schäfer, A.; Huber, C.; Ahlrichs, R. Fully optimized contracted Gaussian basis sets of triple zeta valence quality for atoms Li to Kr. *The Journal of Chemical Physics* **1994**, *100*, 5829–5835.

[35] Weigend, F.; Ahlrichs, R. Balanced basis sets of split valence, triple zeta valence and quadruple zeta valence quality for H to Rn: Design and assessment of accuracy. *Physical Chemistry Chemical Physics* **2005**, *7*, 3297.

[36] Weigend, F. Accurate Coulomb-fitting basis sets for H to Rn. *Physical Chemistry Chemical Physics* **2006**, *8*, 1057.

[37] Jensen, F. *Introduction to Computational Chemistry Computational Chemistry*; 2007.

[38] Gell-Mann, M.; Brueckner, K. A. Correlation energy of an electron gas at high density. *Physical Review* **1957**, *106*, 364–368.

[39] Vosko, S. H.; Wilk, L.; Nusair, M. Accurate spin-dependent electron liquid correlation energies for local spin density calculations: a critical analysis. *Canadian Journal of Physics* **1980**, *58*, 1200–1211.

[40] Perdew, J. P.; Wang, Y. Accurate and Simple Representation of the Electron-Gas Correlation-Energy. *Physical Review B* **1992**, *45*, 13244–13249.

[41] Ma, S.-K.; Brueckner, K. A. Correlation Energy of an Electron Gas with a Slowly Varying High Density. *Physical Review* **1968**, *165*, 18–31.

[42] Langreth, D. C.; Perdew, J. P. Theory of nonuniform electronic systems. I. Analysis of the gradient approximation and a generalization that works. *Physical Review B* **1980**, *21*, 5469–5493.

[43] Langreth, D. C.; Mehl, M. J. Beyond the local-density approximation in calculations of ground-state electronic properties. *Physical Review B* **1983**, *28*, 1809–1834.

[44] Becke, A. D. Density-functional exchange-energy approximation with correct asymptotic behavior. *Physical Review A* **1988**, *38*, 3098–3100.

[45] Lee, C.; Yang, W.; Parr, R. G. Development of the Colle-Salvetti correlation-energy formula into a functional of the electron density. *Physical Review B* **1988**, *37*, 785–789.

[46] Perdew, J. P. Density-functional approximation for the correlation energy of the imhomogeneous electron gas. *Phys. Rev. B* **1986**, *33*, 8822.

[47] Perdew, J. P.; Yue, W. Accurate and simple density functional for the electronic exchange energy: Generalized gradient approximation. *Physical Review B* **1986**, *33*, 8800–8802.

[48] Perdew, J. P.; Burke, K.; Ernzerhof, M. Generalized gradient approximation made simple. *Physical Review Letters* **1996**, *77*, 3865–3868.

[49] Perdew, J. P.; Burke, K.; Ernzerhof, M. Errata: Generalized Gradient Approximation Made Simple. *Physical Review Letters* **1996**, *77*, 3865–3868.

[50] Koch, W.; Holthausen, M. C. *A Chemist's Guide to Density Functional Theory*; 2001; Vol. 3.

[51] Becke, A. D. A new mixing of Hartree-Fock and local density-functional theories. *Journal of Chemical Physics* **1993**, *98*, 1372–1377.

[52] Becke, A. D. Density-functional thermochemistry. III. The role of exact exchange. *Journal of Chemical Physics* **1993**, *98*, 5648–5652.

[53] Perdew, J. P.; Ernzerhof, M.; Burke, K. Rationale for mixing exact exchange with density functional approximations. *Journal of Chemical Physics* **1996**, *105*, 9982–9985.

[54] Ernzerhof, M.; Scuseria, G. E. Assessment of the Perdew-Burke-Ernzerhof exchange-correlation functional. *Journal of Chemical Physics* **1999**, *110*, 5029–5036.

[55] Adamo, C.; Barone, V. Toward reliable density functional methods without adjustable parameters: The PBE0 model. *Journal of Chemical Physics* **1999**, *110*, 6158–6170.

[56] Tao, J.; Perdew, J. P.; Staroverov, V. N.; Scuseria, G. E. Climbing the density functional ladder: Nonempirical meta–generalized gradient approximation designed for molecules and solids. *Physical Review Letters* **2003**, *91*, 3–6.

[57] Perdew, J. P.; Kurth, S.; Zupan, A.; Blaha, P. Accurate density functional with correct formal properties: A step beyond the generalized gradient approximation. *Physical Review Letters* **1999**, *82*, 2544–2547.

[58] Perdew, J. P.; Zupan, A.; Blaha, P.; Kurth, S. Erratum: Accurate Density Functional with Correct Formal Properties: A Step Beyond the Generalized Gradient Approximation. *Physical Review Letters* **1999**, *82*, 2544–2547.

[59] Zhao, Y.; Truhlar, D. G. Density functional for spectroscopy: No long-range self-interaction error, good performance for Rydberg and charge-transfer states, and better performance on average than B3LYP for ground states. *Journal of Physical Chemistry A* **2006**, *110*, 13126–13130.

[60] Zhao, Y.; Truhlar, D. G. The M06 suite of density functionals for main group thermochemistry, thermochemical kinetics, noncovalent interactions, excited states, and transition elements: Two new functionals and systematic testing of four M06-class functionals and 12 other function. *Theoretical Chemistry Accounts* **2008**, *120*, 215–241.

[61] Whitten, J. L. Coulombic potential energy integrals and approximations. *Journal of Chemical Physics* **1973**, *4496*.

[62] Vahtras, O.; Almlöf, J.; Feyereisen, M. W. Integral approximations for LCAO-SCF calculations. *Chemical Physics Letters* **1993**, *213*, 514–518.

[63] Weigend, F. A fully direct RI-HF algorithm: Implementation, optimised auxiliary basis sets, demonstration of accuracy and efficiency. *Physical Chemistry Chemical Physics* **2002**, *4*, 4285–4291.

[64] London, F. Zur Theorie und Systematik der Molekularkräfte. *Zeitschrift für Physik* **1930**, *63*, 245–279.

[65] Eisenschitz, R.; London, F. Über das Verhältnis der van der Waalsschen Kräfte zu den homoopolaren Bindungskräften. *Zeitschrift für Physik* **1930**, *60*, 491–527.

[66] David Sherrill, C.; Takatani, T.; Hohenstein, E. G. An assessment of theoretical methods for nonbonded interactions: Comparison to complete basis set limit coupled-cluster potential energy curves for the benzene dimer, the methane dimer, benzene-methane, and benzene-H2S. *Journal of Physical Chemistry A* **2009**, *113*, 10146–10159.

[67] Slaviček, P.; Kalus, R.; Paška, P.; Odvárková, I.; Hobza, P.; Malijevský, A. State-of-the-art correlated ab initio potential energy curves for heavy rare gas dimers: Ar2, Kr2, and Xe2. *Journal of Chemical Physics* **2003**, *119*, 2102–2119.

[68] London, F. The general theory of molecular forces. *Transactions of the Faraday Society* **1937**, *33*, 8–26.

[69] Grimme, S. Density functional theory with London dispersion corrections. *Wiley Interdisciplinary Reviews: Computational Molecular Science* **2011**, *1*, 211–228.

[70] Grimme, S.; Antony, J.; Ehrlich, S.; Krieg, H. A consistent and accurate ab initio parametrization of density functional dispersion correction (DFT-D) for the 94 elements H-Pu. *Journal of Chemical Physics* **2010**, *132*, 154104.

[71] Grimme, S.; Ehrlich, S.; Goerigk, L. Effect of the damping function in dispersion corrected density functional theory. *Journal of Computational Chemistry* **2011**, *32*, 1456–1465.

[72] Cohen, J. S.; Pack, R. T. Modified statistical method for intermolecular potentials. Combining rules for higher van der Waals coefficients. *Journal of Chemical Physics* **1974**, *61*, 2372–2382.

[73] Pyykko, P.; Desclaux, J. P. Relativity and the Periodic System of Elements. *Accounts of Chemical Research* **1979**, *12*, 276–281.

[74] Dolg, M.; Cao, X. Relativistic pseudopotentials: Their development and scope of applications. *Chemical Reviews* **2012**, *112*, 403–480.

[75] Klamt, A. Conductor-like screening model for real solvents: A new approach to the quantitative calculation of solvation phenomena. *Journal of Physical Chemistry* **1995**, *99*, 2224–2235.

[76] Klamt, A.; Jonas, V.; Bürger, T.; Lohrenz, J. C. Refinement and parametrization of COSMO-RS. *Journal of Physical Chemistry A* **1998**, *102*, 5074–5085.

[77] Klamt, A.; Schüürmann, G. COSMO: a new approach to dielectric screening in solvents with explicit expressions for the screening energy and its gradient. *Journal of the Chemical Society, Perkin Transactions 2* **1993**, 799–805.

[78] Eckert, F.; Klamt, A. Fast Solvent Screening via Quantum Chemistry: COSMO-RS Approach. *AIChE Journal* **2002**, *48*, 369–385.

[79] Feng, X.; Gu, J.; Xie, Y.; King, R. B.; Schaefer, H. F. Homoleptic carbonyls of the second-row transition metals: Evaluation of Hartree-Fock and density functional theory methods. *Journal of Chemical Theory and Computation* **2007**, *3*, 1580–1587.

[80] Plessow, P. N. New Insights into Homogeneously Catalyzed Reactions: Theoretical Investigations. Ph.D. thesis, Universität Heidelberg, 2014.

[81] Pople, J. A.; Head-Gordon, M.; Fox, D. J.; Raghavachari, K.; Curtiss, L. A. Gaussian-1 theory: A general procedure for prediction of molecular energies. *Journal of Chemical Physics* **1989**, *90*, 5622–5629.

[82] Mardirossian, N.; Head-Gordon, M. Thirty years of density functional theory in computational chemistry: An overview and extensive assessment of 200 density functionals. *Molecular Physics* **2017**, *115*, 2315–2372.

[83] Steinmetz, M.; Grimme, S. Benchmark study of the performance of density functional theory for bond activations with (Ni,Pd)-based transition-metal catalysts. *ChemistryOpen* **2013**, *2*, 115–124.

[84] Dohm, S.; Hansen, A.; Steinmetz, M.; Grimme, S.; Checinski, M. P. Comprehensive Thermochemical Benchmark Set of Realistic Closed-Shell Metal Organic Reactions. *Journal of Chemical Theory and Computation* **2018**, *14*, 2596–2608.

[85] Riplinger, C.; Sandhoefer, B.; Hansen, A.; Neese, F.; Riplinger, C.; Sandhoefer, B.; Hansen, A.; Neese, F. Natural triple excitations in local coupled cluster calculations with pair natural orbitals. *Journal of Chemical Physics* **2013**, *139*, 134101.

[86] Riplinger, C.; Pinski, P.; Becker, U.; Valeev, E. F.; Neese, F. Sparse maps — A systematic infrastructure for reduced-scaling electronic structure methods. II. Linear scaling domain based pair natural orbital coupled cluster theory. *Journal of Chemical Physics* **2016**, *144*, 024109.

[87] Lyngvi, E.; Sanhueza, I. A.; Schoenebeck, F. Dispersion Makes the Difference: Bisligated Transition States Found for the Oxidative Addition of Pd(PtBu3)2 to Ar-OSO2R and Dispersion-Controlled Chemoselectivity in Reactions with Pd[P(iPr)(tBu2)]2. *Organometallics* **2015**, *34*, 805.

[88] Wei, D.; Roisnel, T.; Darcel, C.; Clot, E.; Sortais, J. B. Hydrogenation of Carbonyl Derivatives with a Well-Defined Rhenium Precatalyst. *ChemCatChem* **2017**, *9*, 80–83.

[89] Kozuch, S.; Martin, J. M. What makes for a good catalytic cycle? A theoretical study of the SPhos ligand in the Suzuki-Miyaura reaction. *Chemical Communications* **2011**, *47*, 4935–4937.

[90] Kozuch, S.; Martin, J. M. What makes for a bad catalytic cycle? A theoretical study on the suzuki-miyaura reaction within the energetic span model. *ACS Catalysis* **2011**, *1*, 246–253.

[91] Breit, B.; Gellrich, U.; Li, T.; Lynam, J. M.; Milner, L. M.; Pridmore, N. E.; Slattery, M.; Whitwood, A. C. Mechanistic insight into the ruthenium-catalysed anti-Markovnikov hydration of alkynes using a self-assembled complex: a crucial role for ligand-assisted proton shuttle processes. *Dalton Transactions* **2014**, *43*, 11277.

[92] Kumar, N. Y.; Rogge, T.; Yetra, S. R.; Bechtoldt, A.; Clot, E.; Ackermann, L. Mild Decarboxylative C–H Alkylation: Computational Insights for Solvent-Robust Ruthenium(II) Domino Manifold. *Chemistry - A European Journal* **2017**, *23*, 17449–17453.

[93] Tinge, J.; Groothaert, M.; op het Veld, H.; Ritz, J.; Fuchs, H.; Kiezcka, H.; Moran, W. C. Caprolactam. *Ullmann's Encyclopedia of Industrial Chemistry* **2018**, 1–31.

[94] Teles, J. H.; Hermans, I.; Franz, G.; Sheldon, R. A. Oxidation. *Ullmann's Encyclopedia of Industrial Chemistry* **2015**, 1–103.

[95] Musser, M. T. Cyclohexanol and Cyclohexanone. *Ullmann's Encyclopedia of Industrial Chemistry* **2000**, *11*, 49–60.

[96] TURBOMOLE V7.0 2015, a development of University of Karlsruhe and Forschungszentrum Karlsruhe GmbH. http://www.turbomole.com.

[97] Eichkorn, K.; Treutler, O.; Ohm, H.; Haser, M.; Ahlrichs, R. Auxiliary basis-sets to approximate coulomb potentials. *Chemical Physics Letters* **1995**, *240*, 283–289.

[98] Deglmann, P.; May, K.; Furche, F.; Ahlrichs, R. Nuclear second analytical derivative calculations using auxiliary basis set expansions. *Chemical Physics Letters* **2004**, *384*, 103–107.

[99] COSMOtherm. http://www.cosmologic.de.

[100] Kollwitz, M.; Gauss, J. A direct implementation of the GIAO-MBPT(2) method for calculating NMR chemical shifts. Application to the naphthalenium and anthracenium ions. *Chemical Physics Letters* **1996**, *260*, 639–646.

[101] Mimoun, H.; Saussine, L.; Daire, E.; Postel, M.; Fischer, J.; Weiss, R. Vanadium(V) Peroxo Complexes. New Versatile Biomimetic Reagents for Epoxidation of Olefins and Hydroxylation of Alkanes and Aromatic Hydrocarbons. *Journal of the American Chemical Society* **1983**, *105*, 3101–3110.

[102] Mimoun, H.; Mignard, M.; Brechot, P.; Saussine, L. Selective Epoxidation of Olefins by Oxo[N-(2-oxidophenyl)salicylidenaminato]vanadium(V) Alkylperoxides. On the Mechanism of the Halcon Epoxidation Process. *Journal of the American Chemical Society* **1986**, *108*, 3711–3718.

[103] Mimoun, H. D0 Metal Peroxides as Homolytic and Heterolytic Oxidative Reagents. Mechanism of the Halcon Epoxidation Process. *Catalysis Today* **1987**, *1*, 281–295.

[104] Saussine, L.; Brazi, E.; Robine, A.; Mimoun, H.; Fischer, J.; Weiss, R. Cobalt(III) Alkylperoxy Complexes. Synthesis, X-ray Structure, and Role in the Catalytic Decomposition of Alkyl Hydroperoxides and in the Hydroxylation of Hydrocarbons. *Journal of the American Chemical Society* **1985**, *107*, 3534–3540.

[105] Chaumette, P.; Mimoun, H.; Saussine, L.; Fischer, J.; Mitschler, A. Peroxo and alkylperoxidic molybdenum(VI) complexes as intermediates in the epoxidation of olefins by alkyl hydroperoxides. *Journal of Organometallic Chemistry* **1983**, *250*, 291–310.

[106] Kundu, R.; Ball, Z. T. Copper-Catalyzed Remote sp3 C-H Chlorination of Alkyl Hydroperoxides. *Organic Letters* **2010**, *12*, 2460–2463.

[107] Hiatt, R.; Mill, T.; Irwin, K. C.; Castleman, J. K. Homolytic Decompositions of Hydroperoxides. III. Radical-Induced Decompositions of Primary and Secondary Hydroperoxides. *Journal of Organic Chemistry* **1968**, *33*, 1428–1430.

[108] Hermans, I.; Nguyen, T. L.; Jacobs, P. A.; Peeters, J. Autoxidation of cyclohexane: Conventional views challenged by theory and experiment. *ChemPhysChem* **2005**, *6*, 637–645.

[109] Hermans, I.; Jacobs, P. A.; Peeters, J. Understanding the autoxidation of hydrocarbons at the molecular level and consequences for catalysis. *Journal of Molecular Catalysis A: Chemical* **2006**, *251*, 221–228.

[110] *CRC Handbook of Chemistry and Physics*, 96th ed.; CRC Press, 2016.

[111] Hermans, I.; Peeters, J.; Jacobs, P. A. Enhanced activity and selectivity in cyclohexane autoxidation by inert H-bond acceptor catalysts. *ChemPhysChem* **2006**, *7*, 1142–1148.

[112] Hermans, I.; Jacobs, P.; Peeters, J. The formation of byproducts in the autoxidation of cyclohexane. *Chemistry - A European Journal* **2007**, *13*, 754–761.

[113] Hermans, I.; Peeters, J.; Jacobs, P. A. Origin of byproducts during the catalytic autoxidation of cyclohexane. *Journal of Physical Chemistry A* **2008**, *112*, 1747–1753.

[114] Hermans, I.; Peeters, J.; Jacobs, P. A. Autoxidation chemistry: Bridging the gap between homogeneous radical chemistry and (heterogeneous) catalysis. *Topics in Catalysis* **2008**, *48*, 41–48.

[115] Djordjevic, C.; Lee, M.; Sinn, E. Oxoperoxo (citrato)-and dioxo (citrato) vanadates (V): synthesis, spectra, and structure of a hydroxyl oxygen bridged dimer. *Inorganic Chemistry* **1989**, *380*, 719–723.

[116] Biagioli, M.; Strinna-Erre, L.; Micera, G.; Panzanelli, A.; Zema, M. Molecular structure, characterization and reactivity of dioxo complexes formed by vanadium(V) with α-hydroxycarboxylate ligands. *Inorganica Chimica Acta* **2000**, *310*, 1–9.

[117] Plass, W.; Yozgatli, H.-P. Synthesis , Reactivity , and Structural Characterization of Dioxovanadium(V) Complexes with Tridentate Schiff Base Ligand: Vanadium Complexes in Supramolecular Networks. *Zeitschrift für anorganische und allgemeine Chemie* **2003**, *629*, 65–70.

[118] Diamantis, A. A.; Frederiksen, J. M.; Salam, M. A.; Snow, M. R.; Tiekink, E. R. T. Structure of Two Vanadium(V) Complexes with Tridentate Ligands. *Australian Journal of Chemistry* **1986**, *39*, 1081–1088.

[119] Sangeetha, N. R.; Kavita, V.; Wocadlo, S.; Powell, A. K.; Pal, S. Vanadium(V) complexes of O,N,O-donor tridentate ligands containing the {VvO(OMe)}2+ unit: syntheses, structures and properties. *Journal of Coordination Chemistry* **2000**, *51*, 55–66.

[120] Hartung, J.; Drees, S.; Greb, M.; Schmidt, P.; Svoboda, I.; Fuess, H.; Murso, A.; Stalke, D. (Schiff-base)vanadium(v) complex-catalyzed oxidations of substituted bis(homoallylic) alcohols - Stereoselective synthesis of functionalized tetrahydrofurans. *European Journal of Organic Chemistry* **2003**, 2388–2408.

[121] Heilbron, I.; Jones, E. R. H.; Sondheimer, F. 129. Researches on acetylenic compounds. Part XV. The oxidation of primary acetylenic carbinols and glycols. *Journal of the Chemical Society (Resumed)* **1949**, 604.

[122] Poos, G. I.; Arth, G. E.; Beyler, R. E.; Sarett, L. H. Approaches to the Total Synthesis of Adrenal Steroids.1 V. 4b-Methyl-7-ethylenedioxy-1,2,3,4,4aα,4b,5,6,7,8,10,10aβ-dodecahydrophenanthrene-4β-ol-1-one and Related Tricyclic Derivatives. *Journal of the American Chemical Society* **1953**, *75*, 422–429.

[123] Collins, J. C.; Hess, W. W.; Frank, F. J. Dipyridine-chromium(VI) oxide oxidation of alcohols in dichloromethane. *Tetrahedron Letters* **1968**, *9*, 3363–3366.

[124] Voskuil, W.; van der Donck, J. J. M.; Wolters, J.; Hennekens, J. L. J. P. Verfahren zur Herstellung von Gemischen aus Cycloalkanonen und Cycloalkanolen, Patentschrift, DE2352378 C2. 1973.

[125] Muzart, J. Chromium(VI) oxide –70% tert.butyl hydroperoxide, a simple catalytic system for oxidation of alcohols to carbonyl compounds. *Tetrahedron* **1987**, *28*, 2133–2134.

[126] Boitsov, S.; Songstad, J.; Muzart, J. Chromium(vi) oxide–tert-butyl hydroperoxide interactions: evidence for a tert-butylperoxychromium complex and its role in the catalytic oxidation of alcohols. *Journal of the Chemical Society, Perkin Transactions 2* **2001**, 2318–2323.

[127] Firouzabadi, H.; Iranpoor, N.; Kiaeezadeh, F.; Toofan, J. Chromium(VI) based oxidants-1: Chromium peroxide complexes as versatile, mild, and efficient oxidants in organic synthesis. *Tetrahedron* **1986**, *42*, 719–725.

[128] Buijs, W.; Raja, R.; Thomas, J. M.; Wolters, H. On the similarity in catalytic activity of homogeneous and heterogeneous Cr(VI) catalysts in the decomposition of cyclohexyl hydroperoxide. *Catalysis Letters* **2003**, *91*, 253–259.

[129] Alexander, J.; Aaseth, J. Uptake of Chromate in Human Red Blood Cells and Isolated Rat Liver Cells: The Role of the Anion Carrier. *Analyst* **1995**, *120*, 1994–1996.

[130] Lay, P. A.; Levina, A. Activation of molecular oxygen during the reactions of chromium(VI/V/IV) with biological reductants: Implications for chromium-induced genotoxicities. *Journal of the American Chemical Society* **1998**, *120*, 6704–6714.

[131] Codd, R.; Dillon, C. T.; Levina, A.; Lay, P. A. Studies on the genotoxicity of chromium: From the test tube to the cell. *Coordination Chemistry Reviews* **2001**, *216-217*, 537–582.

[132] Salnikow, K.; Zhitkovich, A. Genetic and Epigenetic Mechanisms in Metal Carcinogenesis and Cocarcinogenesis : Nickel, Arsenic, and Chromium. *Chemical Research in Toxicology* **2008**, *21*, 28–44.

[133] Bundesministerium der Justiz und für Verbraucherschutz, Verordnung über die Qualität von Wasser für den menschlichen Gebrauch (Trinkwasserverordnung - TrinkwV). 2001.

[134] Brito, F.; Ascanio, J.; Mateo, S.; Hernández, C.; Araujo, L.; Gili, P.; Martín-Zarza, P.; Domínguez, S.; Mederos, A. Equilibria of chromate(VI) species in acid medium and ab initio studies of these species. *Polyhedron* **1997**, *16*, 3835–3846.

[135] Breuer, M.; Ditrich, K.; Habicher, T.; Hauer, B.; Keßeler, M.; Stürmer, R.; Zelinski, T. Industrial methods for the production of optically active intermediates. *Angewandte Chemie - International Edition* **2004**, *43*, 788–824.

[136] Eschweiler, W. Ersatz von an Stickstoff gebundenen Wasserstoffatomen durch die Methylgruppe mit Hülfe von Formaldehyd. *Berichte der deutschen chemischen Gesellschaft* **1905**, *38*, 880–882.

[137] Clarke, H. T.; Gillespie, B.; Weisshaus, S. Z. The Action of Formaldehyde on Amines and Amino Acids. *Journal of the American Chemical Society* **1933**, *55*, 4571–4587.

[138] Leuckart, R. Ueber eine neue Bildungsweise von Tribenzylamin. *Berichte der deutschen chemischen Gesellschaft* **1885**, *18*, 2341–2344.

[139] Wallach, O. Zur Kenntniss der Terpene und der ätherischen Oele; Zweiundzwanzigste Abhandlung. I. Ueber die Bestandtheile des Tujaöls. *Justus Liebig's Annalen der Chemie* **1893**, *272*, 99–122.

[140] Mannich, C.; Krösche, W. Ueber ein Kondensationsprodukt aus Formaldehyd, Ammoniak und Antipyrin. *Archiv der Pharmazie* **1912**, *250*, 647–667.

[141] Ingersoll, A. W. α-Phenylethylamine. *Organic Syntheses* **1937**, *17*, 76.

[142] Vineyard, B. D.; Knowles, W. S.; Sabacky, M. J.; Bachman, G. L.; Weinkauff, D. J. Asymmetric Hydrogenation. Rhodium Chiral Bisphosphine Catalyst. *Journal of the American Chemical Society* **1977**, *99*, 5946–5952.

[143] Noyori, R.; Ohkuma, T.; Kitamura, M.; Takaya, H.; Sayo, N.; Kumobayashi, H.; Akutagawa, S. Asymmetric Hydrogenation of β-Keto Carboxylic Esters. A Practical, Purely Chemical Access to β-Hydroxy Esters in High Enantiomeric Purity. *Journal of the American Chemical Society* **1987**, *109*, 5856–5858.

[144] Sharpless, K. B.; Patrick, D. W.; Truesdale, L. K.; Biller, S. A. A New Reaction. Stereospecific Vicinal Oxyamination of Olefins by Alkyl Imido Osmium Compounds. *Journal of the American Chemical Society* **1975**, *97*, 2305–2307.

[145] Katsuki, T.; Sharpless, K. B. The First Practical Method for Asymmetric Epoxidation. *Journal of the American Chemical Society* **1980**, *102*, 5974–5976.

[146] Jacobsen, E. N.; Markó, I.; Mungall, W. S.; Schröder, G.; Sharpless, K. B. Asymmetric Dihydroxylation via Ligand-Accelerated Catalysis. *Journal of the American Chemical Society* **1988**, *110*, 1968–1970.

[147] Blaser, H.-U.; Buser, H.-P.; Jalett, H.-P.; Pugin, B.; Spindler, F. Iridium Ferrocenyl Diphosphine Catalyzed Enantioselective Reductive Alkylation of a Hindered Aniline. *Synlett* **1999**, *1999*, 867–868.

[148] Li, W.; Zhang, X. In *Stereoselective Formation of Amines*; Li, W., Zhang, X., Eds.; Topics in Current Chemistry; Springer Berlin Heidelberg: Berlin, Heidelberg, 2014; Vol. 343.

[149] Togni, A.; Breutel, C.; Schnyder, A.; Spindler, F.; Landert, H.; Tijani, A. A Novel Easily Accessible Chiral Ferrocenyldiphosphine for Highly Enantioselective Hydrogenation, Allylic Alkylation, and Hydroboration Reactions. *Journal of the American Chemical Society* **1994**, *116*, 4062–4066.

[150] Blaser, H.-U. The Chiral Switch of (S)-Metolachlor: A Personal Account of an Industrial. *Advanced Synthesis and Catalysis* **2002**, *344*, 17.

[151] Xiao, D.; Zhang, X. Highly enantioselective hydrogenation of acyclic imines catalyzed by Ir-f-binaphane complexes. *Angewandte Chemie - International Edition* **2001**, *40*, 3425–3428.

[152] Hou, G.; Gosselin, F.; Li, W.; McWilliams, J. C.; Sun, Y.; Weisel, M.; O'Shea, P. D.; Chen, C.-Y.; Davies, I. W.; Zhang, X. Enantioselective Hydrogenation of N–H Imines. *Journal of the American Chemical Society* **2009**, *131*, 9882–9883.

[153] Hou, G.; Tao, R.; Sun, Y.; Zhang, X.; Gosselin, F. Iridium - Monodentate Phosphoramidite-Catalyzed Asymmetric Hydrogenation of Substituted Benzophenone N - H Imines active compounds of pharmaceutical relevance to human and animal. *Journal of American Chemical Society* **2010**, *132*, 2124–2125.

[154] Chang, M.; Liu, S.; Huang, K.; Zhang, X. Direct catalytic asymmetric reductive amination of simple aromatic ketones. *Organic Letters* **2013**, *15*, 4354–4357.

[155] Zhang, Y.; Lim, C. S.; Boon Sim, D. S.; Pan, H. J.; Zhao, Y. Catalytic enantioselective amination of alcohols by the use of borrowing hydrogen methodology: Cooperative catalysis by iridium and a chiral phosphoric acid. *Angewandte Chemie - International Edition* **2014**, *53*, 1399–1403.

[156] Tararov, V. I.; Kadyrov, R.; Riermeier, T. H.; Borner, A. On the reductive amination of aldehydes and ketones catalyzed by homogeneous Rh(I) complexes. *Chemical Communications* **2000**, 1867–1868.

[157] Zhao, Q.; Wen, J.; Tan, R.; Huang, K.; Metola, P.; Wang, R.; Anslyn, E. V.; Zhang, X. Rhodium-catalyzed asymmetric hydrogenation of unprotected NH imines assisted by a thiourea. *Angewandte Chemie - International Edition* **2014**, *53*, 8467–8470.

[158] Rubio-Pérez, L.; Javier Pérez-Flores, F.; Sharma, P.; Velasco, L.; Cabrera, A. Stable preformed chiral palladium catalysts for the one-pot asymmetric reductive amination of ketones. *Organic Letters* **2009**, *11*, 265–268.

[159] Kadyrov, R.; Riermeier, T. H. Highly Enantioselective Hydrogen-Transfer Reductive Amination: Catalytic Asymmetric Synthesis of Primary Amines. *Angewandte Chemie - International Edition* **2003**, *42*, 5472–5474.

[160] R. Boyd, D.; Hamilton, R.; T. Thompson, N.; E. Stubbs, M. Base catalysed decomposition of oxaziridines to yield N-unsubstituted aldimines. *Tetrahedron Letters* **1979**, *20*, 3201–3204.

[161] Gallardo-Donaire, J.; Ernst, M.; Trapp, O.; Schaub, T. Direct Synthesis of Primary Amines via Ruthenium-Catalysed Amination of Ketones with Ammonia and Hydrogen. *Advanced Synthesis and Catalysis* **2016**, *358*, 358–363.

[162] Zimmerman, P. M. Single-ended transition state finding with the growing string method. *Journal of Computational Chemistry* **2015**, *36*, 601–611.

[163] VandeVondele, J.; Krack, M.; Mohamed, F.; Parrinello, M. QUICKSTEP: Fast and accurate density functional calculations using a mixed Gaussian and plane waves approach. *Computer Physics Communications* **2005**, *167*, 103–128.

[164] Hutter, J.; Iannuzzi, M.; Schiffmann, F.; Vandevondele, J. CP2K: Atomistic simulations of condensed matter systems. *Wiley Interdisciplinary Reviews: Computational Molecular Science* **2014**, *4*, 15–25.

[165] VandeVondele, J.; Hutter, J. Gaussian basis sets for accurate calculations on molecular systems in gas and condensed phases. *Journal of Chemical Physics* **2007**, *127*, 114105.

[166] Goedecker, S.; Teter, M.; Hutter, J. Separable dual-space Gaussian pseudopotentials. *Physical Review B* **1996**, *54*, 1703–1710.

[167] Hartwigsen, C.; Goedecker, S.; Hutter, J. Relativistic separable dual-space Gaussian pseudopotentials from H to Rn. *Physical Review B* **1998**, *58*, 3641–3662.

[168] Krack, M. Pseudopotentials for H to Kr optimized for gradient-corrected exchange-correlation functionals. *Theoretical Chemistry Accounts* **2005**, *114*, 145–152.

[169] Martínez, L.; Andrade, R.; Birgin, E. G.; Martínez, J. M. PACKMOL: A package for building initial configurations for molecular dynamics simulations. *Journal of Computational Chemistry* **2009**, *30*, 2157–2164.

[170] Humphrey, W.; Dalke, A.; Schulten, K. VMD: Visual Molecular Dynamics. *Journal of Molecular Graphics* **1996**, *14*, 33–38.

[171] Wiberg, K. B.; Crocker, L. S.; Morgan, K. M. Thermochemical Studies of Carbonyl Compounds. 5. Enthalpies of Reduction of Carbonyl Groups. *Journal of the American Chemical Society* **1991**, *113*, 3447–3450.

[172] Kubas, G. J. Dihydrogen complexes as prototypes for the coordination chemistry of saturated molecules. *Proceedings of the National Academy of Sciences* **2007**, *104*, 6901–6907.

[173] Jia, G.; Lau, C. P. Structural, acidity and chemical properties of some dihydrogen/hydride complexes of Group 8 metals with cyclopentadienyls and related ligands. *Coordination Chemistry Reviews* **1999**, *190-192*, 83–108.

[174] Noyori, R.; Ohkuma, T. Asymmetric catalysis by architectural and functional molecular engineering: Practical chemo- and stereoselective hydrogenation of ketones. *Angewandte Chemie - International Edition* **2001**, *40*, 40–73.

[175] Dub, P. A.; Gordon, J. C. The mechanism of enantioselective ketone reduction with Noyori and Noyori-Ikariya bifunctional catalysts. *Dalton Transactions* **2016**, *45*, 6756–6781.

[176] Dub, P. A.; Scott, B. L.; Gordon, J. C. Why does alkylation of the N-H functionality within M/NH bifunctional Noyori-type catalysts lead to turnover? *Journal of the American Chemical Society* **2017**, *139*, 1245–1260.

[177] Zhang, J.; Leitus, G.; Ben-David, Y.; Milstein, D. Efficient homogeneous catalytic hydrogenation of esters to alcohols. *Angewandte Chemie - International Edition* **2006**, *45*, 1113–1115.

[178] Balaraman, E.; Gunanathan, C.; Zhang, J.; Shimon, L. J.; Milstein, D. Efficient hydrogenation of organic carbonates, carbamates and formates indicates alternative routes to methanol based on CO2 and CO. *Nature Chemistry* **2011**, *3*, 609–614.

[179] Langer, R.; Fuchs, I.; Vogt, M.; Balaraman, E.; Diskin-Posner, Y.; Shimon, L. J. W.; Ben-David, Y.; Milstein, D. Stepwise metal-ligand cooperation by a reversible aromatization/deconjugation sequence in ruthenium complexes with a tetradentate phenanthroline-based ligand. *Chemistry - A European Journal* **2013**, *19*, 3407–3414.

[180] Matthes, J.; Gründemann, S.; Toner, A.; Guari, Y.; Donnadieu, B.; Spandl, J.; Sabo-Etienne, S.; Clot, E.; Limbach, H. H.; Chaudret, B. Ortho-Metalated Ruthenium Hydrido Dihydrogen Complexes: Dynamics, Exchange Couplings, and Reactivity. *Organometallics* **2004**, *23*, 1424–1433.

[181] Zeise, W. C. Von der Wirkung zwischen Platinchlorid und Alkohol, und von den dabei enstehenden neuen Substanzen. *Annalen der Physik und Chemie* **1831**, *4*, 497–541.

[182] Black, M.; Mais, R. H. B.; Owston, P. G. The crystal and molecular structure of Zeise's salt, KPtCl3.C2H4.H2O. *Acta Crystallographica B* **1969**, *25*, 1753–1759.

[183] Peris, E.; Lee, J. C.; Rambo, J. R.; Eisenstein, O.; Crabtree, R. H. Factors Affecting the Strength of X-H H-M Hydrogen Bonds. *Journal of the American Chemical Society* **1995**, *117*, 3485–3491.

[184] Giese, M.; Albrecht, M.; Bannwarth, C.; Raabe, G.; Rissanen, K. From attraction to repulsion: anion – pi interactions between bromide and fluorinated phenyl groups. *Chemical Communications* **2011**, *47*, 8542–8544.

[185] Sinnokrot, M. O.; Valeev, E. F.; Sherrill, C. D. Estimates of the Ab Initio Limit for π–π Interactions: The Benzene Dimer. *Journal of the American Chemical Society* **2002**, *124*, 10887–10893.

[186] Koenig, K. E.; Sabacky, M. J.; Bachman, G. L.; Christopfel, W. C.; Bamstorff, H. D.; Friedman, R. B.; Knowles, W. S.; Stults, B. R.; Vineyard, B. D.; Weinkauff, D. J. Asymmetric Hydrogenations With Rhodium Chiral Phosphine Catalysts. *Annals of the New York Academy of Sciences* **1980**, *333*, 16–22.

[187] Kitamura, M.; Tsukamoto, M.; Bessho, Y.; Yoshimura, M.; Kobs, U.; Widhalm, M.; Noyori, R. Mechanism of Asymmetric Hydrogenation of α-(Acylamino)acrylic Esters Catalyzed by BINAP−Ruthenium(II) Diacetate. *Journal of the American Chemical Society* **2002**, *124*, 6649–6667.

[188] Noyori, R.; Kitamura, M.; Ohkuma, T. Toward efficient asymmetric hydrogenation: architectural and functional engineering of chiral molecular catalysts. *Proceedings of the National Academy of Sciences* **2004**, *101*, 5356–62.

[189] Jeulin, S.; de Paule, S. D.; Ratovelomanana-Vidal, V.; Genet, J.-P.; Champion, N.; Dellis, P. Asymmetric Catalysis Special Feature Part II: Chiral biphenyl diphosphines for asymmetric catalysis: Stereoelectronic design and industrial perspectives. *Proceedings of the National Academy of Sciences* **2004**, *101*, 5799–5804.

[190] Hoge, G.; Wu, H.-P.; Kissel, W. S.; Pflum, D. A.; Greene, D. J.; Bao, J. Highly Selective Asymmetric Hydrogenation Using a Three Hindered Quadrant Bisphosphine Rhodium Catalyst. *Journal of the American Chemical Society* **2004**, *126*, 5966–5967.

[191] Hedberg, C.; Källström, K.; Brandt, P.; Hansen, L. K.; Andersson, P. G. Asymmetric Hydrogenation of Trisubstituted Olefins with Iridium−Phosphine Thiazole Complexes: A Further Investigation of the Ligand Structure. *Journal of the American Chemical Society* **2006**, *128*, 2995–3001.

[192] Spindler, V. F.; Pugin, B.; Blaser, H.-U. Neuartige Diphosphinoiridium-Katalysatoren für die enantioselektive Hydrierung von N-Arylketiminen. *Angewandte Chemie* **1990**, *102*, 561–562.

[193] Kang, G.-J.; Cullen, W. R.; Fryzuk, M. D.; James, B. R.; Kutney, J. P. Rhodium(I)-catalysed Asymmetric Hydrogenation. *Journal of the Chemical Society, Chemical Communications* **1988**, *0*, 1466–1467.

[194] Fagnou, K.; Lautens, M. Halide Effects in Transition Metal Catalysis Halide Effects in Transition Metal Catalysis. *Angewandte Chemie - International Edition* **2002**, *41*, 26–47.

[195] Shannon, R. D. Revised Effective Ionic Radii and Systematic Studies of Interatomic Distances in Halides and Chalcogenides. *Acta Crystallographica A* **1976**, *32*, 751.

[196] Iwadate, Y.; Kawamura, K.; Igarashi, K.; Mochinaga, J. Effective ionic radii of nitrite and thiocyanate estimated in terms of the Boettcher equation and the Lorentz-Lorenz equation. *The Journal of Physical Chemistry* **1982**, *86*, 5205–5208.

[197] Tolman, C. A. Steric Effects of Phosphorus Ligands in Organometallic Chemistry and Homogeneous Catalysis. *Chemical Reviews* **1977**, *77*, 313–348.

[198] Aigueperse, J.; Mollard, P.; Devilliers, D.; Chemla, M.; Faron, R.; Romano, R.; Cuer, J. P. Fluorine Compounds, Inorganic. *Ullmann's Encyclopedia of Industrial Chemistry* **2000**, *15*, 735–768.

[199] Kranenburg, M.; Kamer, P. C. J.; van Leeuwen, P. W. N. M. The Effect of the Bite Angle of Diphosphane Ligands on Activity and Selectivity in Palladium-Catalyzed Allylic Alkylation. *European Journal of Inorganic Chemistry* **1998**, *1*, 25–27.

[200] Dierkes, P.; van Leeuwen, P. W. N. M. The bite angle makes the difference: a practical ligand parameter for diphosphine ligands. *Journal of the Chemical Society, Dalton Transactions* **1999**, 1519–1530.

[201] The Cambridge Structural Database. https://www.ccdc.cam.ac.uk/solutions/csd-system/components/csd/.

[202] Tauchert, M. E.; Kaiser, T. R.; Göthlich, A. P. V.; Rominger, F.; Warth, D. C. M.; Hofmann, P. Phosphonite ligand design for nickel-catalyzed 2-methyl-3-butenenitrile isomerization and styrene hydrocyanation. *ChemCatChem* **2010**, *2*, 674–682.

[203] Tauchert, M. E.; Warth, D. C.; Braun, S. M.; Gruber, I.; Ziesak, A.; Rominger, F.; Hofmann, P. Highly efficient nickel-catalyzed 2-methyl-3-butenenitrile isomerization: Applications and mechanistic studies employing the TTP ligand family. *Organometallics* **2011**, *30*, 2790–2809.

[204] Mormul, J.; Mulzer, M.; Rosendahl, T.; Rominger, F.; Limbach, M.; Hofmann, P. Synthesis of Adipic Aldehyde by n-Selective Hydroformylation of 4-Pentenal. *Organometallics* **2015**, *34*, 4102–4108.

[205] Mormul, J.; Breitenfeld, J.; Trapp, O.; Paciello, R.; Schaub, T.; Hofmann, P. Synthesis of Adipic Acid, 1,6-Hexanediamine, and 1,6-Hexanediol via Double-n-Selective Hydroformylation of 1,3-Butadiene. *ACS Catalysis* **2016**, *6*, 2802–2810.

[206] Kranenburg, M.; van der Burgt, Y. E.; Kamer, P. C.; van Leeuwen, P. W.; Goubitz, K.; Fraanje, J. New Diphosphine Ligands Based on Heterocyclic Aromatics Inducing Very High Regioselectivity in Rhodium-Catalyzed Hydroformylation: Effect of the Bite Angle. *Organometallics* **1995**, *14*, 3081–3089.

[207] Devon, T. J.; Phillips, G. W.; Puckette, T. A.; Stavinoha, J. L.; Vanderbilt, J. J. Chelate Ligands for Low Pressure Hydroformylation Catalyst and Process Employing Same, United States Patent, US4694109. 1987.

[208] Rosenblatt, M. Remarks on Some Nonparametric Estimates of a Density Function. *The Annals of Mathematical Statistics* **1956**, *27*, 832–837.

[209] Parzen, E. On Estimation of a Probability Density Function and Mode. *The Annals of Mathematical Statistics* **1962**, *33*, 1065–1076.

[210] Haaland, A.; Nilsson, J. E.; Olson, T.; Norin, T. The Determination of Barriers to Internal Rotation by Means of Electron Diffraction. Ferrocene and Ruthenocene. *Acta Chemica Scandinavica* **1968**, *22*, 2653–2670.

Eidesstattliche Versicherung gemäß § 8 der Promotionsordnung der Naturwissenschaftlich-Mathematischen Gesamtfakultät der Universität Heidelberg

1. Bei der eingereichten Dissertation zu dem Thema

   "Quantum Chemical Investigations in Homogeneous Catalysis: Dehydroperoxidation and Asymmetric Reductive Amination"

   handelt es sich um meine eigenständig erbrachte Leistung.

2. Ich habe nur die angegebenen Quellen und Hilfsmittel benutzt und mich keiner unzulässigen Hilfe Dritter bedient. Insbesondere habe ich wörtlich oder sinngemäß aus anderen Werken übernommene Inhalte als solche kenntlich gemacht.

3. Die Arbeit oder Teile davon habe ich bislang nicht an einer Hochschule des In- oder Auslands als Bestandteil einer Prüfungs- oder Qualifikationsleistung vorgelegt.

4. Die Richtigkeit der vorstehenden Erklärungen bestätige ich.

5. Die Bedeutung der eidesstattlichen Versicherung und die strafrechtlichen Folgen einer unrichtigen oder unvollständigen eidesstattlichen Versicherung sind mir bekannt.

Ich versichere an Eides statt, dass ich nach bestem Wissen die reine Wahrheit erklärt und nichts verschwiegen habe.

Ort und Datum	Unterschrift